Quantifying Data Quality and Its Impact on Functional Brain Imaging Experiments

Elliot Howley

Thesis submitted to the University of Nottingham for the degree of Doctor of Philosophy

Supervised by:
Denis Schluppeck
Sue Francis

University of Nottingham, UK
July 2024

Acknowledgements

I would like to express immense gratitude to my supervisors, Denis Schluppeck and Sue Francis, for their guidance throughout my PhD, answering all the many questions I had, and helping this thesis be the best it can be. I would also like to thank Jan Alappadan Paul for his help and conversations during scan sessions, they would have been a lot more boring without him. I'm also incredibly grateful for all the amazing people I've met and become friends with over the course of my PhD, especially my office mates: Richard Leadbeater, Oliver Dibb, Karl Miller, and Felix Lewandowski. In particular, I want to thank Richard Leadbeater and Aimee Theyer for being there for me since our time on the Brain Imaging master's course until now. I'm also immensely grateful for my partner Christina Davidson. Without her love and support, I wouldn't have been able to finish this thesis. I'm so happy we were both able to take this PhD journey together. And finally, thank you to my parents for their unwavering guidance and belief in me throughout my life. I couldn't have got to where I am today without them.

Abstract

Functional Magnetic Resonance Imaging (fMRI) is a widely-used tool in neuroscience research. While there is general agreement on what imaging sequences and methods work best overall, there is much less agreement and consistency on how particular parameter choices are made. These parameter choices can have an effect on data quality, which can negatively affect analysis of this data. It is therefore important to characterise this effect. The thesis investigates the impact of image acceleration techniques on fMRI data quality, quantified using temporal Signal-to-Noise Ratio (tSNR), and explores how these effects vary across different brain regions. The thesis then investigates the impact of higher levels of Gaussian noise and head motion on an important and widely adopted analysis method: population Receptive Field (pRF) analysis. Assessment of the effects of applying image denoising to fMRI data are also investigated throughout.

Chapter 3 presents development and use of the fMRI ROI Analysis Tool (fRAT), software designed to provide a comprehensive Region-of-Interest (ROI) analysis toolset for fMRI data. fRAT addresses the lack of existing fMRI tools making it easy to analyse multiple ROIs with data quality metrics. This tool enables researchers to easily study spatial variations in the relationship between scanning parameters and data quality. The software's features, including statistical analysis and data visualisation capabilities are detailed, and current and potential future applications are highlighted.

Chapter 4 uses fRAT to characterise the effect of hardware (3T Philips Achieva and 3T Philips Ingenia), image acceleration (in-plane SENSE factor and through-plane Multiband factor) and a post-hoc denoising technique (using NOise reduction with DIstribution Corrected [NORDIC] PCA) on

data quality across a selection of regions of interest: the Frontal Pole, the posterior Inferior Temporal Gyrus and the Occipital Pole. The relationship between these variables was found to vary between these regions, supporting the idea that region-wise data quality (tSNR) reporting provides important information.

Chapter 5 evaluates the robustness of pRF analysis in the visual domain to decreased levels of tSNR and increased levels of participant motion through adding simulated thermal noise and head motion to a pre-existing pRF dataset collected in stroke patients (Beh et al., 2021). Work in this chapter also makes use of fRAT to first quantify noise levels and then provide a convenient way to manipulate the data before pRF analysis. It is shown that in general, pRF analysis is more robust to the addition of head motion than to noise, with the polar angle of the pRF estimates being the property most consistently affected by these factors.

Overall, this thesis provides a detailed analysis of the spatially dependent effects of image acceleration on fMRI data quality and underscores the practical consequences of changes in the level of data quality and motion in pRF analysis. The findings aim to inform best practices when conducting fMRI research, and importantly, the software developed within this thesis has been made open-source with usage tutorials to enable it to be used across a wide range of applications in future research.

Table of Contents

List of Figures

List of Tables

Chapter 1

Introduction

1.1 Overview of Thesis

The two main causes of discomfort in magnetic resonance imaging (MRI) scanning sessions are the level of acoustic noise and remaining still for the duration of the scanning session (Chou et al., 2014; Heilmaier et al., 2011). For patients and other vulnerable groups, such as younger participants, these factors can be particularly problematic aggravating issues such as participant motion, which is much more likely to occur in clinical groups and younger children (Pardoe et al., 2016). This can make scanning of such subjects difficult and in extreme examples of subject motion or sensitivity to scanner noise, can lead to unusable data or aborted scan sessions.

Image acceleration techniques can be used to speed up acquisitions, collecting an fMRI volume in a shorter acquisition time, and can be used to reduce scanner noise, but care must be taken as such methods can also negatively affect data quality (Demetriou et al., 2018; Molloy et al., 2014; Todd et al., 2016). Therefore there is a tradeoff between increasing subject comfort and limiting reduction in data quality, which for fMRI data is often assessed through measuring the temporal Signal-to-Noise Ratio (tSNR). This thesis aims to quantify the effect of image acceleration techniques on fMRI data and investigate how this relationship changes across brain regions. Further, this thesis also aims to investigate the impact of additional noise and subject motion on pRF analysis.

In Chapter 2, key concepts underlying the work in this thesis are laid out. First, the basis of the MR signal is discussed, followed by how data is spatially encoded to generate an MR image and the use of acceleration techniques to speed up acquisitions. This is followed by an outline of fMRI, including the nature of the Blood Oxygenation Level Dependent (BOLD) signal and the Haemodynamic Response Function (HRF). Following this, a summary of visual field mapping and population Receptive Field (pRF) analysis is presented – this is an influential and widely used method for analysing fMRI data, particularly in brain areas relating to sensation and perception of vision, touch, and sound. Finally, key concepts relating to data quality are described, including tSNR, assessment of g-factor for fMRI, and principal component analysis (PCA) methods that can be used to denoise fMRI

data, with particular emphasis on the NOise Reduction with DIstribution Corrected (NORDIC) method.

Chapter 3 presents the development and use cases of a Python-based tool to conduct Region-of-Interest (ROI) analysis on fMRI data, termed the fMRI ROI Analysis Tool (fRAT) which has been made available to users on the Python Package Index (PyPi) and is published in the Journal of Open Science Software (Howley et al., 2023). The development of this software became an aim, as there was no current, easy-to-use software available to conduct analysis on multiple ROIs with data quality metrics. The software allows researchers to assess the relationship between scanning parameters (such as SENSE and Multiband [MB] acceleration factors) and data quality metrics (such as tSNR), and how it changes spatially. In this chapter, the design goals of this software are first presented, such as providing a comprehensive Region-of-Interest (ROI) analysis toolset. The functionality of this software is then described, including the ability to conduct inferential statistics with, and create visualisations of the data. Additional use-cases are then outlined. This includes using fRAT to conduct atlas-based power analyses, which avoids the common issue in fMRI research of circular analysis when the effect size statistic and selection criteria are not independent (Kriegeskorte et al., 2010). The fRAT software is freely available, and one of the efforts in the work for this chapter was to also develop guides for a robust software installation experience, and a usage tutorial together with a sample data set (fmri-roi-analysis-tool.readthedocs.io).

Chapter 4 explores the effect of hardware by comparing two MRI scanners and image acquisition parameters (IAPs) on data quality (as measured using tSNR) and acoustic noise using fRAT. The fRAT software developed in Chapter 3 is used to analyse, summarise and report this data. Specifically, work in this chapter varies image acceleration factors (SENSE and MB), and compares results across 3T scanner models (a Philips 60-cm Achieva scanner and a Philips 70-cm wide bore scanner with dStream technology). Additionally, the benefits provided by NORDIC denoising for each image acceleration factor and scanning hardware is also assessed. This chapter uses fRAT to analyse the differing effect of these variables across cortical areas as a whole, as well as for specific regions: the Frontal Pole (FP), the Occipital

Pole (OP) and the posterior Inferior Temporal Gyrus (pITG). The chapter concludes with an assessment of these differences between ROIs and how future research could further explore this topic.

Chapter 5 examines the practical effect of different tSNR and participant motion levels on population Receptive Field (pRF) analysis of visual data. To achieve this, functions provided by fRAT were used to estimate the ground truth noise and motion, and add simulated thermal noise and motion to the fMRI data in a participant dependent manner. This chapter demonstrates how robust pRF analysis is to thermal noise and subject motion.

Chapter 6 concludes with the main findings of this work to quantify the spatially dependent effect of image acceleration techniques on data quality, and the practical effect of various data quality and motion levels on a real-world data analysis application: pRF analysis. It is hoped that this research can be used to guide best practices when collecting fMRI data, to retain optimal image quality whilst minimising acoustics to reduce subject discomfort. Additionally, the open-source software developed within this thesis can be used by other researchers in a wide variety of research applications, for example, when planning studies it can ensure the optimal image acquisition parameters are used for the ROIs and experimental paradigm for a given study.

1.2 COVID Statement

This PhD was undertaken during the COVID-19 pandemic. Some aspects of my thesis work were heavily impacted by the COVID-19 pandemic, causing changes to the initial plans for my thesis. In particular, access to scan facilities was not possible for an extended period of time, therefore additional emphasis in my work was placed on the development of software (Chapter 3). Further, due to university restrictions on MR research scanning of vulnerable subjects during and following the COVID-19 pandemic, a planned study could not be completed. Therefore instead, a dataset which had been collected in stroke patients prior to the pandemic was used for Chapter 5. The data set employed was that published in Beh et al. (2021).

Chapter 2

Background

2.1 Functional Magnetic Resonance Imaging (fMRI)

2.1.1 The MRI signal

The basis of Magnetic Resonance Imaging (MRI) is that certain atomic nuclei when exposed to a strong external magnetic field (B_0), are able to selectively absorb and re-emit radio-frequency (RF) waves. This phenomenon is known as Nuclear Magnetic Resonance (NMR). Atomic nuclei possess an intrinsic fundamental property called nuclear spin (I), which describes the angular momentum of a particle. I is dictated by the ratio of protons to neutrons in an atom, such that an atom with an equal number of protons and neurons have $I = 0$. The criteria for atomic nuclei to be able to undergo NMR is to have a non-zero I, therefore atoms require an uneven number of protons and neutrons to undergo NMR. The most common nucleus for MRI is that of hydrogen (^{1}H), which comprises only a single proton and no neutrons, and so has a $I = \frac{1}{2}$. Since a significant proportion of the human body contains hydrogen atoms, primarily due to water (H_2O) but also from other molecules, hydrogen is the most commonly used atomic nucleus for MRI (Huettel et al., 2014).

The I of protons, creates a magnetic moment, μ. This magnetic moment allows for the interaction between protons and the strong external magnetic field (B_0). The number of possible spin states that a nucleus can have is given by $2I + 1$. Therefore, as protons have $I = \frac{1}{2}$, they have two observable spin states, either parallel or anti-parallel to B_0. Magnetic moments preferentially align (are parallel) with B_0 as this is the lowest energy state. However the proportion of protons that are in the parallel or anti-parallel spin state is a function of the field strength B_0 and temperature T, as described by the Boltzmann distribution (Huettel et al., 2014), such that an increase in field strength or a decrease in temperature increases the net number of protons in the parallel spin state. On average, there is slightly more protons in the parallel spin state than the anti-parallel state, and this creates a net magnetisation vector (M_0) aligned parallel to B_0.

When protons are placed in the external B_0 field, their spin states also begin

to undergo precession (with random phase) on an axis around B_0. The frequency of this precession is known as the Larmor (or resonant) frequency. This is directly proportional to the strength of B_0 (T) and the gyromagnetic ratio (γ) of the atomic nuclei (which for protons is 42.58 MHz/Tesla) and is given by:

$$\omega = \gamma B \tag{2.1}$$

with the Larmor frequency in MHz which is in the radiofrequency (RF) range.

The application of an RF (B_1) field at the Larmor frequency applied orthogonal to B_0 can be used to rotate the orientation of the spin states and thus cause M_0 to rotate by a given flip angle dependent on the duration and amplitude of the B_1 field. For example, the application of a 90° (also termed excitation) RF pulse will tip the M_0 magnetisation which is aligned along z into the transverse (xy-) plane. This will also cause spins that before were preferentially aligned with B_0 to come into phase, leading to phase coherence. The net magnetisation then precesses in the transverse plane, inducing a current in the receiver coils at the Larmor frequency. At this point immediately after the 90° RF pulse there is transverse (M_{xy}) but not longitudinal (M_z) magnetisation. After the B_1 pulse ends, two processes then occur, the spins begin to relax back into the parallel state causing an exponential increase in longitudinal magnetisation, and the spins experience a scrambling of their phase leading to an exponential decrease in transverse magnetisation. The time it takes for 63% of the longitudinal magnetisation to recover is known as the T_1 time, whilst the time for the transverse magnetisation to decay is known as the T_2 time. T_1 and T_2 relaxation times are intrinsic properties that vary between tissue types. By choosing appropriate imaging sequences, scans can be weighted to highlight the difference in T_1 or T_2 values between tissues, creating MRI contrast in structural imaging. For example, if a short time between repetitions (TR) of successive B_1 pulses is used, the longitudinal magnetisation is not able to fully recover between TRs. Thus the signal is dependent on the varying longitudinal magnetisation recovery time (T_1) between tissues, creating a T_1-weighted image. This type

of image is commonly used for standard brain imaging, as it clearly depicts grey matter, white matter, and cerebrospinal fluid.

2.1.2 Spatial encoding of the data

The signal generated after a 90° RF pulse represents the sum of the signals from over the entire imaged object and is called the Free Induction Decay (FID), this signal needs to be spatially encoded to allow for the accurate localization of signal intensities. To do this, in addition to the static strong magnetic field, time varying magnetic fields generated using gradient coils can be switched on to create a linearly changing magnetic field along a chosen axis. As ω is dependent on field strength B, the spatially varying magnetic fields caused by the gradient coils causes an additional spatially-dependent modulation of the precession frequency of the protons. If the carrier frequency and bandwidth of the B_1 pulse is tuned, then applying a RF pulse with a slice gradient gives a slice-selective excitation, typically this is termed to be applied in the z-axis. As this B_1 pulse only tips the spins from a single slice into the transverse plane, these are the only spins that will induce a current in the RF receivers. After slice-excitation, a spatially varying magnetic field in the x and y-axis is also induced by the gradient coils, to create a varying precession frequency within these planes. The variation of ω in this slice frequency-encodes the location of the protons in this axis. A linearly changing magnetic field is also induced in the other orthogonal axis, causing a cumulative phase shift for the protons depending on the strength of the gradient. This induces phase decoherence in the slice and phase-encodes the location of the protons in this final plane.

Through the combination of the slice-selective pulse, the frequency-encoding gradient, and the phase-encoding gradient, the location of protons are spatially encoded along each axis. This spatial frequency information is represented by k-space (Figure 2.1). A 2D inverse Fourier Transform is then used to convert this k-space data into the final image space. For a given field-of-view, increasing the k-space matrix size increases the spatial resolution of the image. While each sample of data in the frequency-encoded direction is collected continuously during the data readout, sampling of data in

Figure 2.1

Example visualisation of k-space

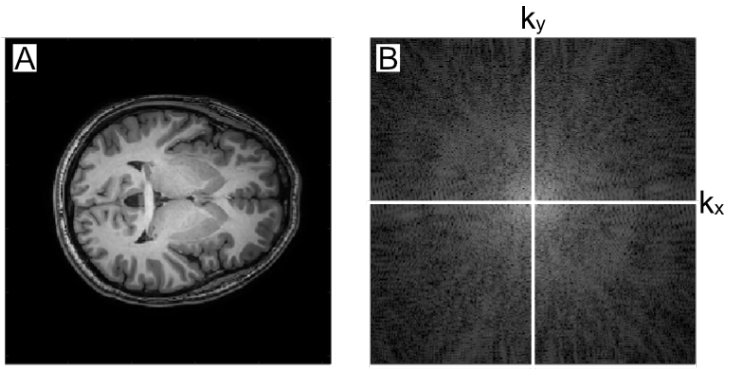

Note. (A) shows a brain in image space, whereas (B) shows the k-space representation. For (B), each row in k_y represents a different application of a phase-encoding gradient, whereas each column in k_x represents the linearly varying frequency-encoding gradient.

the phase-encoded direction requires the application of a different gradient magnetic field. Each application of the phase-encoding gradient is repeated every TR, with a different phase-encoding gradient strength used in each repetition. Therefore, imaging time is highly dependent on the number of data samples (and thus the spatial resolution) in the phase-encoding axis, whereas increased resolution in the frequency-encoded axis only requires an increased sampling rate.

A high resolution structural image can be generated by collecting a single line of k-space per excitation pulse, known as a spin-warp acquisition scheme. However when performing fMRI, rapid image acquisition is crucial. Therefore for fMRI an Echo-Planar-Imaging (EPI) scheme is used, which collects the entire k-space in a single shot following one excitation pulse. This is demonstrated in Figure 2.2.

2.1.3 Image acceleration techniques

The possibility of accelerating imaging through methods such as the simultaneous excitation of multiple slices was explored early in MRI's development

Figure 2.2

Comparison between k-space acquisition techniques

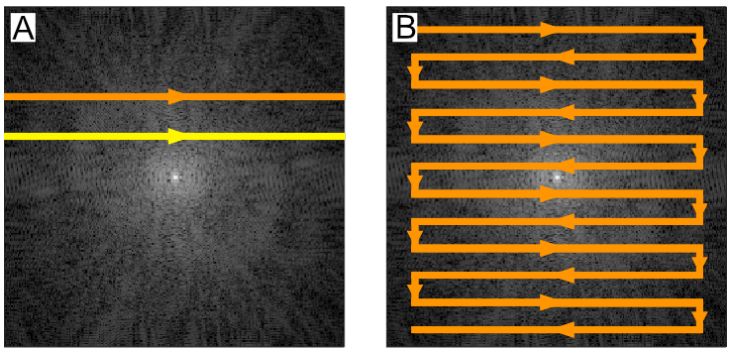

Note. (A) shows k-space acquisition with a spin warp acquisition scheme. The orange and yellow lines in k-space show data collected during separate applications of the phase-encoding gradient and RF-excitation pulse. (B) shows k-space acquisition with a Echo-Planar-Imaging acquisition scheme. k-space data is collected here during a single RF-excitation pulse with a zig-zag traversal pattern of k-space.

(Maudsley, 1981). Early methods of multislice excitation, such as Phase-offset multiplanar (POMP) volume imaging (Glover, 1991), increased signal sensitivity compared to standard sequential data collection. However, there was no reduction in acquisition time (Barth et al., 2016). Early methods of multislice excitation were limited by coil design, primarily due to the prevalent use of single-channel RF coils at the time. However, with the development of multi-channel RF coils (for example 32-channel head coils as used for work in this thesis), the spatially varying placement and sensitivities of RF receiver coils could be utilised to achieve more precise spatial localisation of the MR signal. This technique, known as parallel imaging, has enabled the development of several methods to accelerate scanning.

SENSitivity Encoding (SENSE) image reconstruction (Pruessmann et al., 1999) is one method that was enabled with the development of parallel imaging, and is widely used today and for the imaging collected in this thesis. With this method, individual images are first reconstructed for each of the coil channels. These images are then combined, with each image weighted according to its coil's spatial sensitivity map. In standard Fourier

Figure 2.3

Example of k-space undersampling

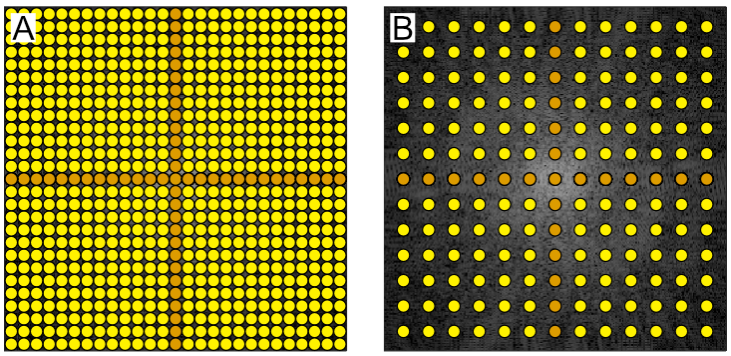

Note. Each point on k-space represents a sample. (B) shows k-space undersampling relative to (A) through increased k-space data spacing in both the frequency-encoding and phase-encoding direction.

imaging, reducing the sampling density of phase-encoding steps results in the reduction of the FOV (Pruessmann et al., 1999). This phase undersampling reduces imaging time but results in gaps in the k-space data, which translates into image space as overlapping or aliased signals in the direction of the phase encoding. However, SENSE combines and unwraps these partial FOV images into full FOV images. Thus, SENSE allows the possibility of reducing the number of phase-encoding steps without a loss in spatial resolution. For example, using an acceleration factor (R) of 2, half of the phase-encoding steps are collected, and a ½FOV image will be created for each coil. These are then combined and unwrapped into full FOV images. The advantage of reducing the number of phase encoding steps is that this shortens the acquisition time linearly, with $R = 2$ reducing acquisition time by half. Figure 2.3 shows an example of k-space undersampling.

The development of multi-channel RF coils also allowed the development of multiband (MB) imaging (Larkman et al., 2001) as termed on Philips scanners, also known as Simultaneous MultiSlice (SMS) on other manufacturer platforms. Similar to in-plane SENSE parallel imaging methods, MB imaging uses coil sensitivity profiles, but here this is used to separate simultaneously acquired slices. MB first uses a shaped MB RF pulse to excite multiple slices (MB factor). While these RF pulses can be designed in sev-

Figure 2.4

Comparison of single-band and Multiband MRI image acquisition

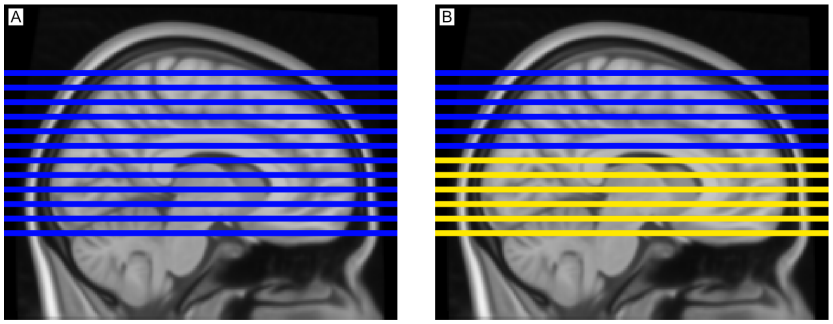

Note. (A) shows a standard single-band acquisition where each blue line represents a separate slice acquisition. (B) shows a multiband acquisition with an acceleration factor of two, where blue and yellow lines represent slices assigned to different bands. Two slices are acquired simultaneously, with each blue slice paired with a corresponding yellow slice, e.g., the lowest blue slice is acquired simultaneously with the lowest yellow slice.

eral ways, the most straightforward method is to sum several standard RF pulse shapes in the time domain. To aid signal separation, these RF pulses are given different phase offsets (Barth et al., 2016). The acquisition time reduction achieved with MB is equal to the number of simultaneously acquired slices (Figure 2.4). MB factors of 2 up to 6 can be collected, however there is a trade-off between image acquisition acceleration, and the resulting slice coupling and reduction in signal-to-noise ratio, as will be discussed later in this thesis.

The reduction in EPI readout duration achievable using SENSE and the reduction in the time to collect an fMRI volume using MB imaging, can both benefit fMRI. For example, reducing the readout duration with SENSE will reduce magnetic susceptibility related artefacts (Weiger et al., 2002), and allows the use of lower echo times (Jaermann et al., 2006). Further, reducing acquisition time with SENSE and collecting multiple slices using MB can be used to increase the temporal resolution of scanning and increase the sampling frequency of the haemodynamic response function (see subsection 2.3.2). There are further possible benefits possible using these methods. If acquisition time is not reduced while using higher MB or SENSE acceler-

ation factors, there is the benefit of reduced acoustic noise generation due to a reduced density of gradients (de Zwart et al., 2002). Further, MB can also be combined with SENSE (Barth et al., 2016; Preibisch et al., 2015) to further reduce scan time or noise. Therefore, these methods provide ways of increasing scan subject comfort through reducing scan length or acoustic scanner noise, however the effect on data quality when using these methods must also be considered.

In SENSE images, the signal-to-noise ratio (SNR) has an upper bound dictated by the square root of the sampling reduction factor (Pruessmann et al., 1999). In essence, SNR is bound by acquisition time, with faster acquisition times leading to a lower, upper bound for SNR. The impact of aliasing also persists after unwrapping the images, leading to a spatially varying noise amplification factor (see subsection 2.3.3). As with SENSE, there is potential issues regarding aliasing with MB imaging. Low coil sensitivity variation between each slice can result in aliasing between slices (Blaimer et al., 2013). Therefore early MB imaging used relatively wide slice separation to increase coil sensitivity variation and reduce aliasing. However there have since been methodological and hardware improvements which reduce this issue. While techniques such as CAIPIRINHA (Breuer et al., 2005) reduce the dependence of aliasing in MB imaging on the coil geometry, improvements in coil design also increased coil sensitivity variation along the slice direction. Therefore modern MB imaging is able to use much more closely spaced slices. Further discussions about data quality can be found in section 2.3. It is important to note that there are also a number of additional image acceleration methods, such as GRAPPA image reconstruction (Griswold et al., 2002), Compressed SENSE (Zong et al., 2014) and partial fourier reconstruction methods (McGibney et al., 1993). However these methods are outside the scope of this thesis.

2.1.4 Blood Oxygenation Level Dependent (BOLD) contrast

As neurons fire, their metabolic requirements increase, necessitating an increase in oxygenated blood flow to the active area to support aerobic respiration. The cerebral blood flow (CBF) and cerebral blood volume (CBV)

Figure 2.5

The effect of oxyhaemoglobin and deoxyhaemoglobin in red blood cells on the main magnetic field

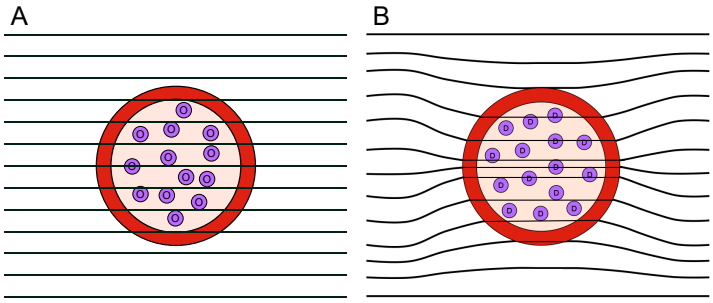

Note. (A) Oxyhaemoglobin (O) is diamagnetic so does not cause local field distortions. (B) Deoxyhaemoglobin (D) is paramagnetic and so causes local field distortions, leading to faster spin dephasing and a shorter T_2^* time.

in response to neuronal activity increases to a level higher than the cerebral metabolic rate for oxygen ($CMRO_2$), leading to an increase in the amount of oxygen-carrying hemoglobin (oxyhemoglobin) and a decrease in the amount of non-oxygen-carrying hemoglobin (deoxyhemoglobin). These two forms of haemoglobin differ in their magnetic properties, with oxyhaemoglobin being diamagnetic, and deoxyhaemoglobin being paramagnetic. Deoxyhemoglobin, being paramagnetic, has a greater tendency to induce local magnetic field inhomogeneities due to its interaction with the external magnetic field (Figure 2.5). This causes local dephasing of protons and thus an increase in the transverse magnetisation decay rate (shorter transverse T_2^* relaxation time). Therefore, when brain regions are active, the relative increase in oxyhaemoglobin compared to deoxyhaemoglobin leads to a decrease in the local magnetic susceptibility, and a larger signal. The signal strength in functional MRI (fMRI) is therefore dependent on the relative ratio of oxyhaemoglobin and deoxyhaemoglobin, and this signal is known as the Blood Oxygenation Level Dependent (BOLD) signal.

In fMRI, the repetition time (volume TR) indicates the time between successive slice-selective pulses applied to a given slice, while the echo time (TE) refers to the time between the slice-selective RF pulse and the collection of the signal or "echo" of the protons at the centre of k-space, typically using

a gradient echo EPI scheme. Note that T_1-weighted images aim to produce contrast by highlighting the inherent differences in T_1 relaxation times between tissues. It does this by using short TRs (~500ms) which, for typical T_1 values in the brain, do not allow the longitudinal magnetisation to fully recover between successive RF pulses, and short TEs (~14ms) which do not allow for significant spin dephasing and transverse magnetisation to occur. Thus the contribution of longitudinal magnetisation to the signal is increased, and the influence of transverse decay to the signal is minimised. In contrast, when performing fMRI this uses a long TR (volume TR ~2000ms) between RF pulses of a given slice allowing spins to fully relax back into the longitudinal plane, and a TE (~30ms) that allows transverse magnetisation decay, with the optimal TE for fMRI being equal to the grey matter T_2^*. By allowing proton dephasing to develop, fMRI creates signal change in time due to contrast between regions with high oxyhaemoglobin levels on activation compared to deoxyhaemoglobin levels at rest, thus enabling the detection of those brain regions with neural activity through the BOLD signal. Images produced by maximising the contrast caused by transverse magnetisation decay are known as T_2^*-weighted images.

2.1.5 Haemodynamic Response Function (HRF)

fMRI aims to measure the change in BOLD signal over time. The typical BOLD response to a single impulse stimulus is characterised by the Haemodynamic Response Function (HRF). The HRF is composed of a number of components (Figure 2.6): an initial dip, a peak after roughly 5-7 seconds, a post-stimulus undershoot and then a return to baseline. In response to repeated stimulus presentation, the HRF also exhibits a plateau phase after the peak. As seen in Figure 2.6 however, the HRF takes ~30 seconds to return to baseline after a single impulse stimulus. This sluggish nature of the HRF heavily limits the temporal resolution of fMRI.

While the peak and plateau are consistently measured effects, measurement of the initial dip (Silva et al., 2000) and post-stimulus undershoot (Mildner et al., 2001) are variable. As a result the BOLD response is typically approximated by a Gamma distribution, with parameters chosen to best fit the

Figure 2.6

BOLD haemodynamic response functions following stimulus presentation

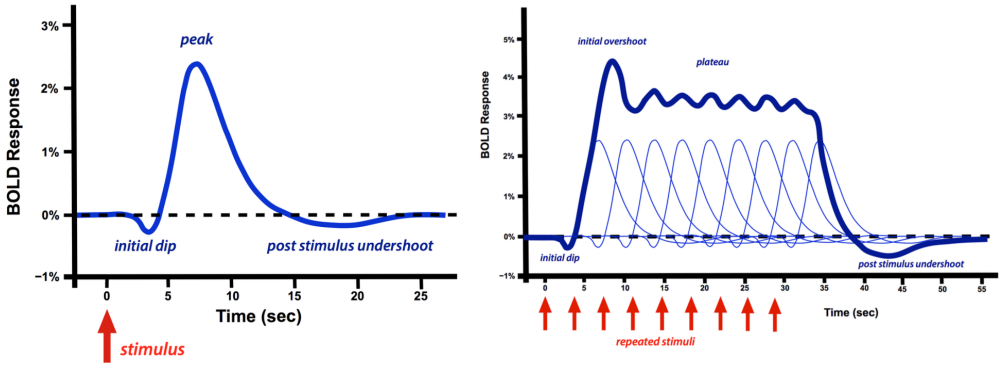

Note. Left panel shows the HRF response to a single stimulus presentation. Right panel shows the HRF response to the presentation of multiple stimuli. Adapted from MRIquestions.com, courtesy of Elster, A. D.

typically observed BOLD response defined as the canonical HRF. However, the actual HRF can exhibit significant variability due to individual differences or the brain region under investigation. Therefore, the shape of the canonical HRF can be adjusted to improve its accuracy and even produce subject-specific HRFs. The chosen HRF is then convolved with a model of the stimuli presented to the participant to create a predicted time course. This predicted time course can then be compared with each voxel's actual time course to identify which voxels are likely to be responding to the stimuli.

Within this thesis the visual cortex is investigated in Chapter 5. Therefore, the following sections outline methods to study visual responses.

2.2 Visual field mapping

Spatial arrangement is the most important element of a visual image (Wandell et al., 2007). The importance of this property to visual processing is reflected in the retinotopic organisation of early visual areas and in many other visual areas to some degree (Wandell et al., 2007). This cortical retinotopic map roughly follows a polar coordinate system (Horton & Hoyt, 1991),

meaning that relative to the central point of the visual field, a polar angle difference in the visual field has a corresponding polar angle difference in the cortical representation. Due to cortical magnification, eccentricity differences in the visual field are mapped non-linearly onto the cortical surface. The relationship between eccentricity in the visual field and distances on the cortical surface in V1 can be approximated by an exponential function (Engel et al., 1997). This means that less eccentric visual areas (those closer to fixation) in the fovea are represented in a larger fraction of visual cortex than the peripheral visual field.

The polar angle property of retinotopic maps can be used to delineate borders in the visual cortex (Engel et al., 1997). This is a fundamental idea underlying the definition of functional regions-of-interest, used for analysing specific visual areas. In addition, delineation of visual areas allows for easier comparison between participants and gives a baseline for typical visual map organisation (Wandell et al., 2007). Other than the retinotopic organisation of visual areas, another property of these areas that can be extracted with the appropriate methodology is the receptive field size of neuronal populations (Dumoulin & Wandell, 2008). Measurements of receptive field sizes are important as they can aid in the understanding of visual processing after injury, with these measurements also potentially serving as a guide for targeted rehabilitation treatment (Papanikolaou et al., 2014).

2.2.1 Travelling-wave retinotopic mapping

The introduction of the travelling-wave retinotopic analysis technique (Engel et al., 1994) made it possible to produce retinotopic maps of multiple areas with high anatomical precision (Engel et al., 1997), using simple visual stimuli and non-invasive fMRI. For travelling-wave analysis, the stimuli consist of cyclical rotating wedges and expanding or contracting rings (Figure 2.7), with a contrast-reversing checkerboard pattern used to increase neural activation. These stimuli are shown to a participant while they undergo a fMRI scan. The travelling-wave analysis leverages the phase-encoded nature of the stimuli to map stimulus locations in the visual field to neuronal activity. This is achieved by determining which phase of the stimulus best corresponds to

Figure 2.7

Typical stimuli used for pRF analysis

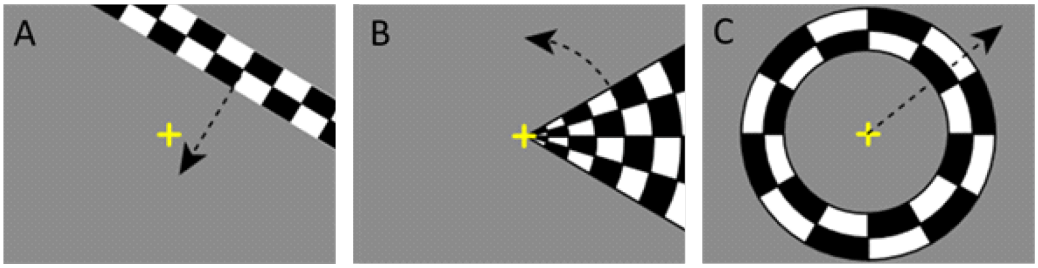

Note. **(A)** showns moving bar stimuli, **(B)** shows rotating wedge stimuli, and **(C)** shows extending/contracting ring stimuli.

each voxel's time-series data, giving the location of the visual field location which provides the highest stimulus driven activity. The wedge and ring stimuli provide polar angle and eccentricity visual field maps respectively, with both visual field maps together providing the polar coordinates for the visual field location which a voxel produces the largest BOLD response to.

2.2.2 Population receptive field mapping

Population receptive field (pRF) analysis, first developed by Dumoulin & Wandell (2008), is an fMRI technique which builds on previous visual field mapping techniques (Engel et al., 1994, 1997). By using the wedge and ring stimuli from the travelling-wave technique as well as a bar stimulus of varying motion and orientation (Figure 2.7), pRF techniques can produce additional visual field map information. While the travelling-wave analysis technique gives estimates for the visual field location which produces the highest cortical activation for each voxel, the pRF technique additionally provides an estimate of a neuronal population's receptive field size. There are two main differences between the procedure of the travelling-wave method and the direct-fit pRF technique that allows the additional pRF size information to be extracted.

Firstly, the pRF method links the exact stimulus location at each point in time as it moves around the visual field with the measured fMRI response.

This means that a cyclical stimulus (such as the wedge or ring stimuli) is no longer required and more complex stimuli is able to be used, such as the moving bar stimulus. However, wedge and ring stimuli are still used commonly with the pRF method, as there are regional activation differences in response to these stimuli. For example, the striate cortex has a higher overall response to presented wedge stimuli than the lateral occipital (Dumoulin & Wandell, 2008). Therefore, having a broad range of stimulus types for pRF analysis can be beneficial.

Secondly, the process for analysing the data for the pRF method is different to the travelling-wave technique (Figure 2.8). An initial pRF model is assigned to each voxel. Using this initial estimate, the assumed HRF, and the location of the visual stimulus over time, a predicted model time course of fMRI responses is generated. This model time course is then compared to the actual time course, and the pRF parameters are iteratively adjusted to best fit the observed responses, resulting in a detailed map of receptive fields across the visual cortex. This is calculated separately for each voxel, with the pRF estimate usually being an isotropic Gaussian shape (Figure 2.9) with 3 parameters: the x and y coordinates of the centre of the receptive field; and the receptive field size (standard deviation of the Gaussian).

This approach provides more accurate visual field maps than the conventional travelling-wave approach, especially in regards to measurements of eccentricity (Dumoulin & Wandell, 2008). Additionally, through giving measurements of the receptive field of neuronal populations, additional conclusions can be drawn. For example, receptive field size was found to be 5 times larger in the lateral and ventral occipital versus early visual areas, and receptive field size increases as a function of eccentricity in early visual areas. pRF analysis provides a moderately reliable measure of pRF size (van Dijk et al., 2016) that in some cases has found to on average account for 60% of the variance in the data (Dumoulin & Wandell, 2008). The advantage provided by the pRF method of allowing a measurement of receptive field size has also allowed it to be a useful technique for research into other areas of the brain. For example, it has been used in the somatosensory cortex to create topographic maps of hand representations (Asghar et al., 2023).

Figure 2.8

Flow chart describing the pRF linear model estimation procedure

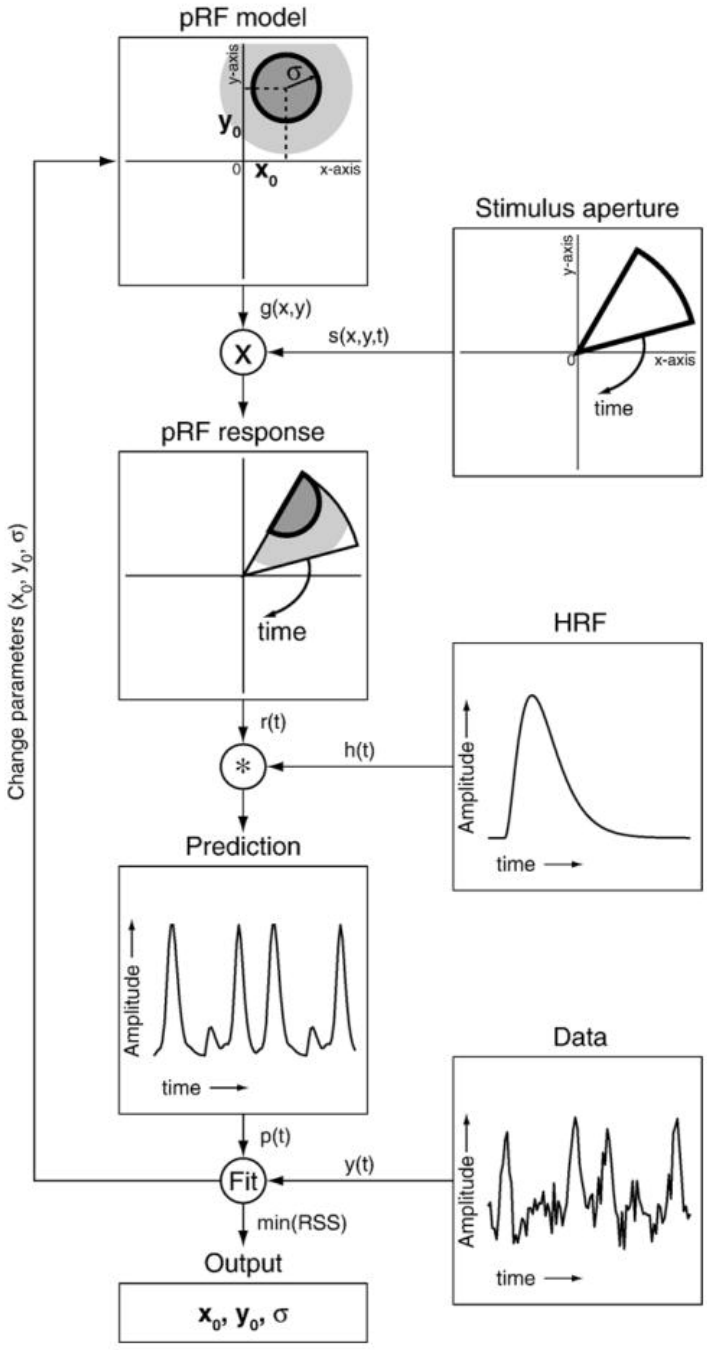

Note. The pRF linear model is calculated for every voxel independently. Adapted from Dumoulin & Wandell (2008).

Figure 2.9

Visualisation of a population receptive field model in visual space

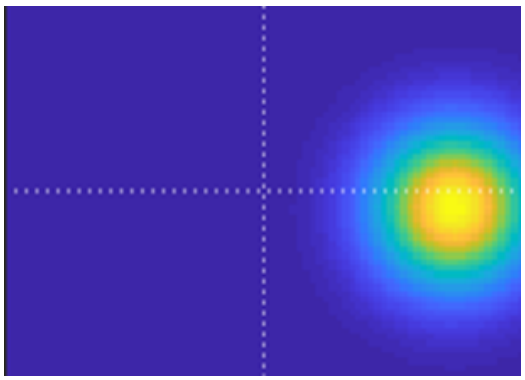

Note. Data is shown for a single voxel.

2.3 Data quality measures

2.3.1 Measuring image quality: image SNR

Signal-to-noise ratio (SNR) is a scientific and engineering metric that quantifies the magnitude of a desired signal compared to the magnitude of background noise. SNR is defined as a ratio where a value higher than 1 indicates that there is more signal than noise. For MRI, the choice of image acquisition protocol and the hardware used significantly contribute to the SNR of the images. For example, image SNR (iSNR) in biological tissue has been found to be approximately proportional to the scanner field strength (Takahashi et al., 2003) and iSNR scales directly with the voxel volume (Parker & Gullberg, 1990). Thus for MRI, the quantification of iSNR allows for the comparison between imaging protocols, imaging hardware, as well as data preprocessing techniques.

A common method for calculating iSNR involves comparing the signal of the imaged object to the background noise of the image (Edelstein et al., 1986). Where S represents the signal intensity, calculated as the mean signal within the imaged object, and σ represents the background noise, calculated as the standard deviation of a region outside the imaged object, iSNR can

Figure 2.10

Background noise distributions for complex and magnitude MR images

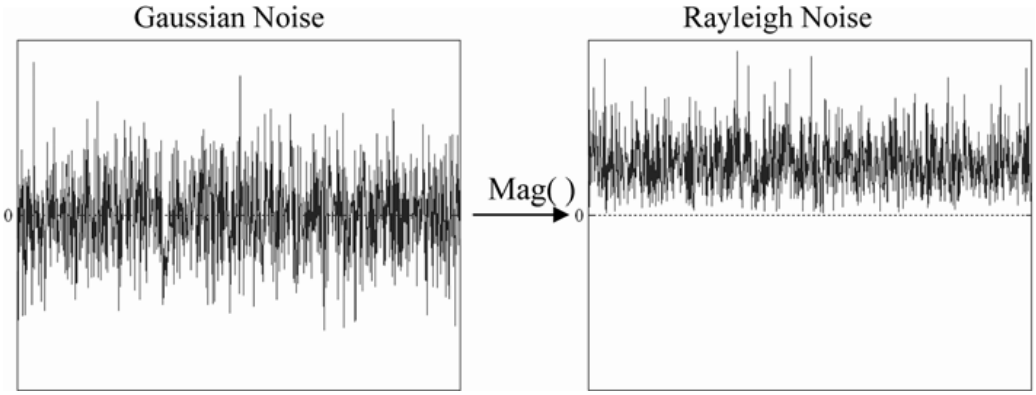

Note. Noise in a complex MR image has a Gaussian distribution with zero mean and standard deviation σ. Noise in magnitude images however follow the Rayleigh distribution, with non-zero mean and a lower standard deviation than for complex images. Adapted from Reeder (2007).

be calculated as:

$$\text{iSNR} = \frac{S}{\sigma} \tag{2.2}$$

Alternatively, instead of selecting a region outside the imaged object to calculate background noise, if the noise distribution is known, for example by collecting a noise scan, the standard deviation of this distribution can be taken as a measure of background noise. A noise scan is collected by acquiring data while radiofrequency pulses and gradient fields are turned off, to provide a measure of the noise distribution in the entire image which also accounts for parallel imaging effects on the noise distribution.

Most research MR images are presented as magnitude images, which alters the behaviour of the background noise as absolute values are used. In regions where only noise is present, such as outside the imaged object, the noise follows a Rayleigh distribution (Gudbjartsson & Patz, 1995). This can be seen in Figure 2.10, where taking the magnitude of the data gives a non-zero mean to the background noise and leads to a lower apparent σ.

As seen in Figure 2.11, this effect of the noise following a Rayleigh distribu-

Figure 2.11

Background noise distributions for complex and magnitude MR images

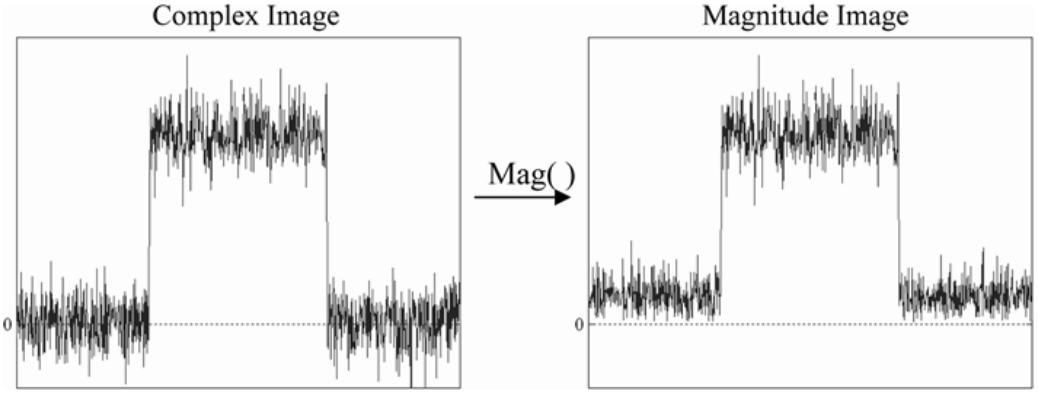

Note. Noise changes from a Gaussian to a Rayleigh distribution when taking the magnitude of a complex image. This reduces the apparent background noise level, whereas noise within regions with high SNR remains unaffected. Adapted from Reeder (2007).

tion varies dependent on SNR. In regions with high SNR, such as regions inside the imaged object, noise is unaffected by the Rayleigh distribution. Therefore, to correct for this underestimation of σ when using magnitude images, a correction factor needs to be applied. In the case of magnitude images collected using four or more coils, the magnitude correction factor is approximately 0.7 (Constantinides et al., 1997). Thus Equation 2.2 becomes:

$$\text{iSNR} = 0.7 \cdot \frac{S}{\sigma} \tag{2.3}$$

2.3.2 Measuring time course stability: temporal SNR

The goal of fMRI is to detect small activation-related changes in the signal across time. However, the fMRI signal also contains noise from various sources that can fluctuate over time. The SNR measure used for fMRI should therefore reflect the temporal stability of the signal, and thus the ability to detect activation-related changes. Therefore, while image SNR is valuable for comparing image acquisition parameters, it does not adequately address the needs of fMRI.

There are a number of different SNR definitions used throughout the fMRI literature, with most simulation studies labelling both contrast-to-noise ratio (CNR) and temporal SNR (tSNR) measures as simply "SNR" (Welvaert & Rosseel, 2013). Further there is significant differences in how CNR is measured across the literature. However, all CNR definitions attempt to provide a measure of noise in the signal, while also providing a measurement of activation signal strength. tSNR in contrast does not provide a measurement of the activation signal strength but instead provides a measurement of the temporal stability of the signal. Additionally, tSNR specifically is affected by many factors such as the degree of image acceleration (Molloy et al., 2014; Todd et al., 2016) or the hardware used to collect data (Petridou et al., 2013). As tSNR plays an important moderating role for BOLD sensitivity, it is widely used as a metric to compare the effect of imaging hardware or acquisition parameters on data quality (Demetriou et al., 2018; Hutton et al., 2011; Todd et al., 2016).

tSNR is not spatially uniform, with regions that have similar anatomy and/or function likely to have similar tSNR values (Welvaert & Rosseel, 2013); therefore tSNR is calculated separately for each voxel. As demonstrated by Welvaert & Rosseel (2013), tSNR can be calculated as:

$$\text{tSNR} = \frac{\bar{S}}{\sigma_N} \tag{2.4}$$

where $\bar{S}$ represents the signal level for that voxel and is calculated as the mean of the timeseries, whereas σ_N represents the noise for that voxel and is calculated as the standard deviation of the timeseries. $\bar{S}$ contains contributions from both the baseline signal and the possible fluctuations in the signal due to the experimental task, whereas σ_N is comprised of several noise sources such as thermal noise, physiological noise and task-related noise. BOLD signal fluctuations are typically small, ranging from approximately 1% to 3% for data collected at 3T (Tjandra et al., 2005). Thus while $\bar{S}$ does contain contributions from task-related BOLD signal changes, tSNR is a measure of data quality and is not informative regarding the task-related activation signal strength. The various CNR measures outlined by

Welvaert & Rosseel (2013) do however include a measurement of the activation signal strength. Due to this, Welvaert & Rosseel (2013) argue that tSNR is only suitable for resting state fMRI, not task-related fMRI with the opposite being true for CNR.

The relationship between BOLD sensitivity and tSNR for task-related fMRI was illustrated by Murphy et al. (2007). In their study, they presented an equation aimed at determining the number of time points (N_t) theoretically necessary to detect an activation, given a set tSNR value, effect size (eff) and α level. When using a block design with a stimulus being shown for 50% of the timepoints, N_t can be calculated as:

$$N_t = 8\left(\frac{erfc^{-1}(\alpha)}{(\text{tSNR})(\text{eff})}\right)^2 \tag{2.5}$$

where $erfc^{-1}$ is the inverse complementary error function. This equation can then be generalised to designs where the stimulus is not shown for 50% of timepoints, where R represents the ratio of the timepoints where the stimulus is shown versus the total number of timepoints, this equation can be expressed as:

$$N_t = \frac{2}{R(1-R)}\left(\frac{erfc^{-1}(\alpha)}{(\text{tSNR})(\text{eff})}\right)^2 \tag{2.6}$$

where R is constrained to values between 0 and 1.

With these equations it can be calculated that given a timeseries with a tSNR of 75, to detect activation with an effect size of 0.5% at an α level of 0.05, ~110 time points are required. This increases to ~250 time points if tSNR decreases to 50. With a TR of 2s, this means that roughly, scan length would need to be 3.5 minutes for the first instance, but decreasing tSNR by 20% would increase scan time by over 100% to roughly 8 minutes. However, this is the case with the liberal α level of 0.05. If the required α level is reduced to 0.001, in the case of a timeseries with a tSNR of 75, ~310 time points (a ~10 minute scan) would be needed, whereas in the case of 50 tSNR, ~690 time points (a ~23 minute scan) would be needed. Using

simulations, Murphy et al. (2007) also derived the equation to calculate the number of timepoints needed to guarantee activation detection (N_g):

$$N_g = 8\left[1.5\left(1 + e^{\log_{10}\alpha/2}\right)\left(\frac{erfc^{-1}(\alpha)}{(\text{tSNR})(\text{eff})}\right)\right]^2 \tag{2.7}$$

The above equation indicates that for a given effect size, α and tSNR, N_g will be much higher than N_t. For example, with a tSNR of 75, at an α level of 0.05 and for an effect size of 0.5%, N_t = ~110 timepoints whereas N_g = ~550 timepoints, or roughly a 3.5 minute or a 18 minute scan respectively with a TR of 2s. However the difference between N_t and N_g decreases as α decreases. Further, while detection of an effect is possible using shorter scan durations than calculated N_g, it is not guaranteed.

Given a set effect size, α level, and statistical power, a power analysis can calculate the sample size necessary to detect an effect in a study. Similarly, given a set effect size, α level, and tSNR, the equations above can be used to calculate either the number of timepoints necessary to detect activation, or the number of timepoints necessary to guarantee detection. Thus as statistical power or tSNR increases, the chance of finding an effect increases. In this way, tSNR is an important data quality metric for fMRI as it can act as a proxy for statistical power. Due to the dependence of BOLD sensitivity on effect size, this means the effect of tSNR is also paradigm dependent, with experimental designs that have lower expected effect sizes requiring a higher tSNR in order to have the same BOLD sensitivity.

In addition to the factors stated above, tSNR is also dependent on factors such as resolution, with tSNR having a very strong negative correlation with spatial resolution ($R^2 = 0.97$), increasing asymptotically as voxel size increases (Yoo et al., 2018). As image acquisition is accelerated using methods such as MB or SENSE, increases in spatial and/or temporal resolution are possible. However, these resolution increases cause reduced net magnetisation and T_1 relaxation effects, leading to a decrease in tSNR (Yoo et al., 2018).

According to the equations derived by Murphy et al. (2007), this suggests

that resolution increases would also lead to an attenuation of BOLD sensitivity. Demetriou et al. (2018) investigated the effect of increased temporal resolution (with temporal resolution increasing as MB acceleration factor increased) on BOLD sensitivity. They found that increased temporal resolution and MB acceleration factor did attenuate tSNR at higher acceleration factors, and this higher temporal resolution did not provide a consistent benefit for task-based data using conventional GLM analysis. However, even with tSNR being attenuated, resting-state data did benefit from a higher temporal resolution. In contrast, Yoo et al. (2018) showed that a high temporal resolution can compensate for the effect of reduced tSNR on BOLD sensitivity for task-based data, but only at high spatial resolutions where there is minimal physiological noise and thermal noise dominates. These contrasting results may be a result of the spatial resolutions used in each study. Yoo et al. (2018) only found benefits to increasing temporal resolution at spatial resolutions of 1.5mm isotropic, but not at 2mm isotropic; however, the spatial resolution used by Demetriou et al. (2018) was even lower than this value, at 3mm isotropic.

Therefore, while the equations presented by Murphy et al. (2007), are useful in highlighting the link between tSNR and BOLD sensitivity, they suggest that lower tSNR results in decreased BOLD sensitivity, given a certain α and effect size. However, this is not necessarily the case. Increasing spatial and temporal resolution typically results in lower tSNR but can, in certain scenarios, yield higher BOLD sensitivity (Yoo et al., 2018). Moreover, the benefits of enhanced temporal resolution are moderated by various factors, including experimental design, statistical outcome measures, and analysis methods (Demetriou et al., 2018), adding further complexity to this relationship.

2.3.3 Noise amplification due to parallel imaging (g-factor)

While parallel imaging reduces imaging time, the tradeoff is that the SNR of parallel imaging accelerated sequences is always lower than that of non-accelerated sequences. In addition to the factors affecting SNR noted in subsection 2.3.1 & subsection 2.3.2, the SNR level of the reconstructed im-

age in parallel imaging accelerated sequences, are further reduced in two additional ways (Reeder, 2007). Firstly, image acceleration through parallel imaging decreases the sampling of the data:

$$\mathrm{SNR}_R = \frac{\mathrm{SNR}_0}{\sqrt{R}} \tag{2.8}$$

where R is the parallel imaging acceleration factor used in image acquisition, and SNR_0 is the SNR of the equivalent un-accelerated image.

As noted in subsection 2.1.3, undersampling of the k-space data leads to aliasing in image space. Therefore the second cause of lower SNR levels when using parallel imaging, is noise amplification relating to the ability of the coil configuration to unwrap aliased pixels (Pruessmann et al., 1999). This noise amplification is highly dependent on coil geometry, and therefore is quantified by the geometry or g-factor:

$$\mathrm{SNR}_R = \frac{\mathrm{SNR}_0}{g\sqrt{R}} \tag{2.9}$$

This equation can be rearranged as:

$$g = \frac{\mathrm{SNR}_0}{\mathrm{SNR}_R\sqrt{R}} \tag{2.10}$$

with the g-factor always having a value of one or more. The g-factor is typically non-uniform across the image, with a higher g-factor representing a local increase in noise, not a decrease in signal. Areas furthest from coil elements and near the center of the imaging FOV typically have the highest g-factors. This can be seen in Figure 2.12, which shows the spatial dependence of the g-factor and greater noise amplification towards the center of the image. It is important to note however, that due to the aliasing resulting from undersampling when using parallel imaging acceleration, local noise amplification primarily affects parallel imaging methods. However, MB acceleration can also be affected by this spatially dependent noise amplification factor if there is not enough variation in coil sensitivity along the slice

Figure 2.12

Visualisation of the effect of parallel imaging acceleration factor on noise

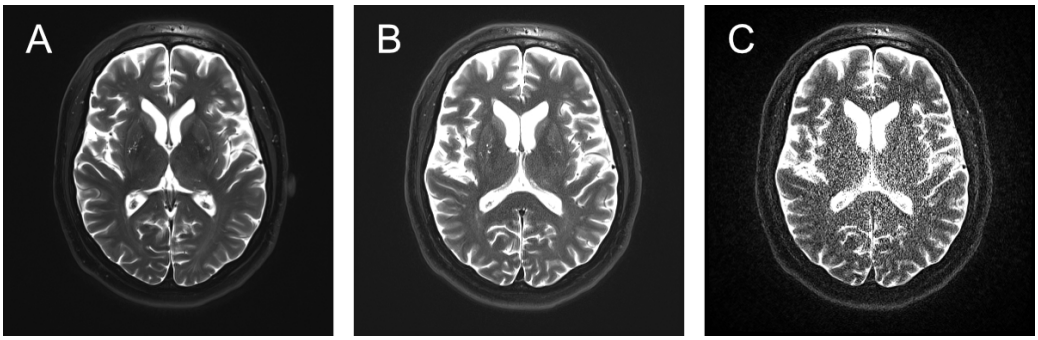

Note. (A) No acceleration. (B) Acceleration factor R = 3. (C) Acceleration factor R = 6. Adapted from MRIquestions.com, courtesy of Elster, A. D.

direction (Blaimer et al., 2013; Risk et al., 2021).

2.3.4 PCA denoising

In many cases, MRI data suffers from low SNR, such as in high resolution fMRI or when high image acceleration factors are used. As outlined in subsection 2.3.2, this in many cases leads to lower BOLD sensitivity, reducing the ability to reliably find activation during functional scanning. Thus noise reduction strategies, are commonly employed during data preprocessing to increase tSNR to improve signal sensitivity (Moeller et al., 2021), an example of which being spatial smoothing (Triantafyllou et al., 2006). Spatial smoothing acts as a low-pass filter, averaging signal intensity across neighbouring voxels. This process reduces the contribution of high-frequency sources, such as thermal noise, while preserving the contribution of low-frequency components, such as task-based signal changes (Worsley et al., 2002). While spatial smoothing is a commonly used approach to improve tSNR, it inherently limits the spatial specificity within the data. To get around this limitation, more targeted denoising methods using principal component analysis (PCA) have been developed.

A principal component analysis of MR data shows that the majority of signal-related variance is contained in a few principal components, whereas noise is spread over a much larger number of components (Veraart, Novikov, et al.,

2016). Therefore, PCA can be used for the identification and subsequent removal of noise. The Marchenko-Pastur Principal Component Analysis (MP-PCA) approach (Veraart, Novikov, et al., 2016) is a commonly used noise suppression method for diffusion MRI (Moeller et al., 2021). However as the MPPCA approach relies on a certain level of information redundancy in order to properly distinguish between signal-only and noise-only principal components, given enough redundant information, this method is also able to work with other imaging modalities, such as fMRI (Veraart, Fieremans, et al., 2016). As the Marchenko-Pastur distribution (Marčenko & Pastur, 1967) characterises the expected distribution of eigenvalues for random matrices, the principal components that follow this distribution are considered to be noise (Veraart, Novikov, et al., 2016). In this context, eigenvalues indicate the amount of variance explained by each principal component, and singular values are their square roots. Thus, the MPPCA approach uses the largest singular value according to the Marchenko-Pastur distribution, to set a threshold to remove noise-only principal components.

There are however a number of noise distribution assumptions made by the Marchenko-Pastur distribution that are often violated. For example, the Marchenko-Pastur distribution assumes uniformity of noise across the image, however as discussed in subsection 2.3.3, the application of parallel imaging techniques such as SENSE introduces spatially non-uniform noise. Further, there is an assumption that the noise will have a zero-mean, however as detailed in subsection 2.3.1, MRI data often exhibits a non-zero-mean Rayleigh distribution when only the magnitude information of MRI data is used.

The **NO**ise **R**eduction with **DI**stribution **C**orrected (**NORDIC**) method introduced by Moeller et al. (2021), attempts to overcome the problems encountered with MPPCA due to violations of these noise distribution assumptions. As both the magnitude and phase information is used for NORDIC, the data follows a zero-mean Gaussian distribution. Further, the noise in the image is transformed from spatially variant to spatially uniform by: 1) quantifying g-factor across the image, and 2) using g-factor as a normalisation factor for the signal. A Monte-Carlo simulation using a noise image (where no radiofrequency excitation is applied), is used to find the mean largest singular value across the sample. As with MPPCA, this value is now

used as a noise threshold, however here, as the noise image quantifies the Gaussian-distributed thermal noise, this threshold represents the point at which components cannot be distinguished from Gaussian noise. As only components that cannot be distinguished from Gaussian noise are removed, the impact on the real MR signal is negligible. As NORDIC removes principal components that are indistinguishable from Gaussian noise, NORDIC can be expected to provide the largest improvement to data in protocols where the Gaussian-distributed thermal noise dominates other noise sources such as physiological noise. For example, thermal noise becomes the most common noise source as voxel volume decreases (Liu, 2016).

Both MPPCA and NORDIC can be effective in recovering underlying signal, however as SNR decreases, the MPPCA approach becomes a less effective de-noising method than NORDIC, potentially removing too many signal components if the transition between signal-only and noise-only components isn't sharp (Moeller et al., 2021). Regardless, while the components removed using the MPPCA approach are difficult to identify, both the NORDIC and MPPCA methods lead to increased SNR (Moeller et al., 2021; Veraart, Novikov, et al., 2016). However, in comparison to MPPCA, the requirements for NORDIC are less demanding, making it easier to implement. Specifically, while NORDIC necessitates a noise image and the acquisition of complex rather than magnitude data, both of these options can be easily implemented on scanner hardware, with the time penalty to collect a noise volume only being a few seconds. On the other hand, MPPCA relies on data redundancy to effectively distinguish between noise and signal during PCA analysis, which for some imaging modalities such as fMRI, can incur considerable time costs.

The effect of spatial smoothing, NORDIC and MPPCA were investigated across a range of fMRI acquisition parameters, with it being found that all three of these strategies increased BOLD sensitivity (Dowdle et al., 2023). Additionally, NORDIC and spatial smoothing were found to provide similar levels of BOLD sensitivity (Dowdle et al., 2023). While NORDIC did cause some degree of spatial smoothing (5.1% on average), this was found to be at a level significantly lower than all other data processing methods (8.0% for MPPCA, 52.7% for 1 voxel of smoothing, and 142.8% for 1.5 voxels of

smoothing). Thus while NORDIC was originally demonstrated using diffusion MRI data, this study demonstrates the benefits that NORDIC can provide to other imaging modalities such as fMRI, especially for thermal noise dominated acquisition protocols.

In this thesis, the NORDIC denoising method is explored in Chapter 4 and Chapter 5.

Chapter 3

Development of fMRI Region-of-Interest Analysis Tool (fRAT)

The software described in this chapter has been published in the Journal of Open Source Software as:

Howley, E., Francis, S., & Schluppeck, D. (2023). fRAT: an interactive, Python-based tool for region-of-interest summaries of functional imaging data. Journal of Open Source Software, 8(85), 5200. https://doi.org/10.21105/joss.05200.

3.1 Introduction

Functional magnetic resonance imaging (fMRI) is widely used to address basic cognitive as well as clinical neuroscience questions. There are numerous parameters that can be changed when collecting fMRI images, with the specific choice of image acquisition and sequence parameters used having a marked effect on the acquired data. The optimal parameter selection may vary across the brain, for example the optimal echo time to image a voxel is equal to the T_2^* of grey matter in that voxel, and since T_2^* varies across the brain (Clare et al., 2001) so does the optimal echo time. Many imaging parameters however do not have a singular optimal value, and the optimal parameter choice has to be considered against trade-offs. For example, increasing the in-plane SENSE parallel acceleration and the through-plane Multiband (MB) acceleration factor can significantly reduce the volume acquisition time (volume TR), however accelerating the image acquisition in this way also leads to spatially dependent noise amplification as quantified by the g-factor (Reeder, 2007).

Investigating the effect of these parameters on data quality across the brain is crucial to ensure scans can provide informative insights. Data quality metrics, in particular temporal signal-to-noise ratio (tSNR) of the fMRI scan, can be used to optimise fMRI scan parameters for a chosen set of regions-of-interest (ROI) relevant to the task under investigation. While ROI analysis is possible with current tools (Poldrack, 2007), reporting of data quality metrics such as tSNR and image SNR (iSNR) is typically performed over the whole brain or for a small number of manually defined voxels. Importantly, this approach can obscure important inter-regional differences in data quality metrics. This is because while the numerous neuroimaging libraries offer a wide range of functionality, no neuroimaging library exists that provides a comprehensive solution for ROI-based investigations. In response to this need, I developed the fMRI ROI Analysis Tool (Howley et al. (2023); fRAT), a Python-based dedicated software solution designed to streamline the assessment of data quality metrics and simplify ROI analysis in neuroimaging studies. This tool addresses the challenges that arise when attempting to extract meaningful insights from specific brain regions by facilitating summary

and multivariate analysis of data quality metrics and functional statistical measures (such as beta maps) simultaneously across multiple ROIs.

In the following section, I will describe the tools and techniques available for fMRI analysis, many of which are used within fRAT.

3.1.1 Overview of fMRI software

With over 30 years of continued research and development, the field of fMRI analysis has expanded significantly, offering a diverse array of approaches to analyse neuroimaging data. This wealth of toolsets serve as a foundation from which it is possible to answer important questions about the human brain. Several general-purpose neuroimaging libraries and analysis toolboxes are available, including AFNI (Analysis of Functional NeuroImages) (Cox, 1996), SPM (Statistical Parametric Mapping) (Penny et al., 2011) and FSL (FMRIB Software Library) (Jenkinson et al., 2012). These libraries support different neuroimaging modalities, for instance, FSL and AFNI have built-in functionality for diffusion-weighted imaging analysis. Their fMRI tools also share common features, such as the ability to preprocess and conduct statistical analysis of fMRI data. Although the fMRI toolset offered by these libraries shares many similarities, there are differences in how data preprocessing and analysis is implemented.

Bowring et al. (2019) examined the cross-software variability of these libraries across multiple datasets, finding significant variation between libraries. For example, while large effects were found to be robust across libraries, with smaller effects there was inconsistency across libraries. Bowring et al. (2022) examined the source of this variability between packages, finding that it is dependent on factors such as task paradigm, with event related-designs more susceptible to factors such as the assumed haemodynamic response model or the orthogonalisation procedure of regressors. While these studies examined the differences and the source of the variability between these packages, they did not examine which package provides the most accurate results. As preprocessing and statistical modelling are multistage processes, the accuracy of each step within the

Figure 3.1

Projects maintained by the NiPreps community

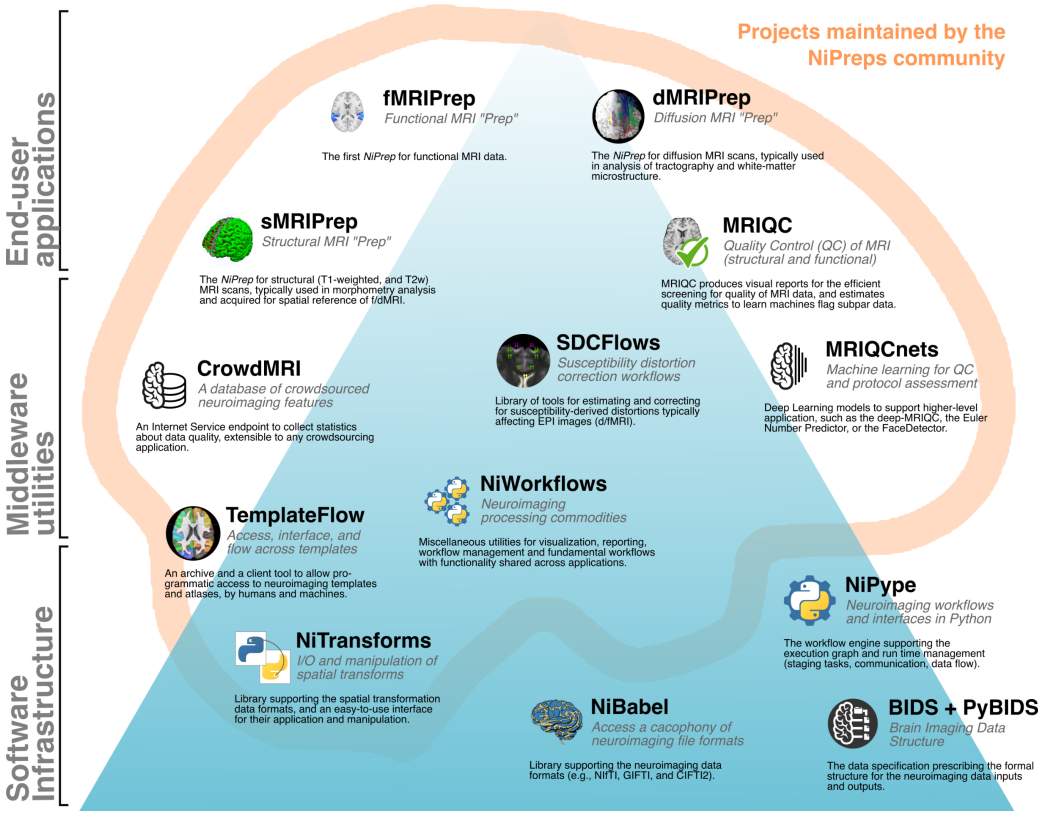

Note. Figure adapted from https://www.nipreps.org/.

analysis pipeline contributes to the total accuracy of the end result. For example, when using the linear registration tools of SPM and FSL with default settings to register participant fMRI data sets to the MNI152 template brain (MNI152 is the Montreal Neurosciences Institute averaging of 3DT1 data sets from 152 different participants), SPM has been shown to have a registration failure rate of 31% compared to FSL which has a 11% failure rate. Further, SPM registration failure was associated with low image Signal-to-Noise Ratio (iSNR) (Dadar et al., 2018).

Many specialized tools have also been developed, with some offering features not found in general-purpose neuroimaging libraries, while others can serve as substitutes for certain functions. For example, optiBET is a specialised brain extraction tool that can be used in place of the brain extraction tools provided by general-use libraries (e.g. BET in FSL). optiBET pro-

duces higher quality brain extraction results than the tools provided by these general-purpose neuroimaging libraries, particularly in cases where data contains severe pathologies that affect brain shape (Lutkenhoff et al., 2014).

There are also broader neuroimaging projects which aim to create neuroimaging tools with a shared design philosophy. One example is the NiPreps (*NiPreps*, n.d.) project which encompasses a variety of specialised Python libraries for working with neuroimaging data. The aim of the NiPreps project is for researchers to be able to produce transparent and reproducible workflows. As seen in Figure 3.1, Nipreps libraries encompass a diverse range of tasks useful for fMRI analysis, from tools such as using Nibabel that provide low-level interfaces to read and write to/from commonly used neuroimaging file formats, to end-user applications such as MRIQC which provides image quality metrics for fMRI data. The Nipreps software infrastructure tool Nipype (Gorgolewski et al., 2011) is used in many other Nipreps libraries, as it provides a universal interface to existing neuroimaging software such as FreeSurfer (Fischl, 2012), FSL (Jenkinson et al., 2012), SPM(Penny et al., 2011) and AFNI (Cox, 1996). This allows multiple software packages to be combined in the same workflow, allowing the user to leverage the advantages of each tool. Example code to combine tools from multiple libraries can be seen in Figure 3.2. MRIQC (Esteban et al., 2017) and fMRIPrep (Esteban et al., 2019) are two Nipreps libraries which use the Nipype workflow engine to combine the tools from multiple neuroimaging software, which in the case of fmriPrep helps it to achieve higher spatial accuracy in its preprocessing pipeline than that of FSL's FEAT preprocessing (Esteban et al., 2019).

There are several tools that provide functionality to report ROI wise summaries, including the widely used Freesurfer infrastructure (Fischl, 2012) and packages built on top of this. For example, the R packages *ggseg* and *ggseg3d* (Mowinckel & Vidal-Piñeiro, 2020) can be used to show aggregated data such as cortical thickness in atlas-derived regions of interest. However, these packages are designed primarily for use with anatomical datasets and would require some additional coding for use with fMRI data quality and statistical metrics. Several tools do provide data quality metrics for fMRI datasets, such as MRIQC (Esteban et al., 2017), which provides important metrics such as Signal-to-Noise Ratio (SNR), Contrast-to-Noise Ratio (CNR), and

Figure 3.2

Python code showing how to connect FSL's BET and AFNI's Despike tools

```
# Import necessary Nipype modules
from nipype import Node, Workflow
from nipype.interfaces import fsl, afni

# Create a workflow
workflow = Workflow(name="preprocessing_workflow")

# Set up neuroimaging functions as nodes and pass in arguments
bet = Node(fsl.BET(frac=0.5), name="brain_extraction")
despike = Node(afni.Despike(), name="despike")

# Connect output of BET to input of Despike
workflow.connect(bet, "out_file", despike, "in_file")
```

participant movement during scanning. These tools are primarily used to identify problematic scans that may need additional preprocessing or removal from the dataset. However, these tools either report voxel wise maps or aggregate metrics over the entire brain.

Welvaert & Rosseel (2013) investigated the reporting of various SNR and CNR metrics in fMRI literature, finding that a third of simulation studies do not report any SNR/CNR metrics, with tSNR only reported in about 4% of simulation studies. This may be because while many SNR equations are relatively simple (e.g. Equation 3.7), analysis tools to calculate SNR are not widely available, thus they are not reported as standard (Welvaert & Rosseel, 2013). For example, in the case of calculating tSNR for fMRI images, as it is only a useful measure in regards to grey matter voxels (Welvaert & Rosseel, 2013), the process of accurate calculation of tSNR mandates the segmentation of tissue types to exclude white matter and cerebrospinal fluid from this calculation. In addition to the difficulty of producing accurate SNR measures, the lack of support in existing tools for ROI-wise summaries of fMRI data quality metrics further increases the difficulty in reporting meaningful SNR metrics, as aggregating these metrics over the brain can obscure important inter-regional differences, which may be particularly informative for the optimisation of scanning parameters when planning fMRI experiments.

The goal of the fMRI ROI Analysis Tool (fRAT) presented here is to provide

an end-user toolset to address this gap, to deliver a straightforward method for conducting multivariate ROI wise analyses of fMRI metrics.

3.2 Design goals

fRAT, an open-source application built in Python (version 3.10), is compatible with Mac, Linux, and Windows (using Windows Subsystem for Linux). Its primary focus is to offer a comprehensive solution for ROI wise analysis of fMRI data. fRAT achieves this by providing a user-friendly and flexible pipeline for converting voxel wise data into ROI wise data. When designing fRAT several goals were set out:

- To abide by open-source software standards
- Ease of installation and use
- Minimally preprocessed data
- Comprehensive ROI analysis toolset

3.2.1 Open-source software standards

To abide by open-source software standards, code for fRAT is publicly available via GitHub (https://github.com/elliohow/fMRI_ROI_Analysis_Tool) which allows full transparency into the development process. Further, the code is under the open source initiative approved Apache 2.0 license. Finally, guidelines for contributing to the software and a contributor code of conduct are available on GitHub to facilitate collaboration and ensure a welcoming environment for all contributors. The publication of fRAT in the Journal of Open Source Software (Howley et al., 2023) shows its adherence to open-source software standards.

3.2.2 Ease of installation and use

There are a number of software tools used in fRAT as described in subsection 3.1.1, including many FSL and Nipreps tools. FSL was chosen to provide

many of the neuroimaging tools for fRAT due to the varied toolset it provides along with anatomical atlases, which are used to define the template used for the ROI analysis. The Nipype framework engine is used extensively throughout to interface and create a processing pipeline using FSL's various tools. While Nipype has the capability to create a workflow combining the tools of multiple neuroimaging libraries, to limit the external dependencies and thus the difficulty of installation, the only necessary external dependency for fRAT is FSL. Originally, Freesurfer was also an essential external dependency due to its segmentation functionality. However, due to the significant computational time required for Freesurfer's segmentation procedure and the marginal improvements it provides over FSL's FAST tool (Zhang et al., 2001), it was instead replaced by FSL FAST.

To meet the user's research needs, the settings of fRAT are customisable through a user-friendly graphical user interface (GUI; Figure 3.3). Further, to aid in ease of installation and use, a website (fmri-roi-analysis-tool.readthedocs.io) was created to provide information on usage of fRAT. This website contains installation instructions as well as a detailed tutorial on how to use fRAT to run an ROI analysis. A sample of the tutorial page can be seen in Appendix 7.1. Finally, an example dataset has been provided (osf.io/pbm3d/) to allow users to run a test analysis to verify their installation.

3.2.3 Minimally preprocessed data

Users are recommended to use optiBET to brain extract anatomical data before running fRAT. In most cases, no other preprocessing is necessary for data collected at 3T (and below), however additional preprocessing may be necessary for data collected at 7T (and above).

3.2.4 Comprehensive ROI analysis toolset

There are several use-cases that researchers have published for ROI wise summaries of data quality metrics, from producing ROI wise data quality

Figure 3.3

A screenshot of fRAT's graphical user interface

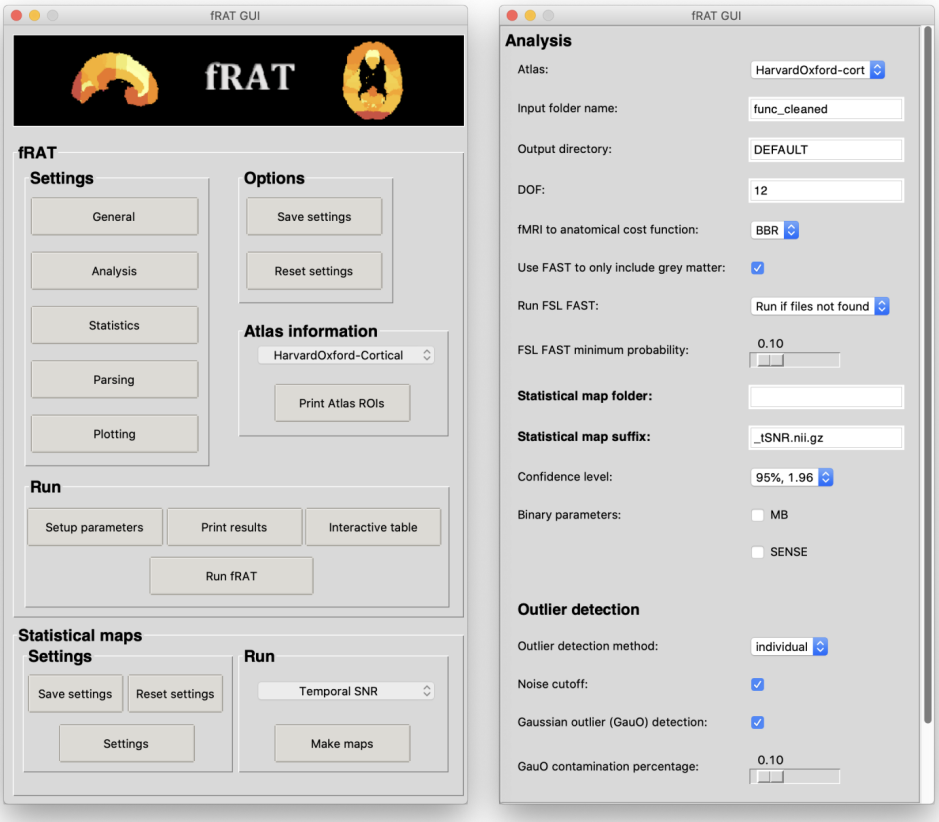

Note. **(Left column)** Main menu screen. **(Right column)** Analysis settings screen.

summaries for a given dataset, to conducting multivariate analysis to investigate the relationship between scanning parameters and data quality to plan studies. The aim of fRAT was to be able to accommodate any of these use-cases. This was achieved by producing a modular toolset allowing users to choose whichever fRAT tools are needed or to change the analysis settings to accommodate their dataset. The functionality of fRAT is discussed in greater detail in section 3.3. With the tools available within fRAT, users are able to take raw data through to the statistical analysis stage without use of additional software. While other tools such as MRIQC can be used to compute tSNR, to further limit the need for additional software, image Signal-to-Noise Ratio (iSNR) and temporal Signal-to-Noise Ratio (tSNR) maps can be created by fRAT, to be used during the ROI analysis. But importantly, fRAT has also been designed to be used with any voxel wise maps, with there being a number of other potential uses of fRAT's ROI analysis. For example, calculating maps of the mean T_2^* of each ROI to optimise echo time for the areas of interest in an fMRI study, reducing the effect of susceptibility artifacts in difficult to image areas. Given the maps are in the same space as their respective fMRI volumes, any pre-computed voxel wise statistical or functional map can be used as an input for the ROI analysis.

One difficulty faced when handling ROI wise data compared to a whole brain aggregate measure, is the size of the resulting data. This is because for a whole brain aggregate measure, a single result is produced across the whole brain, whereas a separate result for each defined region must be produced for an ROI wise analysis. In the case of the Harvard-Oxford atlas of cortical structures (Desikan et al., 2006), there are 48 distinct regions, which will each produce a separate result. Data complexity also increases significantly as the number of statistics calculated increases. To address this, fRAT provides several options for displaying and interacting with the analysis results. For example, an interactive "*dash*" table is available for the ROI analysis results, and these results can also be printed to the terminal. Alternatively, if users wish to explore the data in a different way, the data is also available in the widely used "*json*" file format.

3.3 Functionality

fRAT contains an array of functionality with the main focus being the Complex Analysis Pipeline (CAP). The CAP is able to use a number of different FSL supplied atlases to convert voxel wise data into ROI-wise data. fRAT also contains the "maps" functions to create voxel wise data quality maps, and the Handy Optional Utilities for Scan Editing (HOUSE) function which contains utilities to edit functional volumes.

3.3.1 The Complex Analysis Pipeline (CAP)

The overall aim of the Complex Analysis Pipeline (CAP) is to combine the numerical information from a voxel wise map with the spatial information of an atlas (Figure 3.5), allowing summaries of that voxel wise map for each ROI. fRAT is able to analyse datasets that contain multiple participants, and if using a multiple participant dataset, these per-ROI summaries will be combined across participants. For the ROI analysis step in CAP, the necessary inputs for each participant include: an anatomical volume, voxel wise statistic maps (e.g., tSNR maps), and the corresponding functional volumes used to generate the voxel wise maps. The processing pipeline for converting voxel wise into ROI wise maps is illustrated in Figure 3.4. The CAP also contains two optional steps: visualisation and statistics. The ROI analysis step of CAP serves to produce descriptive statistics for each ROI. In contrast, the statistics step serves as a valuable tool when a user intends to produce inferential statistics on their dataset. The statistics step also supports multivariate analysis as seen in Chapter 4. Finally, the visualisation step is used to produce figures from the results of the ROI analysis step, and contains a wide range of options to highlight different aspects of these results.

3.3.1.1 ROI analysis

The first step of the ROI analysis is to convert the chosen atlas into a participant's native space. As FSL's atlases are in the MNI152 standard space,

Figure 3.4

Flowchart showing fRAT's processing pipeline

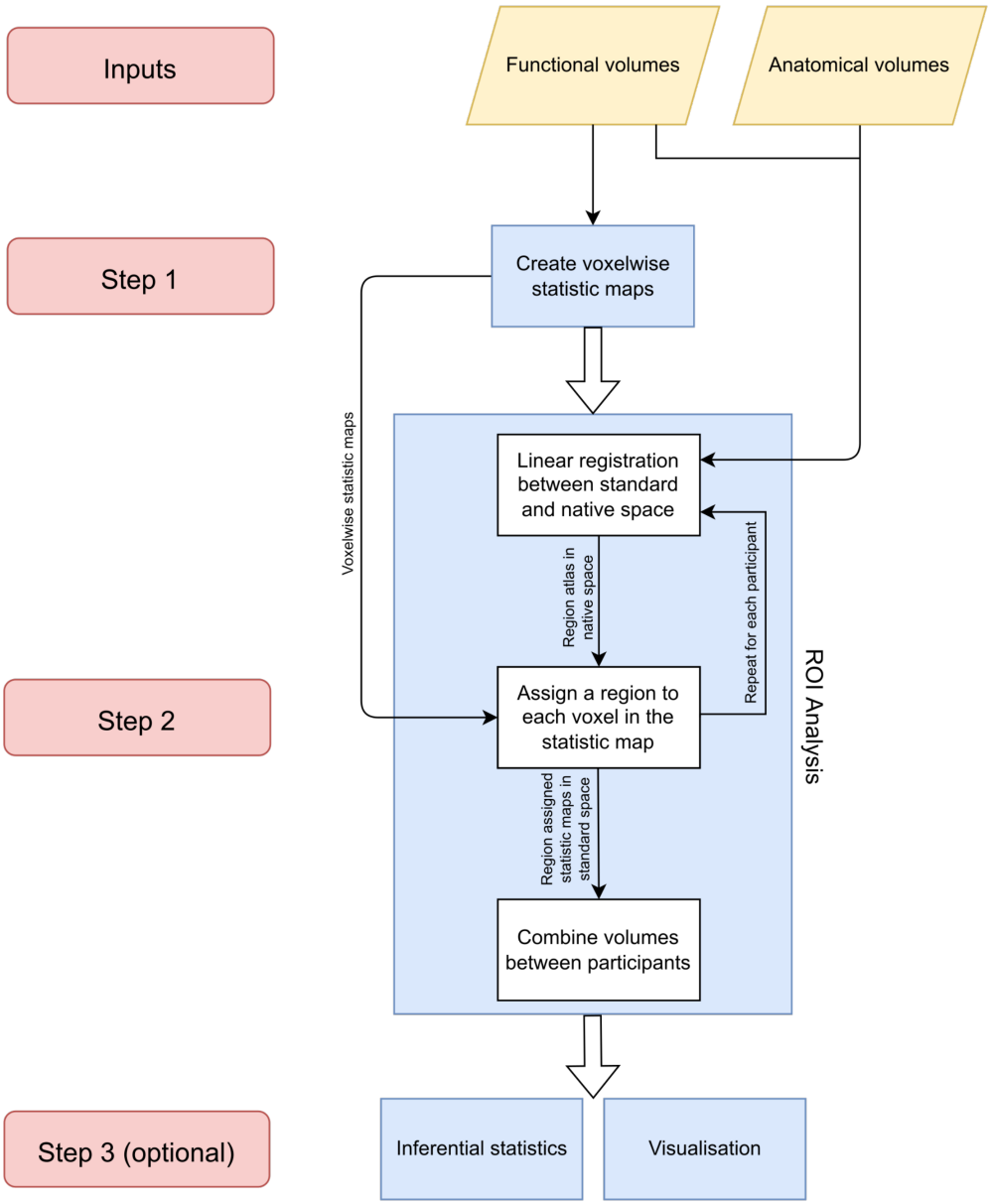

Figure 3.5

Representation CAP's ROI wise map creation process

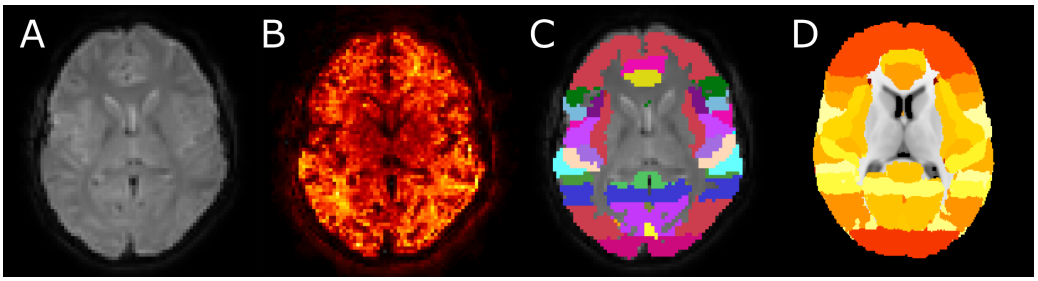

Note. Data from a single participant is shown here. All figures are in native space apart from (D), which is in standard space. **(A)** Original functional volume. **(B)** Voxel wise temporal signal-to-noise ratio (tSNR) map (brighter colours, higher tSNR values). **(C)** Harvard-Oxford Cortical atlas regions assigned to participant anatomy. **(D)** Combination of (B) and (C) to produce final ROI wise tSNR map.

if the linear transform can be found between the native space of a participant's functional volumes and the MNI152 standard space, then the inverse transform can be applied to FSL's atlases to convert them from standard to native space. Once each functional volume has an associated atlas volume in the same space, each voxel in the voxel wise map (which is in the same space) can be assigned to an ROI from the atlas. After this process has been repeated for each participant, the ROI information from each participant can be combined.

As seen in Figure 3.6 and Figure 3.7, a number of changes have been made to the ROI analysis phase of CAP compared to its initial inception. These changes have been made to improve the accuracy of linear registration between the standard and functional spaces, and to remove the influence of "noise voxels". The first major change to the initial pipeline was that an anatomical volume needed to be provided for each participant. Due to the lower resolution of functional volumes, registration accuracy is lower when directly aligning functional volumes to standard space, compared to when anatomical volumes are used as an intermediary registration step. While requiring anatomical files to be provided slightly limits the datasets fRAT CAP can be used with, due to the importance of accurate registration to provide proper estimation of ROIs, it was decided that the provision of an anatomical file should be a requirement.

Figure 3.6

Flowchart showing original fRAT CAP process for conducting analysis on a single participant

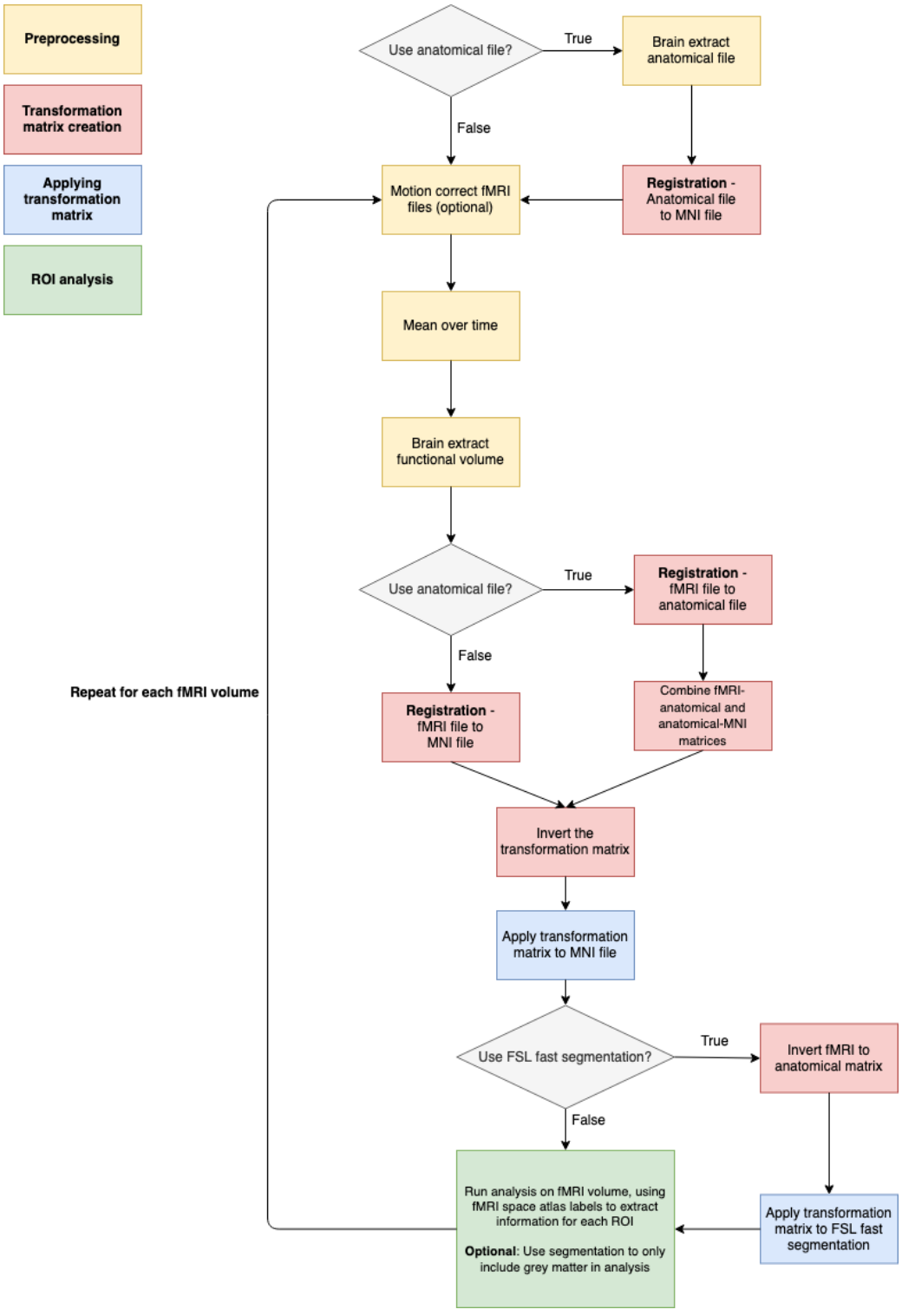

Figure 3.7

Flowchart showing new fRAT CAP process for conducting analysis on a single participant

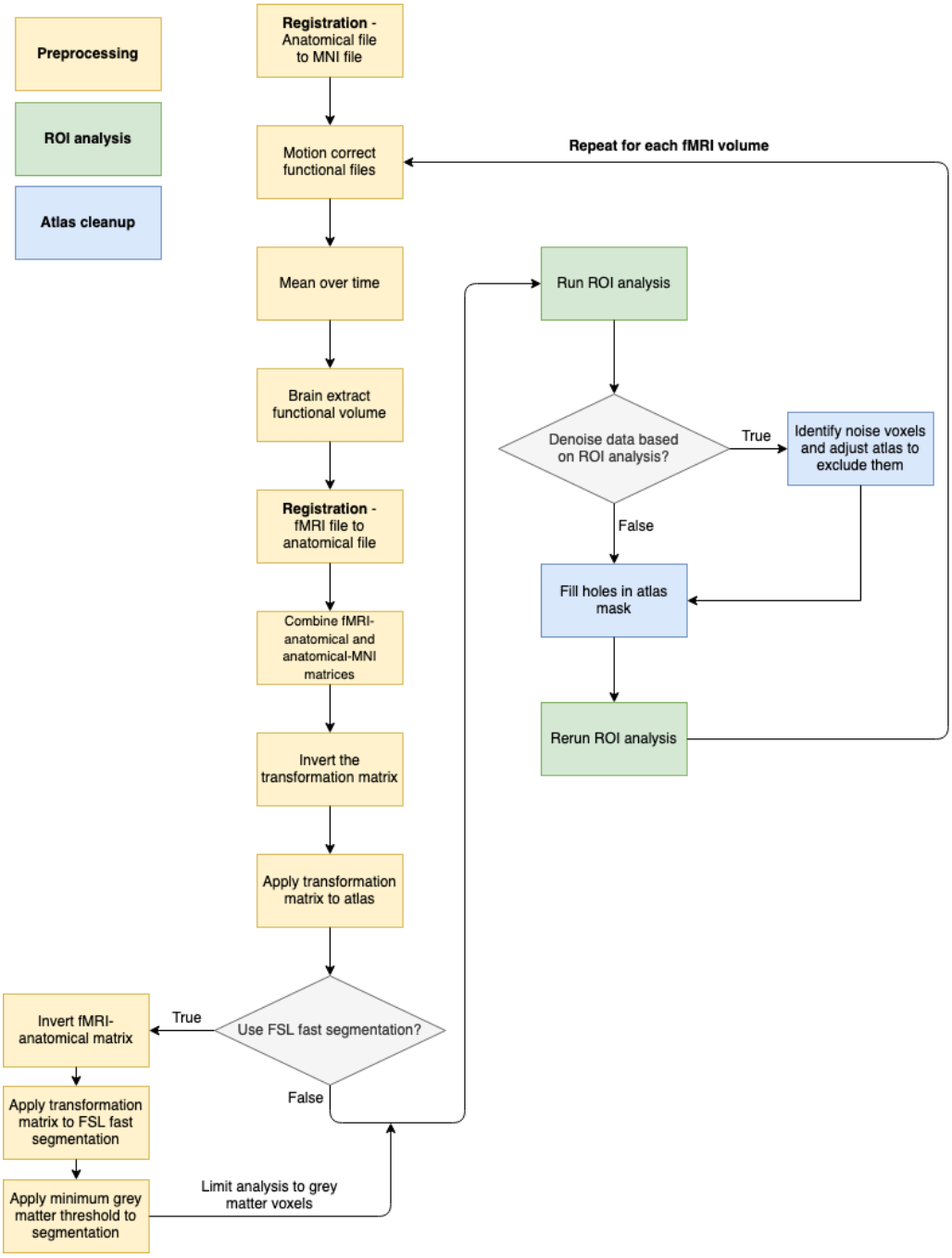

Precise spatial normalisation is an essential step in fRAT (Figure 3.4), and as brain extraction leads to more accurate registration to MNI templates (Fischmeister et al., 2013) and aids in segmentation (Fatima et al., 2020), accurate brain extraction is also essential. BET (Smith, 2002) was part of the original analysis pipeline (Figure 3.6), however one issue encountered was the optimisation of BET parameters for a given volume, due to the default BET options producing unsatisfactory results in many cases. In particular, differences in the scanning protocols used such as the number of slices present to cover the neck, or the amount of spatial intensity inhomogeneity across the volume can contribute to the performance of BET (Popescu et al., 2012). Popescu et al. (2012) investigated how to optimise BET parameters to produce the best results for a wide range of acquisition protocols. They found that by using the bias field correction and neck cleanup (option "B" for BET) alongside setting the fractional intensity threshold at 0.1 (parameter "f"), a substantial improvement in performance was seen across all scanning protocols. Lutkenhoff et al. (2014) assessed several brain extraction toolsets, including BET with the parameters suggested by Popescu et al. (2012), finding that optiBET performed better than all other brain extraction tools. Typically, lesions within the brain can pose a significant challenge for skull-stripping algorithms (Lutkenhoff et al., 2014), however these tools were compared using a dataset presenting gross brain pathologies, suggesting that optiBET outperforms other brain extraction algorithms in even the most challenging of datasets. As illustrated in Figure 3.8, this was also reflected in the current data with brain extraction performance on healthy brains varying between optiBET and BET. It was found that BET in many cases either removed small sections of grey matter or retained large sections of non-brain matter. In the case of lesioned brains, the difference between brain extraction performance was even more stark. As seen in Figure 3.9, BET struggled with lesioned brains and in particular, struggled to identify brain tissue close to lesion sites, whereas optiBET performed substantially better.

While optiBET significantly outperforms BET, this increase in skull stripping performance comes at the expense of significantly increased computation time. Brain extraction using BET with the default options takes

Figure 3.8

Extraction accuracy of BET and optiBET for a healthy brain

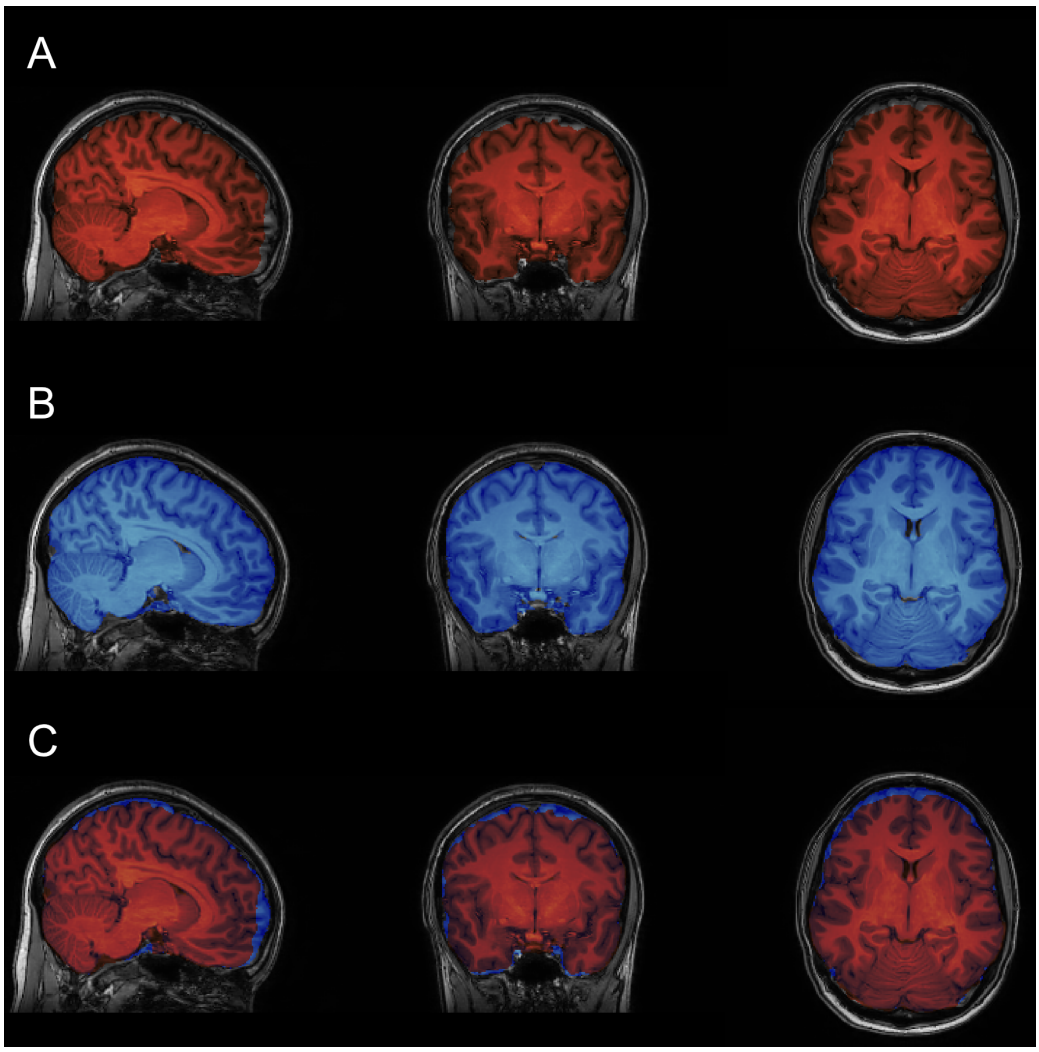

Note. **(A)** BET extraction overlaid on top of original anatomical volume. **(B)** optiBET extraction overlaid on top of original anatomical volume. **(C)** Overlay of both BET and optiBET extractions on top of original anatomical volume.

roughly 3 seconds whereas using the optimal BET settings as determined by Lutkenhoff et al. (2014) takes roughly 9 minutes. optiBET's brain extraction algorithm however almost doubles that number, taking approximately 17 minutes to run (Lutkenhoff et al., 2014). This increased computation time for optiBET is a relatively small drawback compared to the accuracy advantages provided by optiBET. Therefore it is the recommended brain extraction toolset to use. However, it may still encounter challenges and fail with certain datasets. Due to the reliance of subsequent ROI analysis steps on accurate brain extraction of the anatomical volume, brain extraction has been removed from the analysis pipeline altogether, with users instead instructed to manually run (and check the results of) the brain extraction on their dataset.

There are many atlases to choose from in FSL, from atlases that focus on cortical or subcortical regions such as the Harvard-Oxford cortical and subcortical structural atlases, or atlases that are more specific in their region definitions, such as the Oxford thalamic connectivity atlas that focuses on 7 sub-thalamic regions. Within each atlas, multiple thresholded variants exist, corresponding to the level of support from segmentations for each region label. For instance, the Harvard-Oxford cortical atlas provides three threshold variants: 0%, 25%, and 50%. A 0% threshold signifies that at least one segmentation supports the region label, while the 25% variant indicates agreement with the region label in 25% of segmentations. Higher threshold values denote increased certainty regarding a voxel's inclusion in a region. However, as illustrated in Figure 3.10, opting for higher thresholds results in reduced sizes for every region label. In this context, the decision was made to prioritize 0% threshold maps. This choice facilitates exploratory analysis by capturing a broader spectrum of structures, which might be overlooked with more conservative threshold maps employing higher thresholds.

However, the use of this threshold level necessitated further clean-up dependent on the atlas chosen, due to a high number of extracranial voxels being included in cortical ROI definitions when using the 0% threshold level. The use of the FSL FAST segmentation to restrict analysis to grey matter voxels typically removes most extracranial voxels, with higher threshold levels set in fRAT providing more conservative grey matter estimates. There are also

Figure 3.9

Extraction accuracy of BET and optiBET for a lesioned brain

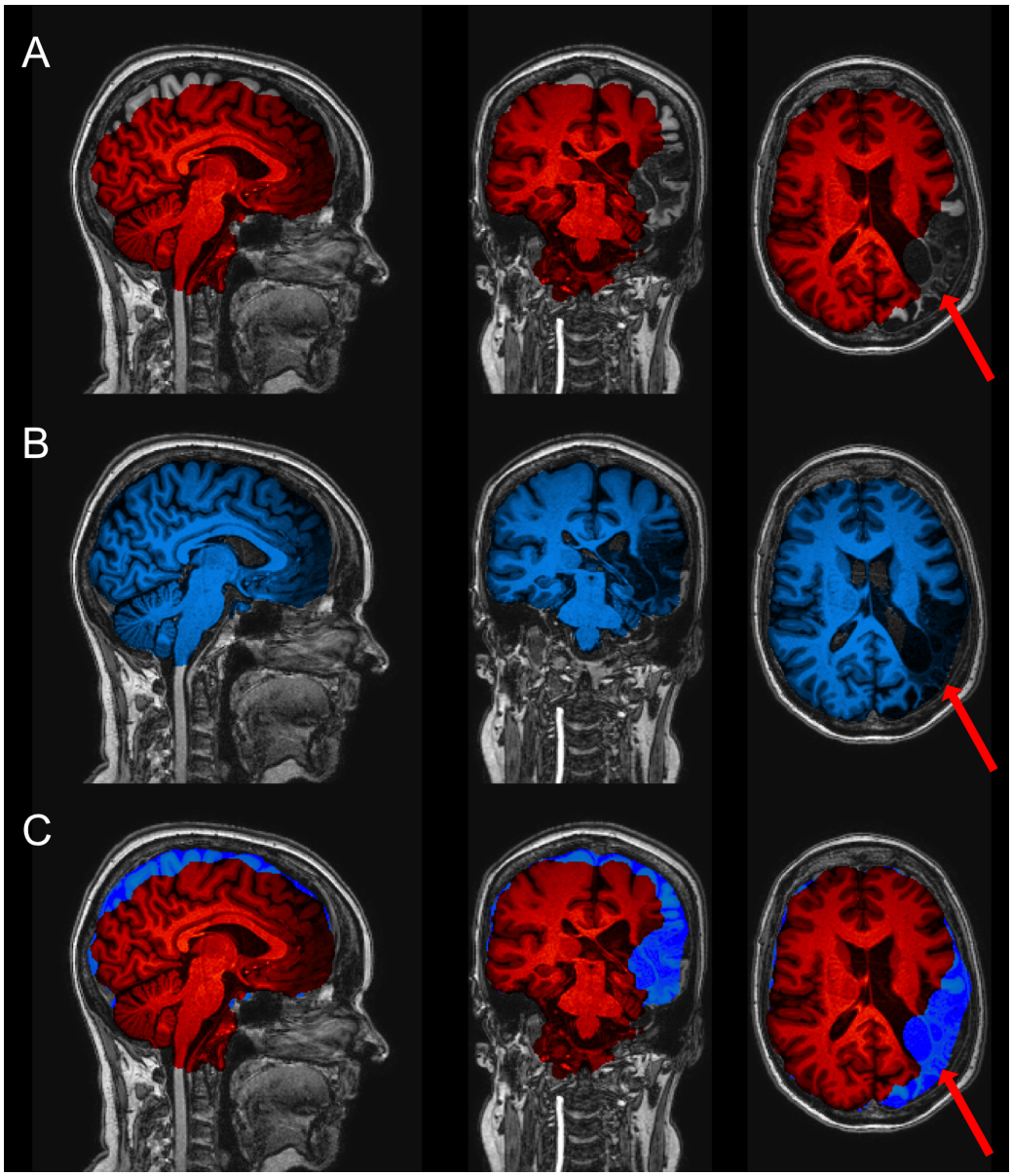

Note. The lesioned area of the brain is indicated by arrows. **(A)** BET extraction overlaid on top of original anatomical volume. **(B)** optiBET extraction overlaid on top of original anatomical volume. **(C)** Overlay of both BET and optiBET extractions on top of original anatomical volume.

Figure 3.10

Harvard-Oxford Cortical atlas threshold map comparison overlaid on MNI template

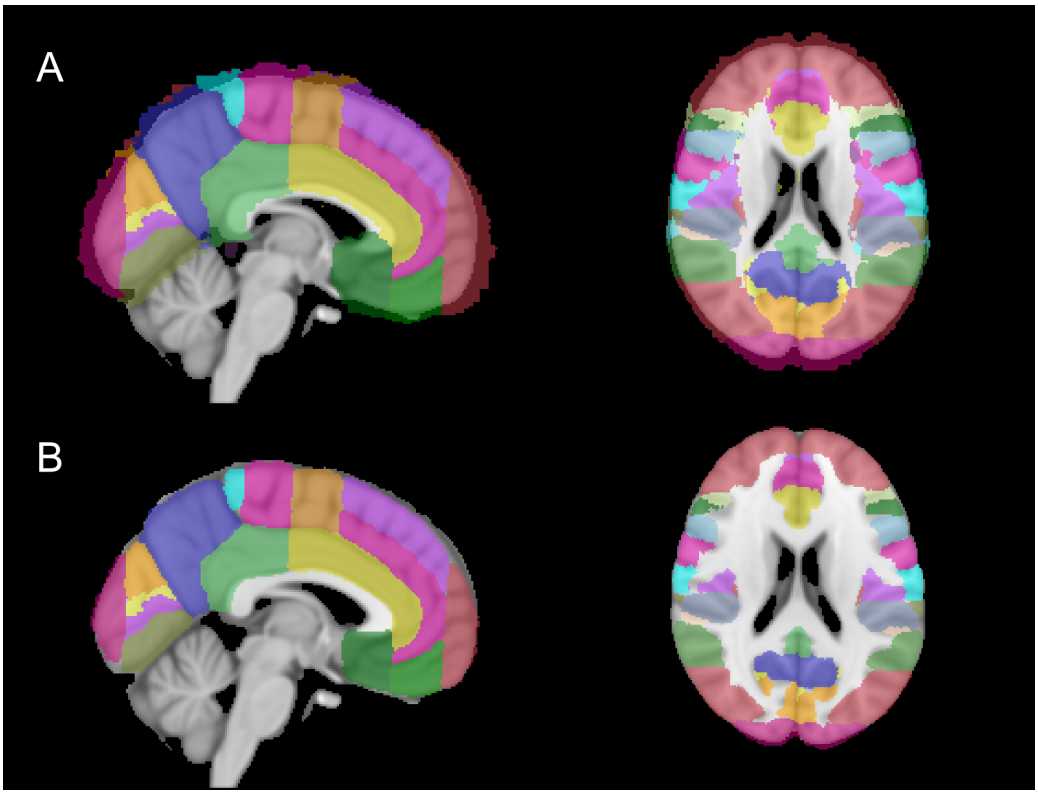

Note. Rows differ in terms of the minimum probability threshold necessary to include a voxel in a region-of-interest. **(A)** Minimum probability threshold of 0%. **(B)** Minimum probability threshold of 25%. Note the inclusion of extracranial voxels in **(A)**.

Figure 3.11

Example of Harvard-Oxford Cortical atlas cleanup

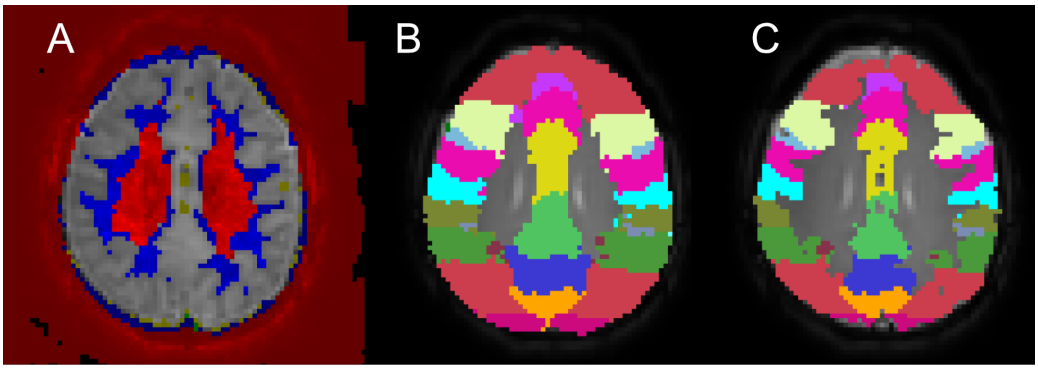

Note. **(A)** Breakdown of atlas clean up steps. In order: red voxels correspond to voxels that were not originally assigned to a region; blue voxels have been determined as non-grey matter using the FSL fast segmentation; green voxels have a value below the mean value outside of the brain; & yellow voxels were determined as outliers after fitting a gaussian to the data. **(B)** Harvard-Oxford Cortical atlas applied to subject brain without any cleanup. **(C)** Harvard-Oxford Cortical atlas applied to subject brain after cleanup.

several post-analysis de-noising options available as an alternative method to clean-up the final ROI definitions. The first de-noising option calculates the average value of the statistic of interest for extracranial voxels, removing any values below this value. The second de-noising option involves using the unsupervised elliptic envelope machine learning technique, which can be used to detect outliers in a Gaussian distributed dataset. In cases where the FSL FAST segmentation fails in one or more anatomical volumes, these additional de-noising options are available to remove extracranial voxels from regions. The effect of atlas mask clean-up on the final ROI definitions can be seen in Figure 3.11. To remedy potential holes in the atlas mask created by de-noising, after running post-analysis de-noising, holes were filled in the atlas mask using the FSL maths "*fillh*" option. The ROI analysis is repeated with this new atlas mask to assign an ROI to each voxel. As seen in Figure 3.4, the final step of the ROI analysis, is to generate the final results by combining the information from each volume, aggregating based on the independent variables used to collect each volume. For example, if MB was the only independent variable, information would be aggregated for each MB level.

3.3.1.2 Statistics

The statistical framework of CAP was designed to analyse the dataset used in Chapter 4. As the primary goal of Chapter 4 was to develop a set of predictive models, regression analysis was the most suitable choice. This is because regression analysis produces beta coefficients that quantify the relationship between predictors and outcomes, making it suitable for predictive modelling. However, applying standard linear regression to non-independent data can lead to significant bias in statistical estimates (Kenny & Judd, 1986). Therefore, a core assumption of linear regressions is the independence of observations. The dataset used in Chapter 4, however, contained a number of within-subject factors, which would violate this core assumption of linear regressions. To produce predictive models that account for non-independence of observations, alternative regression approaches such as repeated-measures regression or linear mixed models (LMMs) can instead be used.

Repeated-measures regression is a form of Analysis of covariance (ANCOVA) which controls for between-participants variance (Bakdash & Marusich, 2017). In contrast, LMMs explicitly model between-participant variance as a random effect. There are several advantages to LMMs over repeated-measures regression. The ability of LMMs to use partial pooling allows extreme estimates to be "shrunk" towards an overall average providing regularized model estimates, however repeated-measures regressions do not have this partial pooling mechanism. For subjects with fewer numbers of observations, such as in the case of missing data, due to this lack of partial pooling, parameter estimates with repeated-measures regressions can be much more extreme than if using LMMs. Thus partial pooling allows LMMs to accommodate missing and unbalanced data more effectively than repeated-measures regressions. Another advantage of LMMs is they are largely robust to violations of model assumptions, with both fixed and random effect estimates being relatively unbiased even in severe cases of model assumption violations (Schielzeth et al., 2020). On the other hand, in cases where the restricted estimate maximum likelihood (REML) algorithms used by LMMs fail to converge, the model fitting process will

not succeed. While there are alternative algorithms that can be used with LMMs if REML model fitting fails (Misztal, 2008), convergence failure is generally not an issue for repeated-measures regression.

Given the benefits provided by LMMs, the statistical phase of fRAT employs LMMs for predictive modeling instead of repeated-measures regressions. As variance estimates are biased when using maximum likelihood (Pinheiro & Bates, 2006), restricted estimate maximum likelihood is generally considered to be better to fit models. On the other hand, when calculating information criteria to compare two models, the likelihoods of two restricted estimate maximum likelihood fit models will not be directly comparable (Faraway, 2016) therefore maximum likelihood is preferred. Thus when calculating LMMs for fRAT, maximum likelihood is used to fit models when using information criteria for model comparison, whereas restricted estimate maximum likelihood is used to fit the final model. Independent & paired sample t-tests can be used to calculate post-hoc contrasts over each level of the factors.

R^2 is a statistical measure for regressions used to quantify the goodness-of-fit of a model. The definition of R^2 is intuitive, being the proportion of variance explained by the model Additionally, R^2 is also a standardised measure of effect size, thus it can be used to compare statistical models within and between studies. These reasons make R^2 a useful and popular model summary statistic. The addition of random effects and the potential hierarchical nature of LMMs make R^2, as calculated for fixed-effect only regression models, unsuitable. Due to the relatively recent development of linear-mixed models, there is no current consensus on alternative goodness-of-fit measures, with many "explained variance" measures being proposed (LaHuis et al., 2014). Likely due to lack of consensus on how to R^2 for LMMs, while R packages such as '*lme4*' (Bates et al., 2015) can be used to calculate effect size statistics for LMMs, there is not currently any statistical package within Python that has this capability. However, due to the usefulness of this statistic, a previously proposed R^2 measure was manually implemented into fRAT.

Nakagawa & Schielzeth (2013) proposed a simple R^2 measure that fulfills most properties of traditional R^2 measures. This measure of R^2 has been

found to have similar levels of bias and efficiency compared to other R^2 measures (LaHuis et al., 2014), however the advantage of using this measure, is the ability to partition the explained variance into variance explained by the fixed effects only (marginal R^2), and variance explained using both the fixed & random effects (conditional R^2). While this method extends to both LMMs and generalised LMMs, in the case of a LMM with an assumed Gaussian distribution of noise and a single random effect, marginal and conditional R^2 can be calculated respectively as:

$$R^2_{(m)} = \frac{\sigma_f^2}{\sigma_f^2 + \sigma_r^2 + \sigma_e^2} \tag{3.1}$$

$$R^2_{(c)} = \frac{\sigma_f^2 + \sigma_r^2}{\sigma_f^2 + \sigma_r^2 + \sigma_e^2} \tag{3.2}$$

Figure 3.12

Python code showing marginal and conditional R^2 calculation

```python
# Find variance for residuals, random and fixed effects
var_resid = result.scale
var_random_effect = float(result.cov_re.iloc[0])
var_fixed_effect = result.predict(current_df).var()

# Calculate total variance
total_var = var_fixed_effect + var_random_effect + var_resid

# Calculate marginal and conditional r2
marginal_r2 = var_fixed_effect / total_var
conditional_r2 = (var_fixed_effect + var_random_effect) /
    total_var
```

where σ_f^2 is the variance calculated from the fixed effect components, σ_r^2 is the variance calculated from the random effect component and σ_e^2 is the residual variance. In fRAT, this was implemented as demonstrated in Figure 3.12, where `result` is the a `statsmodels` class of type `MixedLMResults`, and `current_df` is a `Pandas` dataframe containing the predictor and outcome variables. σ_f^2 is calculated in this way as it can be estimated by predicting fitted values based on the fixed effects alone and then calculating the variance of these fitted values. As R^2 increases with every new predictor added into

the model, relying solely on R^2 as a measure of goodness-of-fit for a model can lead to model overfitting. Thus R^2_{adj} is an extension of R^2 that adjusts for the number of terms in the model, only increasing when a new term improves the model more than by chance:

$$R^2_{adj} = 1 - \frac{(1 - R^2)(n - 1)}{n - k} \tag{3.3}$$

where n is the number of observations and k is the number of terms in the model (including the intercept). While it is possible for $R^2_{(m)}$ and $R^2_{(c)}$ to decrease with new terms added into the model, it is unlikely as σ^2_f tends to increase when predictors are added into the model. The potential issue of overfitting a model then, applies to $R^2_{(m)}$ & $R^2_{(c)}$ as with R^2. Thus Equation 3.3 was used in fRAT to calculate R^2_{adjm} & R^2_{adjc} as seen in Figure 3.13.

Figure 3.13

Python code showing adjusted marginal and conditional R^2 calculation.

```
adj_marginal_r2 = 1 - ((1 - marginal_r2) * (result.nobs - 1) / (
    result.nobs - len(result.params)))

adj_conditional_r2 = 1 - ((1 - conditional_r2) * (result.nobs -
    1) / (result.nobs - len(result.params)))
```

3.3.1.3 Visualisation

fRAT contains several figure creation options to visualise different aspects of the data. These figures have built-in capability to compare multiple levels of (up to) two independent variables.

The first option, histograms, are created separately for each ROI, and aim to highlight the distribution of values within that ROI. These are useful to identify cases where fRAT's ROI analysis settings need to be modified to improve analysis of a voxel wise map. In the case of tSNR, visualising the data using histograms highlighted that ROI's commonly had a large tSNR spike at ~ 5 which did not fit the Gaussian distribution of the data otherwise. This spike was removed by using the de-noising options as described in

subsubsection 3.3.1.1. The option to plot the mean and/or median as measures of central tendency for the data is available. The ability to compare multiple levels of independent variables allows users to examine the changing distribution in response to each level. While histograms in fRAT are used to visualise the distribution of values within an ROI, the joint box & violin plots are instead used to examine the mean values for each ROI. These plots allow the user to compare the overall effect of each independent variable across all ROIs, with the box plots representing the central tendency and spread of the data, and the violin plots representing the probability distribution of the data. An example is shown in Figure 3.14.

The previous two figure types can be used to summarise any data, however both bar charts and brain grids can be used here only when the dataset includes at least one independent variable with two distinct levels. Bar charts are created separately for each ROI, with them displaying both the mean and confidence interval summary statistics for the data at each level of the independent variable, to examine the effect of the independent variable on that ROI. On the other hand the brain grids plot the results for each ROI in standard space, and are used to examine the spatial effect of each level of the independent variables, such as seeing if different levels affect anterior or posterior regions more. An example of the brain grid figure for tSNR is shown in Figure 3.15.

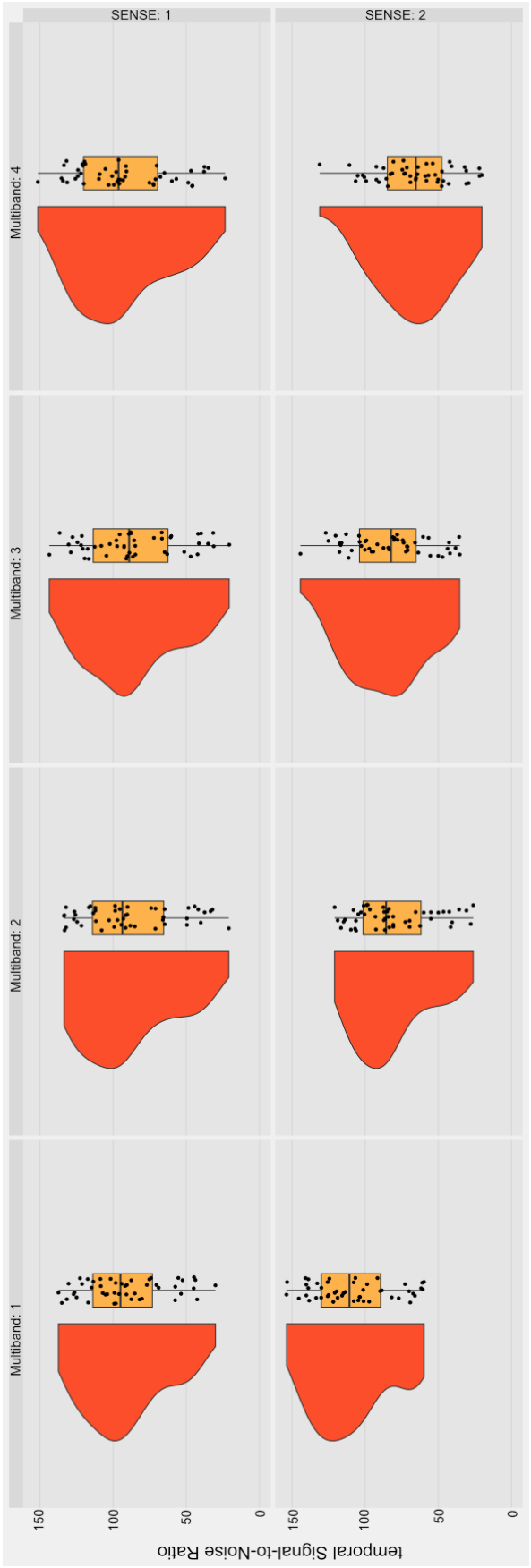

Figure 3.14

Example of a joint box & violin and plot created by fRAT

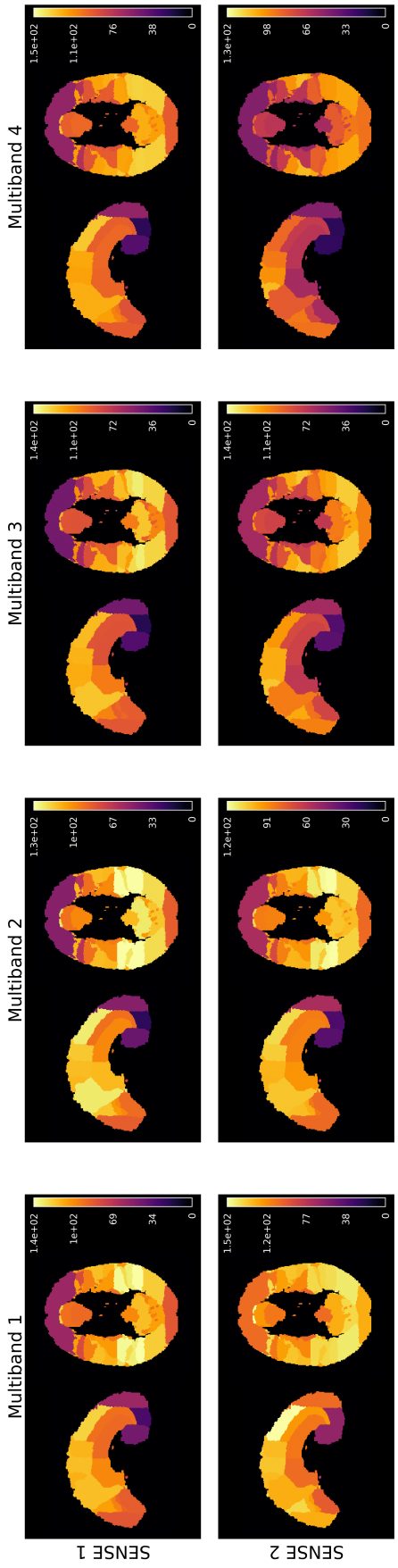

Figure 3.15

Example of a brain grid created fRAT

Note. Values represent the mean across each ROI.

3.3.2 Maps

The aim of the '*Maps*' functions are to create voxel wise maps that are able to used with fRAT CAP to provide per-ROI summaries. Currently two types of data quality maps can be created by "maps": image Signal-to-Noise Ratio (iSNR) and temporal Signal-to-Noise Ratio (tSNR), however there are several preprocessing options available to clean the functional files before creating these maps. The first is the option to use temporal filtering to use a high pass filter which removes low frequency drift. A default high pass filter cutoff frequency is set to 0.01 Hz, although the user can change this value. This cutoff frequency is converted to sigma in volumes using the formula:

$$\sigma = \frac{1}{2 \cdot f \cdot \mathrm{TR}} \tag{3.4}$$

where f represents the cutoff frequency and TR represents the repetition time of the data (Webster, 2017). There are also two preprocessing options concerned with motion available. The first uses the FSL tool "*fsl_motion_outliers*" to detect timepoints that have been corrupted by large motion, with these timepoints then removed from the timeseries. The second motion preprocessing option employs FSL's MCFLIRT (Jenkinson et al., 2002) to motion correct each time series using linear registration. In addition to using them for the calculation of the voxel wise maps, the output of these motion preprocessing steps are then retained to be used during fRAT CAP's ROI analysis step to improve registration performance. The final preprocessing option spatially smooths data using FSL's SUSAN (Smith & Brady, 1997). While spatial smoothing is available using the "s" option of fslmaths, the advantage of using SUSAN for spatial smoothing is only local voxels which have a similar intensity are averaged, preserving the underlying structure of data. The user is able set both the spatial extent of the Gaussian kernel (in mm) as well as the brightness threshold to be used by SUSAN.

After running these preprocessing steps, the voxel wise maps are created. One available option is the creation of iSNR maps. A common equation for

calculating iSNR involves dividing the voxel wise average signal (S) by the standard deviation of the background noise (σ):

$$\text{iSNR} = \frac{S}{\sigma} \tag{3.5}$$

As the calculation of σ is necessary for the iSNR equation, two options are given within fRAT. The first option allows a user to manually define a noise value for each functional volume. In this case, it is typical to calculate σ as the standard deviation of a number of voxels outside of the brain. The second option is to specify that each time series contains a "noise volume". A noise volume being a single time point collected at the end of the time series, that contains data collected without using a radiofrequency pulse or gradients. This allows for the characterisation of the background noise present in the imaging system. σ is then calculated as the standard deviation over the entire noise volume. While background noise in a complex MR image has a Gaussian distribution with zero mean, the background noise within a magnitude image (as is commonly used in MR imaging) follows a Rayleigh distribution with a non-zero mean, and the σ is under-estimated (Reeder, 2007). Voxels with sufficiently high SNR and high signal however (such as within the brain) are unaffected by this conversion. Thus, when using a magnitude image to measure σ, iSNR will be overestimated. To correct for this underestimation of σ, a correction factor can be applied. In the case of magnitude images collected using four or more coils, the magnitude correction factor is approximately 0.7 (Constantinides et al., 1997), and Equation 3.5 therefore becomes:

$$\text{iSNR} = 0.7 \cdot \frac{S}{\sigma} \tag{3.6}$$

Thus when creating iSNR maps, the option to enable this correction factor is given. The next map option is the calculation of tSNR maps. This is calculated similarly to iSNR with the tSNR calculation with the numerator referring to the voxel wise average signal (S) and the denominator referring to the noise (σ):

$$\text{tSNR} = \frac{S}{\sigma} \tag{3.7}$$

However, in this case, instead of σ being calculated as the standard deviation of the background noise, for tSNR σ is calculated as the voxel wise standard deviation of the signal over time. Thus tSNR, is a measure of the time course stability.

3.3.3 HOUSE

The Handy Optional Utilities for Scan Editing (HOUSE) functions provide options for altering pre-existing functional volumes. Currently, two HOUSE functions have been incorporated into fRAT: one for introducing motion and another for adding thermal noise to the data, with both of these functions used in Chapter 5. These two functions both base the addition of simulated head motion/thermal noise on the actual head motion/thermal noise seen for each participant, with a multiplier setting able to be changed which specifies how much head motion/thermal noise is added to each file. The "*add motion*" function aims to simulate additional motion during scanning by applying affine transformations to each file, based on each participant's actual motion during scanning. To do this, FSL's MCFLIRT (Jenkinson et al., 2002) is first used to calculate the mean angles of rotation and translation about the x, y and z axes for each participant. For each timepoint of a file, a value for each rotation and translation parameter is randomly drawn from a normal distribution (X), which is parameterised as:

$$X \sim \mathcal{N}(0,\ (p \cdot m)^2). \tag{3.8}$$

where p represents the calculated participant's mean for that parameter and m represents the multiplier. The final transformation matrix for that timepoint is then formed as a composite transformation of translation and rotation matrices:

$$A = \begin{bmatrix} 1 & 0 & 0 & \Delta_x \\ 0 & 1 & 0 & \Delta_y \\ 0 & 0 & 1 & \Delta_z \\ 0 & 0 & 0 & 1 \end{bmatrix} \begin{bmatrix} 1 & 0 & 0 & 0 \\ 0 & \cos\theta_x & \sin\theta_x & 0 \\ 0 & -\sin\theta_x & \cos\theta_x & 0 \\ 0 & 0 & 0 & 1 \end{bmatrix} \begin{bmatrix} \cos\theta_y & 0 & -\sin\theta_y & 0 \\ 0 & 1 & 0 & 0 \\ \sin\theta_y & 0 & \cos\theta_y & 0 \\ 0 & 0 & 0 & 1 \end{bmatrix} \begin{bmatrix} \cos\theta_z & \sin\theta_z & 0 & 0 \\ -\sin\theta_z & \cos\theta_z & 0 & 0 \\ 0 & 0 & 1 & 0 \\ 0 & 0 & 0 & 1 \end{bmatrix} \quad (3.9)$$

where A is the final transformation matrix, the first matrix represents the translation, and the next three matrices represent rotation about the x, y and z axes respectively. Finally, FSL's "*applyxfm4D*" function is used to apply each created timepoint's transformation matrix (A) to the data. The "add noise" function works similarly to the previous function in that a noise value is generated for each element of the original 4D matrix from the distribution Equation 3.8. However here, p represents the noise level for each participant as calculated by the fRAT user. The original 4D matrix (O) can then be combined with the 4D matrix representing the generated noise values (N) using element-wise matrix addition to create the final matrix (F), with the minimum value of each value being thresholded to 0. This can be expressed as:

$$F = max(O + N,\, 0) \quad (3.10)$$

During scanning, thermal fluctuations of the system, either within the subject or the receiver electronics within the MRI, create Gaussian-distributed additive noise (Wald & Polimeni, 2017), with thermal noise becoming the most common form of noise within the MRI signal as voxel volume decreases (Liu, 2016). Thus, for high spatial resolutions, the noise in the data appears Gaussian (Murphy et al., 2007). The "add noise" function aims to serve as an analog for this common noise source by adding gaussian distributed noise to the data, simulating increased thermal noise in the system. Whereas the "add motion" function calculates actual participant motion during program runtime, the calculation of actual participant noise must be performed by the user before initiating the "add noise" function. In order to calculate voxel wise tSNR as in Equation 3.7, the tSNR function of fRAT map first calculates the voxel wise mean signal over time (S) and the voxel wise standard deviation of the signal over time (σ). The σ map can then serve as the

input for the fRAT CAP to derive the mean σ ($\bar{\sigma}$) across the brain. This enables the "add noise" function to utilize the $\bar{\sigma}$ value across the whole brain, or for a specific ROI.

3.4 Usage

fRAT was originally designed with the aim of determining the ROI dependent effect of different MRI parameters on tSNR, as tSNR provides a rough estimate of activation detection power in fMRI studies (Murphy et al., 2007; Welvaert & Rosseel, 2013). Calculating this metric for multiple ROIs is particularly useful for planning studies aimed at specific brain regions. One example use-case of this is using the tools provided by fRAT to enable imaging sites to provide guidance on the optimal fMRI parameters, such as the MB factor (Risk et al., 2021), parallel imaging (SENSE) acceleration factor (Schmidt et al., 2005), and echo time (Clare et al., 2001), taking into account different experimental requirements and the regions of the brain being investigated. This is beneficial as the effect of fMRI sequence and hardware on data quality metrics can vary spatially over the brain in a way that is difficult to understand without pilot data. Another potential application is for the interrogation of data sets that require aggregation within ROIs, such as statistical maps for a power analysis (Geuter et al., 2018). Effect size estimations based on statistical maps from functionally derived ROIs are common in fMRI analysis but can lead to inflated estimates if the selection criteria are not independent from the effect statistic (Kriegeskorte et al., 2010). Defining ROIs based on atlases, as is performed with fRAT, prevents a circular analysis and leads to more accurate effect size estimations. The flexibility offered by fRAT CAP to be able to use any voxel wise maps as an input allows researchers to optimise the sensitivity of their scanning parameters for an ROI, from a range of statistic or data quality maps, regardless of if they were created by fRAT maps, which can aid in planning studies. In particular, as the values of these maps are then summarised for each region across participants, fRAT is also useful for larger, multi-participant datasets.

The statistics and visualisation options provided by fRAT also allow for

quantitative comparisons of the effect of different fMRI sequences or hardware on data quality. This may make it particularly useful for experimental studies as seen in Chapter 4 or for comparisons across datasets obtained at different imaging sites. As seen in Chapter 5, the current options available within fRAT HOUSE allows researchers to experimentally investigate the characterise the effect of statistical noise and participant motion on an experimental paradigm.

3.5 Discussion and future directions

This chapter has outlined the development of the fMRI ROI Analysis Tool (fRAT) which has been published in the Journal of Open Source Software (Howley et al. (2023)).

There are a number of features that are planned for fRAT in future versions that would add additional functionality and enhance overall user experience. Future developments aim to extend both the '*Maps*' and '*HOUSE*' functions with additional functionality. An example of a potential expansion for '*Maps*' is the incorporation of multi-echo functional data processing capability to calculate voxel wise T_2^* maps. Maximum BOLD contrast is achieved with an echo time that equals the local T_2^* (Bandettini et al., 1994) and as T_2^* varies between brain regions (Halai et al., 2014), single echo sampling leads to a decrease in overall sensitivity across the brain. Assuming a mono-exponential decay, multi-echo sampling can be used to calculate per voxel T_2^* (Posse et al., 2003). Created voxel wise T_2^* maps can then be used as an input to the fRAT CAP function to calculate average T_2^* per ROI. This would allow a user to adjust the echo time to optimise sensitivity for a given ROI. This may be particularly beneficial in areas that can be difficult to image due to strong local susceptibility gradients, such as the lateral inferior temporal cortex caused by air-tissue interfaces (Olman et al., 2009), with past research finding that a shorter echo time can help when imaging areas that are vulnerable to susceptibility artefacts (Stöcker et al., 2006). Although software that can use multi-echo data to calculate T_2^* maps already exists (DuPre et al., 2021), integrating this capability into fRAT can simplify the pipeline for ROI wise

analysis of this data, given the versatility of fRAT CAP to use any voxel wise maps.

Other planned features include improving the overall usability of fRAT, such as allowing multiple configuration files to be saved, as currently only one configuration file may be saved. Any changes made by the user to the settings thus override the previous settings. This can make it hard to analyse multiple datasets where different configuration settings need to be used, as these settings must currently be manually changed each time a different dataset is analysed. To solve this issue, one planned feature is the ability to save multiple, named configuration files for conducting '*CAP*', '*Maps*', or '*HOUSE*', in the user's documents. One advantage of this feature would be the ability to designate a specific analysis pipeline for different voxel wise map types. For example, while the unsupervised elliptic envelope technique can be used for de-noising tSNR maps, this denoising technique will not be suitable for voxel wise maps where the values do not follow a gaussian distribution. In this case, users can then create configuration files with different denoising options to use unique analysis pipelines when analysing the voxel wise tSNR maps compared to other voxel wise maps. As this would also make it easier to import new configuration files into fRAT, users could also more easily share configuration files, potentially facilitating collaboration to optimise fRAT analysis pipelines.

Currently, 0% threshold variants of atlases are used to define ROI in fRAT. As stated in subsubsection 3.3.1.1, the benefits of this threshold is that the more liberal threshold can allow for a broader range of voxels to be assigned to ROIs. One disadvantage of this approach is that extracranial voxel can be included in ROIs. While fRAT's current de-noising options can remove most of the extracranial voxels from ROIs (Figure 3.11), this approach may not be suitable for all types of voxel wise maps. For example, the elliptic envelope method would not be effective to remove extracranial voxels in cases where the distribution of the values in the voxel wise map is non-normal. Therefore, in the future, options will be added to allow users to use the higher threshold variants of atlases. This would also be beneficial in cases where more conservative estimates of ROIs are necessary.

In the next chapter, fRAT will be used to assess the effect of increasing MB and SENSE acceleration factors on the tSNR of fMRI scans.

Chapter 4

Effect of hardware and image acquisition parameters (IAPs) on tSNR and acoustic noise

4.1 Introduction

Subject comfort during scanning is an important consideration as many participants suffer from MRI related stress. Murphy & Brunberg (1997) found that in clinical MRI scanning, 14.3% of subjects required sedation to tolerate scanning, with 66.4% of these sedated subjects undergoing brain MRI. Further, they estimated that 3-5% of clinical scan subjects terminate scanning early due to these stresses. Tackling issues that cause subject discomfort during MR scans is important as it may reduce costs associated with early scan termination or sedation, while also making subjects more likely to consent to repeated scans.

While increasing scan times can improve the reliability of results (Birn et al., 2013) or improve the statistical detection of effects (Murphy et al., 2007), the length of scans is one of the main determining factors of subject discomfort (Heilmaier et al., 2011). Further, increased scan time can also increase the likelihood of motion artefacts, which can cause false positive activation even after motion correction (Yakupov et al., 2017). Therefore, scan duration is limited by subject motion (Maclaren et al., 2013) and discomfort. This may be particularly problematic in certain vulnerable groups, as subject motion is more likely to occur in clinical groups and younger children (Pardoe et al., 2016). Therefore, when scanning vulnerable subjects, length of scans may need to be limited further than is necessary for non-vulnerable groups. Another common cause of subject discomfort is acoustic scanner noise (Chou et al., 2014), with less than 5 seconds of unprotected exposure to scanner acoustic noise exceeding the maximum dosage acceptable according to the UK industry guidelines (Foster et al., 2000). While hearing protective devices reduce sound pressure levels, many participants still view scans as uncomfortably noisy (Chou et al., 2014). Further, the presence of acoustic noise during scans can not only interfere with stimulus presentation (De Martino et al., 2015), but can also change the BOLD response during auditory (Amaro Jr. et al., 2002), working memory (Tomasi et al., 2005) or visual (Zhang et al., 2005) studies.

There are a number of methods that can be employed to reduce acoustic noise/scan duration such as in-plane acceleration or multiband (MB) imag-

ing. One commonly used method of in-plane acceleration is sensitivity encoding (SENSE; Pruessmann et al. (1999)). SENSE undersamples k-space (usually in the phase encoding direction) and while this initially results in partial field-of-view images and wraparound aliasing, each surface coil has its sensitivity map combined with its partial field-of-view image in order to "unwrap" and combine the images into a full field-of-view image. Simultaneous multislice (SMS) or MB is the excitation and collection of data from multiple slices simultaneously (Barth et al., 2016), as outlined in subsection 2.1.3. MB and SENSE can be used to lower scan time (Barth et al., 2016), with the in-plane acceleration provided by SENSE speeding up acquisition of each slice, while MB lowers the amount of time necessary to acquire a full volume. The scan time reduction factor when using either in-plane acceleration or MB are equal to the acceleration factor of the method used (Barth et al., 2016). In the context of fMRI, increasing acquisition speed allows an increased sampling rate of the BOLD signal. However, whether this provides statistical benefits depends on a number of factors such as task type (Demetriou et al., 2018). Instead, if temporal resolution is held constant, usage of MB allows acoustic noise reduction due to reduced density of radiofrequency pulses, with a similar effect seen when using SENSE (de Zwart et al., 2002). Additionally, combining MB with SENSE (Barth et al., 2016; Preibisch et al., 2015) can further decrease both scan time and noise. However, while these methods enhance subject comfort by shortening scan duration or reducing acoustic noise, it is essential to consider their impact on data quality.

The quantification of data quality through measuring signal-to-noise ratio (SNR) allows for comparisons between imaging hardware and acquisition sequences (Parrish et al., 2000) with there currently being several methods of calculating SNR (Dietrich et al., 2007). In fMRI, the signal is a result of fluctuations due to the haemodynamic response to a task (Welvaert & Rosseel, 2013). In comparison, noise is a result of sources such as: system noise, physiological noise and task-related noise (Welvaert & Rosseel, 2013). As some sources of signal/noise in functional imaging are time dependent, such as low frequency drift (Smith et al., 1999) or the task-related signal, it is the stability of the signal over time which is central for fMRI (Welvaert &

Rosseel, 2013). Therefore, temporal Signal-to-Noise Ratio (tSNR) is a more informative measure for assessing the quality of an fMRI time series than image SNR (Wald, 2012).

As brain activations cause small signal changes, large tSNR is critical in measurement of brain activations (Welvaert & Rosseel, 2013). Indeed it has been found that there is a minimum tSNR necessary to reliably measure brain activations at a given statistical confidence level, and that higher tSNR allows scan times to be shorter while still being able to reliably measure brain activation (Murphy et al., 2007). Previous research has investigated the effect of MB and SENSE on tSNR, finding that higher MB (Demetriou et al., 2018; Todd et al., 2016) and SENSE factors (Molloy et al., 2014) result in lower tSNR. Additionally, regions that have similar anatomy and/or function are likely to have similar SNR values (Welvaert & Rosseel, 2013). Therefore prior knowledge of the tSNR of a particular acquisition sequence with given imaging hardware can potentially be used to guide the maximum MB and SENSE acceleration factor that should be used for a given ROI, allowing lower scan times/acoustic noise and increasing scan subject comfort while limiting tSNR reduction. However, in research where tSNR is reported, it is usually reported as a single value calculated across the whole brain or for a small cluster of voxels. As the use of both MB and SENSE acceleration are subject to spatially dependent noise amplification, (Blaimer et al., 2013; Risk et al., 2021), regions with higher noise amplification levels, characterised by g-factor (Pruessmann et al., 1999), have an intrinsically lower tSNR. Reporting a single tSNR value over the entire brain thus obscures potential inter-regional differences, and prevents the optimisation of tSNR according to ROI.

One method of increasing tSNR is to use NORDIC PCA denoising (Moeller et al., 2021). As NORDIC is designed to identify and remove Gaussian-distributed noise, it is particularly useful in scan sequences in which the data is dominated by thermal noise. fMRI at spatial resolutions of 1.5mm is approximately where thermal noise is the dominant noise source (Liu, 2016; Yoo et al., 2018), and where prior fMRI studies have applied NORDIC denoising (Dowdle et al., 2023). However, it is also beneficial to characterise the expected benefits of NORDIC PCA denoising in the non-thermal domi-

nated scan.

In this chapter, the fRAT software, as described in Chapter 3 (Howley et al., 2023), is used to investigate how imaging hardware (3T Philips Achieva or Ingenia MRI scanner) and image acquisition parameters affect regional differences in tSNR. The effect of NORDIC denoising will also be assessed due to its potential to mitigate lower tSNR levels resulting from higher acceleration factors. Additionally, the benefits of NORDIC to a non-thermal noise dominated scan (with a spatial resolution of 3mm isotropic tested here) is investigated. Finally, the acoustic noise reduction benefits of increasing MB and SENSE acceleration factor are also investigated.

4.2 Methods

4.2.1 Study Design

To assess the effect of imaging hardware and image acquisition parameters (IAPs) on tSNR across brain regions, tSNR was measured in a series of scans collected on two 3T Philips MR scanner platforms, obtained with 16 different IAP combinations. There were 16 participants in total, with each participant scanned using only one scanner platform. Therefore, 8 participants were scanned on each platform, and each participant was scanned with all 16 parameter combinations. Additionally, the effect of NORDIC denoising on tSNR was examined for this dataset.

In this study, a mixed-design using four independent variables - three within-subjects variables and one between-subjects variable - was employed. Two within-subjects variables focused on varying the image acquisition parameters: SENSE acceleration factor and MB acceleration factor, with each of these being tested at four different levels as shown in Table 4.1. The third within-subjects variable involved the data preprocessing, specifically whether NORDIC PCA denoising was applied to the data.

Table 4.1

Table showing number of slices for each image acceleration parameter combination

	Multiband			
SENSE	1	2	3	4
1.0	24	36	36	36
1.5	30	30	36	36
2.0	30*	36	36	36
2.5	28	36	36	36

Note. The same parameters were used for data collected on the 3T Philips Achieva and 3T Philips Ingenia. 16 participants were included in the study, with 8 scanned on each scanner platform. Each participant was scanned using all 16 parameter combinations, except for one participant on the Ingenia, where data for one parameter combination was not collected. This missing parameter combination is represented with an asterisk, meaning data for this combination is available for only 7 participants on the Ingenia.

To examine the effect of imaging hardware on tSNR, scans were collected on both 3T Philips Achieva and 3T Philips Ingenia 3T MR scanners, which will be referred to as 'Achieva' and 'Ingenia' respectively. As participants were only scanned on one scanner, MRI scanner was a between-subjects variable.

The dependent variable is tSNR, which was calculated using fRAT for each ROI defined by the Harvard-Oxford atlas of cortical structures (Desikan et al., 2006) and consisted of 48 cortical regions. The frontal pole (FP) and occipital pole (OP) were selected as specific regions to be studied in this chapter due to their spatial separation, and their significance in decision making and visual experiments respectively. The posterior inferior temporal gyrus (pITG) was also selected for analysis due to susceptibility artifacts being common in lateral regions of the inferior temporal cortex caused by air-tissue interfaces (Olman et al., 2009), which methods such as SENSE can help to reduce (Yang et al., 2004). Figure 4.1 displays the location of these regions. Finally, the effect of image acquisition parameters across all regions defined by the Harvard-Oxford cortical atlas, including those previously mentioned, will also be reported.

The order of the image acquisition parameters were randomised for each participant to minimise potential confounding factors in the data and lessen

Figure 4.1

Coronal and axial images showing location of studied regions

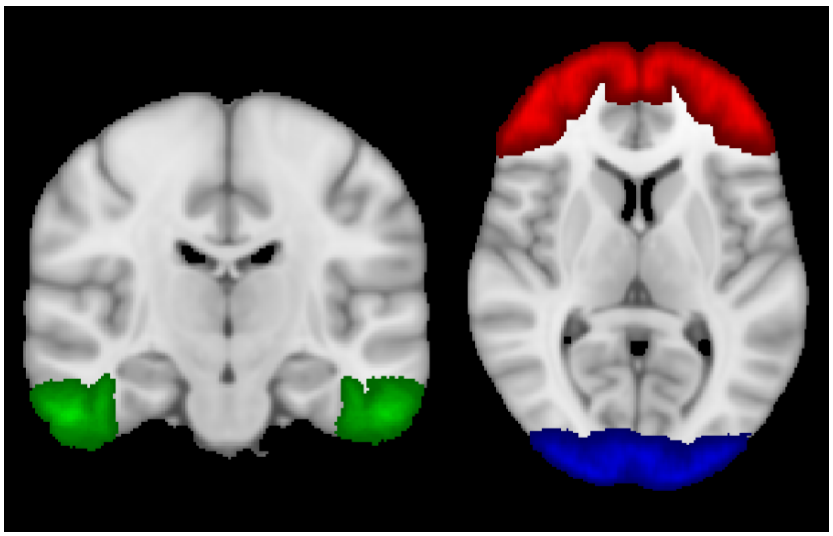

Note. Frontal Pole is shown in red, Occipital Pole is shown in blue and the posterior Inferior Temporal Gyrus is shown in green.

any potential systematic biases in participant movement, such as increased movement towards the end of a scanning session due to fatigue.

4.2.2 Participants

16 participants took part in this study, with 8 participants scanned on the Achieva and a different set of 8 participants scanned on the Ingenia. The average age across the participants was 27.3 ($SD = 5.8$) years, and 68.75% of the participants identified as female. One participant's scan session from the Ingenia did not include the collection of a noise volume at the end of their functional scans, and so NORDIC denoising was applied to 15 participants.

4.2.3 Scan parameters

Scans on both the 3T Achieva and 3T Ingenia were collected using a 32-channel head RF coil. The 3T Ingenia used the upgraded Philips dStream

technology. dStream digitizes the signal in the coil, reducing noise influences typical of analog pathways, to capture the MR signal without pre-distortion or compression. A fibre-optic connection from the coil to the image reconstructor then enables lossless broadband data transmission. Imaging data for each participant was collected in a single scan session.

T_2^*-weighted gradient-echo echo planar imaging (GE-EPI) sequence scans collected functional data at baseline. To reduce discomfort related movement, short functional scans were used with each functional scan lasting for just over one minute (dynamics=31). MB and SENSE factors were varied for each functional scan (subsection 4.2.1). The number of slices in a volume was set to 36 slices (a number allowing a MB factor of 1,2,3, and 4 to be used), but if this was not possible for the lower MB factors due to not fitting within the TR then the slice number was lowered with the central slice matched. Slice numbers for each IAP combination is shown in Table 4.1. Other scan parameters were constant between scanners (voxel size=3mm isotropic; TR=2000ms; TE=30ms; FA=80°; matrix size=80x80) with the bandwidth in the EPI frequency direction matched as closely as possible given the integer limit of the water fat shift (WFS), resulting in a bandwidth of 1570 ± 50 Hz for the Ingenia and 1700 ± 60 Hz for the Achieva (due to the difference in gradient hardware between the systems). For the final dynamic of each scan, the radiofrequency pulses and gradient fields were not applied to allow collection of a thermal noise scan.

To examine the impact of IAPs on acoustic noise the estimated acoustic noise for each scan, reported by the scanners using the A-weighted root mean square sound pressure level (SPL), was recorded. To calculate the change in perceived volume from the perspective of the scanned subject, the relative difference between the SPL of each IAP combination was compared to the SPL for the IAP which should theoretically have the highest acoustic noise level: the MB 1 SENSE 1 condition. Where x represents the perceived loudness difference, this can be calculated as:

$$x = 2^{\left(\frac{\Delta \mathrm{dB}}{10}\right)} \tag{4.1}$$

This therefore means that a 10dB difference between the two SPLs equates to a loudness difference of 2:1.

Anatomical images were also collected on both scanners using a T_1-weighted MPRAGE sequence. This sequence used Compressed SENSE (CS) on the Ingenia (scan parameters: voxel size=1mm isotropic, TR=8.4ms, TE=3.9ms FA=8°, matrix 256x256x162) but no CS was available on the Achieva (scan parameters: voxel size=1mm isotropic, TR=8.3ms, TE=4.6ms FA=8°, matrix size=180x256x256).

4.2.4 Data preprocessing

fRAT (version 1.6.4) and FSL (version 6.0.6.2) commands were used for data preprocessing. The fRAT *Maps* functions were used to create tSNR maps for each participant, while fRAT's Complex Analysis Pipeline (*CAP*) was used to conduct the ROI analysis. Before creating the tSNR maps, a temporal high pass filter of 0.01 Hz was used to remove low frequency drift from the signal. Motion correction was also applied to reduce the effect of subject motion on tSNR. Prior to running fRAT *CAP',* optiBET* (Lutkenhoff et al., 2014) was used for brain extraction of the anatomical files. During fRAT *CAP*, a segmentation created by FSL FAST was used to limit analysis to grey matter voxels, with a 10% threshold used as the minimum grey matter probability necessary to be included in the analysis. Noise cutoff and gaussian outlier detection were used to remove extracranial voxels. The settings used for fRAT *Maps* and the *CAP* analysis are provided in Appendix 7.2 and Appendix 7.3.

An additional NORDIC denoised functional scan was created before using fRAT using the default NORDIC settings provided on GitHub (github.com/SteenMoeller/NORDIC_Raw).

4.2.5 Statistical analysis

Statistical analysis was conducted using fRAT *CAP* with an example of the settings used found in Appendix 7.4. Linear mixed models with random in-

tercepts were employed to assess the impact of image acquisition parameters on tSNR. In this analysis, subjects were treated as random effects, while the predictors such as MB and SENSE were considered fixed effects. Due to the large number of comparisons made, the Benjamini-Hochberg procedure for controlling the False Discovery Rate (Benjamini & Hochberg, 1995) will be used to adjust p-values. Benjamini-Hochberg adjusted p-values will be reported as q-values.

Marginal R^2 ($R^2_{MargAdj}$) describes the proportion of variance explained by the fixed factors, whereas conditional R^2 ($R^2_{CondAdj}$) describes the variance accounted for with both the fixed and random factors (Nakagawa & Schielzeth, 2013). Model selection will involve a comparison of models with solely main effects against those incorporating both main and interaction effects, and those incorporating only interaction effects. Selection will depend on a dual criterion considering both the $R^2_{CondAdj}$ and the significance of fixed effects within the model. Additionally, simpler models with fewer regressors will be considered if more complex models are found to be nonsignificant.

For each functional volume, the voxel count of each region was evaluated. Regions with voxel counts < 200 were excluded from the linear mixed model analysis, as low voxel counts may indicate poor fitting. The number of observations excluded for each region is provided in Appendix 7.5.

Multiple regressions were also conducted to investigate the effect of MB and SENSE acceleration factors on SPL (dB).

4.3 Results

Linear mixed models were employed to investigate the relationship between image acquisition parameters (MB & SENSE) and MRI scanner model on tSNR, across all cortical areas collectively to provide an overall metric, and specific brain regions (Occipital Pole, Frontal Pole, and posterior Inferior Frontal Gyrus). For this analysis, NORDIC denoised data was not used.

4.3.1 Effect of IAP on the overall brain tSNR

The mean and standard deviation of tSNR across all cortical regions are shown in Figure 4.2 and Figure 4.3, with supplementary figures provided in 7.8. For both the Ingenia and Achieva, across all cortical regions, the model incorporating both MB and SENSE as fixed effects, provided the best predictive model (Ingenia: M group size = 16.1, n = 129; Achieva: M group size = 16, n = 128).

For the Ingenia, both MB (z = -8.85, q = .001, B = -8.57, 95% CI [-10.47, -6.67]) and SENSE (z = -8.47, q = .001, B = -16.50, 95% CI [-20.32, -12.68]) added significantly to the model predicting tSNR. For the Achieva, both MB (z = -20.061, q = .001, B = -10.96, 95% CI [-12.03, -9.89]) and SENSE (z = -15.075, q = .001, B = -16.47, 95% CI [-18.617, -14.333]) also significantly added to the model and had similarly large effects on tSNR as for the Ingenia. This can be seen in Figure 4.4, where for both the Ingenia and the Achieva, there is a clear decrease in tSNR as both MB and SENSE factor increases.

Without considering subject variance, there was a medium sized effect of MB and SENSE on tSNR for the Ingenia ($R^2_{MargAdj} = 0.33$) and a large effect for the Achieva ($R^2_{MargAdj} = 0.74$). When the participant variance (Ingenia: S = 13.61; Achieva: S = 5.53) is taken into account, the variance explained by the model more than doubles for the Ingenia ($R^2_{CondAdj} = 0.70$) and increases to $R^2_{CondAdj} = 0.84$ for the Achieva. These large $R^2_{MargAdj}$ and $R^2_{CondAdj}$ values reflect the high dependence that tSNR has on MB and SENSE for both the Ingenia and Achieva. However, these values also show that tSNR has a greater dependence on these image acquisition parameters for the Achieva than for the Ingenia.

When examining the standardised coefficients, for the Ingenia, the difference in effect size between MB (β = -.44 95% CI [-.53 -.34]) and SENSE (β = -.42 95% CI [-.51 -.32]) was found to be very small. On the other hand, for the Achieva, the difference between β values for MB (β = -.70, 95% CI [-.77, -.63]) and SENSE (β = -.52, 95% CI [-.59, -.46]) was much larger. Further, the effect of MB in particular was much larger for the Achieva than for the Ingenia.

Figure 4.2

Mean tSNR values on the Ingenia

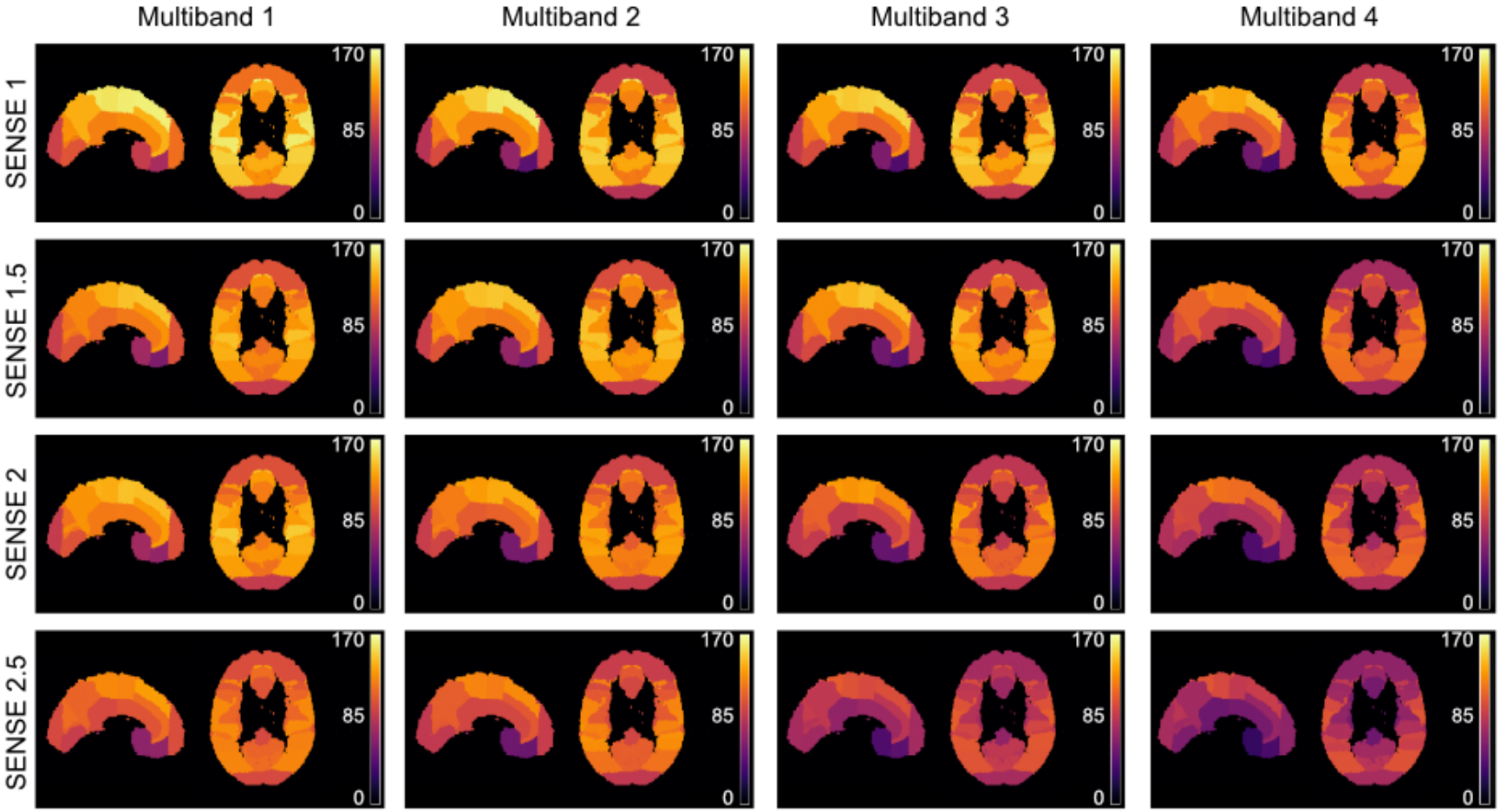

Note. Values represent the mean across each ROI. Note the reduction of mean tSNR across the entire brain as both Multiband and SENSE factor increases. Data for the Achieva follows a similar pattern.

Figure 4.3

tSNR standard deviation on the Ingenia

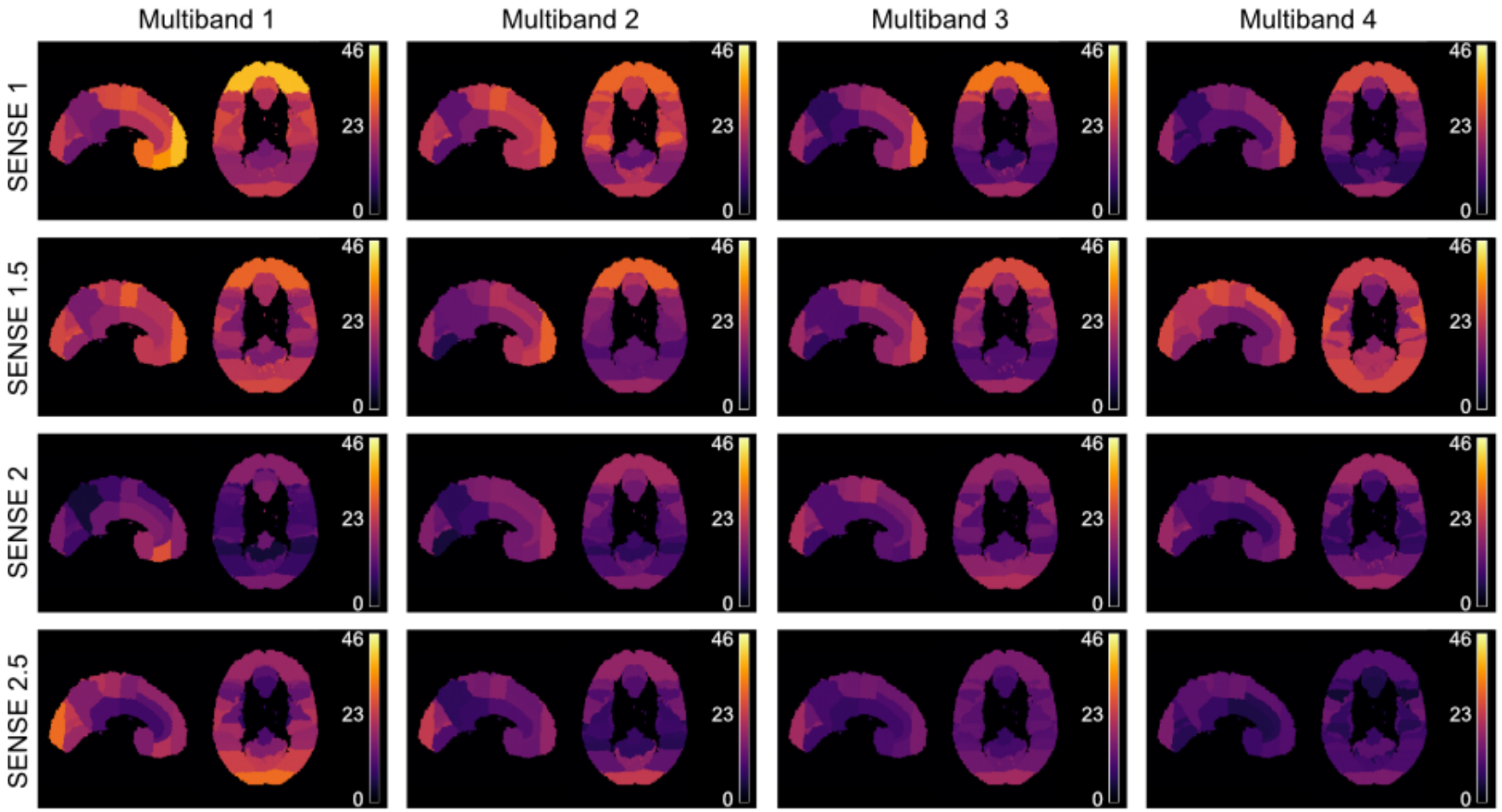

Note. Values represent the standard deviation across each participant for each ROI. Note the reduction of standard deviation of tSNR across the entire brain as both Multiband and SENSE factor increases. Data for the Achieva follows a similar pattern.

Figure 4.4

Barchart showing effect of multiband and SENSE factor on tSNR across all cortical regions

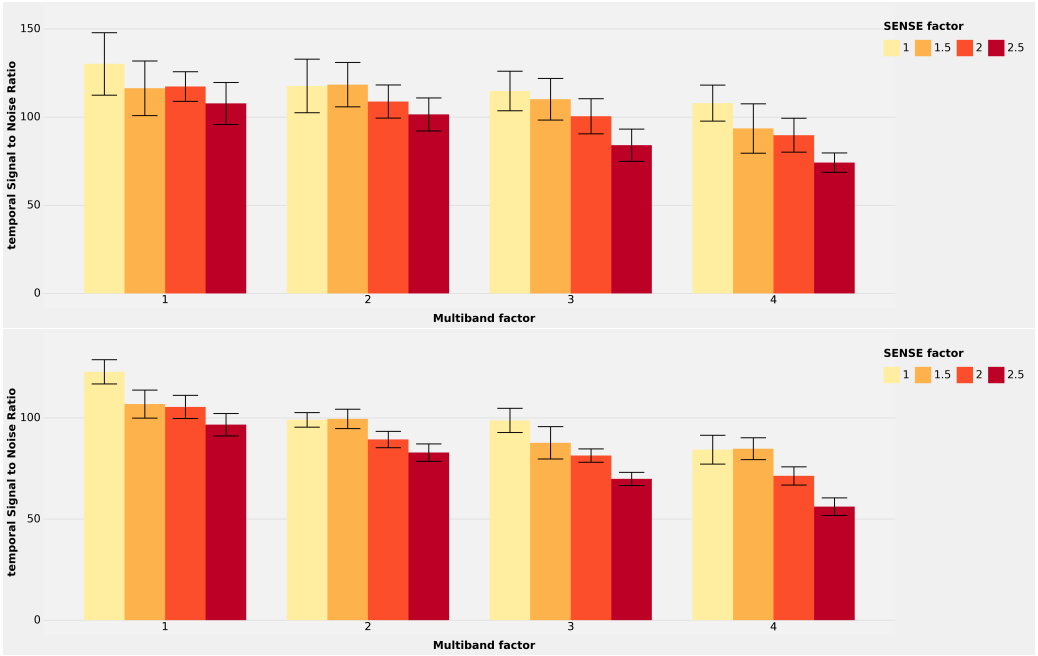

Note. Top row shows data from the Ingenia, whereas bottom row shows data from the Achieva. Error bars show 95% confidence intervals. While increasing Multiband and SENSE acceleration decreases tSNR for both the Ingenia and the Achieva, the overall reduction in tSNR is slightly greater at higher acceleration factors for the Achieva.

The final predictive models across all cortical regions for the Ingenia and Achieva are:

$$\text{tSNR} = 155.85 - 8.57x_{\text{MB}} - 16.50x_{\text{SENSE}} \qquad \text{(Ingenia)} \qquad (4.2)$$

$$\text{tSNR} = 146.05 - 10.96x_{\text{MB}} - 16.48x_{\text{SENSE}} \qquad \text{(Achieva)} \qquad (4.3)$$

As seen in Table 4.2, within the studied regions, the relationship between image acquisition parameters and tSNR varies dramatically by region. Further, as seen in Figure 4.5 and Figure 4.6, MB and SENSE both have an effect across the brain, with only a few regions (such as occipital pole and frontal pole) not meeting the $p < .001$ threshold for SENSE. Central regions also seem to have a higher baseline tSNR compared to more posterior and anterior regions. Further, the effect of SENSE on tSNR seems to vary to a greater degree than MB.

When the scanner type was added as a fixed effect, the model which contained only main effects for the factors: scanner type, MB, and SENSE, provided the best predictive value ($R^2_{MargAdj} = .56, R^2_{CondAdj} = .78$, Participant S = 10.39, M group size = 16.1, n = 257). Scanner type was represented as a dummy-coded categorical variable, indicating whether the data was collected from the Ingenia (1 = Ingenia).

MB (z = -17.41, q = .001, β = -.51, B = -9.76, 95% CI [-10.86, -8.66]), SENSE (z = -14.66, q = .001, β = -.43, B = -16.48, 95% CI [-18.68, -14.28]) and the scanner used (z = 2.94, q = .003) all added significantly to the model, with scans on the Ingenia increasing the overall tSNR by B = 15.72 (95% CI [5.24, 26.20], β = .73). The final predictive model is:

$$\text{tSNR} = 143.05 + 15.72d_{\text{Ingenia}} - 17.41x_{\text{MB}} - 14.66x_{\text{SENSE}} \qquad (4.4)$$

The Ingenia provided an average increase in tSNR of ~16 over all cortical regions compared to the Achieva, and as indicated by the higher β, had a larger effect on tSNR than both MB and SENSE. Figure 4.7 shows that

Table 4.2

Predictive equations for tSNR, modelling the effect of Multiband and SENSE on Ingenia and Achieva scanning platforms

	Scanner	
Region	**Ingenia**	**Achieva**
Occipital Pole	$\text{tSNR} = 94.84 - 4.41x_{\text{MB}}$	$\text{tSNR} = 92.10 - 8.12x_{\text{MB}}$
Frontal Pole	$\text{tSNR} = 124.72 - 8.64x_{\text{MB}} - 8.68x_{\text{SENSE}}$	$\text{tSNR} = 94.44 - 10.14x_{\text{MB}}$
pITG	$\text{tSNR} = 74.92 - 5.30x_{\text{MB}} - 7.91x_{\text{SENSE}}$	$\text{tSNR} = 62.41 - 3.13x_{\text{MB}\times\text{SENSE}}$
Overall	$\text{tSNR} = 155.85 - 8.57x_{\text{MB}} - 16.50x_{\text{SENSE}}$	$\text{tSNR} = 146.05 - 10.96x_{\text{MB}} - 16.48x_{\text{SENSE}}$

Note. pITG = posterior Inferior Temporal Gyrus. Overall = all cortical areas as defined by the Harvard-Oxford Cortical atlas.

Figure 4.5

Coefficient variability across the brain for the Ingenia

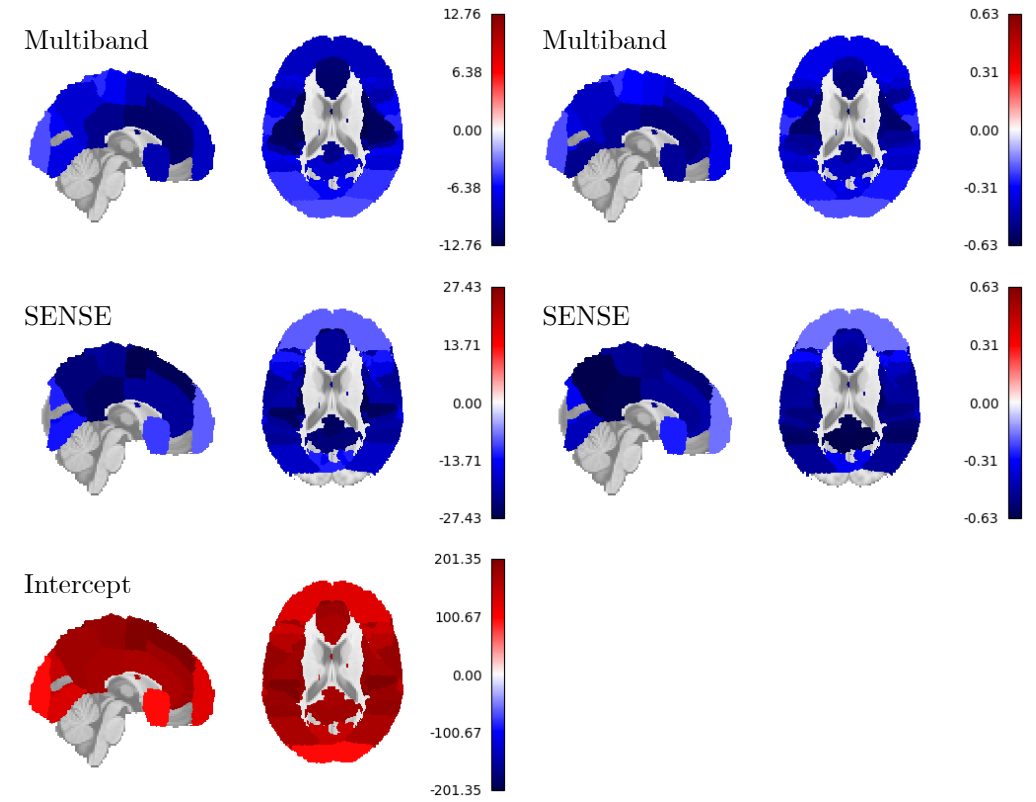

Note. Figure reflects the results from linear mixed models including both multiband and SENSE as fixed effects, with only main effects included in the model. Regions with a $p < .001$ are shaded. Overall, there are large differences in coefficients across the brain.

Figure 4.6

Coefficient variability across the brain for the Achieva

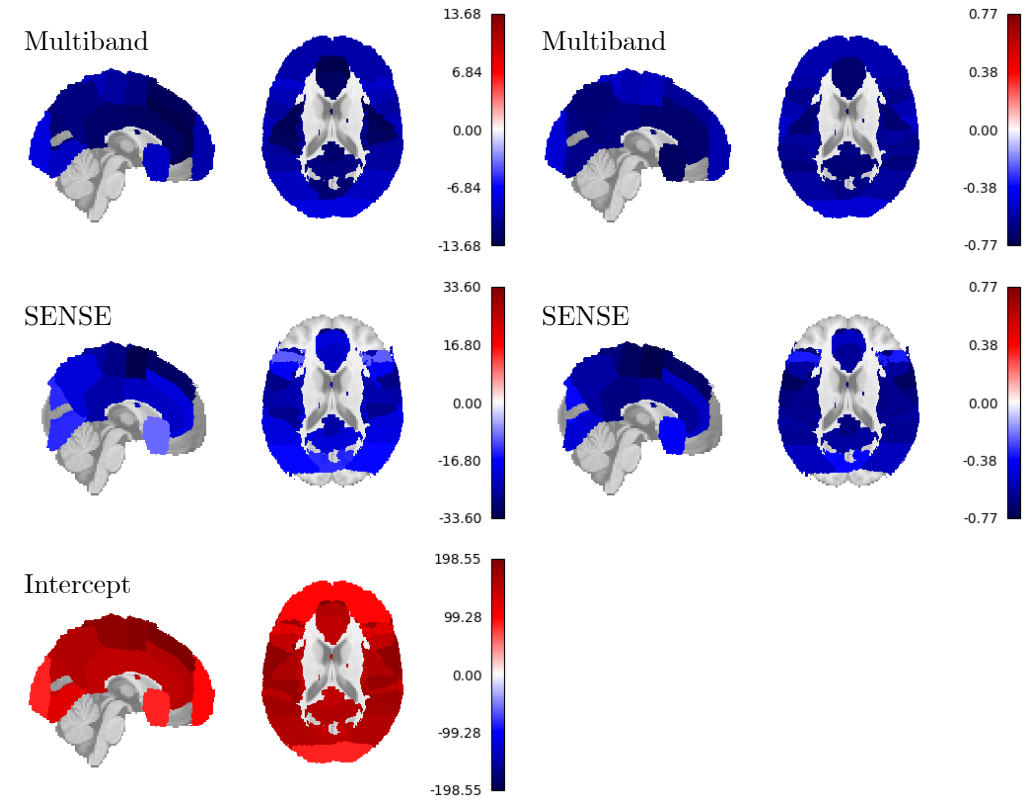

Note. Figure reflects the results from linear mixed models including both multiband and SENSE as fixed effects, with only main effects included in the model. Regions with a $p < .001$ are shaded. Overall, there are large differences in coefficients across the brain.

there are a number of brain regions where the difference between scanners did not match the $p<.001$ threshold which was commonly met by both MB and SENSE (Figure 4.5 & Figure 4.6).

4.3.2 Effect of IAP on the Occipital Pole (OP) tSNR

For data collected on the Ingenia in the OP, the model including only MB as a fixed effect was the best model for predicting tSNR (M group size = 16.1, $n = 129$). This can be seen in Figure 4.8 where increasing SENSE factor had only a marginal effect, if any, on tSNR. While there was a significant effect of MB on tSNR (z = -3.90, q = .001, β = -.22, B = -4.41, 95% CI [-6.63, -2.19]), the variance explained when accounting for only this fixed effect was very small ($R^2_{MargAdj} = .029$). When also accounting for the random effect of subject (S = 17) in the model, a much larger percentage of variance of tSNR was explained ($R^2_{CondAdj} = .62$).

Similar to the Ingenia, for the Achieva, the model containing only MB as a predictor provided the best model (M group size = 16, $n = 128$). There was a statistically significant main effect of MB on tSNR (z = -8.51, q = .001, β = -.48, B = -8.12, 95% CI [-9.99, -6.25]), with a moderate amount of variance explained by the fixed effect of MB alone $R^2_{MargAdj} = .20$. With the inclusion of the random effect of subject in the model ($S = 12.45$), a large amount of variance is explained by the model $R^2_{CondAdj} = .61$.

The final prediction models for the Ingenia and Achieva are:

$$\text{tSNR} = 94.84 - 4.41x_{\text{MB}} \qquad \text{(Ingenia)} \qquad (4.5)$$

$$\text{tSNR} = 92.10 - 8.12x_{\text{MB}} \qquad \text{(Achieva)} \qquad (4.6)$$

Figure 4.7

Coefficient variability across the brain for the Ingenia and Achieva.

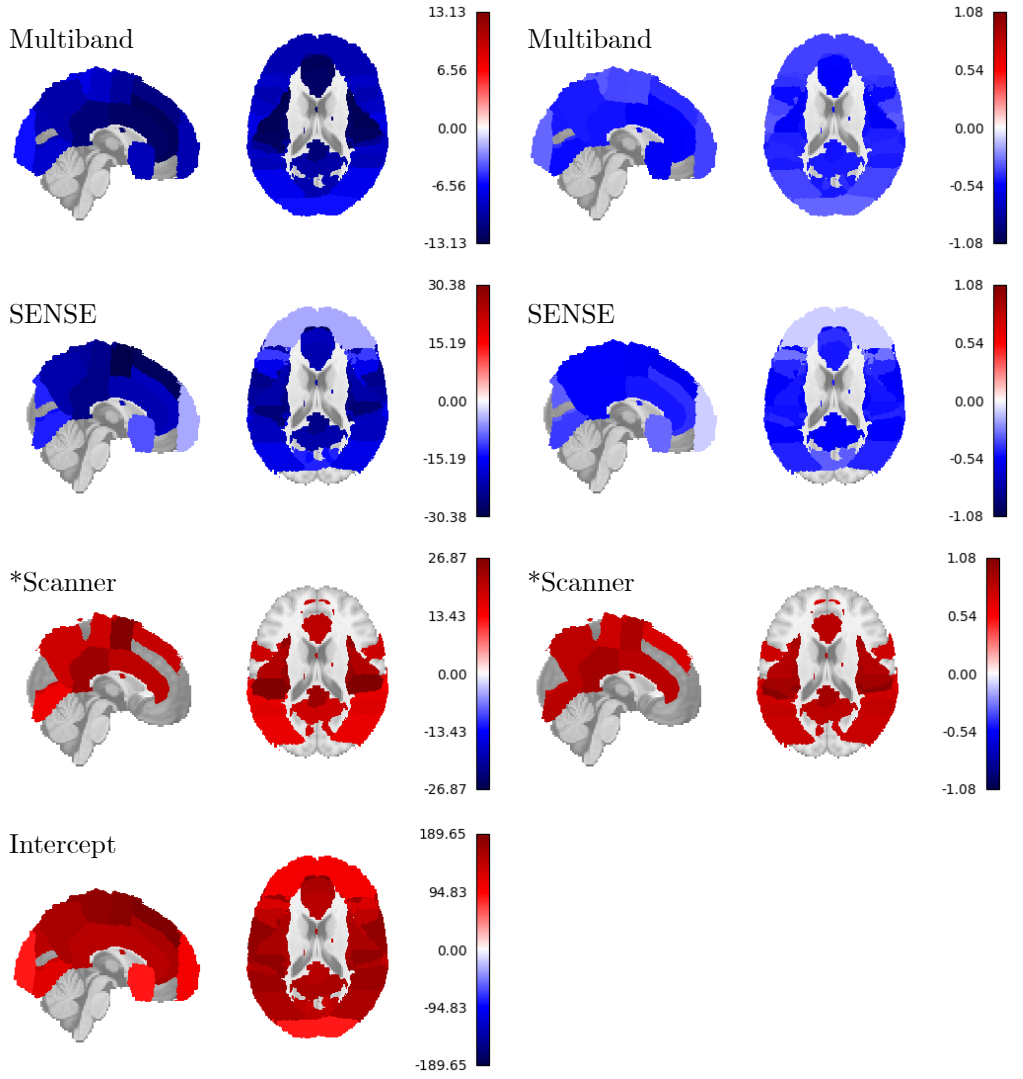

Note. The figure reflects the results from a linear mixed model which included scanner (dummy-coded where 1 = Ingenia), multiband, and SENSE as fixed effects, with only main effects included in the model. Regions with a $p < .001$ are shaded. While overall, there are large differences in coefficients across the brain, there are a number of regions that do not significantly vary between scanner platform.

Figure 4.8

Barchart showing effect of multiband and SENSE factor on tSNR for the Occipital Pole

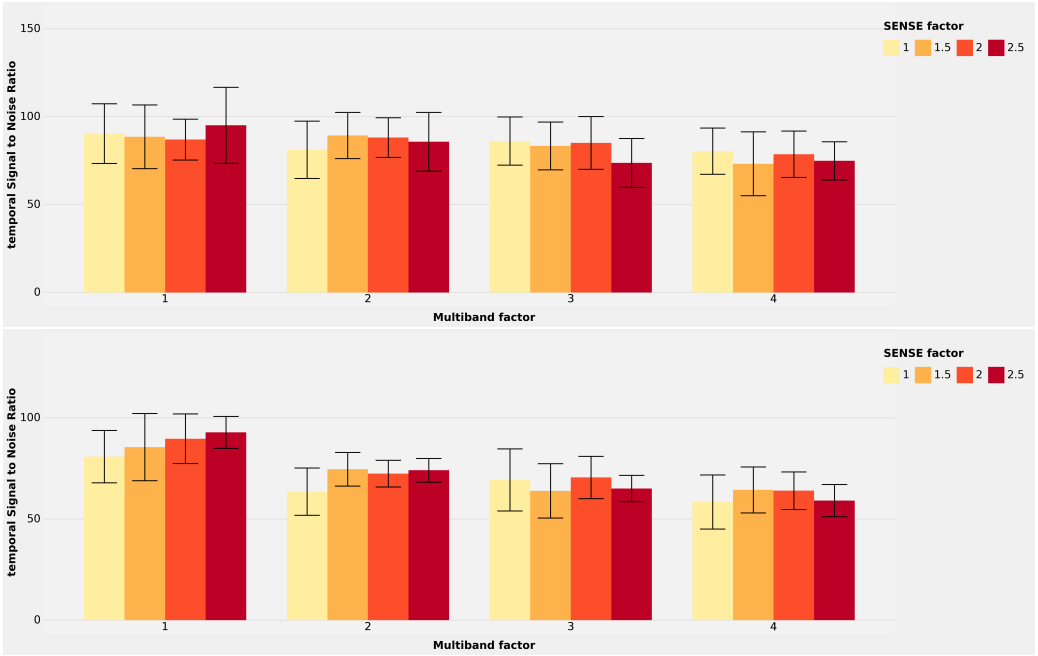

Note. Top row shows data from the Ingenia, whereas bottom row shows data from the Achieva. Error bars show 95% confidence intervals. Increasing the Multiband acceleration factor produces a small decrease in tSNR, however SENSE acceleration factor does not have a significant impact on tSNR.

4.3.3 Effect of IAP on the Frontal Pole (FP) tSNR

For data collected on the Ingenia, the model containing both MB and SENSE as fixed effects without the inclusion of interaction effects, provided the best predictive model for the FP (M group size = 16.1, n = 129). There were significant effects of both MB (z = -7.52, q = .001, β = -.35, B = -8.65, 95% CI [-10.90, -6.39]) and SENSE (z = -3.75, q = .001, β = -.17, B = -8.68, 95% CI [-13.21, -4.15]) on tSNR (as shown in Figure 4.9), however as with the OP, the inclusion of the random effect of subject (S = 22.46) increased the explained variance by a large amount, from $R^2_{MargAdj}$ = 0.12 to $R^2_{CondAdj}$ = .74.

In contrast, for data collected on the Achieva, the model containing only MB provided the best model (M group size = 16, n = 128). There was a statistically significant main effect of MB on tSNR (z = -12.98, q = .001, β = -.55, B = -10.14, 95% CI [-11.67, -8.61]), with a moderate amount of variance explained by the fixed effect of MB alone $R^2_{MargAdj}$ = .28. With the inclusion of the random effect of subject in the model (S = 14.93), a large amount of variance is explained by the model $R^2_{CondAdj}$ = .78. The final prediction models for the Ingenia and Achieva are:

$$\text{tSNR} = 124.72 - 8.64x_{\text{MB}} - 8.68x_{\text{SENSE}} \quad \text{(Ingenia)} \quad (4.7)$$

$$\text{tSNR} = 94.44 - 10.14x_{\text{MB}} \quad \text{(Achieva)} \quad (4.8)$$

4.3.4 Effect of IAP on the Posterior Inferior Temporal Gyrus (pITG) tSNR

For data collected on the Ingenia, the model containing main effects for both MB and SENSE provided the best predictive value for the pITG (M group size = 13.9, n = 97), with the main effects for both MB (z = -5.30, q = .001, β = -.21, B = -6.55, 95% CI [-6.88, -3.71]) and SENSE (z = -7.91, q = .001, β = -.27, B = -5.22, 95% CI [-10.88, -4.94]) added significantly to the

Figure 4.9

Barchart showing effect of multiband and SENSE factor on tSNR for the Frontal Pole

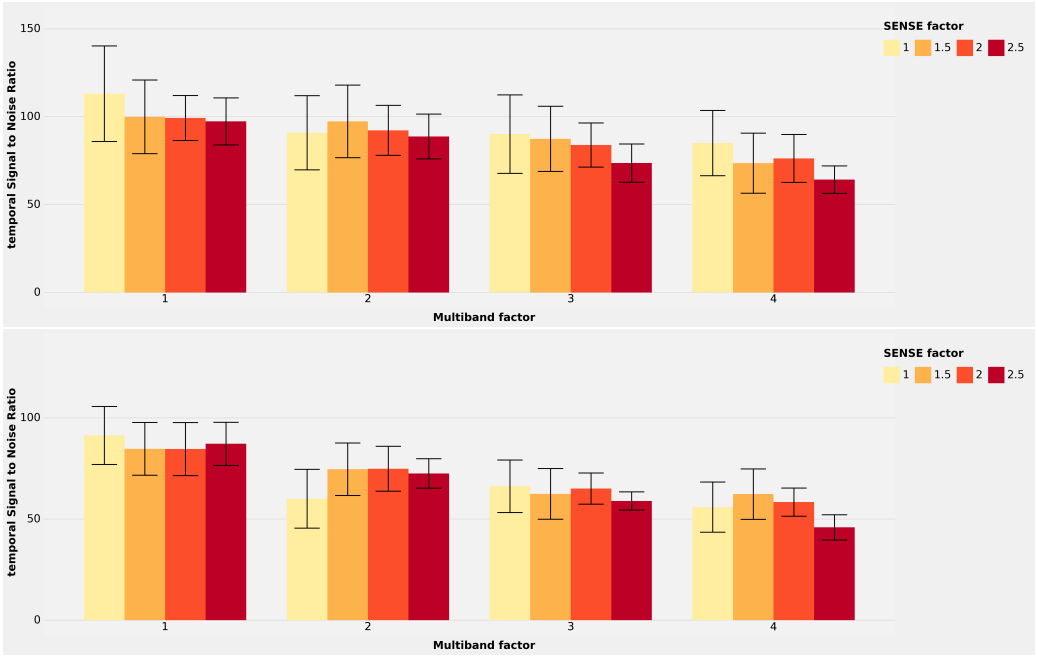

Note. Top row shows data from the Ingenia, whereas bottom row shows data from the Achieva. Error bars show 95% confidence intervals. Both Multiband and SENSE acceleration modulates tSNR for the Ingenia, however only Multiband acceleration produced a significant impact on tSNR for the Achieva.

model. When taking into account the subject variance (S = 20.84), a very large proportion of variance was explained by the model ($R^2_{MargAdj} = 0.061$, $R^2_{CondAdj} = .87$).

For data collected on the Achieva, the model which contained only the interaction effect between MB and SENSE provided the best predictive value for the pITG (M group size = 13.4, $n = 107$), with there being a significant interaction effect between MB and SENSE on tSNR (z = -12.49, $q = .001$, β = -.22, B = -3.13, 95% CI [-3.62, -2.64]). A moderate amount of variance was explained by this interaction effect alone $R^2_{MargAdj} = 0.38$. However as shown in Figure 4.10, this result is likely primarily driven by very high level of tSNR for the MB1S1 condition. When taking into account the participant variance ($S = 7.16$), a large proportion of variance was explained by the model ($R^2_{CondAdj} = .74$). The final predictive models for the Ingenia and Achieva are:

$$\text{tSNR} = 74.92 - 5.30x_{\text{MB}} - 7.91x_{\text{SENSE}} \quad \text{(Ingenia)} \quad (4.9)$$

$$\text{tSNR} = 62.41 - 3.13x_{\text{MB}\times\text{SENSE}} \quad \text{(Achieva)} \quad (4.10)$$

4.3.5 Effect of NORDIC denoising on tSNR

The effect of NORDIC on tSNR was also compared between the Ingenia and Achieva. For these analyses, data that was both not denoised and that which had been through the NORDIC denoising pipeline were included in the dataset. The NORDIC predictor was represented as a dummy-coded categorical variable, indicating whether the data was NORDIC denoised (1 = NORDIC denoised). The mean and standard deviation of tSNR across all cortical regions are shown in Figure 4.11 and Figure 4.12, with supplementary figures provided in 7.8. For the Ingenia, across all cortical regions, including both MB and SENSE as fixed effects without the inclusion of interaction effects, provided the best predictive model ($R^2_{MargAdj} = .31, R^2_{CondAdj} = .64$, Participant S = 14.26, M group size = 30.2, $n = 242$). MB (z = -10.25, q =

Figure 4.10

Barchart showing effect of multiband and SENSE factor on tSNR for the posterior Inferior Temporal Gyrus

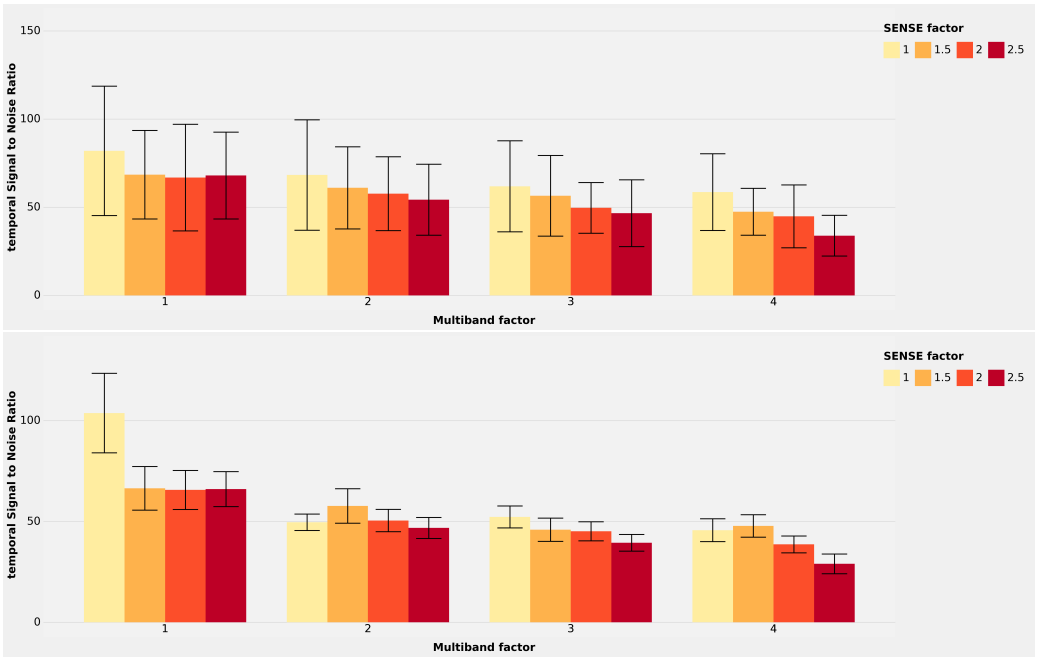

Note. Top row shows data from the Ingenia, whereas bottom row shows data from the Achieva. Error bars show 95% confidence intervals. Both Multiband and SENSE acceleration factor significantly impacted tSNR for the Ingenia. However for the Achieva, only the interaction effect between these two predictors was found to be significant. This may be driven by the large spike in tSNR seen in the MB1S1 condition, however this may be the result of poor ROI fitting of this region, due to its relatively small size.

.001, β = -.40, B = -8.67, 95% CI [-10.32, -7.01]), SENSE (z = -8.37, q = .001, β = -.33, B = -14.25, 95% CI [-17.59, -10.91]) and NORDIC denoising (z = 6.60, q = .001) added significantly to the model, with NORDIC denoising increasing the overall tSNR by B = 12.93 (95% CI [9.09, 16.77], β = .53).

For the Achieva across all cortical regions, as with the Ingenia, including both MB and SENSE as fixed effects without the inclusion of interaction effects, provided the best predictive model ($R^2_{MargAdj}$ = .74, $R^2_{CondAdj}$ = .84, Participant S = 5.75, M group size = 32, n = 256). MB (z = -27.16, q = .001, β = -.68, B = -10.98, 95% CI [-11.78, -10.19]), SENSE (z = -19.96, q = .001, β = -.50, B = -16.14, 95% CI [-17.73, -14.56]) and NORDIC denoising (z = 8.15, q = .001) added significantly to the model. NORDIC denoising increased the overall tSNR by B = 7.37 (95% CI [5.59, 9.14], β = .41).

As seen in Figure 4.13 & Figure 4.14, NORDIC denoising had a larger impact on tSNR in regions such as the Occipital and Frontal Poles for the Achieva. As indicated by the β values however, NORDIC denoising had a larger overall effect for scans collected on the Ingenia than on those collected on the Achieva. The predictive equations for both the Ingenia and Achieva are:

$$\text{tSNR} = 152.16 - 8.67x_{\text{MB}} - 14.25x_{\text{SENSE}} + 12.93d_{\text{NORDIC On}}(\text{Ingenia}) \tag{4.11}$$

$$\text{tSNR} = 145.52 - 10.98x_{\text{MB}} - 16.14x_{\text{SENSE}} + 7.37d_{\text{NORDIC On}}(\text{Achieva}) \tag{4.12}$$

4.3.6 Impact of Multiband (MB) and SENSE on acoustic noise levels

While the overall SPLs of the Ingenia (Table 4.3) and Achieva (Table 4.4) were similar, the relationship between MB and SENSE on SPL slightly was different between the scanners (see Figure 7.1 in 7.8 for the supplementary figure). Generally on the Ingenia, the SPL decreased as MB and SENSE factors increase. It should be noted that at MB1 a lower number of slices

Figure 4.11
Mean tSNR values on the Ingenia with NORDIC denoising

Note. Values represent the mean across each ROI. Data on the Achieva follows a similar pattern. As with when the data was not denoised, overall there is a decrease in tSNR as Multiband and SENSE factor increases, however the decline as acceleration factors is not as steep when NORDIC PCA denoising has been applied.

Figure 4.12

tSNR standard deviation on the Ingenia with NORDIC denoising

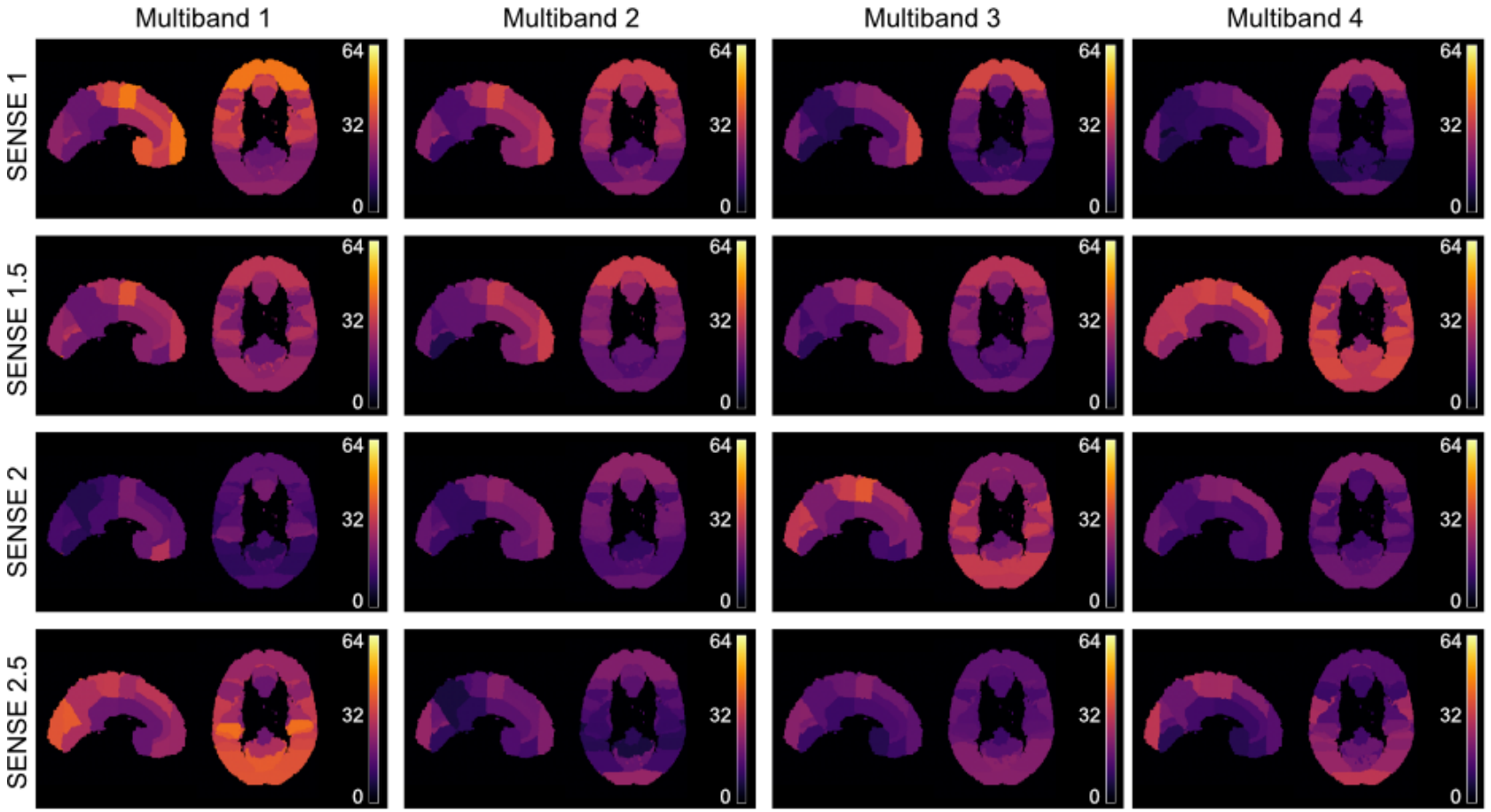

Note. Values represent the standard deviation across each participant for each ROI. Data on the Achieva follows a similar pattern. This figure shows a similar relationship between Multiband and SENSE on standard deviation of tSNR, as when the data has not been denoised, indicating that standard deviation of the tSNR does not seem to be greatly effected by the application of NORDIC.

Figure 4.13

Effect of NORDIC on coefficient variability across the brain for the Ingenia

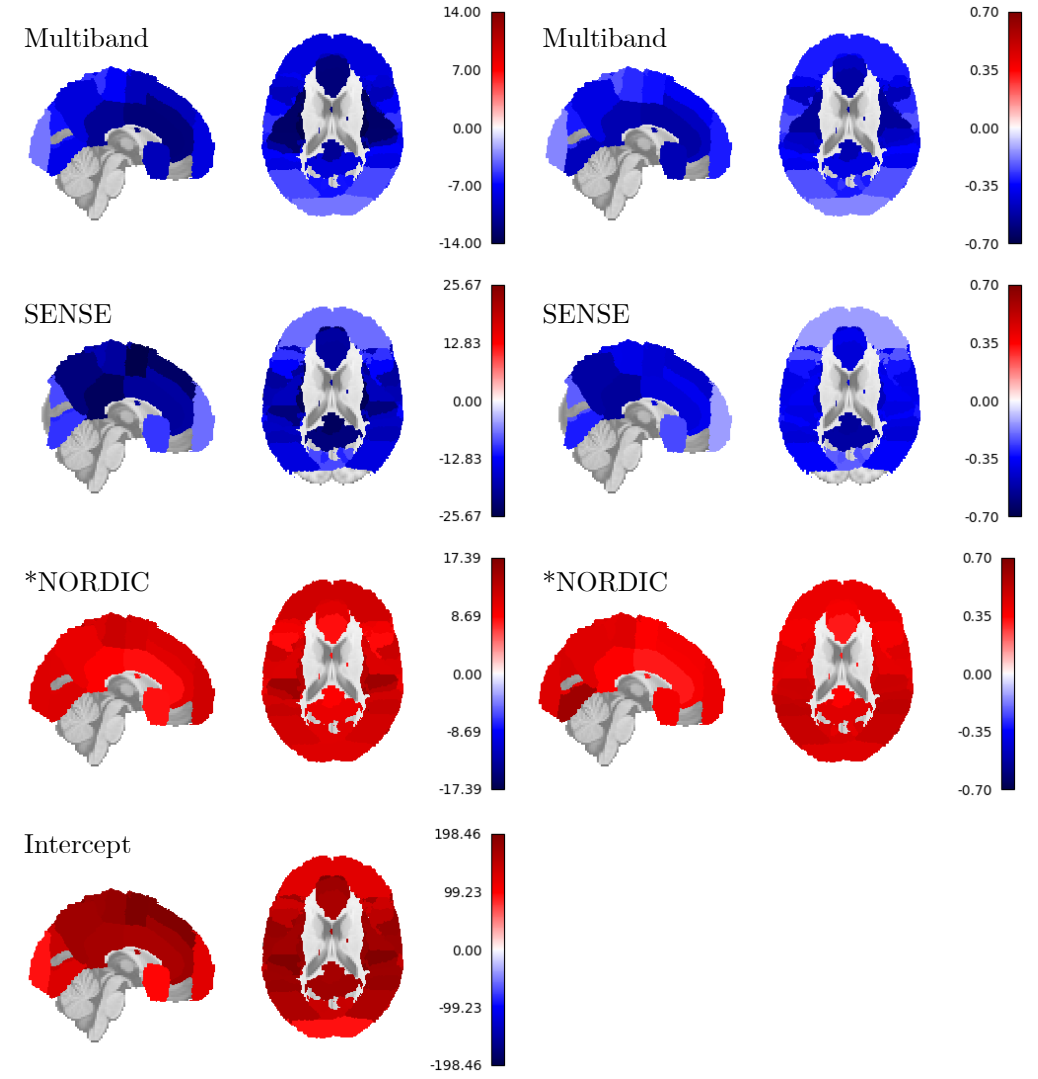

Note. The figure reflects the results from a linear mixed model which included NORDIC denoising (dummy-coded where 1 = NORDIC denoised), multiband, and SENSE as fixed effects, with only main effects included in the model. Regions with a $p < .001$ are shaded. Of note is that, NORDIC on the Ingenia produces a significantly beneficial (and consistent) impact to tSNR across the entire brain.

Figure 4.14

Effect of NORDIC on coefficient variability across the brain for the Achieva

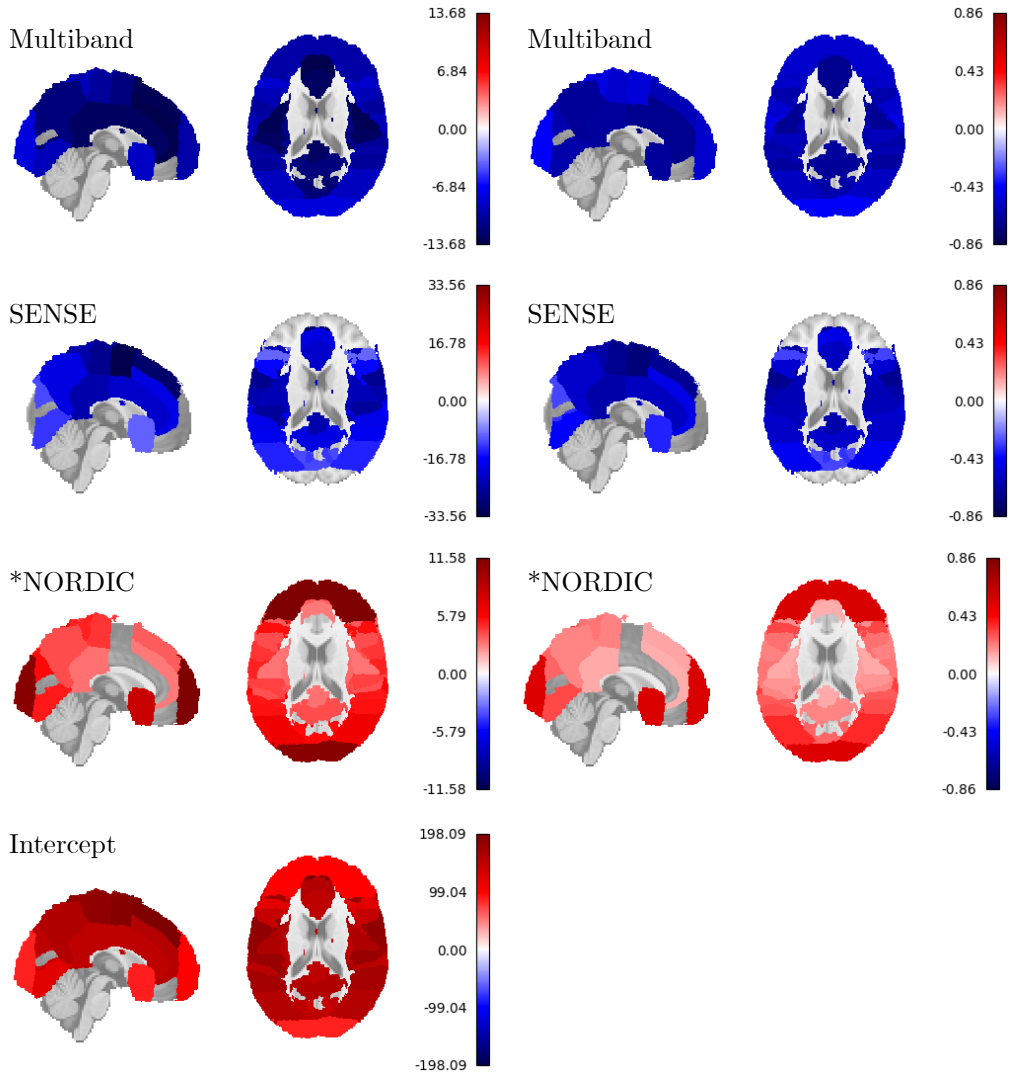

Note. The figure reflects the results from a linear mixed model which included NORDIC denoising (dummy-coded where 1 = NORDIC denoised), multiband, and SENSE as fixed effects, with only main effects included in the model. Regions with a $p < .001$ are shaded. For NORDIC on the Achieva, there is not a consistent beneficial impact of NORDIC on tSNR, with regions such as the Occipital and Frontal Poles benefitting more greatly from NORDICś application than more central regions.

are collected in some cases, which lowers the SPL. For the Achieva, at every MB factor, SENSE 1 produced lower SPL than higher SENSE factors, likely because of the change in bandwidth in the EPI frequency direction on this scanner based on the gradient model. Also note a reduction in SPL for MB1 SENSE 2 on both scanners. This was due to an error in setting the water fat shift, resulting in a low EPI bandwidth on both scanners, with the Achieva having a relatively lower bandwidth.

Table 4.3

Table of sound pressure levels (dB) and relative loudness (in brackets) for Philips Ingenia 3T

	Multiband			
SENSE	1	2	3	4
1.0	119.7 *(1.0)*	117.9 *(0.88)*	116.9 *(0.82)*	116.1 *(0.78)*
1.5	119.5 *(0.99)*	116.5 *(0.8)*	115.4 *(0.74)*	114.8 *(0.71)*
2.0	117.8 *(0.88)*	116.6 *(0.81)*	114.7 *(0.71)*	114.1 *(0.68)*
2.5	118.3 *(0.91)*	116.3 *(0.79)*	114.4 *(0.69)*	113.6 *(0.66)*

Note. Relative loudness is calculated using the equation $x = 2^{(\frac{\Delta \text{dB}}{10})}$ and is relative to the sound pressure level for the multiband 1 SENSE 1 condition. Of note is there is a consistent decrease of sound pressure levels seen, as Multiband and SENSE acceleration is increased.

A multiple regression was run to predict SPL from MB and SENSE acceleration factor. For the Ingenia, these variables statistically significantly predicted SPL, $F(2, 13) = 78.8$, $p < .001$, $R^2_{Adj} = .91$. Both MB (t = -11.30, $p < .001$) and SENSE (t = -5.452, $p < .001$) acceleration factor added statistically significantly to the prediction of SPL, with the increase of MB (β = -.86, B = -1.4, 95% CI [-1.67, -1.13]) acceleration factor having a stronger impact on SPL than increasing SENSE (β = -.42, B = -1.35 95% CI [-1.89, -0.82]). Therefore the final prediction model for SPL for the Ingenia is:

$$\text{SPL} = 122.27 - 1.4x_{\text{MB}} - 1.35x_{\text{SENSE}} \tag{4.13}$$

Table 4.4

Table of sound pressure levels (dB) and relative loudness (in brackets) for Philips Achieva 3T

	Multiband			
SENSE	1	2	3	4
1.0	119.0 *(1.0)*	117.3 *(0.89)*	115.5 *(0.78)*	114.3 *(0.72)*
1.5	120.5 *(1.11)*	119.1 *(1.01)*	118.2 *(0.95)*	117.0 *(0.87)*
2.0	114.4 *(0.73)*	118.4 *(0.96)*	116.8 *(0.86)*	115.7 *(0.8)*
2.5	117.1 *(0.88)*	117.2 *(0.88)*	115.7 *(0.8)*	114.6 *(0.74)*

Note. Relative loudness is calculated using the equation $x = 2^{(\frac{\Delta \text{dB}}{10})}$ and is relative to the sound pressure level for the multiband 1 SENSE 1 condition. While overall the trend is for sound pressure levels to decrease as Multiband and SENSE factor increases, this relationship is much less consistent than seen on the Ingenia, with MB2 S1.5 having a higher relative loudness than MB1S1.

For the Achieva, the model that contained both the MB and SENSE factor was not significant $F(2, 13) = 3.36$, $p = .067$, $R^2_{Adj} = .24$, with MB (t = -2.40, $p = .032$) but not SENSE factor (t = -0.99, $p = .34$) adding statistically significantly to the model. As SENSE factor had the least significant regressor, it was removed from the model for the Achieva. However, the model only containing MB also did not statistically significantly predict SPL, with the predictive value of this model being smaller than for the Ingenia ($F(1, 14) = 5.7$, $p = .031$, $R^2_{Adj} = .24$), as MB factor had a smaller effect on SPL for the Achieva (t = -2.40, $p = .031$, β = -.54, B = -0.85, 95% CI [-1.61, -0.09]) than for the Ingenia.

4.4 Discussion

4.4.1 Influence of Multiband (MB) and SENSE acceleration on tSNR

As expected, a strong relationship was found between tSNR and both MB and SENSE acceleration factor. This relationship was found to explain 70% of the variance of the data for the Ingenia and 84% for the Achieva. Notably, cortical regions exhibited distinct differences in this relationship (see

Table 4.2 for predictive equations). For instance, the Frontal Pole had the highest base tSNR level, but suffered a greater tSNR penalty when increasing MB and SENSE acceleration factor.

Furthermore, the association between image acceleration parameters (IAP) and tSNR explained a substantial proportion of the data variance only when considering inter-subject variability. This is evident from the observation that $R^2_{CondAdj}$ values significantly exceeded $R^2_{MargAdj}$ values in many instances. Consequently, employing statistical tests capable of modeling between-subject variance, such as linear mixed models, is essential for this dataset. Additionally, scanner choice was found to have a strong effect on tSNR level, with this effect being larger than that of MB or SENSE acceleration factor. Finally, it was found that the NORDIC denoising method increased tSNR for both the Ingenia and Achieva.

4.4.2 Influence of imaging hardware on tSNR

It was found that overall, scanner choice (Achieva or Ingenia) had a larger effect on tSNR than both MB and SENSE factor with, as expected, the Ingenia platform having a significantly higher tSNR than the Achieva. This difference is likely in large part driven by the integration of the dStream technology on the Ingenia platform. It should be noted however, that while it is possible to upgrade Achieva scanners to use dStream, the scanner used in this study did not use this technology. In the electronics architecture for the Achieva, analog-to-digital conversion (ADC) is the last step in the electronics chain before reconstruction, meaning that the data is transmitted as an analog signal through most of the processing chain before being digitised. In contrast, the Philips dStream technology positions the ADC electronics at each coil element, allowing the MR signal to be digitised from the source of the signal (Possanzini, Ham, et al., 2011).

The ability to digitise the data at the source of the signal provides a number of benefits over the older analog architecture. With the analog radiofrequency architecture, signals are transmitted over long distances in bundles of cables before being digitised. This causes crosstalk, or the electromag-

netic coupling between the cables, increasing the amount of noise in the signal. With higher numbers of coil elements also requiring more cables to transmit this data, this crosstalk becomes increasingly worse as the number of coil elements are increased. For the digital radiofrequency architecture this is not the case, as there only one cable is required for the coil regardless of the number of channels in the coil (Possanzini, van Liere, et al., 2011). Additionally, as analog signals are continuous, noise introduced to the signal from external factors can more readily lead to a degredation of the signal's fidelity. In contrast, the discrete nature of digital signals means that the signal can withstand a certain level of noise without significantly impacting the data quality. Therefore, analog signals are more prone to interference from noise than digital signals.

A further consideration that may contribute to increased noise is the dynamic range of the ADCs for the Achieva and Ingenia platforms. Ideally, the ADCs should be able to digitise the full range of signals from the maximum at the central k-space point to the thermal noise level of the receiver (Behin et al., 2005). For example, a 7T whole body mouse scan at a resolution of $75\mu m$ requires 20-bits of dynamic range in order to fully digitise the MR signal (Behin et al., 2005). A dynamic range that is too narrow increases the likelihood of quantization errors, where small signal variations are lost in the noise floor of the ADC, degrading the quality of the digitized signal and reducing SNR. Analog systems such as the Achieva typically have 16-bits of dynamic range, whereas the dStream architecture allows a dynamic range between 22- and 26-bits (Possanzini, Ham, et al., 2011). It is unclear however whether 16-bits of dynamic range is a limitation in this study, as required dynamic range is dependent on factors such as spatial resolution.

4.4.3 Influence of Multiband (MB) and SENSE acceleration factors on sound pressure level (SPL)

While our study primarily focused on examining the relationship between IAPs and tSNR, the relationship between IAPs and sound pressure level (SPL) was also studied. The main source of acoustic noise in an MR scanner

comes from the rapid switching of magnetic field gradients during image acquisition (McJury, 2022). Increasing MB acceleration factor while holding constant the TR reduces the time for which the readout gradient is applied, as fewer excitations are needed to cover the same volume compared to conventional single-band imaging. This reduces the number of gradient switches per unit time and consequently also reduces the overall acoustic noise level. Similarly, parallel imaging methods such as SENSE reduce the amount of time needed to collect an image, which reduces the time required for gradient switching. This reduction in acquisition time has previously been used to allow silent periods during functional scanning to present auditory stimuli (De Martino et al., 2015). As acoustic noise was measured here as the root mean square SPL, it was expected that increasing MB and SENSE acceleration would reduce the SPL.

This was seen for the Ingenia, with a very strong negative relationship being found between SPL and both MB and SENSE acceleration factor for the Ingenia, with the model shown in Equation 4.13 accounting for 91% if the variance in the data. However, no such relationship was found for the Achieva. On closer examination, it was found that the MB1 SENSE 2 acquisition on both scanners was not matched for bandwidth in the EPI frequency direction. Further, on the Achieva, since the water fat shift was not adjusted when the exam card was moved across, EPI bandwidth was not matched for MB1 data collected across SENSE factors. Since the scanner hardware (including gradient characteristics) are different, acoustic performance also differs. Additionally it should be noted that in this study, slice number had to be reduced for MB1 in some cases to fit within the TR of the volume without the acquisition being split into two packages. However the collection of fewer slices also dampens the SPL of the sequence.

4.4.4 Effect of NORDIC PCA denoising

As the Achieva was found to have lower tSNR levels than the Ingenia, it would also be expected that NORDIC denoising would have a larger effect on the Achieva. In fact, the opposite was found to be true, with NORDIC being found to have a larger effect for the Ingenia. One possible explanation

for this might be the distribution of the additional noise present on the Achieva. NORDIC is designed to identify and remove Gaussian-distributed noise (Moeller et al., 2021); therefore this may indicate that the additional noise on the Achieva does not follow this distribution, and thus is unable to be removed using NORDIC. As seen in Figure 4.13 & Figure 4.14, another factor that may contribute to this result is that the variance of B values across cortical ROIs is higher for the Achieva than the Ingenia. While it is at resolutions of approximately 1.5mm isotropic that Gaussian-distributed thermal noise begins to dominate the noise in the data (Yoo et al., 2018), as seen here, even with a resolution of 3mm isotropic for functional volumes, NORDIC still provided a large benefit to tSNR level for both the Ingenia and the Achieva. This indicates that with the relatively low requirement to run NORDIC, that being outputting the phase data in additional to the magnitude data as well as collecting a single noise scan, researchers should strongly consider running NORDIC on data to improve BOLD sensitivity, even in non-thermal noise dominated scans.

4.4.5 Summary

Overall, these findings contribute to existing literature indicating the substantial effect of image acceleration techniques on tSNR. However, they also underscore that this association varies across brain regions. For instance, the Occipital Pole exhibited lower baseline tSNR than the Frontal Pole but also had a less pronounced response to increased acceleration factors than the Frontal Pole. Thus these results highlight the limitations of traditional tSNR calculation and reporting methods that do not take into account variance between regions. One significant factor contributing to the spatially variant effect of image acceleration methods on tSNR, is the g-factor of the image. Parallel imaging methods such as SENSE aim to speed up in-plane data acquisition by reducing the number of phase encoding steps. However this undersampling leads to aliasing within the image (Deshmane et al., 2012). g-factor is the characterisation of the ability of the current coil configuration to separate pixels superimposed by this aliasing (Pruessmann et al., 1999), akin to a "noise amplification" factor. As the g-factor is contingent upon the

coil geometry, it exhibits spatial variability. As seen in the below equation, apparent SNR is a function of both the reduction of scan time due to parallel imaging (R), and g factor:

$$SNR_{\text{parallel}} = \frac{SNR}{g\sqrt{R}} \tag{4.14}$$

Since the g-factor has been identified as a significant contributor to the SNR variance across the image in both SENSE (Pruessmann et al., 1999) and MB (Todd et al., 2017), it is likely that this factor largely accounts for the reliance on MB and SENSE for temporal SNR observed here. Therefore even on the same scanning platform, it is probable that the difference between head coils with differing coil geometries on the spatial non-uniformity of tSNR would be significant.

Past research has also found a spatially varying relationship between image acceleration methods and tSNR (Demetriou et al., 2018; Todd et al., 2017). However, the current study demonstrates a novel analysis pipeline using fRAT (Howley et al., 2023) which enables the investigation of differences between ROIs in the relationship between image acceleration methods and tSNR. This approach utilises atlas-defined ROIs to be able to analyse many regions simulatenously, with minimal data preprocessing requirements. Here, the only preprocessing step was skull stripping of the anatomical volumes using optiBET (Lutkenhoff et al., 2014). This pipeline could also be extended to convert other voxelwise maps into ROI-wise maps. This could be useful in the future to conduct ROI-wise analyses of both g-factor and tSNR maps, which could be used to determine how much of the spatial differences seen in this study were driven by non-uniformity in g-factor across the image.

Due to uniformity of coil sensitivity in the center of the brain, g-factor in subcortical areas is typically higher than in cortical areas, which consequently causes a large decrease in tSNR (Todd et al., 2017). Therefore, future research could also use fRAT to investigate the tSNR differences between subcortical and cortical areas within the brain. While it would be expected that subcortical areas have a lower base tSNR and a steeper decline in data quality

in response to higher acceleration factors compared to cortical regions, the variance between regions may be much lower for subcortical regions due to their small size relative to many cortical areas. Another factor that affects tSNR is the distance from head coil elements and magnetic susceptibility, with lower tSNR values seen in regions further from coil elements or with high magnetic susceptibility (Demetriou et al., 2018).

Unusually, an interaction effect between MB and SENSE was found for the pITG on the Achieva, with no interaction effects being found for any other condition. In Figure 4.10 it can be seen there is a large spike in tSNR for the MB1S1 condition, which is likely the cause of this interaction effect. As reported by fRAT, the average number of voxels per session (M_{vox}) for the MB1S1 condition on the Achieva was 91.57 while the overall $M_{vox}was409.52$ ($SD_{vox} = 148.92$). In contrast, it is possible that the timing limitations imposed by the MB1S1 condition caused this effect, with this being the only condition limited to 24 slices. Thus part of the pITG may reside outside the scan FOV, reducing the total number of voxels. However this is unlikely to be the case, as the scans collected on the Ingenia used the same imaging parameters as those collected on the Achieva, but the MB1S1 condition for the pITG had a similar M_{vox} value (228.17) to the rest of the conditions ($M_{vox} = 378.16$, $SD_{vox} = 88.40$). Instead the MB1S1 on the Achieva may have suffered from poor fitting in some scan sessions. A threshold of 200 voxels was set as the minimum voxel count necessary for a datapoint to be included in the linear mixed model, in total removing 16.41% of data points for the pITG (21/128), therefore some of these potentially problematic tSNR measurements would have been removed. However this interaction effect still remained. This result makes it clear that fRAT's default options may need to be optimised to reduce the chance of poor fitting in small areas (such as the pITG), or to remove the effect of poor fitting on the statistics step of fRAT CAP.

In conclusion, these results clearly show distinct differences between the tSNR of the measured cortical ROIs, with each region having a different relationship between image acquisition parameters and tSNR. The typically reported whole-brain measures of tSNR obscures the difference between ROIs, but more seriously, the tSNR for both cortical and subcortical regions are

combined, either over- or under- reporting tSNR depending on the location of the region being investigated. tSNR can also be reported for an ROI as localised by functional activity, however this leads to a circular analysis where the selection criteria for the region is not independent from the test statistic (Kriegeskorte et al., 2010). Therefore it is suggested that whole-brain measures of tSNR are replaced by ROI-wise measures of tSNR, with ROIs defined by anatomical atlases. The extent to which the findings from this study apply to other imaging centers is determined by the hardware available at those sites. Nevertheless, the outcomes presented here can offer a broad understanding of how both MB and SENSE techniques influence tSNR across the brain and highlight the importance of optimising image acquisition parameters for a given study. Additionally, since fRAT only necessitates anatomical and functional volumes without the need for non-standard scans, researchers can employ the same analysis pipeline outlined in this study to conduct pilot investigations, allowing them to optimise scanning parameters according to the regions being investigated. Employing an equation such as that proposed by Murphy et al. (2007) can then be used to estimate the number of time points necessary to reliably find activation.

While this chapter investigated the expected tSNR at different acceleration factors, the next chapter will investigate the impact of various tSNR levels in a population receptive field experiment through adding simulated noise.

Chapter 5

Examining the effect of simulated noise and motion on a population Receptive Field analysis

The work described in this chapter has been presented as a poster at the European Conference of Visual Perception:

Howley, E., Francis, S., & Schluppeck, D. (2023, August). The effect of reduced temporal signal-to-noise ratio and participant motion on a population receptive field analysis. Poster session presented at the European Conference on Visual Perception 2023, Paphos, Cyprus. Retrieved from URL: https://journals.sagepub.com/page/pec/collections/ecvp-abstracts/index/ecvp-2023

5.1 Introduction

Early visual areas are organised retinotopically (Engel et al., 1997). The delineation and identification of borders between these visual areas is possible by creating visual field maps (Wandell et al., 2007) on which region-of-interest (ROI) analysis can be ran (Wandell et al., 2007). The ability to produce accurate visual field maps is therefore essential for many aspects of vision research. Population Receptive Field (pRF) analysis, as first performed by Dumoulin & Wandell (2008), uses fMRI to characterise the spatial receptive fields of neuronal populations in the visual cortex (Figure 5.1). While there have been a number of alternative methods proposed to produce visual field maps (Greene et al., 2014; Lee et al., 2013; Merkel et al., 2018), the pRF method is still widely used.

Visual field maps can help to identify residual visual activity which would not be captured by standard clinical tests such as static perimetry (Beh et al., 2021; Papanikolaou et al., 2014). Thus pRF analysis is increasingly being used to study visual disorders (Beh et al., 2021; Dumoulin & Knapen, 2018) to aid rehabilitation for which the ability to produce accurate and reliable pRF estimates is critical. pRF estimates of size, eccentricity and polar angle have been shown to be very reliable within a single scan session (van Dijk et al., 2016). However, the reliability and accuracy of pRF estimates can be compromised by the various sources of noise which can affect data quality, such as thermal noise, scanner artifacts such as gradient instability and RF noise, as well as subject head motion.

Temporal Signal-to-Noise Ratio (tSNR) is commonly used to measure the data quality in fMRI research and is affected by factors including the imaging hardware and acquisition parameters (Demetriou et al., 2018; Hutton et al., 2011; Todd et al., 2016) as well as subject motion and physiological noise. Additionally, it has been shown that acquisition parameters impact the tSNR in a spatially varying manner (Chapter 4). As the measure of tSNR serves as a proxy for BOLD sensitivity (Murphy et al., 2007), measuring tSNR level is crucial for determining whether a dataset is likely to have false-negative errors.

Figure 5.1

Example visual field maps derived from a population Receptive Field analysis

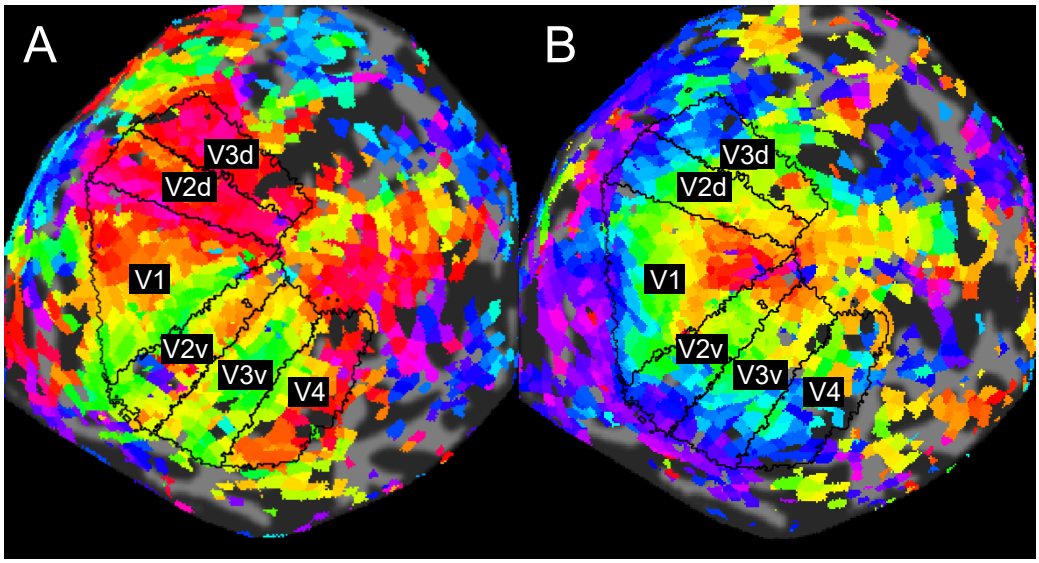

Note. Polar angle (A) and eccentricity (B) maps of receptive field centers are shown overlaid on a flattened map of the right visual cortex. The visual regions V1 through V4 are labeled, with V2 and V3 further divided into dorsal (e.g. V2d) and ventral (e.g. V2v) regions. A minimum R^2 threshold of 20% is used to display data.

One common method of increasing the reliability of activation detection is by increasing the number of time points in each fMRI scan (Murphy et al., 2007), as combining data across multiple scans increases tSNR to allow reliable activation detection in voxels that would otherwise have low levels of tSNR (Saad et al., 2003). However one of the main causes of MRI subject discomfort is the length of scans (Chou et al., 2014; Heilmaier et al., 2011), therefore the scan time of the given fMRI run is necessarily restricted. Scan time is also limited by subject motion (Maclaren et al., 2013) which has been suggested to be the second biggest determinant of test-retest reliability (Gorgolewski et al., 2013). Further, as longer scan times increase the chance of subject movement, this can mean that the theoretical increase in activation detection at longer scan times is not realised. This is especially the case as some visual disorders are associated with movement disorders, affecting their ability to tolerate longer scanning sessions. Recent advances in data preprocessing methods such as NOise Reduction with DIstribution Corrected (NORDIC) PCA denoising (Moeller et al., 2021) have also been developed (see subsection 2.3.4 for details). NORDIC PCA denoising suppresses Gaussian distributed thermal noise contributions in images, resulting in a reduction in noise without the requirement for increased scan time. However, the extent to which NORDIC PCA denoising improves pRF maps is so far unclear.

While NORDIC PCA denoising is available to reduce thermal noise (and consequently increase tSNR), the tSNR necessary to have adequate BOLD sensitivity is task dependent (Murphy et al., 2007), with tasks that elicit smaller task-related BOLD changes requiring higher levels of tSNR to reliably detect. To date, there has been little research to investigate the effect of tSNR on the results of pRF analysis. To address this gap in the literature, this chapter aims to characterise the impact of thermal noise on a pRF experiment, by parametrically varying added noise. Through investigating the sensitivity of pRF analyses to changes in tSNR levels, the necessary tSNR to produce accurate visual field maps is estimated. Additionally, the impact of simulated head motion on a pRF experiment is investigated, due to its significant impact in fMRI studies (Gorgolewski et al., 2013). By systematically manipulating tSNR levels and introducing controlled motion artifacts, the

extent to which these factors degrade the accuracy of pRF estimates is quantified. Importantly, this study aims to investigate the relative contributions of these factors to overall measurement variability of pRF analysis. Further, NORDIC PCA denoising will be used to investigate whether increased tSNR translates to an increase in pRF estimates accuracy. This study aims to advance the understanding of the noise-related challenges inherent in pRF mapping.

5.2 Methods

5.2.1 MRI Dataset

The data for this study came from a pre-existing pRF dataset (Beh et al., 2021) which was collected at the University of Nottingham under ethics code F944/F1055R. This comprised datasets from 4 stroke survivors (Participants 13978, 14326, 11773 and 14196) with unilateral brain lesions resulting in homonymous visual field loss. To ensure the visual field maps were as accurate as possible, only participants with high fixation stability were used in this study. In Beh et al. (2021), fixation stability of participants was measured during microperimetry using the Bivariate Contour Ellipse Area measure (Steinman, 1965) which contained 63% of fixations. This is a widely used method to determine of fixation stability (Crossland et al., 2004). As Participants 14326, 11773 and 14196 had relatively small BCEA values (ranging from $0.4^{\circ 2}$ to $1.7^{\circ 2}$) these participants were used for the study in this chapter, whilst Participant 13978 was excluded due to low fixation stability (BCEA values ranging from $17.9^{\circ 2}$ to $26.9^{\circ 2}$).

To derive information about the visual field maps, Beh et al. (2021) integrated information from a variety of stimuli types, including expanding/-contracting rings and rotating wedges typically seen in the travelling-wave method of retinotopy mapping (Engel et al., 1997; Wandell et al., 2007), as well as moving bars as introduced by the pRF method (Dumoulin & Wandell, 2008). Imaging data was acquired on a 3T Philips Achieva using a 32-channel head coil. This comprised an anatomical scan, functional scans,

a T2-weighted scan and a diffusion weighted scan, however the latter two scan types were not used here. Anatomical scans were acquired using a 1mm isotropic T1-weighted 3D MPRAGE sequence (SENSE factor 3, TE = 3.7 ms, TR = 8.13 ms, FA = 8°, TI = 960 ms, FOV 160 × 256 × 256 mm^3). Functional MRI data were acquired using a 2D gradient echo EPI scheme (24 slices at 3mm isotropic resolution, SENSE factor 2, TE = 35 ms, TR = 1500 ms, flip angle = 75°) in a close to axial slice prescription covering most of the head from frontal to occipital cortex. Participants 14326, 11773 and 14196 were presented with expanding/contracting ring and rotating wedge stimuli. Additionally, Participants 14326 and 14196 were presented with moving bar stimuli.

See Beh et al. (2021) for further details on the MRI scan parameters used and stimuli presentation.

5.2.2 Study Design

To assess the effect of noise and motion on pRF analysis, a pRF analysis was first conducted on the original dataset to get voxel wise pRF estimates. Next, we independently varied the tSNR of the data in two ways: by adding Gaussian noise and by introducing a Gaussian-distributed motion artefact, ensuring both methods had a similar impact on tSNR. Additionally, tSNR was varied by using the NORDIC PCA denoising method (Moeller et al., 2021). We then performed a pRF analysis on these modified datasets and compared the results to the original data.

The independent variable was the data modification technique used, with there being 8 levels of this variable: unmodified data, de-noised data, 3 levels of added simulated thermal noise and 3 levels of added head motion. Both the simulated thermal noise and head motion was Gaussian-distributed with mean (μ) equal to zero and standard deviation (σ) equal to 1x, 2x, or 5x the values in the original data. As thermal noise is Gaussian distributed (Wald & Polimeni, 2017) this addition of noise simulates increased thermal noise.

Analyses were conducted on each participant independently, with the level

of ground truth thermal noise and head motion first calculated for each participant, resulting in the simulated absolute level of thermal noise and head motion σ being different for each participant. When adding simulated head motion, translations and rotations along the x, y, and z axes were separately calculated and integrated into the scans.

Three dependent variables were compared between the 8 levels: R^2, which represents the variance in the signal that the final pRF model can explain, the pRF parameter estimates for receptive field half-width and the pRF parameter estimates for receptive field centre location. As the receptive field centre location is two-dimensional, the distance between the receptive field centres was calculated as the one-dimensional euclidean distance (d):

$$d = \sqrt{(x_2 - x_1)^2 + (y_2 - y_1)^2} \tag{5.1}$$

where x_1 and y_1 are the coordinates of one pRF centre, and x_2 and y_2 are the coordinates of the other.

5.2.3 Defining visual area Regions of Interest

There is a strong link between the structure and function of the visual cortex, with anatomy scans able to be used to predict the retinotopic organisation of the striate cortex with accuracy equivalent to 10-25 minutes of functional mapping (Benson et al., 2012). Therefore anatomical templates such as the Wang Probability Atlas (Wang et al., 2015) are widely used when defining visual area ROIs (Himmelberg et al., 2021). The Beh et al. (2021) study used ROIs defined using the Wang Maximum Probability Atlas (Figure 5.2) to also account for the fact that stroke damage in the cortex can make it impossible to define ROIs using cortical surfaces and flat maps. Therefore, relying on voxel-based template atlases may be the only approach possible. Anatomical atlases tend to be more accurate when defining early visual areas, as early visual areas have less inter-subject variability than higher-order areas (Benson et al., 2012; Himmelberg et al., 2021; Wang et al., 2015). Thus in this study, we focus on the early visual areas of V1, V2 and V3. As

Figure 5.2

Sagittal and axial images showing visual regions defined by the Wang Maximum Probability Atlas

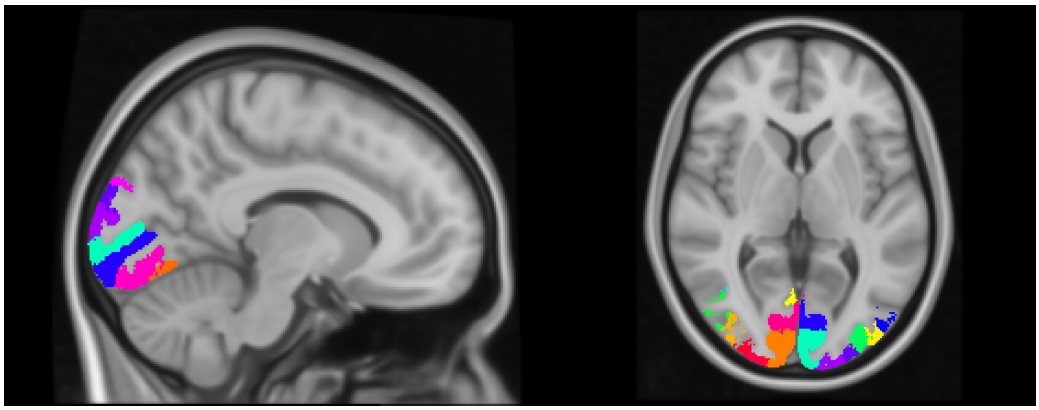

participants had unilateral brain lesions, analyses were only conducted in the early visual areas of the un-lesioned hemisphere.

5.2.4 Adding simulated thermal noise and head motion

To tailor the simulated thermal noise and motion levels to match those observed in participants, we initially determined the thermal noise and head motion levels present in the ground-truth data, using the analysis steps outlined below, for each participant.

The first step was the creation of tSNR maps using fRAT *Maps* (Howley et al., 2023). Prior to creating these maps, a temporal highpass filter of 0.01 Hz was used to remove low frequency drift from the signal. Motion correction was also applied to reduce the effect of subject motion on tSNR in this "ground-truth" data set. The settings used with fRAT to create these maps are the same as those in subsection 4.2.4 which are provided in Appendix 7.2. As seen in Equation 3.7, a measure of voxelwise noise (σ) must be calculated before creating the tSNR maps.

As fRAT *Maps* also output the σ maps when creating the tSNR maps, the next step was to run fRAT *CAP*'s analysis step on these σ maps (see Appendix 7.6 for the settings used) to provide an ROI-wise measurement of σ. The shell script optiBET (Lutkenhoff et al. (2014); montilab.psych.ucla.

edu/fmri-wiki/optibet/) was used for brain extraction of the anatomical images. The choice of optiBET was crucial, as fRAT requires a high degree of accuracy for brain extraction if, as is the case here here, the analysis is restricted to only grey matter voxels. Restricting analysis to grey matter here was helpful in avoiding the inclusion of lesioned regions in the analysis. Further, typical brain extraction tools can struggle in cases where the data contains severe pathologies (Lutkenhoff et al., 2014) as is the case in the current dataset. ROIs for use with fRAT CAP were defined using the Harvard-Oxford atlas of cortical structures (Desikan et al., 2006).

This analysis created ROI-wise summary statistics for σ across the brain. The mean σ value for the region closest to the voxels being investigated in the occipital pole was then used as the starting thermal noise level for the noise addition manipulation. Further, the fRAT reported translations (x, y, and z) and rotations (yaw, pitch and roll) of head motion during scanning which were used as the ground-truth motion levels. These measures of ground-truth thermal noise and head motion were used with fRAT HOUSE to add simulated thermal noise and head motion to the data after motion correction using mrTools. The equations used to generate the simulated thermal noise and head motion values are shown in subsection 3.3.3. tSNR across the Occipital Pole for each data type was then calculated using fRAT (see Appendix 7.7 for the settings used).

5.2.5 Population Receptive Field (pRF) analysis

The mrTools neuroimaging analysis package (Gardner et al., 2018) was used to perform pRF analysis and other standard preprocessing steps such as linear detrending and motion correction. As multiple scans were collected per participant, these scans needed to be registered into the same native space. Therefore within and between-scan alignment (motion correction) was performed on the time average of each original data scan using mrTools. Simulated thermal noise, simulated head motion, or NORDIC PCA denoising was then applied to this preprocessed data to create the different modified datasets.

The following steps were then performed to the original and all simulated data sets. Alignment to the anatomical volume was performed using the mrAlign tool within mrTools. Alignment was calculated between the original data and the anatomical volume and this transformation matrix was then applied to the fMRI data sets. Before the model fitting, the scans for each data type were concatenated in time, keeping track of the transition points, to allow for fitting a model to the entire timeseries for each voxel. Low-frequency drift correction was applied using a highpass filter at 0.01Hz. Visual regions were delineated using the Wang Maximum Probability Atlas (Wang et al., 2015) which was registered to the anatomical volume. Finally, 2D Gaussian pRF models were fit using the Nelder-Mead Simplex algorithm (Nelder & Mead, 1965). pRF analyses was conducted in the early visual areas (V1-V3) of the participant's non-lesioned hemisphere.

5.2.6 Statistical analysis

The aim of the analysis was to establish to what extent different aspects of the pRF estimates were affected by added thermal noise and head motion. To assess this, voxel wise permutation tests were used with paired t-test statistics to compare the original data with the modified data. An $\alpha = .05$ was used as a threshold to determine statistical significance. The maxT permutation adjustment (van der Laan et al., 2004; Westfall & Young, 1993) was used in order to control the family-wise error rate, with the reported p-values being the multiple comparisons corrected values. Statistical tests were multiple comparison corrected both within and between participants. The total number of voxels within each participant's early visual areas (V1-V3) as defined by the Wang Maximum Probability Atlas (Wang et al., 2015), were as follows: Participant 11773: 264 voxels; Participant 14196: 435 voxels; Participant 14326: 493 voxels.

For effect size, mean paired difference was reported as well as the proportion of voxels exhibiting greater values in each condition. This proportion was calculated using the expression as $pr_{m>o}$, where a value of 0.5 would represent 50% of the values for the modified data are above those of the original data, and a value of 1 would represent that all values for the modified data are

above those of the original data. Bootstrapping was conducted to calculate the 95% confidence intervals for the mean differences. A total of 10,000 samples were used for both bootstrapping and permutation tests.

The following results describe the effect of simulated head motion, simulated thermal motion and NORDIC PCA denoising on the pRF analysis. For brevity, some figures are only shown for a representative participant (Participant 14196). Data from the other participants are provided in Appendix 7.9.

5.3 Results

5.3.1 Analysis of ground truth head motion and tSNR levels

As shown in Table 5.1, translational movements were minimal and relatively stable across participants, however there was a large degree of variation for rotational movement. For example, Participant 11773 exhibited a large amount of rotational movement across all axes, whereas Participant 14326 exhibited a large degree of rotational movement only in the yaw axis. Participant 14196 demonstrated the least rotational movement overall. There was a large difference in tSNR levels in each participant's Occipital Pole (Table 5.2), with Participant 11773 demonstrating a much lower tSNR level than the other participants. The differences found in the "ground truth" head motion and thermal noise for each participant highlight the necessity for scaling the simulated thermal noise and head motion levels according to a participants original data. An example of how adding simulated thermal noise or head motion, or applying NORDIC PCA denoising, affects the fMRI time series is shown in Figure 5.3.

Table 5.1

Table of average rotational and translational head motion for each subject

	Rotation (rad)			Translation (mm)		
Subj.	Roll	Pitch	Yaw	x	y	z
11773	0.0038	0.0015	0.0022	0.11	0.098	0.091
14196	0.0011	0.00010	0.0026	0.083	0.026	0.042
14326	0.0028	0.0018	0.0022	0.047	0.070	0.10

Note. Stated rotation and translation parameters are the estimated transformation parameters as reported by FSL. Note that the translation values represent the movement of the center of mass of the imaged object. As a result, rotational movements can cause translational displacements much larger than reported here for voxels at the edge of the brain. To retain consistency, simulated motion is added into the data using FSL's "*applyxfm4D*" function.

Table 5.2

Descriptive statistics of the tSNR for each participant

Participant	**Mean** (*SD*)	**Maximum**
11773	25.83 *(25.85)*	117.34
14196	77.73 *(42.19)*	230.74
14326	59.31 *(33.17)*	188.11

Note. tSNR data shown is from the Occipital Pole. SD = Standard Deviation.

Table 5.3 illustrates the effect across the 8 modifications on tSNR levels. As expected, denoising using NORDIC PCA slightly increased the overall tSNR, with a substantial increase in the maximum voxelwise tSNR compared to the control data. Conversely, adding simulated thermal noise or head motion to the data decreased the tSNR levels. Notably, higher relative thermal noise levels resulted in a greater reduction in tSNR than higher relative head motion levels. Additionally, the standard deviation relative to the mean indicates that the variability of tSNR increased more when adding thermal noise than adding head motion. Overall, these summaries provide an important reality check for the manipulations evaluated in this chapter.

Figure 5.3

Example time series illustrating effects of adding head motion and thermal noise, and applying NORDIC PCA denoising

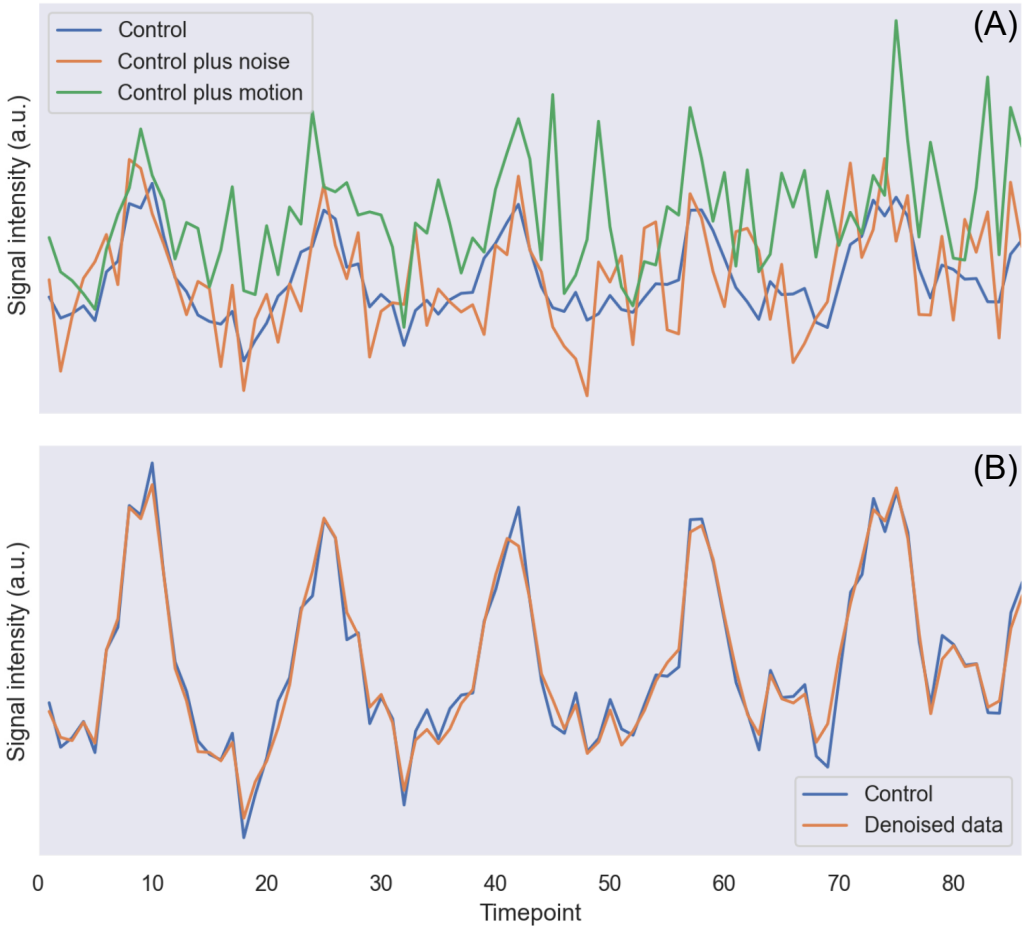

Note. The data presented here is from a single, highly stimulus-responsive voxel in Participant 11773 during a rotating wedge scan. (A) illustrates the effects of adding thermal noise and head motion to the data at 2x original data, (B) shows the effect of NORDIC PCA denoising. Notice that random fluctuations are visible in both the thermal noise and head motion added time series, but the thermal noise time series is centred about the original data whilst the motion data is not.

Table 5.3

Descriptive statistics of tSNR level for each data type

Data type	**Mean** (*SD*)	**Maximum**
Control	54.29 *(21.48)*	275.61
Denoised	59.95 *(25.96)*	507.40
Noise level		
1	29.48 *(14.82)*	126.63
2	17.50 *(9.06)*	65.98
5	7.59 *(3.93)*	26.76
Motion level		
1	32.60 *(13.25)*	190.36
2	21.83 *(7.88)*	157.85
5	12.65 *(2.66)*	112.19

Note. tSNR data shown is from the Occipital Pole. SD = Standard Deviation.

5.3.2 Effect of simulated thermal noise on the pRF analysis

Overall, the pRF estimates for original data consistently exhibited higher R^2 values than the noise-added data. This is not surprising as adding noise increases the amount of variance that is unexplained by the model. Permutation tests showed that this difference was statistically significant across all noise levels for all participants. For Participant 11773 (Noise level 1: $t = 18.22, pr_{m>o} = .011$; Noise level 2: $t = 17.85, pr_{m>o} = .038$; Noise level 5: $t = 17.72, pr_{m>o} = .023$), 14196 (Noise level 1: $t = 20.40, pr_{m>o} = .15$; Noise level 2: $t = 20.11, pr_{m>o} = .15$; Noise level 5: $t = 19.27, pr_{m>o} = .16$), and 14326 (Noise level 1: $t = 23.61, pr_{m>o} = .077$; Noise level 2: $t = 23.81, pr_{m>o} = .073$; Noise level 5: $t = 23.64, pr_{m>o} = .061$) the permutation tests all yielded p values of 0 after multiple comparison correction. This indicates that none of the permuted samples produced a t-statistic as extreme or more extreme than these t-statistics.

Table 5.4

R^2 values for various noise levels

Data type	Mean R^2	Mean paired R^2 difference
Participant 11773		
Control	.26	-
Noise level		
1	.03	-.22
2	.02	-.24
5	.01	-.25
Participant 14196		
Control	.21	-
Noise level		
1	.11	-.10
2	.05	-.15
5	.02	-.18
Participant 14326		
Control	.21	-
Noise level		
1	.09	-.12
2	.04	-.17
5	.02	-.19

As expected, it was found that the R^2 values were noticeably higher for the original data compared to the noise-added data for every participant (Table 5.4). As shown in Table 7.1 and 7.3, Participant 11773 experienced a substantial deterioration to R^2 values even at noise level 1. For the original data, the number of voxels exceeding an R^2 threshold of 0.1 decreased by 35% from 265 to 171 voxels, however for noise level 1 this instead reduced to 18, a decrease of 93%. At relative noise levels of 2x and 5x, this participant had no surviving pRF estimates at this threshold.

In contrast, the data for Participants 14196 and 14326 were much more resistant to the addition of thermal noise. For Participant 14196 (Table 5.7 and 5.8), at an R^2 threshold of 0.1, the number of voxels for the original and noise level 1 data that exceeded this threshold decreased from 436 to 232 (a 47% decrease) and 157 (a 64% decrease) respectively. At an R^2 threshold of 0.2, it decreased further to 179 (a 59% decrease) and 77 (a 82% decrease)

respectively. Similarly, for Participant 14326 (Table 7.2 and 7.4) the voxels that exceeded an R^2 threshold of 0.1 for the original data was 299, down from 494 (a 39% decrease), dropping further to 214 (a 57% decrease) at a threshold of 0.2. For the noise level 1 data the voxel count at thresholds of 0.1 and 0.2 was 167 (a 66% decrease) and 63 (a 87% decrease) respectively.

As seen in Table 5.5, Participants 14196 and 14326 have similar distributions of euclidean distances, pRF size differences and R^2 values with each level of thermal noise decreasing the maximum R^2 value and seeming to increase the euclidean distance. Participant 11773's R^2 values however are much closer to 0 for all noise levels. There also does not seem to be a bias towards larger or smaller receptive field sizes for any of the participants for the original data compared to the noise-added data. This was true for noise level 1 and 2 for which there was no significant differences found between the original data and these noise levels for any participants (noise level 1 maximum t statistic: $t = 2.24, p = .67$; noise level 2 maximum t statistic: $t = 2.93, p = .1$). However pRF sizes for noise level 5 were found to be significantly smaller than the original data in Participant 11773 ($t = 5.28, p < .001, pr_{m>o} = .2, \text{MD} = -5.45$), Participant 14196 ($t = 3.21, p = .037, pr_{m>o} = .35, \text{MD} = -0.50$), and Participant 14326 ($t = 7.0, p < .001, pr_{m>o} = .26, \text{MD} = -1.13$).

As shown in Table 5.6, as with euclidean distance polar angle difference systematically increases as thermal noise level increases, whereas this is not the case with eccentricity. This is reflected by there being inconsistent statistical significance for eccentricity, with no statistically significant differences between the original data and any level of noise-added data for eccentricity at noise level 1 (maximum t statistic: $t = 1.52$, $p = 1$, $pr_{m>o} = .48$) or noise level 2 (maximum t-statistic: $t = 1.76, p = .99$). However at a relative thermal noise level of 5x, the pRF estimates had significantly lower eccentricity than the original data for Participant 11773 ($t = 3.61$, $p = .009$, $pr_{m>o} = .54$, MD $= -32.65$) and Participant 14196 ($t = 3.15$, $p = .046$, $pr_{m>o} = .64$, MD $= 3.57$), but this was not the case for Participant 14326 ($t = 1.87$, $p = .96$, $pr_{m>o} = .61$, MD $= 1.93$).

Table 5.5

Population receptive field parameters for noise-added data

Participant	R^2 values	Euclidean distances	Receptive field size differences
11773	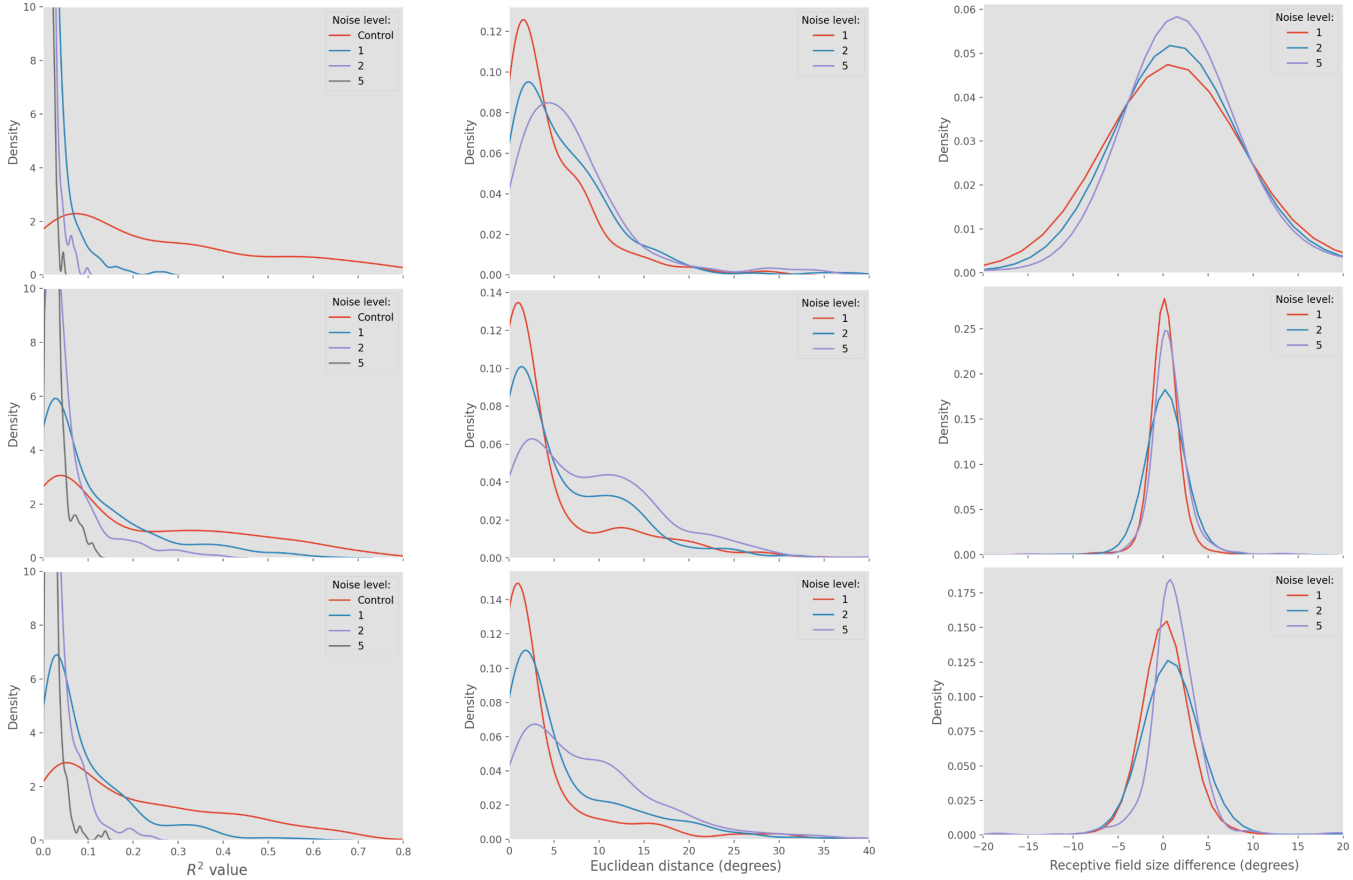		
14196			
14326			

Note. Euclidean distance and receptive field size difference is calculated as the pairwise difference. Receptive field size is calculated as the half width at half maximum. Participants 14196 and 14326 have similar distributions for all parameters, with R^2 values with each level of thermal noise decreasing the maximum R^2 value. Participant 11773's R2 values however are much closer to 0 for all noise levels.

Table 5.6

Polar angle and eccentricity differences for noise-added data

Participant	Polar angle differences	Eccentricity differences
11773	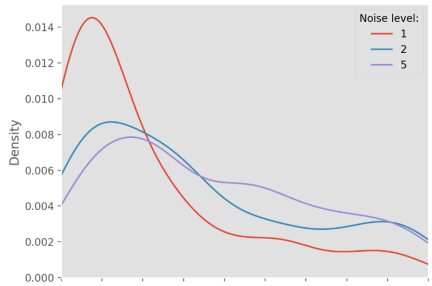	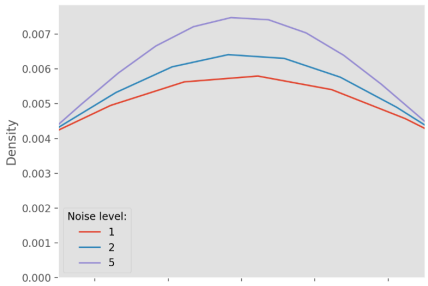
14196	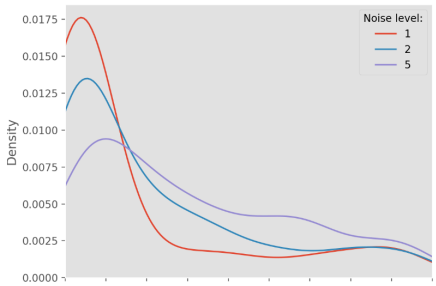	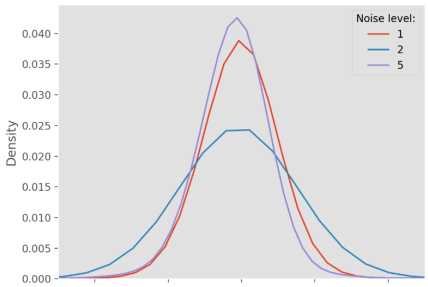
14326	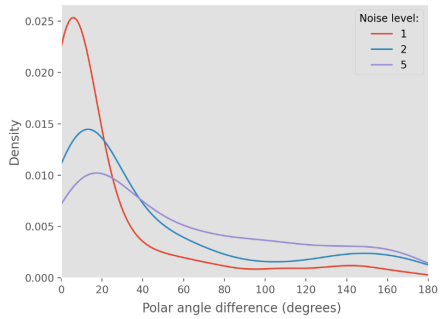	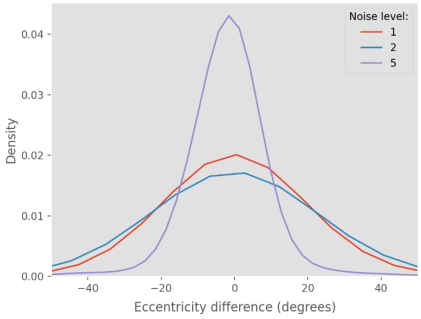

Note. Polar angle difference represents the minimum angular separation between the paired polar angles. Polar angle difference systematically increased as thermal noise level increases, whereas this is not the case for eccentricity. case with eccentricity

Table 5.7

Receptive field maps at various noise levels for Participant 14196

	Data type			
R^2 threshold	Original data	Noise level 1	Noise level 2	Noise level 5
0	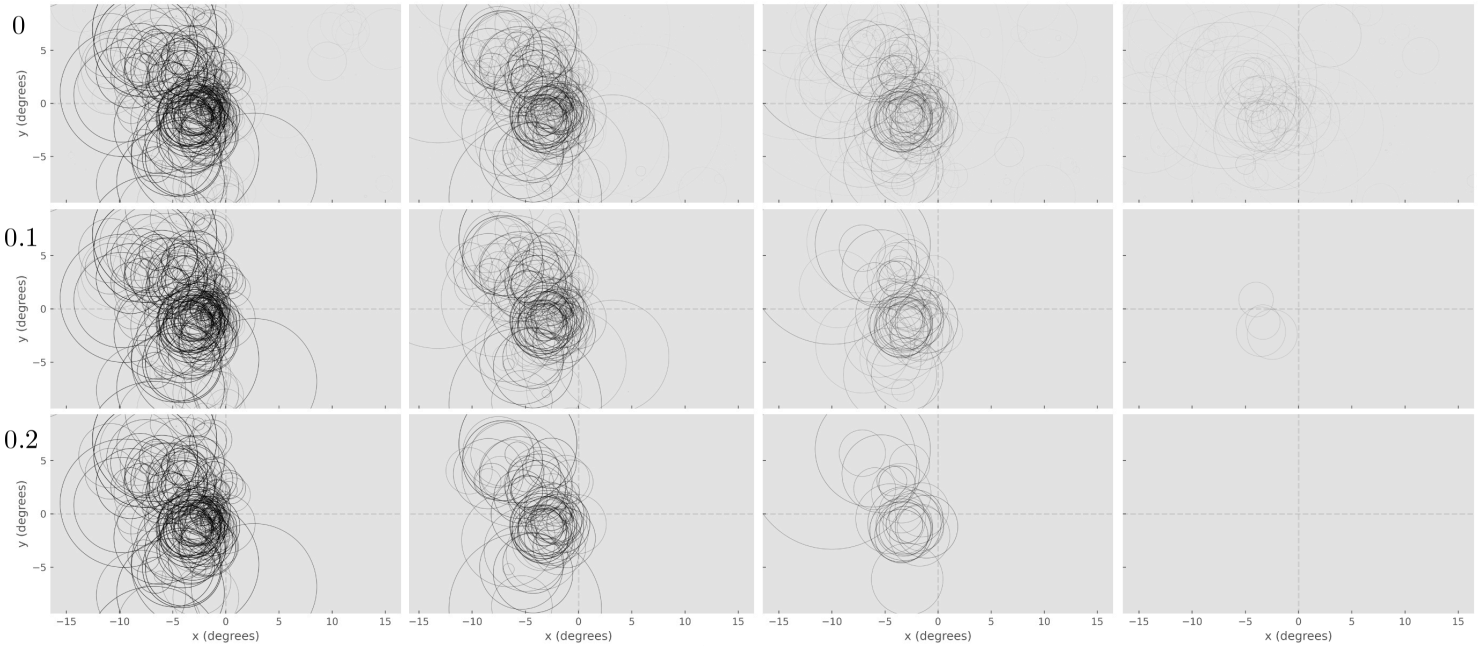			
0.1				
0.2				

Note. The transparency of the receptive fields represent their R^2. As shown by there being fewer plotted receptive fields at higher R^2 thresholds, there was a systematic decrease in overall R^2 values as noise level increased. This pattern was also observed in the other two participants.

Table 5.8

Receptive field centre differences at various noise levels for Participant 14196

R^2 threshold	Data type: Noise level 1	Noise level 2	Noise level 5
0	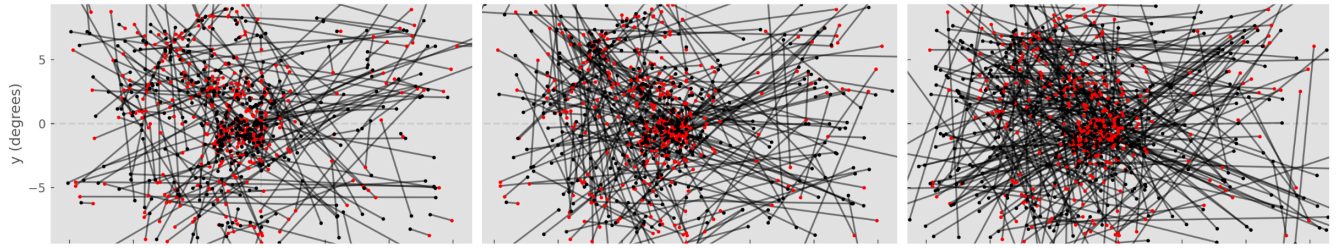		
0.1	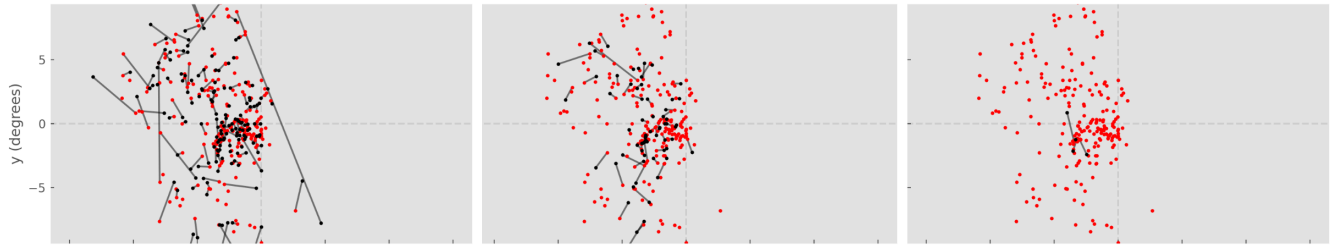		
0.2	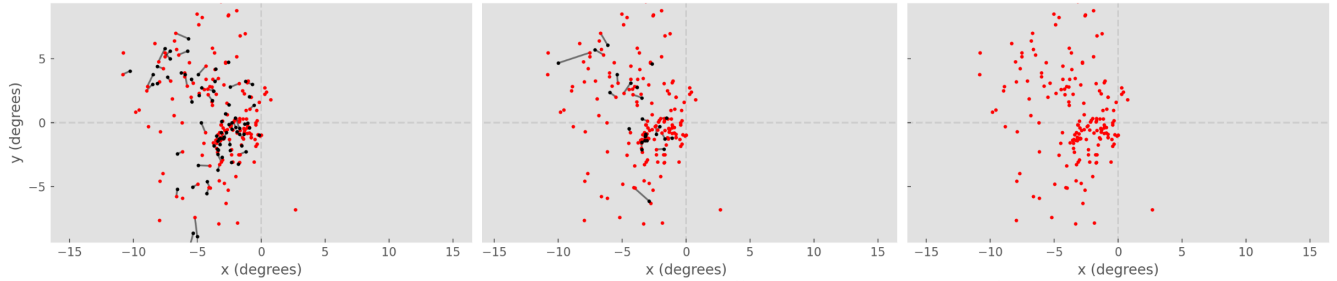		

Note. Red data points represent the original data. Lines illustrate the difference in receptive field centre estimations for each pair of data points. Data points that are unpaired due to one of the pair not exceeding the R^2 threshold are shown without a line. With high R^2 thresholds, the surviving noise-added receptive field centers show only small differences compared to the original data, representing the stability of pRF center estimation for high R^2 voxels. This was also observed in the other two participants.

5.3.3 Effect of simulated head motion on the pRF analysis

As with the noise-added data, the pRF estimates for the original data consistently yielded higher R^2 values than for the motion-added data. Permutation tests showed that this difference was also statistically significant across all motion levels for all participants, with the permutation tests yielding a p value of 0 for Participant 11773 (Motion level 1: $t = 5.59$, $pr_{m>o} = .36$; Motion level 2: $t = 12.82$, $pr_{m>o} = .068$; Motion level 5: $t = 12.56$, $pr_{m>o} = .084$), Participant 14196 (Motion level 1: $t = 14.61$, $pr_{m>o} = .22$; Motion level 2: $t = 16.96$, $pr_{m>o} = .20$; Motion level 5: $t = 18.16$, $pr_{m>o} = .22$) and Participant 14326 (Motion level 1: $t = 16.23$, $pr_{m>o} = .15$; Motion level 2: $t = 19.91$, $pr_{m>o} = .0.087$; Motion level 5: $t = 23.23$, $pr_{m>o} = .061$).

Table 5.9

R^2 values for various motion levels

Data type	Mean R^2	Mean paired R^2 difference
Participant 11773		
Control	.26	-
Motion level		
1	.22	-.01
2	.18	-.07
5	.09	-.15
Participant 14196		
Control	.21	-
Motion level		
1	.13	-.07
2	.09	-.12
5	.04	-.17
Participant 14326		
Control	.21	-
Motion level		
1	.13	-.08
2	.08	-.13
5	.04	-.18

While the impact of adding head motion to the data varies among participants, the degree of difference compared to adding thermal noise is consider-

ably smaller. As shown in Table 5.9 and Table 5.10, as with the noise-added data, the impact of head motion on the data for Participants 14196 and 14326 is notably similar, with comparable effects on both R^2 values and pRF parameters. In contrast, data from Participant 11773 was more resilient to the addition of simulated head motion than the two other participants. This is despite their dataset having a higher relative amount of simulated rotational head motion added to their data as they exhibited more rotational head movement in the "ground truth" data across all axes (Table 5.1).

In regards to pRF parameters, no significant difference was found for pRF size between the original data and the motion level 1 data (maximum t-statistic: $t = 2.38$, $p = .5$), however a significantly lower pRF size was found for Participant 14326 for motion level 2 ($t = 7.88$, $p < .001$, $pr_{m>o} = .36$, MD $= -0.85$) and motion level 5 data ($t = 9.61$, $p < .001$, $pr_{m>o} = .32$, MD $= -1.13$). This was not the case for Participant 11773 (Motion level 2: $t = 0.63$, $p = 1$, $pr_{m>o} = .56$, MD $= 0.77$; Motion level 5: $t = 0.64$, $p = 1$, $pr_{m>o} = .38$, MD $= -1.14$) or Participant 14196 (Motion level 2: $t = 1.14$, $p = 1$, $pr_{m>o} = .46$, MD $= 0.25$; Motion level 5: $t = 1.92$, $p = .94$, $pr_{m>o} = .44$, MD $= 0.61$).

Similar to the thermal noise-added data, polar angle difference systematically increased as head motion level increased (Table 5.11), whereas this was not seen with eccentricity. As with the noise-added data this is also reflected in statistical tests, with no significant differences being found between eccentricity parameters for the original and the motion-added data for either Participant 11773 (maximum t-statistic: $t = 0.70$, $p = 1$) or Participant 14326 (maximum t-statistic: $t = 1.86$, $p = .96$). However, for Participant 14196 while no significant difference was found for motion level 2 ($t = 2.47$, $p = .41$), a significant increase in eccentricity was found for motion level 1 ($t = 3.36$, $p = .02$, $pr_{m>o} = .55$, MD $= 3.65$) and level 5 ($t = 3.87$, $p = .004$, $pr_{m>o} = 0.003$, MD $= 10.67$).

Overall, while there were significant decreases between the R^2 for the pRF estimates from the original data compared to the motion-added data, the pRF analysis seemed to be much more resilient to adding head motion to the data (Table 7.5 - 7.8). For Participant 11773 there was a reduction of

93% in the number of voxels that exceeded an R^2 threshold of 0.1 with noise level 1, whilst there was only a 46% decrease for motion level 1 (from 164 to 89 voxels). At motion level 1, there was a larger drop of 60% (from 436 to 175 voxels) and 59% (from 494 to 204 voxels) for Participants 14196 and 14326 respectively.

5.3.4 Effect of NORDIC PCA denoising data on the pRF analysis

R^2 values for the denoised data were consistently higher than those for the original data, with 89%, 93% and 98% of the R^2 values for the denoised data being higher than their paired voxel equivalent from the original data set (for Participant 11773, 14196 and 14326 respectively). This effect was also significant for all 3 participants (11773: $t = 18.12$, $p < .001$; 14196: $t = 21.64$, $p < .001$; 14326: $t = 15.91$, $p < .001$). However this effect, while consistent, was also relatively small (Table 5.14), as can be seen when examining the number of voxels that exceed the R^2 thresholds of 0.1 and 0.2.

Table 5.14

R^2 values for denoised data

Data type	Mean R^2	Mean paired R^2 difference
Participant 11773		
Control	.26	-
Denoised	.28	.02
Participant 14196		
Control	.21	-
Denoised	.27	.06
Participant 14326		
Control	.21	-
Denoised	.23	.02

For Participant 11773, at an R^2 threshold of 0.1, the number of surviving voxels decreased by 35% in the original dataset and 32% in the denoised

Table 5.10

Population receptive field parameters for motion-added data

Participant	R^2 values	Euclidean distances	Receptive field size differences
11773	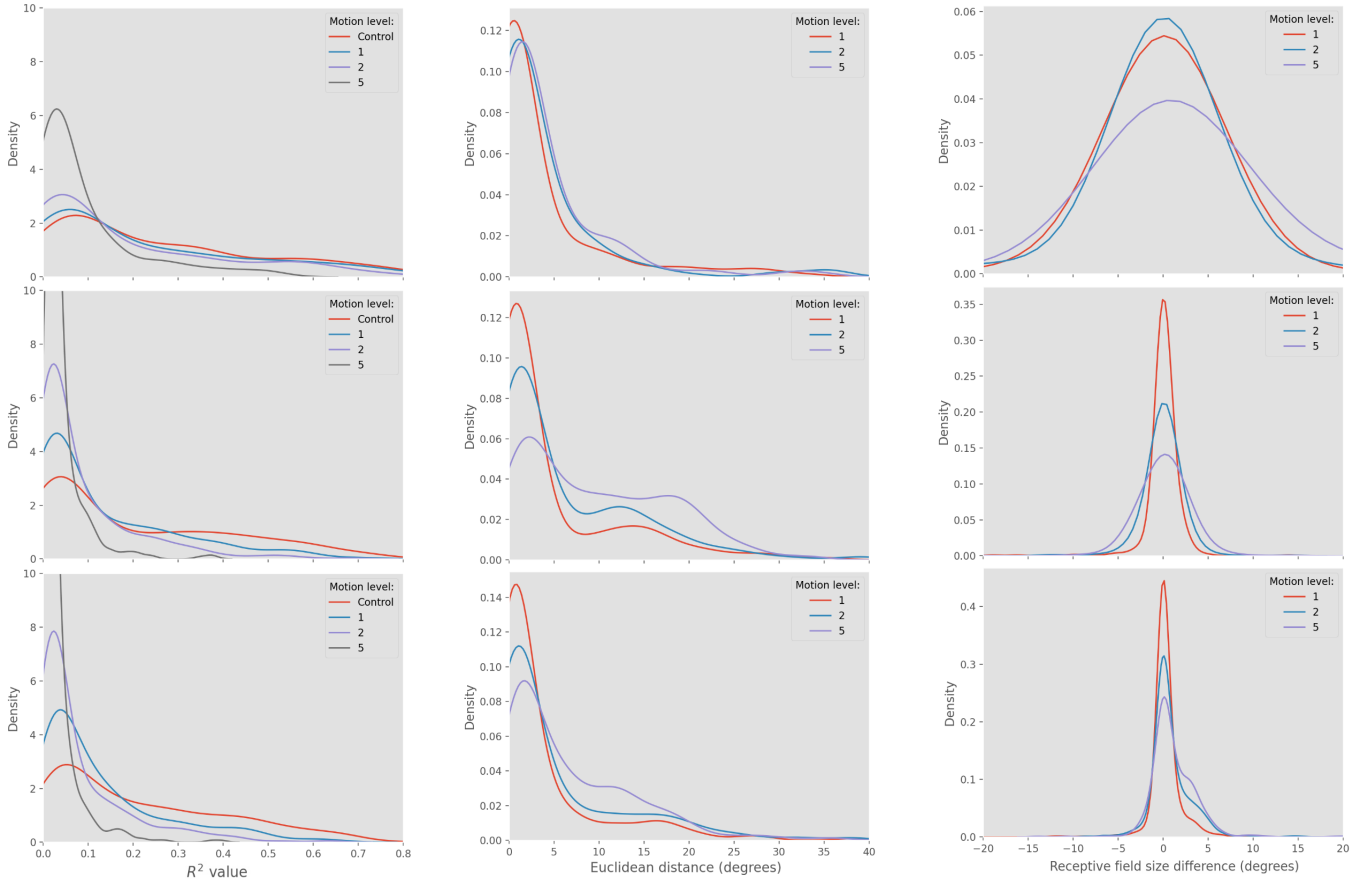		
14196			
14326			

Note. Euclidean distance and receptive field size difference is calculated as the pairwise difference. Receptive field size is calculated as the half width at half maximum. The impact of head motion on the data for Participants 14196 and 14326 is notably similar, with comparable effects on both R^2 values and pRF parameters. In contrast, data from Participant 11773 was more resilient to the addition of simulated head motion than the two other participants.

Table 5.11

Polar angle and eccentricity differences for motion-added data

Participant	Polar angle differences	Eccentricity differences
11773	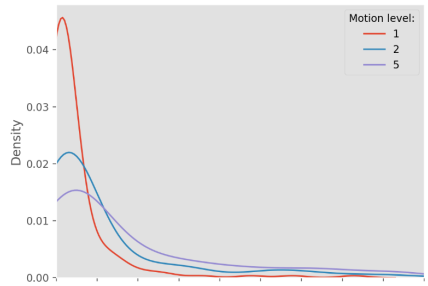	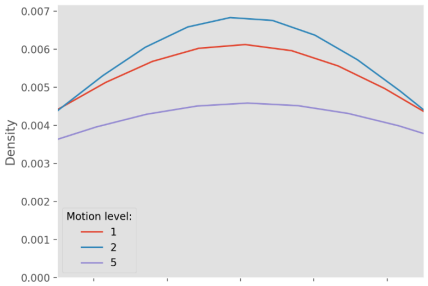
14196	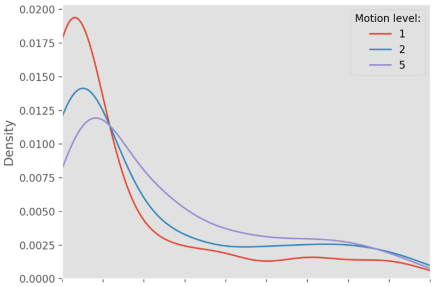	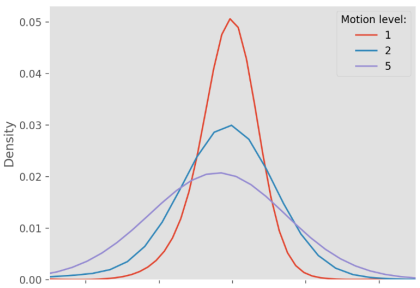
14326	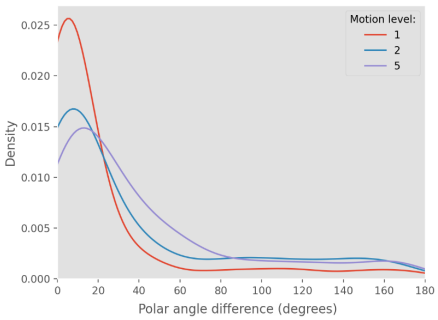	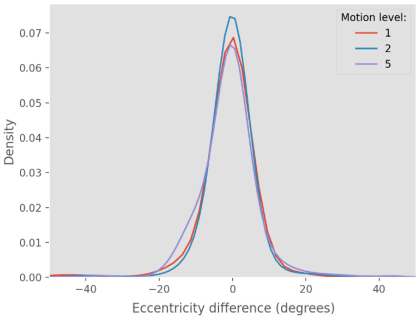

Note. Polar angle difference represents the minimum angular separation between the paired polar angles. Similar to the thermal noise-added data, polar angle difference systematically increased as head motion level increased, whereas this was not the case for eccentricity.

Table 5.12

Receptive field maps at various motion levels for Participant 14196

	Data type			
R^2 threshold	Original data	Motion level 1	Motion level 2	Motion level 5
0	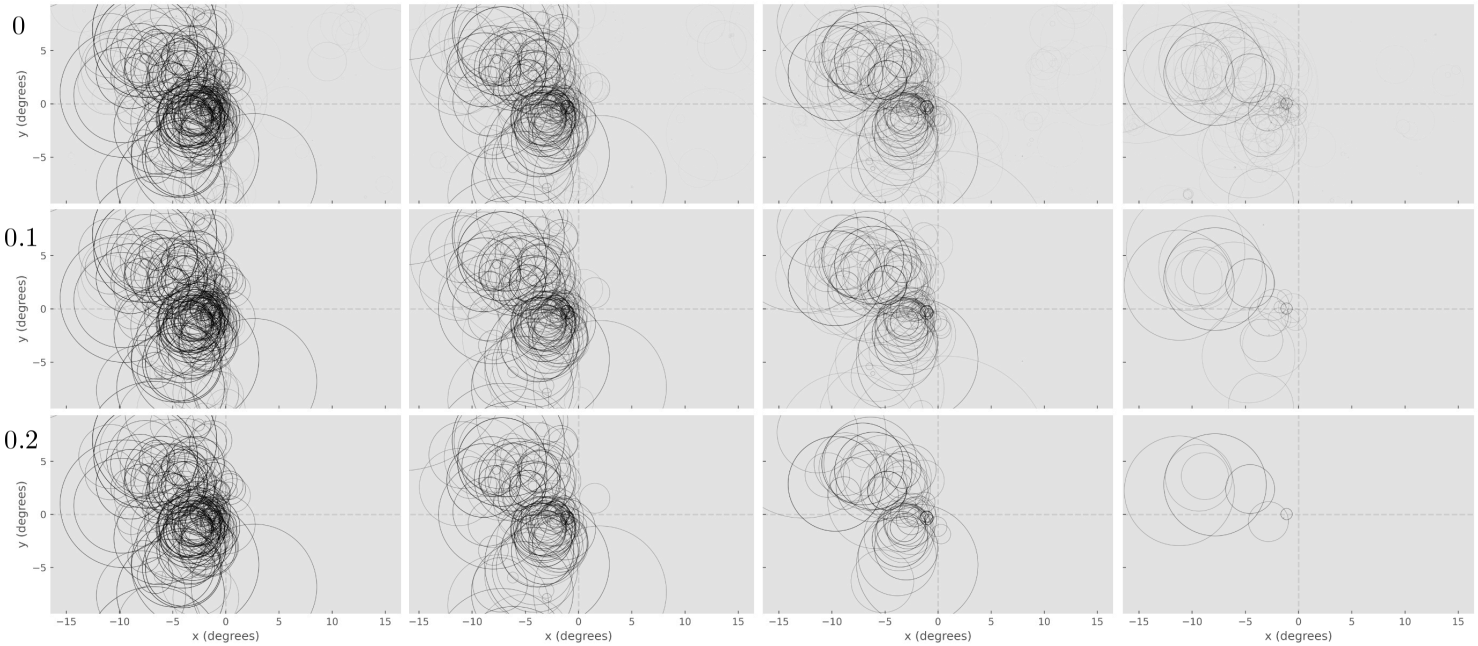			
0.1				
0.2				

Note. The transparency of the receptive fields represent the R^2 value. As with noise-added data, R^2 values systematically decreased as motion level increased. A similar pattern was observed for all 3 participants, with Participant 11773 being slightly more resilient to added motion than other participants.

Table 5.13

Receptive field centre differences at various motion levels for Participant 14196

R^2 threshold	Data type: Motion level 1	Motion level 2	Motion level 5
0	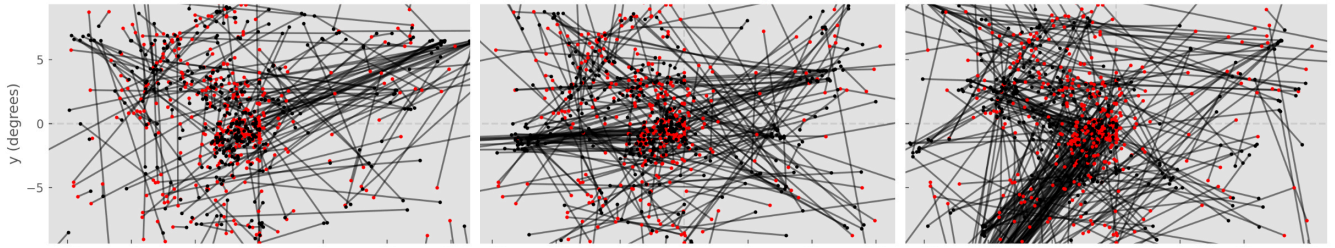		
0.1	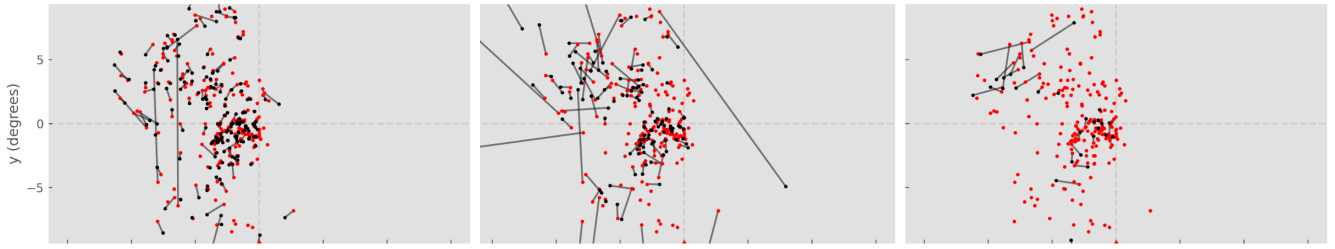		
0.2	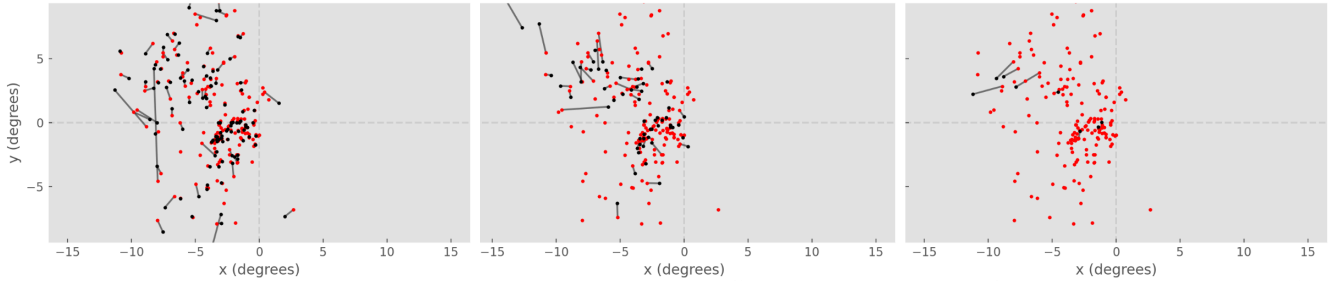		

Note. Red data points represent the original data. Lines illustrate the difference in receptive field centre estimations for each pair of data points. Data points that are unpaired due to one of the pair not exceeding the R^2 threshold are shown without a line. With high R^2 thresholds, the surviving noise-added receptive field centers show only small differences compared to the original data, representing the stability of pRF center estimation for high R^2 voxels. This was also observed in the other two participants.

dataset; at an R^2 threshold of 0.2, the decreases were 51% and 48%, respectively. Similarly, for Participant 14326 the decrease in the number of surviving voxels at an R^2 threshold of 0.1 was 39% for the original dataset and 37% for the denoised dataset, and at an R^2 threshold of 0.2, the decreases were 57% and 54%, respectively. The benefits to R^2 were slightly more pronounced for Participant 14196 though, with the original dataset showing a decrease of 47% at the 0.1 threshold and 59% at the 0.2 threshold, while the denoised dataset exhibited decreases of 40% and 50% respectively.

Compared to the thermal noise-added and head motion-added scans, paired euclidean distance between the denoised and the original data was also much smaller (Table 5.15). This can also be seen in the pRF size differences for the denoised data (Table 7.9 - 7.10) compared to those in previous sections. On the other hand, the pRF size differences were similar to noise and motion-added data, with the RFs for Participant 11773 having larger size differences than the other two participants. Additionally as shown in Table 5.16, eccentricity differences for Participant 11773 were also much higher than for the other participants. However, there was no significant difference between the original data and the denoised data for any of the participants for either pRF eccentricity (maximum t-statistic: $t = 1.83$, $p = .97$) or pRF size (maximum t-statistic: $t = 1.65$, $p = 1$). Additionally polar angle differences closely mirror euclidean distance (Table 5.16).

5.4 Discussion

The results here show pRF estimates are more resistant to the addition of relative head motion than to the addition of relative thermal noise. Furthermore, while higher levels of head motion and thermal noise resulted in both lower R^2 levels and greater differences in pRF centre locations, the differences in pRF size and eccentricity were inconsistent. On the other hand, polar angle differences systematically increased as thermal noise and head motion values increased. Therefore, polar angle differences are likely to be the main driving force behind both the pRF centre and R^2 differences seen here. NORDIC PCA denoising (Moeller et al., 2021) was also shown to pro-

Table 5.15

Population receptive field parameters for denoised data

Participant	R² values	Euclidean distances	Receptive field size differences
11773	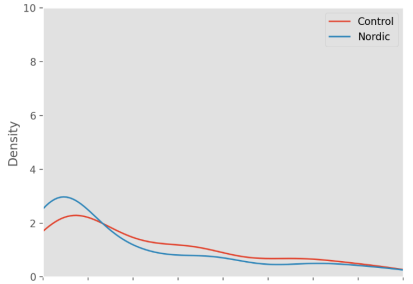	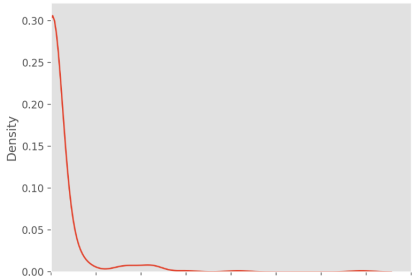	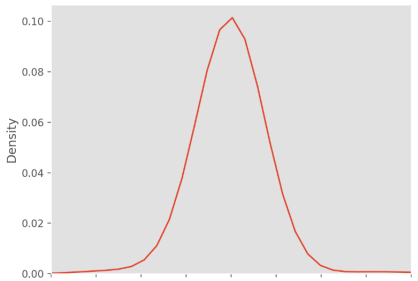
14196	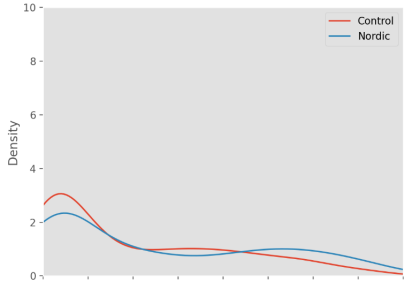	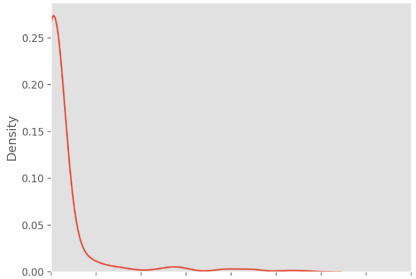	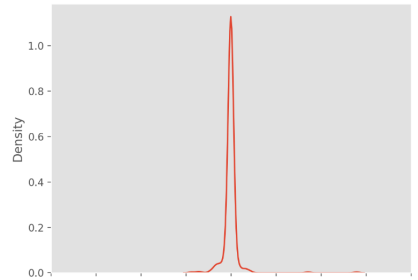
14326	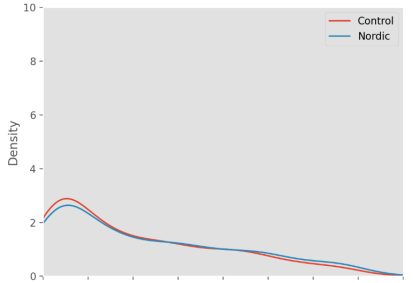	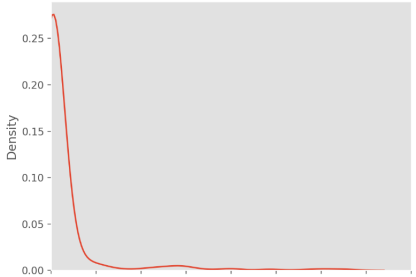	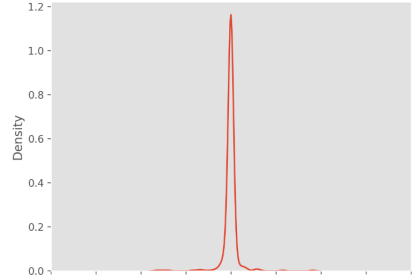

Note. Euclidean distance and receptive field size difference is calculated as the pairwise difference. Receptive field size is calculated as the half width at half maximum. Participants 14196 and 14326 showed similar increases to R^2 values after NORDIC denoising, with minimal receptive field size differences. In contrast, Participant 11773 showed much higher receptive field size differences after NORDIC denoising.

Table 5.16

Polar angle and eccentricity differences for denoised data

Participant	Polar angle differences	Eccentricity differences
11773	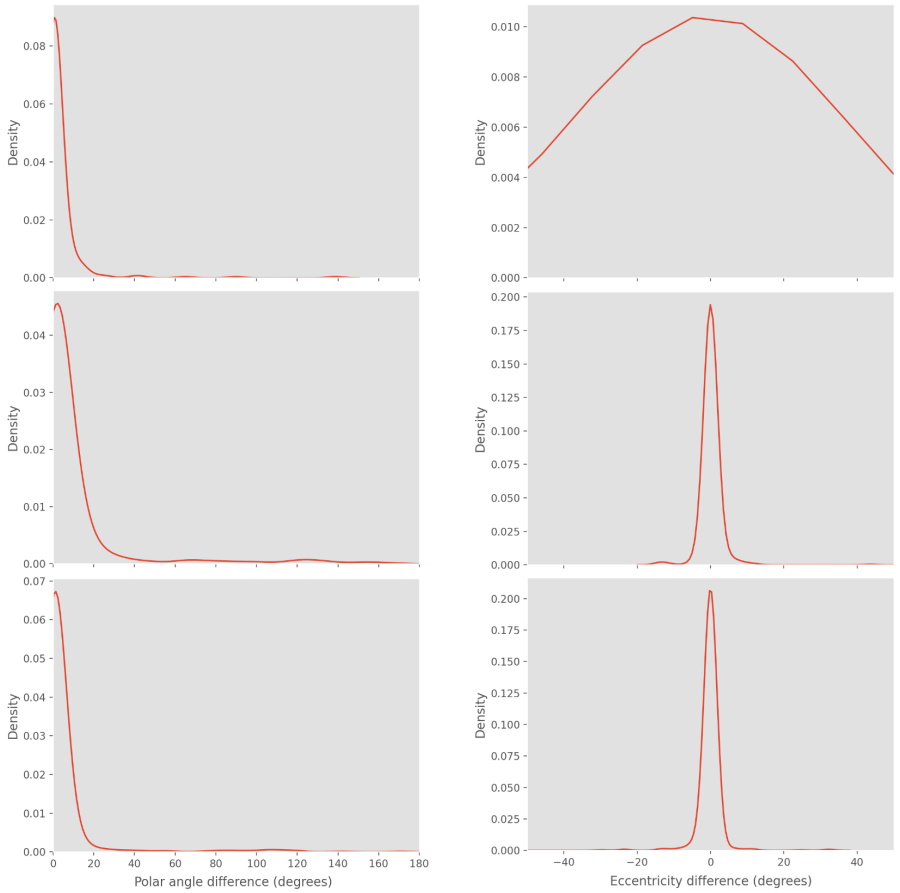	
14196		
14326		

Note. Polar angle difference represents the minimum angular separation between the paired polar angles. As with receptive field size, Participants 14196 and 14326 showed only small eccentricity differences between the original and NORDIC denoised data, whereas for Participant 11773 this difference was much higher.

Table 5.17

Table showing receptive field maps and differences for denoised data for Participant 14196

R^2 threshold	Receptive field maps: Original data	Receptive field maps: Denoised data	Receptive field centre differences
0	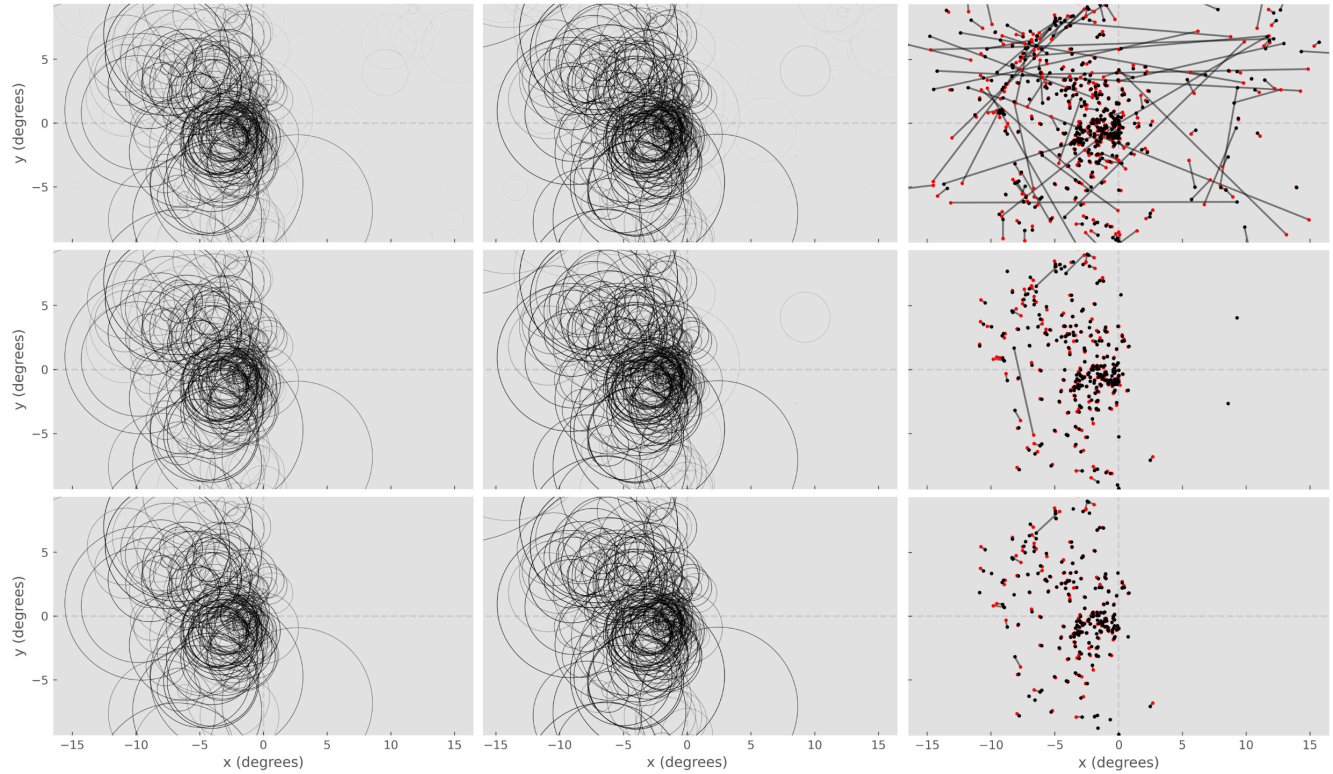		
0.1			
0.2			

Note. For the receptive field map images, the transparency of the receptive fields represent the R^2 value. For the receptive field centre difference images, red data points represent the original data. Lines illustrate the difference in receptive field centre estimations for each pair of data points. Data points that are unpaired due to one of the pair not exceeding the R^2 threshold are shown without a line. NORDIC denoising produced a small increase to the number of voxels above R^2 thresholds of 0.1 and 0.2, indicating a small (but beneficial) effect of this denoising process.

vided a small but consistent benefit to the pRF analysis, with between 89 and 98% of the voxels shown to have a higher R^2 value after denoising.

When comparing the "ground truth" data to the simulated thermal noise data, the R^2 of the pRF estimates for Participant 11773 declined much faster than for Participant 14196 and 14326 at higher noise levels. In contrast, the pRF estimates for Participant 11773 were more resistant to higher simulated motion levels than for Participant 14196 and 14326. The decline in R^2 values for Participant 11773 may be due to the higher noise level for this participant relative to the other participants (which is reflected in this participant having the lowest tSNR Table 5.2). However while all participants had similar levels of translational motion, Participant 11773 had higher overall rotational motion than the other participants. It would thus be expected that the higher resulting relative simulated motion levels for this participant would cause faster degradation of the pRF estimate's R^2 values which was not the case here.

It should be noted that while Participant 14196 and 14326 had similar results throughout, Participant 11773 typically exhibited higher eccentricity and pRF size differences, as well as a smaller distinction between head motion and thermal noise levels for Euclidean distance. All participants showed a similar distribution of R^2 values for the original data and similar movement values (Table 5.1), however Participant 11773 had fewer defined voxels (256 voxels compared to 436 and 496 voxels) and larger pRF sizes (6.26 degrees compared to 1.54 and 2.30 degrees) with significantly higher mean eccentricity values (39.084 degrees compared to 6.86 and 8.03 degrees). Further, mean pRF size and eccentricity for voxels exceeding an R^2 threshold of 0.1 were still higher than those of the other participants (5.93 degrees and 32.54 degrees, respectively).

It may be the case that voxels from higher order regions, such as the lateral occipital area and V4 may have been included in this participant's data, as these regions are known for larger pRF sizes compared to early visual areas (Dumoulin & Wandell, 2008; Gattass et al., 1988). On the other hand, as early visual area locations are very consistent between participants (Benson et al., 2012; Himmelberg et al., 2021; Wang et al., 2015), it is unlikely that a

significant proportion of higher visual order areas has been included in this participant's data. Moreover, this does not account for why the mean pRF eccentricity is significantly beyond the stimulus space, with the maximum eccentricity of the stimuli being 9.39 degrees.

The most likely explanation for Participant 11773's inconsistent results is the minimization algorithm used here fitting pRFs models, the Nelder-Mead Simplex algorithm (Nelder & Mead, 1965). This algorithm is used as the default in mrTools, however an alternative, the Levenberg-Marquardt algorithm (Levenberg, 1944; Marquardt, 1963), is also available. Because the Nelder-Mead Simplex algorithm is an unconstrained algorithm, it is possible for pRF models with biologically implausible parameters to be fit. In contrast, the implementation of the Levenberg-Marquardt algorithm in mrTools allows for the use of constraints to ensure that the fitted parameters remain biologically plausible. However as noted in the mrTools documentation, the Nelder-Mead algorithm is less likely to get stuck in a local minimum compared to the Levenberg-Marquardt algorithm.

A potential explanation for why this limitation of the Nelder-Mead algorithm has affected this participant's data and not the others is the stimuli presented to this participant. During data acquisition, Participant 11773 was only presented expanding/contracting ring and rotating wedges, whereas the other two participants were presented these stimuli as well as moving bar stimuli. These ring and wedge stimuli are "phase-encoded" stimuli as their movement during a scan is repeated and predictable over time. In contrast the moving bar stimuli are not "phase-encoded" as the bars change direction and orientation within a scan (Dumoulin & Wandell, 2008). As wedge and ring stimuli tend to bias towards lower pRF eccentricity and size than bar stimuli (Linhardt et al., 2021), this discrepancy might result from a combination of the Nelder-Mead algorithm and phase-encoded stimuli. The algorithm might have found it easier to fit large pRF estimates far outside the stimulus space to the predictable "phase-encoded" stimuli compared to the moving bar stimuli, explaining why Participant 11773 was uniquely affected. This highlights the importance of considering the impact algorithm choice may have on pRF models and how this may interact with the stimuli used. Furthermore, due to the significant influence the pRF fitting algorithm can

have, it is essential that research clearly states the algorithm used to ensure transparency and reproducibility.

Comparing the effects of thermal noise and head motion in Participant 14196 and 14326, to the levels used in this study, pRF analysis was more sensitive to the addition of thermal noise than head motion, with many more pRF models exceeding an R^2 threshold of 0.2 in the motion level 5 condition than the noise level 5 condition. However, head motion levels were relatively low across participants (Table 5.1). While this was the case, simulated head motion did produce a similar effect on tSNR to simulated thermal noise (Table 5.3). Therefore, the levels of simulated head motion and thermal noise here can be seen as roughly comparable. It should be noted that the effect of motion on pRF estimates is normally actively reduced by using motion correction as a standard pre-processing step, whereas here motion correction was only applied prior to the creation of the modified data. However, gross motion artifacts are often hard to remove and may lead to situations where data cannot be included in an analysis, even after motion correction.

One potential method for decreasing noise, is spatially smoothing the data (Dumoulin & Wandell, 2008), a common technique in experimental fMRI designs. While this produces a reliable increase in tSNR by removing high frequency spatial noise, this comes with the drawback of lowering the spatial resolution. This can make visual area delineation using retinotopic maps less accurate, although this can be somewhat mitigated using spatial interpolation (Dumoulin & Wandell, 2008). On the other hand, NORDIC PCA denoising produces similar levels of BOLD sensitivity to spatial smoothing, while producing minimal increases in overall smoothness of the image (Dowdle et al., 2023). Thus, NORDIC PCA denoising can be used as an alternative to conventional spatial smoothing, offering an approach to enhance tSNR without significantly compromising spatial resolution, ensuring robust and accurate visual area delineation. Here, NORDIC PCA denoising only provided a small, but consistent, benefit to pRF modelling, potentially reflecting the fact that the scanning parameters used here were such that thermal noise was not an issue. For measurements with much smaller voxels and higher levels of thermal noise, NORDIC would be expected to provide a clear benefit. However it should also be noted that NORDIC PCA denoising

was used here with magnitude data, without the use of the phase component of the functional data or a noise scan (for image SNR estimation), which can enhance the denoising results (Moeller et al., 2021).

Due to the retinotopic organisation of many visual areas, the pRF properties can be used to identify delineate these visual areas. Visual area delineation is commonly performed using the polar angle properties of pRFs, as the boundaries of these areas are defined by a reversal in the polar angle property of the RFs (Engel et al., 1997). Here, polar angle differences consistently increased as head motion and thermal noise level increased; on the other hand, eccentricity and pRF size differences were inconsistent as thermal noise and head motion level increased. This indicates that it will be increasingly difficult to delimit visual areas as thermal noise or head motion level increases due to increased polar angle pRF estimation error using this method of visual area identification. On the other hand, anatomical atlases can reliably identify visual areas without relying on pRF properties for visual area delineation (Wang et al., 2015). Thus, these results imply that in cases of high thermal noise or head motion, anatomical atlases may provide more accurate visual area identification than methods than rely on pRF parameters; particularly in lower visual areas which have lower anatomical variability between subjects than higher order areas (Himmelberg et al., 2021).

In conclusion, this chapter demonstrates the deleterious effect of both head motion and thermal noise on pRF analyses, while also showing that the pRF analysis was more resilient to the addition of simulated head motion than thermal noise. While the effect of retrospective motion correction software tools are broadly similar (Oakes et al., 2005), prospective motion correction can provide a significant benefit to image quality over retrospective motion correction (Slipsager et al., 2022), therefore further research can investigate the benefits provided by using one motion correction technique over the other in the presence of heavily motion corrupted data for pRF analyses.

Additionally, mitigation strategies for thermal noise, such as NORDIC PCA denoising and spatial smoothing can also be compared at 3T (Dowdle et al., 2023). As this dataset did not contain the phase and noise scan information that NORDIC PCA denoising can use to provide more accurate denoising,

it is also worth future research investigating the additional benefit of this to pRF analysis. The difference between results for Participant 11773 compared to Participants 14196 and 14326 may potentially be the result of an interaction between the unconstrained minimization algorithm used here and the "travelling wave" stimuli used for Participant 11773. Further research is necessary to determine whether unconstrained algorithms may be more suitable for certain stimuli choices. Despite this, the results for Participant 14196 and 14326 contribute valuable insights into the resiliency of pRF parameters to head motion and thermal noise.

Chapter 6

General discussion

This thesis explores the effects of different MRI image acquisition parameters (IAPs) on the key data quality metric of temporal signal-to-noise ratio (tSNR), which is a major determinant for how well given MRI parameters optimally detect functional MRI (fMRI) signals. The subsequent impact of varying tSNR levels on the population Receptive Field (pRF) analysis method, widely used in sensory neuroscience, is then examined. This chapter summarises the main findings and implications of the work outlined in this thesis.

The first aim of this thesis was to develop a tool to determine how different MRI acquisition parameters systematically influence tSNR across different brain regions. Because currently available software for fMRI data lacked easy-to-use support for region-wise analysis of data quality metrics, I developed software to facilitate such region-wise summaries of data quality maps (Chapter 3). Rather than developing a one-off solution for use solely in my work, I developed and published an open-source software solution that provides a comprehensive region-of-interest (ROI) analysis toolset allowing assessment of data quality metrics in standard template space, this is termed the fMRI ROI Analysis Tool (fRAT).

As tSNR plays an important role in modulating BOLD sensitivity (subsection 2.3.2), measuring tSNR is beneficial as it allows the determination of whether non-significant results may be the result of poor BOLD sensitivity caused by low tSNR, or whether other factors, such as differences in study populations or other confounders may be the cause. However, tSNR is not standardly reported (Welvaert & Rosseel, 2013), and where tSNR has been reported, it is usually reported as a single figure representing the mean value over the whole brain, thus obscuring inter-regional differences which are important when planning fMRI studies. One likely reason for this lack of methods to assess fMRI data quality metrics is that tSNR in fMRI is only an informative measure for grey matter, so an accurate brain segmentation first needs to be performed to separate tissue types. Additionally, to produce an ROI wise measure of tSNR, matrix transformations between functional and standard template space must be performed, adding to the complexity of the analysis. Using the analysis tools of fRAT, region-wise summaries of data quality metrics (such as tSNR) over a single or multi-user dataset can

be easily produced in a given template space. It is hoped that fRAT can be used by other researchers in the future to increase the reporting of important metrics such as tSNR in research, as this would allow other researchers to assess the results in the context of the data quality.

To increase the general applicability of fRAT, while it was designed with data quality statistics (such as tSNR and image SNR [iSNR]) in mind, it can be used to convert any voxelwise statistical map into region-wise summaries. In addition, a number of analysis options were later added to fRAT to tailor its use to the needs of different researchers and projects. The flexibility of fRAT allows for a number of use-cases, some of which are discussed in this thesis. The statistics and figure creation options available within fRAT also allow multivariate ROI analyses. One example of this may be seen in the examination of the effect of multiple MR image acquisition parameters on a statistic of interest as seen in Chapter 4. Thus fRAT facilitates research into the optimisation of MRI parameters (or other variables) based on a chosen ROI. fRAT can also be used when planning studies to determine the influence image acquisition parameters such as acceleration factor have on data, to ensure suitable factors are used for the areas of interest in a study.

Given the numerous fMRI research applications that benefit from regional aggregation, fRAT was designed to be compatible with other voxel wise statistical maps. Specifically, in some research applications, atlas-derived ROIs provide advantages over functionally derived ROIs. For instance, for power analyses, aggregating statistical maps using atlas-defined ROIs can prevent inflated statistical power estimates. Such inflation can occur particularly if functionally derived ROIs which are not independent of the effect statistic are used, leading to biased results (Kriegeskorte et al., 2010). Atlas-defined ROIs, on the other hand, resolve this issue by maintaining independence between the ROI definition and the effect statistic. This flexibility of fRAT allows it to be used in a wide range of research applications beyond those presented in this thesis.

Chapter 4 then utilised fRAT to investigate a specific question about the relationship between image acquisition parameters and tSNR and how it varies across different regions of the brain. The common method of reporting a sin-

gle tSNR value across the whole brain, by necessity, obscures inter-regional differences, providing an average value that will not correctly represent many of the brain regions. Consequently, it is useful if researchers provide more specific tSNR measurements, such as is possible with the fRAT software. Furthermore, the results of Chapter 4 demonstrate that the regional effect of MRI parameters on tSNR is heavily dependent on the hardware used (here a Philips 3T Achieva or Ingenia MR scanner). Therefore, researchers may benefit from using fRAT to conduct pilot studies to optimize MRI parameter settings according to their chosen ROI and available MR scanner hardware, aiming for a specific tSNR level.

The importance of tSNR level was then explored in Chapter 5, which examined the effect of artificially inflated thermal noise and head motion on pRF analysis. It was found that additional relative thermal noise had a much larger effect on pRF estimates than additional relative head motion. This chapter also showed the potential interaction between pRF fitting algorithms and stimuli, showing that unconstrained fitting algorithms might be better suited to the use of moving bar stimuli (Dumoulin & Wandell, 2008). Finally, it was found that the addition of noise and motion had a more consistent effect on the polar angle of the pRF estimates, rather than the eccentricity or receptive field size. The results of Chapter 4 showed that the Occipital Pole had a significantly lower baseline tSNR level than the tSNR over all cortical regions (a tSNR level of ~90 versus ~130 on the Ingenia). In contrast, Multiband (MB) acceleration was found to have a much smaller effect in the Occipital Pole than for other regions, and SENSE was not found to significantly influence tSNR level in our measurements. Therefore, while Chapter 5 indicates that pRF estimates are sensitive to high noise levels, Chapter 4 shows that researchers may be able to use moderate levels of both MB and SENSE image acceleration without a large effect on pRF analysis.

6.1 Limitations and future directions

As the aim of Chapter 4 was to characterise the effect of image acceleration methods on tSNR, with a particular emphasis on their potential to reduce

acoustic noise. To match conditions closely across repeated scans, only the number of slices collected was varied between scans, although there is of course a much larger space of image acquisition parameters.

The data quality of the fMRI time series' in Chapter 4 was quantified using tSNR. However additional considerations beyond tSNR should be made when evaluating the impact of image acceleration methods on data. For instance, the undersampling of k-space with SENSE also produces a directly proportional decrease in the time required to obtain each image, which can provide a number of benefits. One benefit is this reduction in image acquisition time also lowers sensitivity to susceptibility related signal dephasing, with SENSE factor 2 producing a reduction in susceptibility related distortions by a factor of two (Schmidt et al., 2005). This results in higher quality images more closely matching the actual anatomy. Assessing the implications of these effects was however beyond the scope of this thesis.

Furthermore, increasing MB acceleration allows for a directly proportional increase in temporal resolution through reduction of the TR. As a more accurate characterisation of the haemodynamic response function is achieved with a higher sampling rate (Dilharreguy et al., 2003), an improvement in BOLD sensitivity may be possible with higher MB acceleration factors if temporal resolution is also increased. This can be the case even in the presence of lower tSNR levels that result from higher MB acceleration (as seen in Chapter 4). Increased sampling rate has been shown to be beneficial to BOLD sensitivity, in some cases, for both resting-state (Risk et al., 2021) and task-based fMRI (Todd et al., 2016). However, the benefits that increasing sampling rate can achieve vary according to factors such as task (Bhandari et al., 2020; Demetriou et al., 2018) and ROI (Todd et al., 2016). On the other hand, MB acceleration factors above 4 can lead to significant noise amplification (Risk et al., 2021), with areas that have higher g-factors being negatively affected by higher acceleration factors (Todd et al., 2017). This indicates that selecting acquisition parameters involves complex trade-offs and necessitates careful consideration based on the application.

There are also complex interactions between MB and the reconstruction method used. With a combination of MB acceleration factor 4 and SENSE

factor 2, increased BOLD sensitivity was achieved due to higher sampling rate without finding slice leakage artefacts (Bhandari et al., 2020). However, MB factor 4 paired with in-plane Slice-GRAPPA acceleration lead to a high number of signal leakage artefacts between simultaneously excited slices, with the number of artefacts being reduced significantly when the Split Slice-GRAPPA method is used (Todd et al., 2016).

Thus the results of Chapter 4 show the effect of MB and SENSE on tSNR, and how this relationship changes over the brain, without considering the temporal advantages these methods can provide. On the other hand, the methodology showed in Chapter 4 could be used in future research, to streamline the characterisation of the spatially variant effect of acceleration methods on BOLD sensitivity, while considering their provided benefits to temporal resolution.

There are other acceleration methods that can be used in addition to SENSE. For example, the field of compressed sensing has shown that data can be acquired with even fewer samples than normally collected using SENSE. This provides a larger reduction in image acquisition time (Liang et al., 2009), without reducing image quality (Vranic et al., 2019). However, the noise characteristics when using compressed sensing are different than that of SENSE and are not well understood (Akcakaya et al., 2014; Jaspan et al., 2015). Further, compressed sensing also introduces unique artefacts into the image (Sartoretti et al., 2018). Future research could therefore compare the spatial characteristics of noise in SENSE and compressed sensing, similar to the study in Chapter 4.

Chapter 5 explores the impact of tSNR levels and additional participant motion on pRF analysis. The addition of simulated noise as added by fRAT was modelled as Gaussian-distributed noise which simulates additional thermal noise (Wald & Polimeni, 2017). This provides an accurate simulation of additional noise, as thermal noise becomes the dominant form of noise as voxel volume decreases (Liu, 2016). On the other hand, as previously discussed, there are additional effects of image acceleration that cannot be modelled with this simple addition of noise. Therefore, these results effectively isolate the influence of increased noise and corresponding tSNR reduction on a pRF

analysis, but do not fully simulate the effects of image acceleration.

It is worth noting that in addition to acoustic noise, how long participants have to stay in the scanner is a significant contributing factor in participant discomfort (Heilmaier et al., 2011). Given the wide range of applications for pRF analysis, such as characterising stroke damage to visual areas (Beh et al., 2021); examining how receptive fields develop with age (Gomez et al., 2018); and creating topographic maps of hand representations (Asghar et al., 2023), it is crucial to ensure the scan experience is as comfortable as possible for vulnerable groups who may struggle to remain still for extended periods during pRF analysis. While reducing scan length would reduce the accuracy of pRF estimates, as the length of scan necessary to find an effect of a given size is dependent on the tSNR of the data (subsection 2.3.2). Therefore it is worth investigating whether pRF scan length can be significantly reduced, if tSNR is increased.

One approach to reducing thermal noise in imaging data is NORDIC PCA denoising (Moeller et al., 2021). This was shown here to provide a noticeable increase in tSNR when additional information is used in denoising (Chapter 4), and a small but consistent increase when it is not (Chapter 5). Therefore, NORDIC can potentially be used to allow higher image acceleration factors, either for reduced acoustic noise or higher temporal resolution, while limiting the tSNR penalty. However there are other methods of increasing tSNR not investigated in this thesis. For example, the sampling of multiple echoes during functional scanning has been shown to increase data quality compared to sampling a single-echo (Puckett et al., 2018) and increase BOLD sensitivity (Posse et al., 1999). Further, sampling of multiple echoes is particularly beneficial when functional measurements are collected from multiple regions. This can be used to assess regional variation in T_2^*, which can then be used to optimise the sampling time of single-echo fMRI for multiple regions (Puckett et al., 2018). Future research will aim to investigate whether methods such as double-echo sequences or the use of post-hoc denoising techniques such as NORDIC (which only requires small changes to scanning protocol covered by changing two scan control parameters and adding a 'noRFGR' noise scan) can provide substantial tSNR level increases to be able to reduce the pRF scan length.

It should also be noted however, that there are diminishing returns when increasing tSNR, with higher tSNR levels not translating into higher BOLD sensitivity above a certain point (Jamil et al., 2021). Therefore as Chapter 5 investigated the detrimental effect of lower tSNR levels on pRF analysis, future research can examine the point at which increasing tSNR stops benefitting pRF analysis. Finally, as compared to retrospective motion correction techniques, the use of prospective motion correction, i.e. dealing with participant motion at the point of data acquisition, allows for increased activation sensitivity in the presence of substantial motion (Zaitsev et al., 2017). Therefore, future research could also characterise the resilience of pRF analysis using prospective motion correction in participants who struggle with involuntary movements, such as post-stroke chorea or tremor patients, as an alternative to reducing scan lengths.

6.2 Concluding remarks

The work presented in this thesis introduces the useful, documented and open-access software fRAT which for example enables researchers to more easily examine the effect of image acquisition parameters on data quality metrics. fRAT was employed to characterise the impact of image acceleration methods on image data quality for functional MRI (using tSNR), as well as the influence of tSNR and motion on pRF analysis.

Ultimately, the findings presented in this thesis provide researchers with the tools to enhance scanning protocols and analysis methodologies by making empirically informed decisions regarding the impact of these choices on data quality.

Chapter 7

Appendices

7.1 Sample of tutorial page on the fRAT website

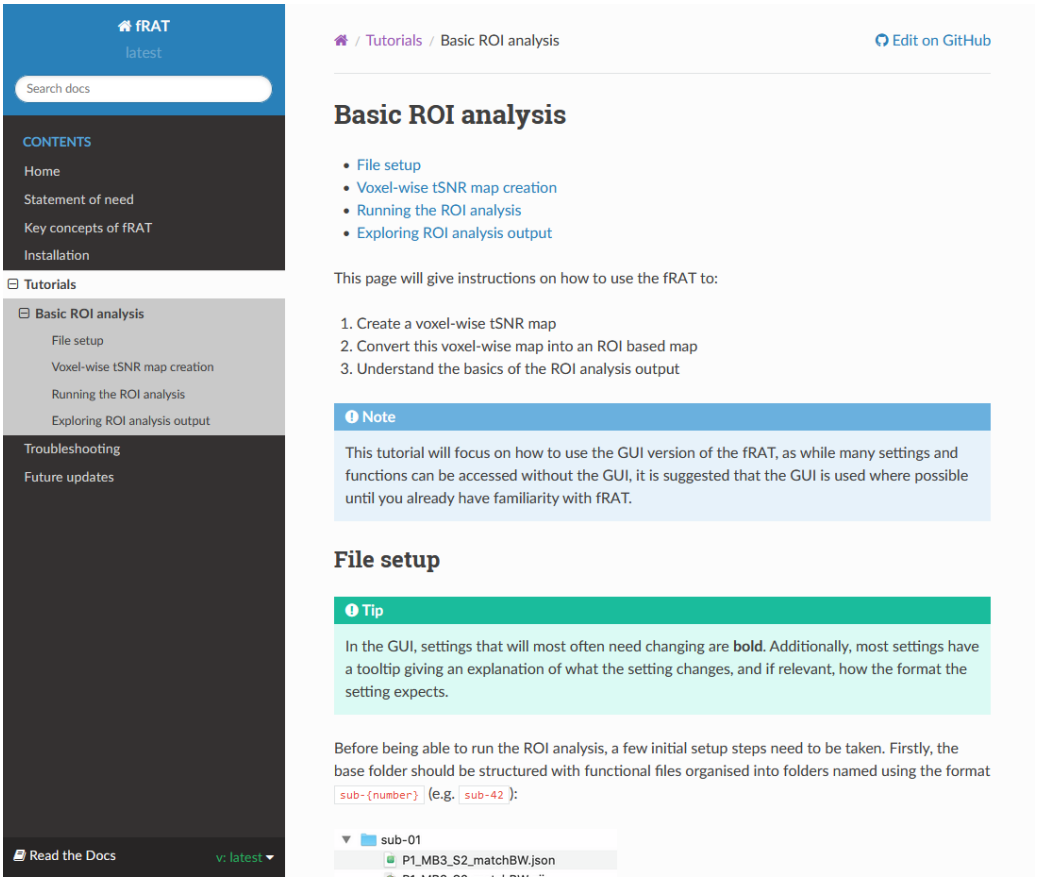

7.2 fRAT tSNR map creation log

```

# General information

version = 1.6.4
config_file_used = 'statmap_config.toml'
statistical_map_created = 'Temporal SNR'

# Statistical_maps

## General settings

verbose = true
multicore_processing = true
max_core_usage = 'max'
base_folder = ''
input_folder_name = 'func_volumes'
output_folder_name = 'DEFAULT'

## High pass filtering

temporal_filter = true
highpass_filter_cutoff = 0.01

## Motion correction

remove_motion_outliers = false
motion_correction = true
```

7.3 fRAT CAP analysis log

```
1
2 # General information
3
4 version = 1.6.4
5 config_file_used = 'fRAT_config.toml'
6
7 # General
8
9 run_analysis = true
10 run_statistics = false
11 run_plotting = false
12 verbose = true
13 verbose_cmd_line_args = false
14 multicore_processing = true
15 max_core_usage = 'max'
16 brain_file_loc = ''
17 report_output_folder = ''
18 averaging_type = 'Participant averaged'
19 parameter_file = 'paramValues.csv'
20 file_cleanup = 'move'
21
22 ## Installation testing
23
24 delete_test_folder = 'If completed without error'
25 verbose_errors = true
26
27 # Analysis
28
29 atlas_number = 'HarvardOxford-cort'
30 input_folder_name = 'func_volumes_preprocessed'
31 output_folder = 'DEFAULT'
32 dof = 12
33 anat_align_cost_function = 'BBR'
34 grey_matter_segment = true
35 run_fsl_fast = 'Run if files not found'
36 fslfast_min_prob = 0.1
37 stat_map_folder = 'temporalSNR_report'
38 stat_map_suffix = '_tSNR.nii.gz'
39 conf_level_number = '95%, 1.96'
40 binary_params = ['Nordic']
```

```
41
42 ## Outlier detection
43
44 noise_cutoff = true
45 gaussian_outlier_detection = true
46 gaussian_outlier_contamination = 0.1
47 gaussian_outlier_location = 'below gaussian'
48
49 # Parsing
50
51 parameter_dict1 = ['MB', 'SENSE', 'Nordic', 'Scanner']
52 parameter_dict2 = ['mb', 's', 'nordic', '']
53 make_folder_structure = true
54 parsing_folder = 'func'
```

7.4 fRAT CAP statistics log

```
1
2 # General information
3
4 version = 1.6.4
5 config_file_used = 'fRAT_config.toml'
6 data_used_for_statistics = "participant_averaged"
7
8 # Statistics
9
10 automatically_create_statistics_options_file = true
11 statistics_subfolder_name = 'brainimg_Ingenia_nordicOff'
12 print_result = true
13 minimum_voxels = 200
14 bootstrap_samples = 1000
15 bootstrap_confidence_interval = 99.9
16 regional_stats_rois = ['all']
17 include_as_variable = ['MB', 'Multiband', 'SENSE']
18 exclude_data = ['', '', 'On', 'Achieva']
19 brain_map_p_thresh = 0.001
20
21 ## T-tests
22
23 run_t_tests = true
24 IV_type = ['Within-subjects', 'Within-subjects', 'Within-
    subjects', 'Between-subjects']
25
26 ## Linear mixed models
27
28 run_linear_mixed_models = true
29 categorical_variables = ['Nordic', 'Scanner']
30 main_effects = true
31 main_and_interaction_effects = true
32 interaction_effects = false
33
34 ## R2 vs voxel count LMM
35
36 max_below_thresh = 20
```

7.5 Number of observations excluded in each region according to exclusion criteria

```

Temporal Pole: 36/498 (7.23%)
Superior Temporal Gyrus, anterior division: 83/498 (16.67%)
Middle Temporal Gyrus, anterior division: 154/498 (30.92%)
Middle Temporal Gyrus, posterior division: 6/498 (1.20%)
Middle Temporal Gyrus, temporooccipital part: 2/498 (0.40%)
Inferior Temporal Gyrus, anterior division: 458/498 (91.97%)
Inferior Temporal Gyrus, posterior division: 127/498 (25.50%)
Inferior Temporal Gyrus, temporooccipital part: 40/498 (8.03%)
Superior Parietal Lobule: 2/498 (0.40%)
Lateral Occipital Cortex, inferior division: 2/498 (0.40%)
Intracalcarine Cortex: 2/498 (0.40%)
Frontal Medial Cortex: 388/498 (77.91%)
Subcallosal Cortex: 74/498 (14.86%)
Frontal Orbital Cortex: 10/498 (2.01%)
Parahippocampal Gyrus, anterior division: 79/498 (15.86%)
Parahippocampal Gyrus, posterior division: 26/498 (5.22%)
Lingual Gyrus: 4/498 (0.80%)
Temporal Fusiform Cortex, anterior division: 494/498 (99.20%)
Temporal Fusiform Cortex, posterior division: 79/498 (15.86%)
Temporal Occipital Fusiform Cortex: 39/498 (7.83%)
Occipital Fusiform Gyrus: 31/498 (6.22%)
Frontal Operculum Cortex: 83/498 (16.67%)
Planum Polare: 41/498 (8.23%)
Heschl's Gyrus (includes H1 and H2): 245/498 (49.20%)
Supracalcarine Cortex: 498/498 (100.00%)
```

7.6 fRAT CAP settings used to calculate noise levels for the Occipital Pole

```

# General information
version = 1.6.4
config_file_used = 'fRAT_config.toml'

# General
run_analysis = true
run_statistics = false
run_plotting = false
verbose = true
verbose_cmd_line_args = false
multicore_processing = true
max_core_usage = 'max'
brain_file_loc = ''
report_output_folder = ''
averaging_type = 'Participant averaged'
parameter_file = 'paramValues.csv'
file_cleanup = 'move'

## Installation testing
delete_test_folder = 'If completed without error'
verbose_errors = true

# Analysis
atlas_number = 'HarvardOxford-cort'
input_folder_name = 'int_preprocessed'
output_folder = 'tStd'
dof = 12
anat_align_cost_function = 'BBR'
grey_matter_segment = true
run_fsl_fast = 'Run if files not found'
fslfast_min_prob = 0.1
stat_map_folder = ''
stat_map_suffix = '_tStd.nii.gz'
conf_level_number = '95%, 1.96'
binary_params = ['Nordic', 'coding']

## Outlier detection
```

```
noise_cutoff = true
gaussian_outlier_detection = true
gaussian_outlier_contamination = 0.1
gaussian_outlier_location = 'below gaussian'

# Parsing
parameter_dict1 = ['coding']
parameter_dict2 = ['code']
make_folder_structure = false
parsing_folder = 'func'
```

7.7 fRAT CAP settings used to calculate tSNR levels for the Occipital Pole

```

# General information
version = 1.6.4
config_file_used = 'fRAT_config.toml'

# General
run_analysis = true
run_statistics = false
run_plotting = false
verbose = true
verbose_cmd_line_args = false
multicore_processing = true
max_core_usage = 'max'
brain_file_loc = ''
report_output_folder = ''
averaging_type = 'Participant averaged'
parameter_file = 'paramValues.csv'
file_cleanup = 'move'

## Installation testing
delete_test_folder = 'If completed without error'
verbose_errors = true

# Analysis
atlas_number = 'HarvardOxford-cort'
input_folder_name = 'int_preprocessed'
output_folder = 'tSNR'
dof = 12
anat_align_cost_function = 'BBR'
grey_matter_segment = true
run_fsl_fast = 'Run if files not found'
fslfast_min_prob = 0.1
stat_map_folder = ''
stat_map_suffix = '_tSNR.nii.gz'
conf_level_number = '95%, 1.96'
binary_params = ['Nordic', 'coding']

## Outlier detection
```

```
noise_cutoff = true
gaussian_outlier_detection = true
gaussian_outlier_contamination = 0.1
gaussian_outlier_location = 'below gaussian'

# Parsing
parameter_dict1 = ['coding']
parameter_dict2 = ['code']
make_folder_structure = false
parsing_folder = 'func'
```

7.8 Supplementary Figures for Chapter 4

Figure 7.1

Barchart showing effect of multiband and SENSE factor on sound pressure level (dB)

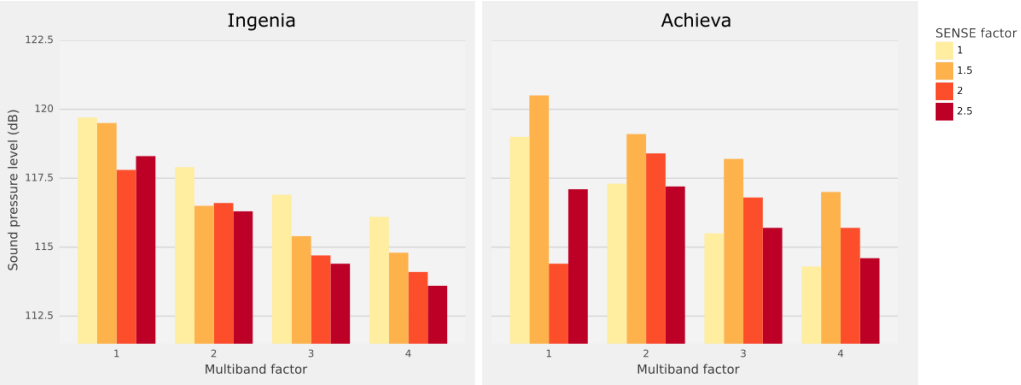

Note. An error was made when setting the water fat shift for MB 1 SENSE 2, resulting in a low EPI bandwidth on both scanners.

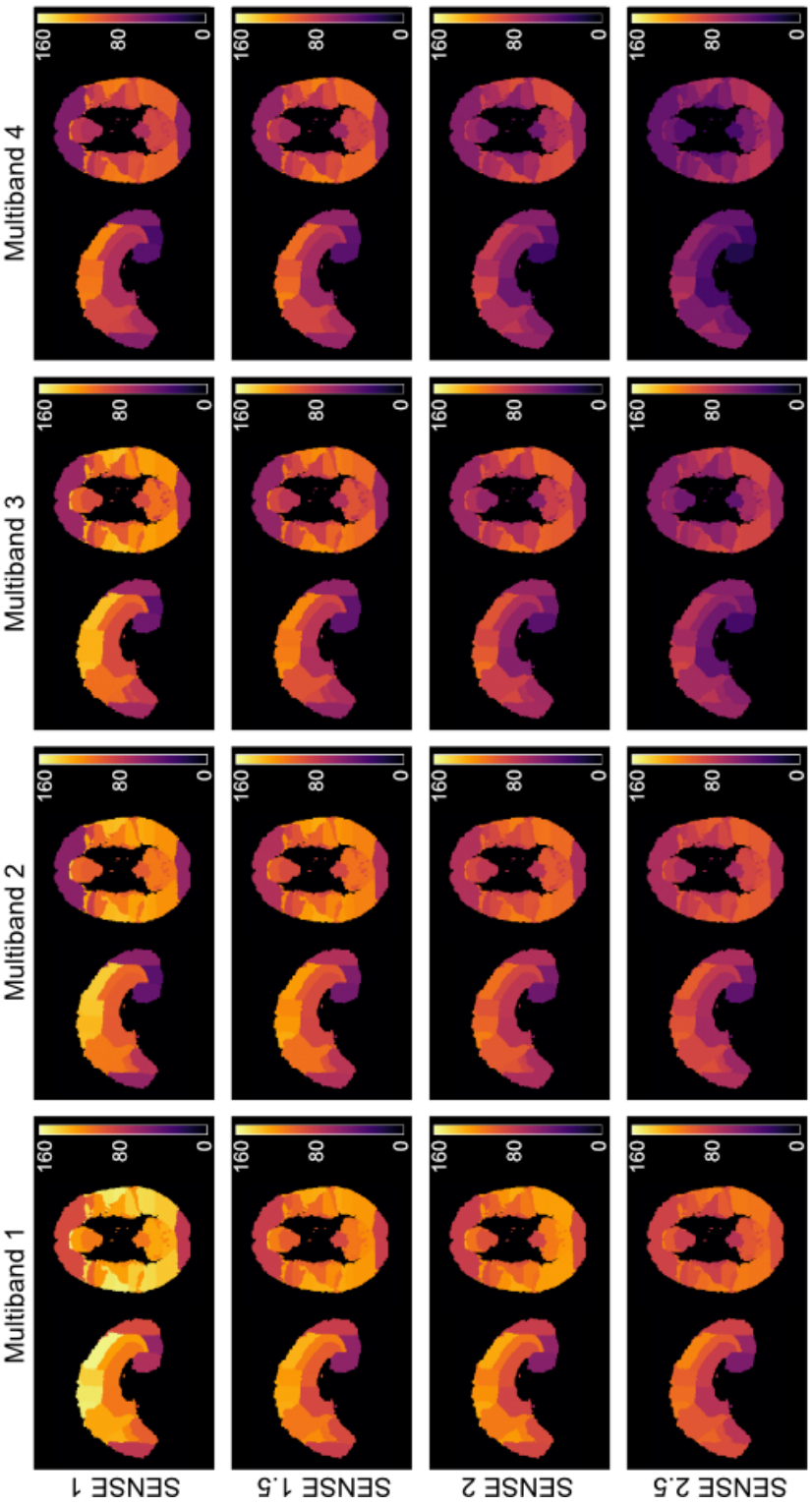

Figure 7.2
Mean tSNR values on the Achieva

Note. Values represent the mean across each ROI.

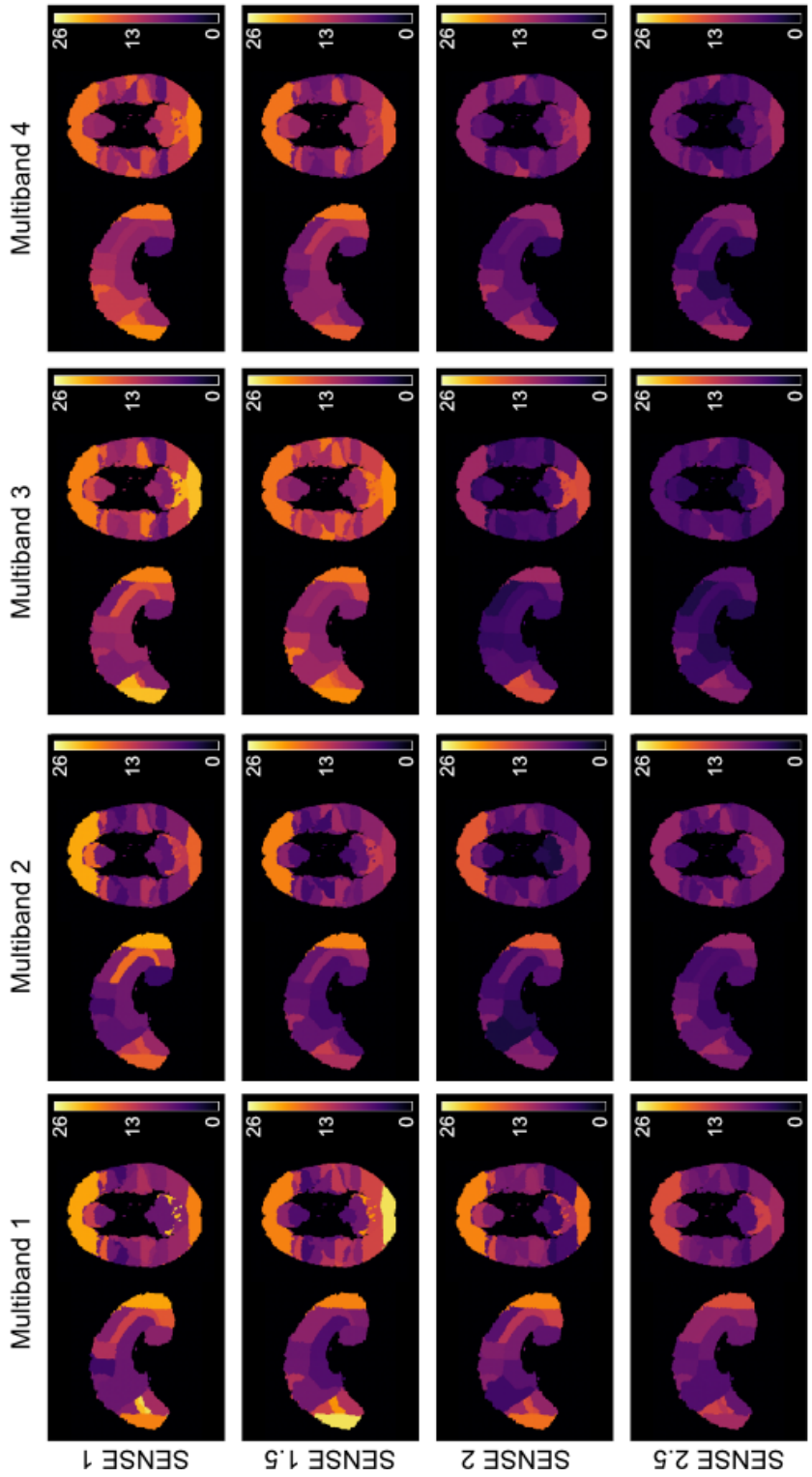

Figure 7.3
tSNR standard deviation on the Achieva

Note. Values represent the standard deviation across each participant for each ROI.

Figure 7.4
Mean tSNR values on the Achieva with NORDIC denoising

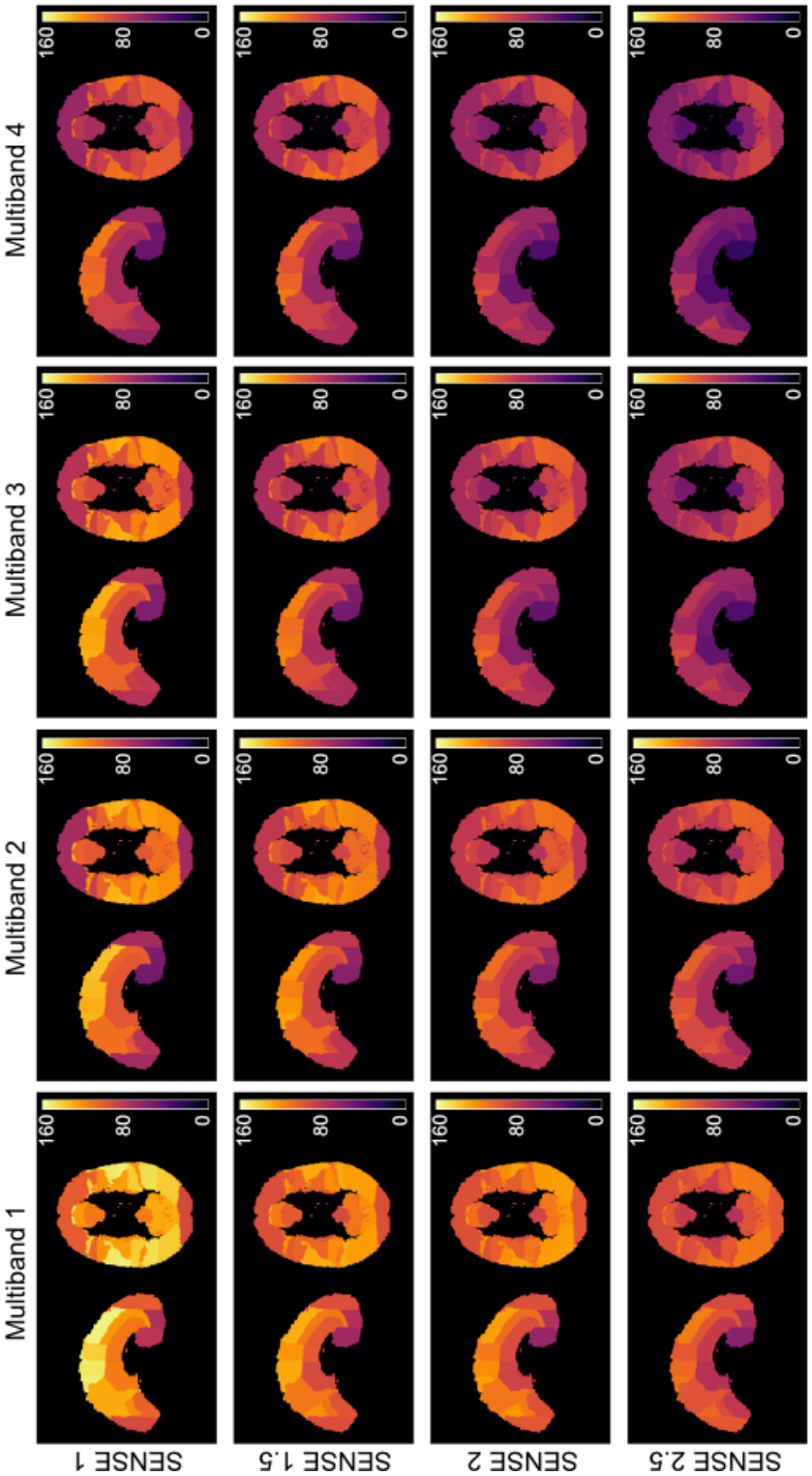

Note. Values represent the mean across each ROI.

Figure 7.5
tSNR standard deviation on the Achieva with NORDIC denoising

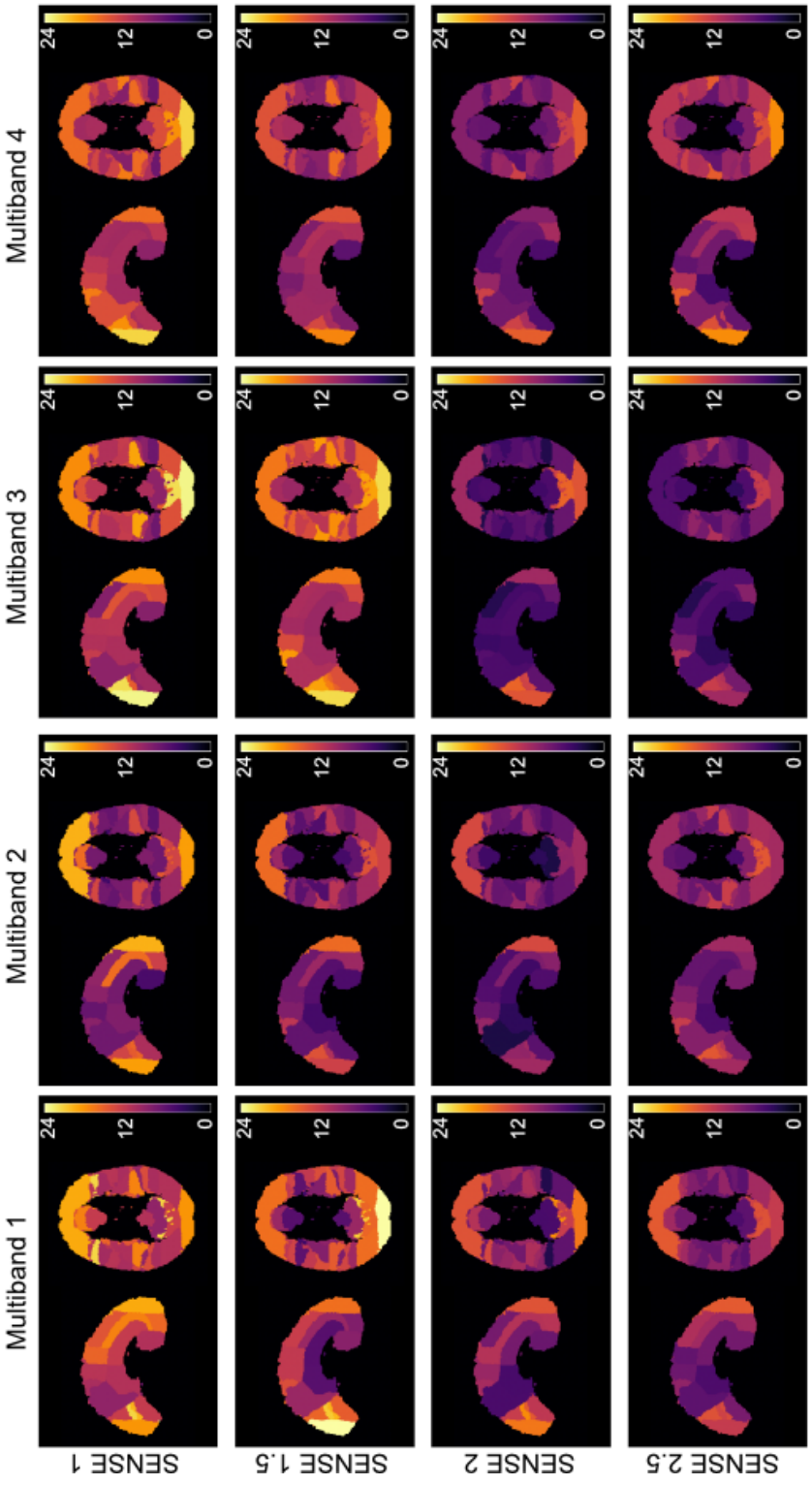

Note. Values represent the standard deviation across each participant for each ROI.

7.9 Supplementary Figures for Chapter 5

Table 7.1

Receptive field maps at various noise levels for Participant 11773

R^2 threshold	Data type			
	Original data	Noise level 1	Noise level 2	Noise level 5
0	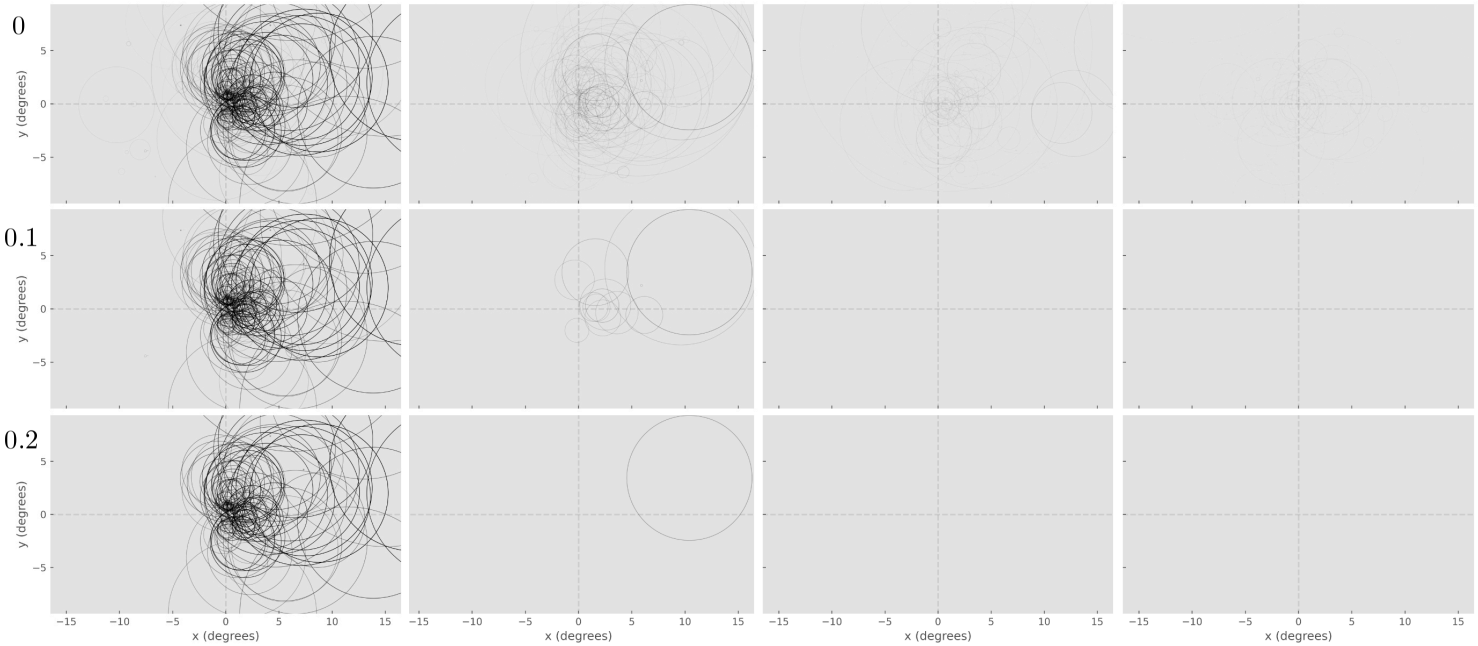			
0.1				
0.2				

Note. The transparency of the receptive fields represent the R^2 value.

Table 7.2

Receptive field maps at various noise levels for Participant 14326

	Data type			
R^2 threshold	Original data	Noise level 1	Noise level 2	Noise level 5
0	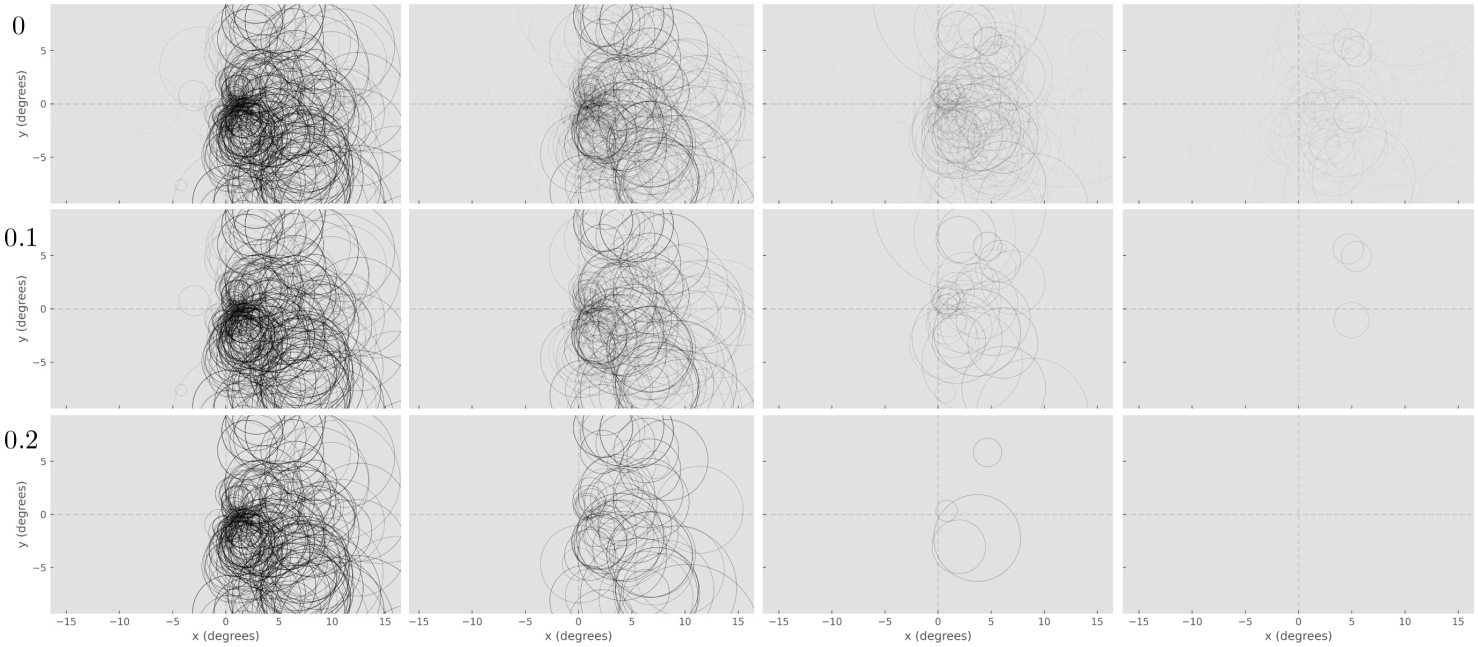			
0.1				
0.2				

Note. The transparency of the receptive fields represent the R^2 value.

Table 7.3

Receptive field centre differences at various noise levels for Participant 11773

	Data type		
R² threshold	Noise level 1	Noise level 2	Noise level 5
0	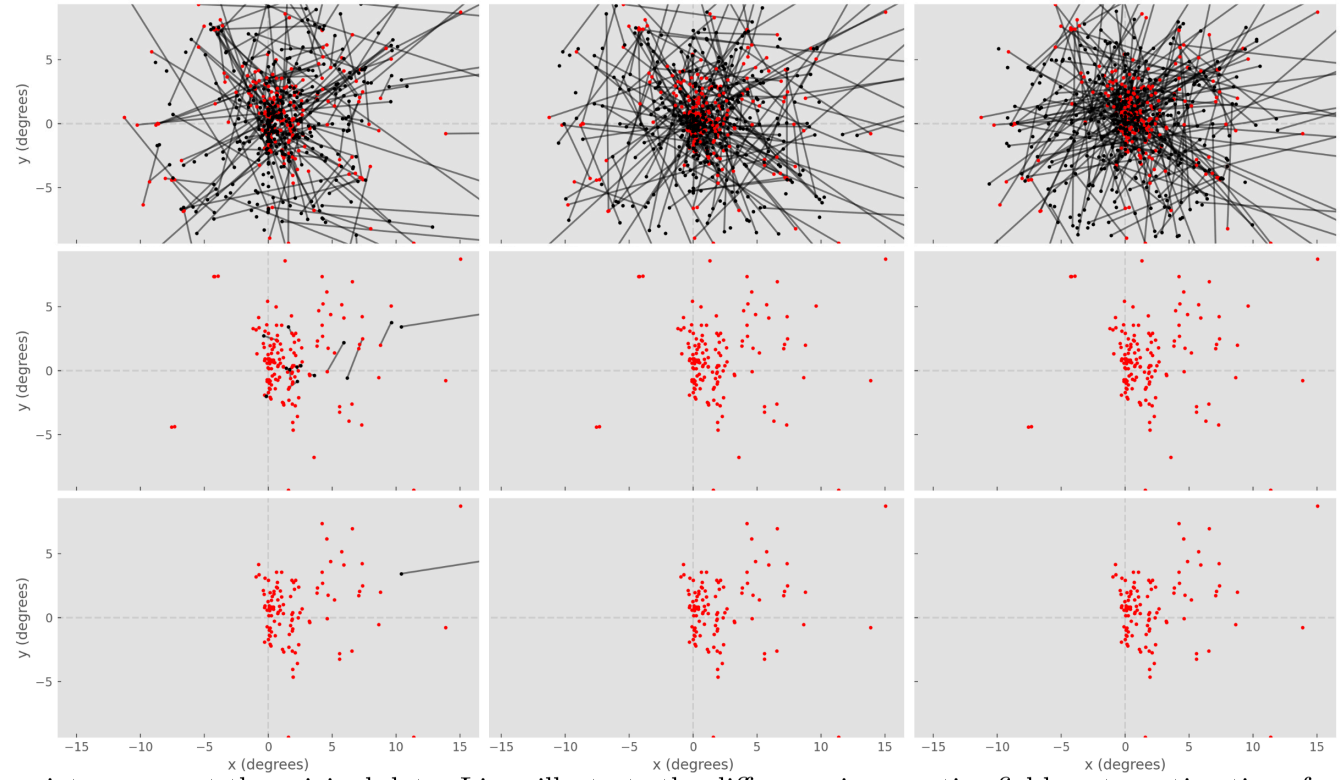		
0.1			
0.2			

Note. Red data points represent the original data. Lines illustrate the difference in receptive field centre estimations for each pair of data points. Data points that are unpaired due to one of the pair not exceeding the R^2 threshold are shown without a line.

Table 7.4

Receptive field centre differences at various noise levels for Participant 14326

	Data type		
R² threshold	Noise level 1	Noise level 2	Noise level 5
0	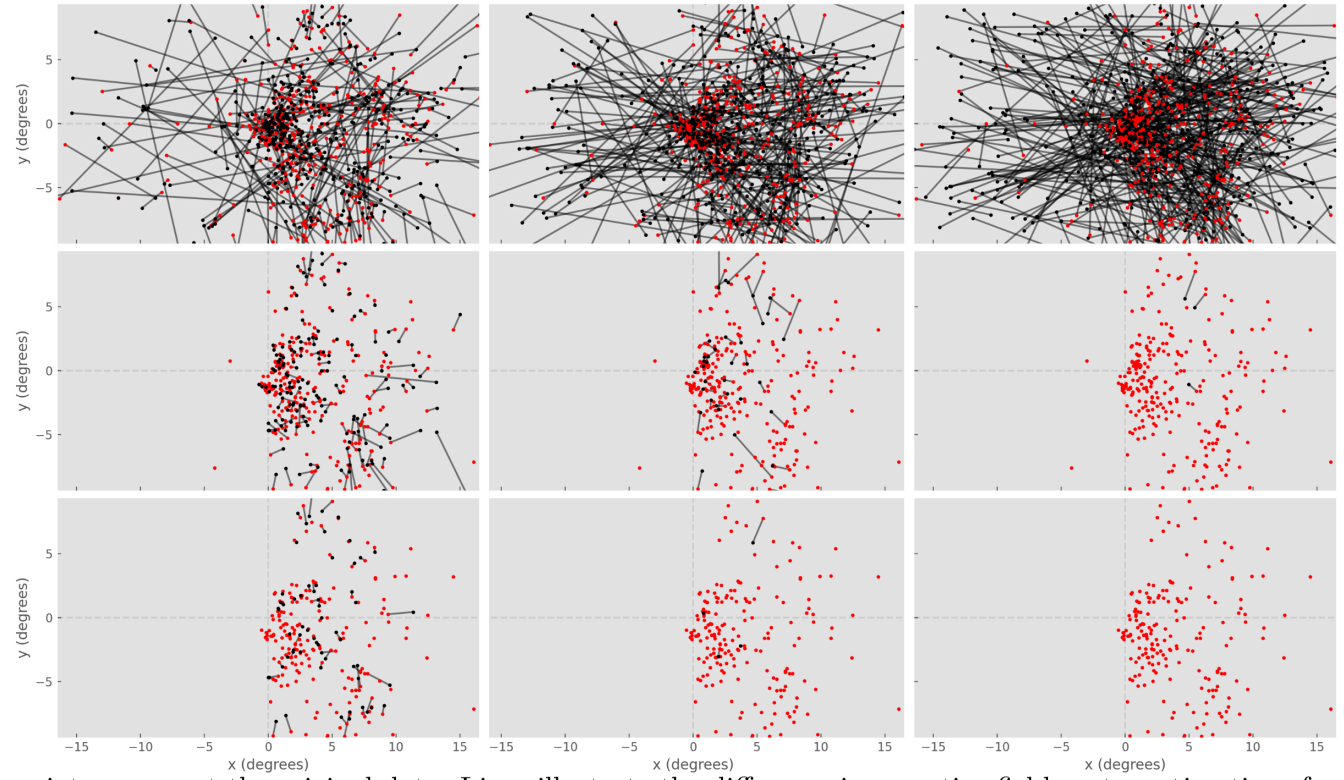		
0.1			
0.2			

Note. Red data points represent the original data. Lines illustrate the difference in receptive field centre estimations for each pair of data points. Data points that are unpaired due to one of the pair not exceeding the R^2 threshold are shown without a line.

Table 7.5

Receptive field maps at various motion levels for Participant 11773

R^2 threshold	Data type			
	Original data	Motion level 1	Motion level 2	Motion level 5
0	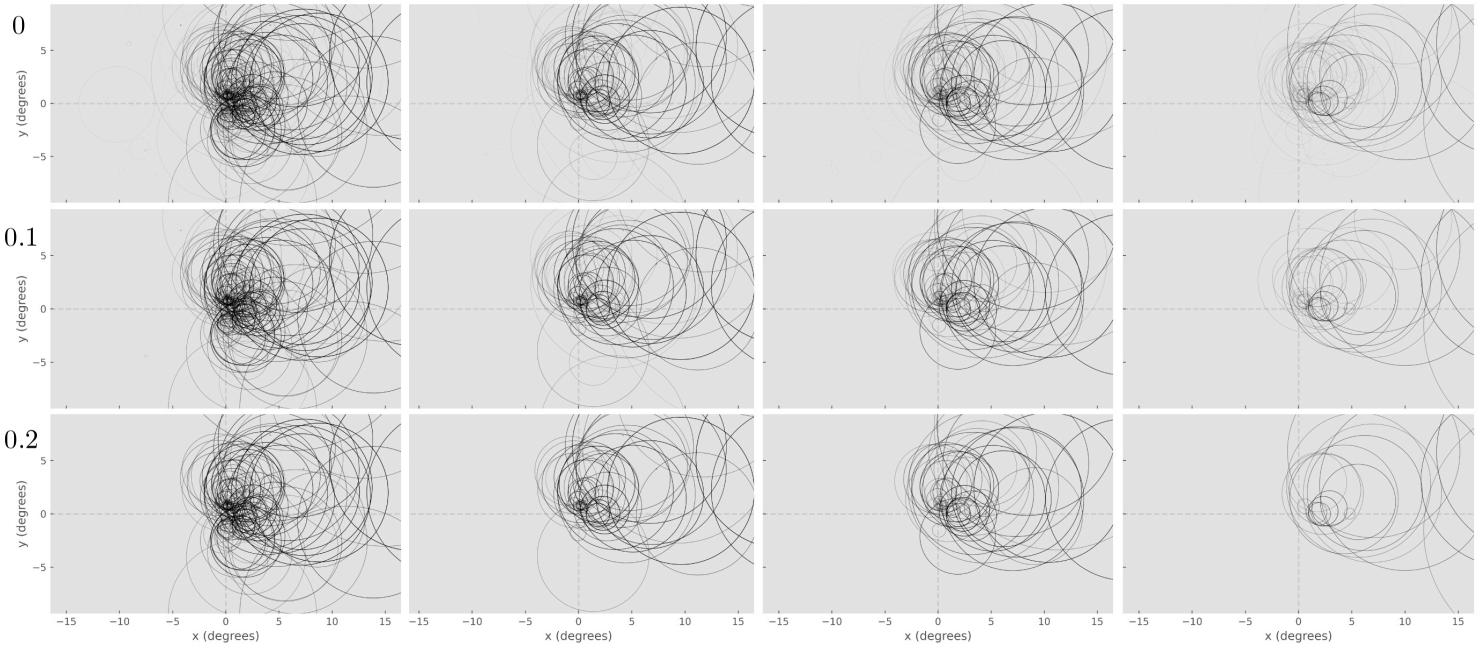			
0.1				
0.2				

Note. The transparency of the receptive fields represent the R^2 value.

Table 7.6

Receptive field maps at various motion levels for Participant 14326

	Data type			
R² threshold	Original data	Motion level 1	Motion level 2	Motion level 5
0	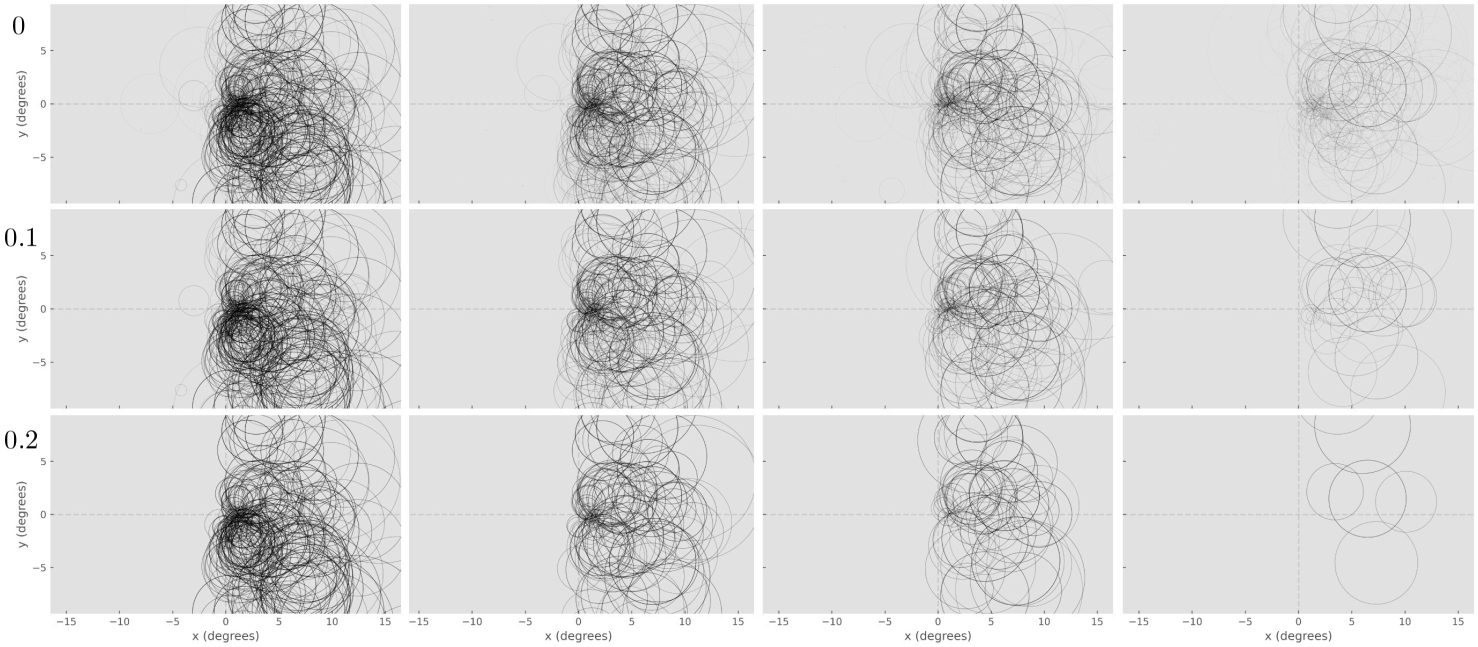			
0.1				
0.2				

Note. The transparency of the receptive fields represent the R^2 value.

Table 7.7

Receptive field centre differences at various motion levels for Participant 11773

	Data type		
R² threshold	Motion level 1	Motion level 2	Motion level 5
0	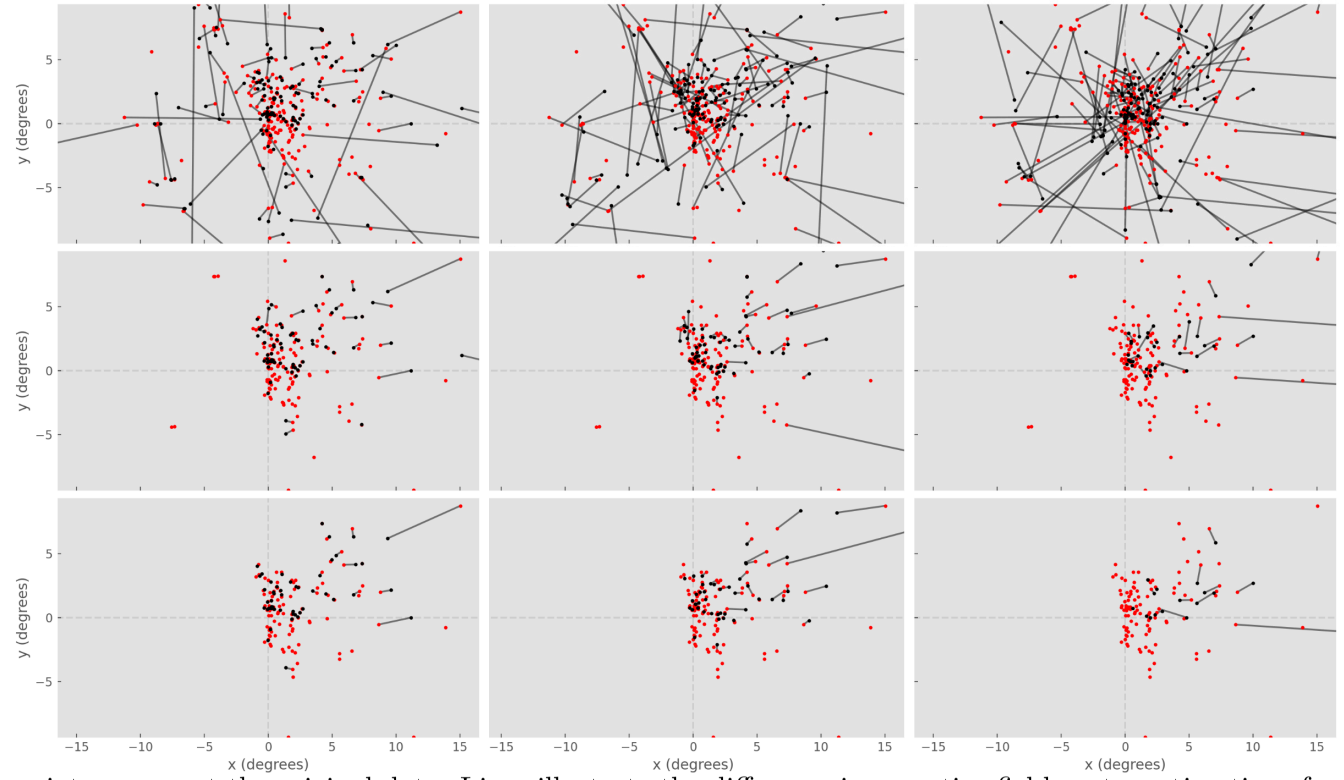		
0.1			
0.2			

Note. Red data points represent the original data. Lines illustrate the difference in receptive field centre estimations for each pair of data points. Data points that are unpaired due to one of the pair not exceeding the R^2 threshold are shown without a line.

Table 7.8

Receptive field centre differences at various motion levels for Participant 14326

	Data type		
R² threshold	Motion level 1	Motion level 2	Motion level 5
0	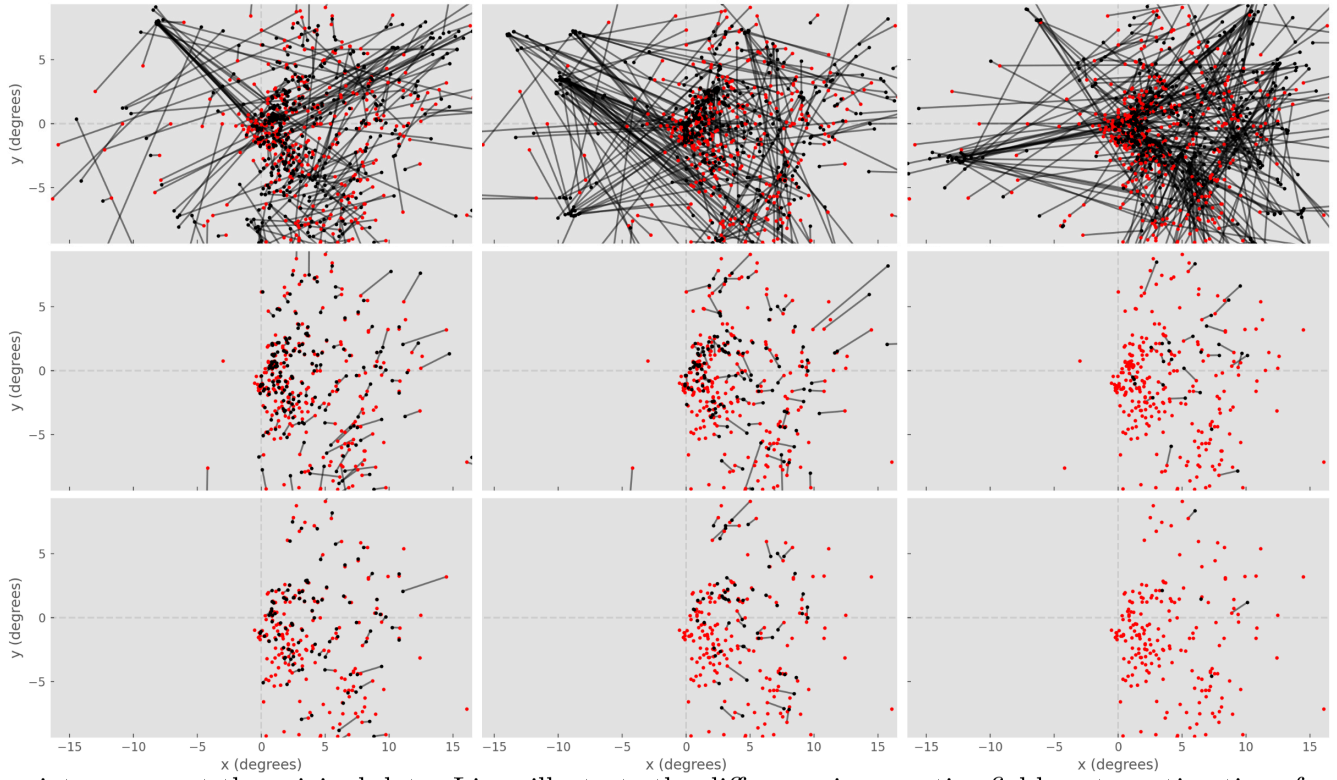		
0.1			
0.2			

Note. Red data points represent the original data. Lines illustrate the difference in receptive field centre estimations for each pair of data points. Data points that are unpaired due to one of the pair not exceeding the R^2 threshold are shown without a line.

Table 7.9

Table showing receptive field maps and differences for denoised data for Participant 11773

R^2 threshold	Receptive field maps: Original data	Receptive field maps: Denoised data	Receptive field centre differences
0	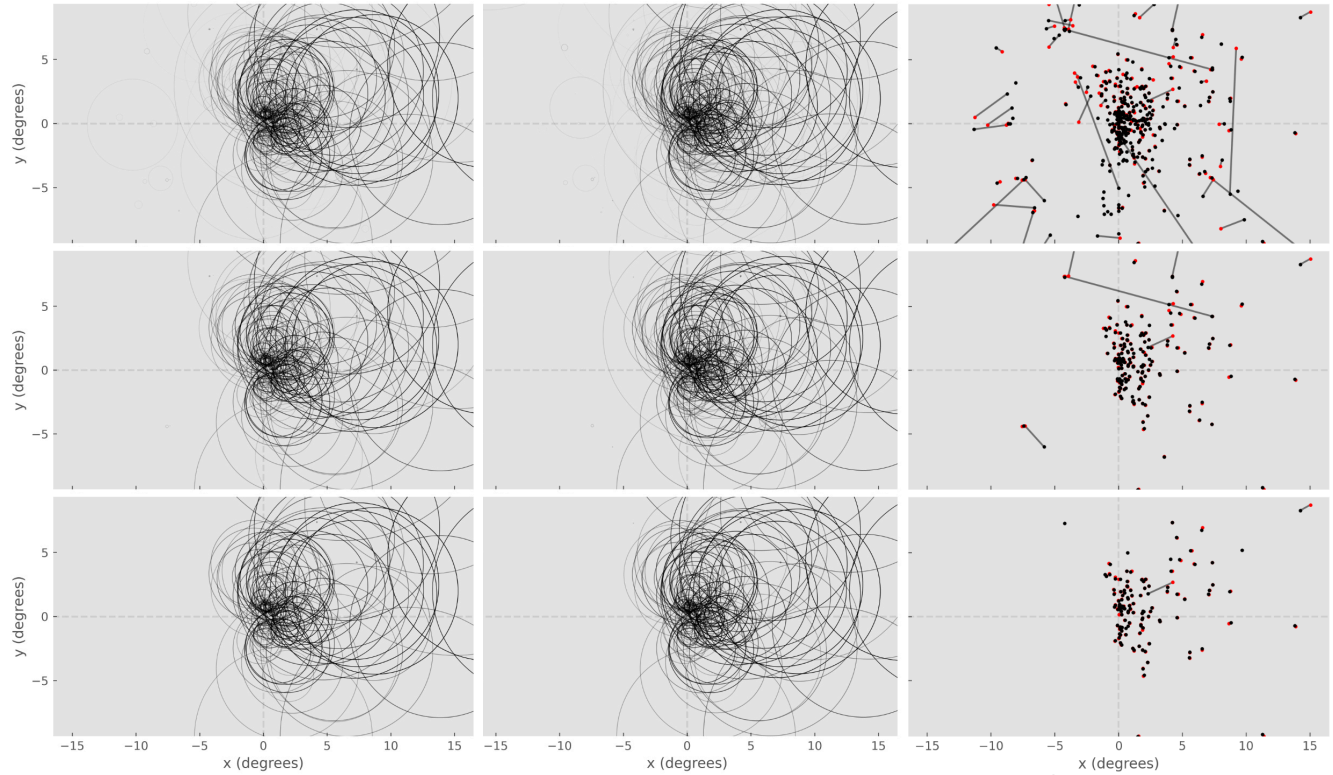		
0.1			
0.2			

Note. For the receptive field map images, the transparency of the receptive fields represent the R^2 value. For the receptive field centre difference images, red data points represent the original data and lines illustrate the difference in receptive field centre estimations for each pair of data points. Data points that are unpaired due to one of the pair not exceeding the R^2 threshold are shown without a line.

Table 7.10

Table showing receptive field maps and differences for denoised data for Participant 14326

R^2 threshold	Receptive field maps: Original data	Receptive field maps: Denoised data	Receptive field centre differences
0	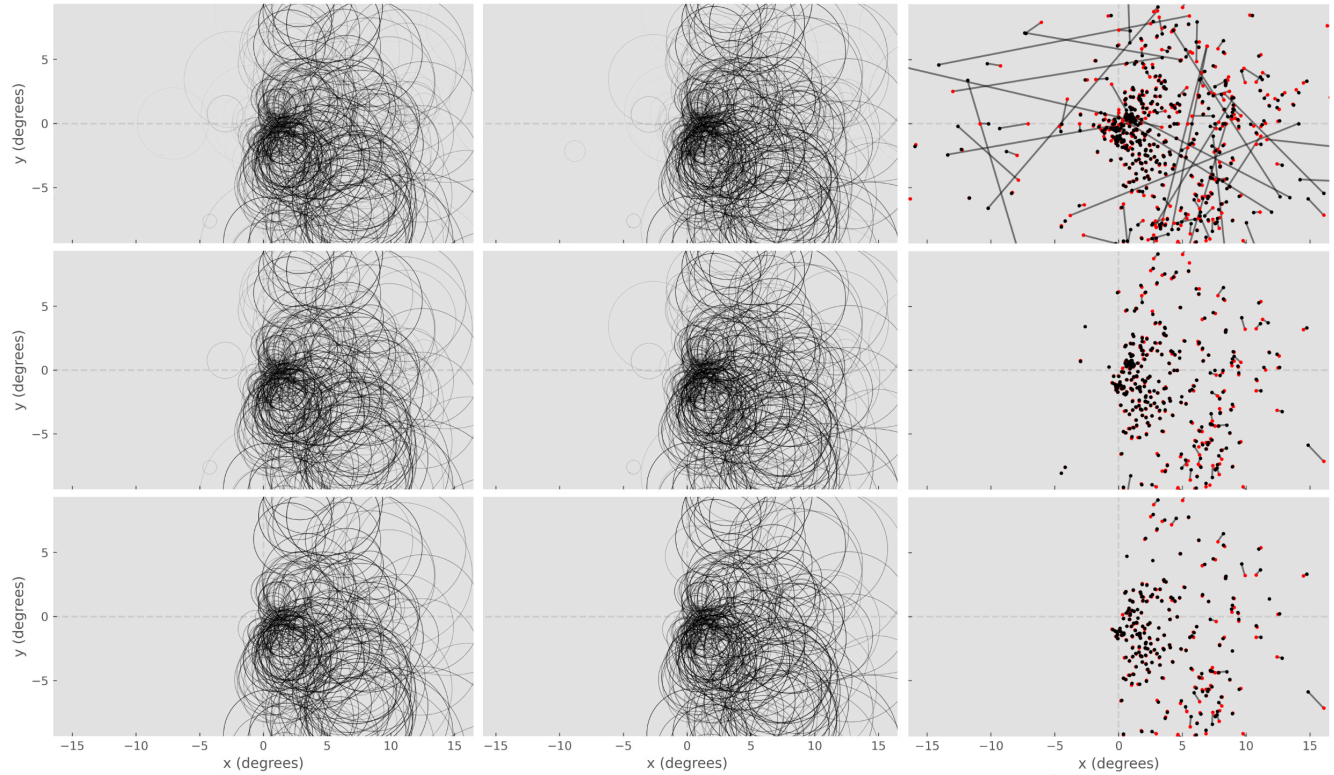		
0.1			
0.2			

Note. For the receptive field map images, the transparency of the receptive fields represent the R^2 value. For the receptive field centre difference images, red data points represent the original data and lines illustrate the difference in receptive field centre estimations for each pair of data points. Data points that are unpaired due to one of the pair not exceeding the R^2 threshold are shown without a line.

Chapter 8

References

Akcakaya, M., Basha, T. A., Manning, W. J., & Nezafat, R. (2014). Efficient calculation of g-factors for CG-SENSE in high dimensions: Noise amplification in random undersampling. *Journal of Cardiovascular Magnetic Resonance*, *16*(1), W28. https://doi.org/10.1186/1532-429X-16-S1-W28

Amaro Jr., E., Williams, S. C. R., Shergill, S. S., Fu, C. H. Y., MacSweeney, M., Picchioni, M. M., Brammer, M. J., & McGuire, P. K. (2002). Acoustic noise and functional magnetic resonance imaging: Current strategies and future prospects. *Journal of Magnetic Resonance Imaging*, *16*(5), 497–510. https://doi.org/10.1002/jmri.10186

Asghar, M., Sanchez-Panchuelo, R., Schluppeck, D., & Francis, S. (2023). Two-Dimensional Population Receptive Field Mapping of Human Primary Somatosensory Cortex. *Brain Topography*, *36*(6), 816–834. https://doi.org/10.1007/s10548-023-01000-8

Bakdash, J. Z., & Marusich, L. R. (2017). Repeated Measures Correlation. *Frontiers in Psychology*, *8*.

Bandettini, P. A., Wong, E. C., Jesmanowicz, A., Hinks, R. S., & Hyde, J. S. (1994). Spin-echo and gradient-echo epi of human brain activation using bold contrast: A comparative study at 1.5 T. *NMR in Biomedicine*, *7*(1-2), 12–20. https://doi.org/10.1002/nbm.1940070104

Barth, M., Breuer, F., Koopmans, P. J., Norris, D. G., & Poser, B. A. (2016). Simultaneous multislice (SMS) imaging techniques. *Magnetic Resonance in Medicine*, *75*(1), 63–81. https://doi.org/10.1002/mrm.25897

Bates, D., Mächler, M., Bolker, B., & Walker, S. (2015). Fitting Linear Mixed-Effects Models Using lme4. *Journal of Statistical Software*, *67*, 1–48. https://doi.org/10.18637/jss.v067.i01

Beh, A., McGraw, P. V., Webb, B. S., & Schluppeck, D. (2021). Linking Multi-Modal MRI to Clinical Measures of Visual Field Loss After Stroke. *Frontiers in Neuroscience*, *15*, 737215. https://doi.org/10.3389/fnins.2021.737215

Behin, R., Bishop, J., & Henkelman, R. M. (2005). Dynamic range requirements for MRI. *Concepts in Magnetic Resonance Part B: Magnetic Resonance Engineering*, *26B*(1), 28–35. https://doi.org/10.1002/cmr.b.20042

Benjamini, Y., & Hochberg, Y. (1995). Controlling the False Discovery Rate: A Practical and Powerful Approach to Multiple Testing. *Journal of the Royal Statistical Society. Series B (Methodological)*, *57*(1), 289–300. http://www.jstor.org/stable/2346101

Benson, N. C., Butt, O. H., Datta, R., Radoeva, P. D., Brainard, D. H., & Aguirre, G. K. (2012). The Retinotopic Organization of Striate Cortex Is Well Predicted by Surface Topology. *Current Biology*, *22*(21), 2081–2085. https://doi.org/10.1016/j.cub.2012.09.014

Bhandari, R., Kirilina, E., Caan, M., Suttrup, J., De Sanctis, T., De Angelis, L., Keysers, C., & Gazzola, V. (2020). Does higher sampling rate (multiband + SENSE) improve group statistics - An example from social neuroscience block design at 3T. *NeuroImage*, *213*, 116731. https://doi.org/10.1016/j.neuroimage.2020.116731

Birn, R. M., Molloy, E. K., Patriat, R., Parker, T., Meier, T. B., Kirk, G. R., Nair, V. A., Meyerand, M. E., & Prabhakaran, V. (2013). The effect of scan length on the reliability of resting-state fMRI connectivity estimates. *NeuroImage*, *83*, 550–558. https://doi.org/10.1016/j.neuroimage.2013.05.099

Blaimer, M., Choli, M., Jakob, P. M., Griswold, M. A., & Breuer, F. A. (2013). Multiband phase-constrained parallel MRI. *Magnetic Resonance in Medicine*, *69*(4), 974–980. https://doi.org/10.1002/mrm.24685

Bowring, A., Maumet, C., & Nichols, T. E. (2019). Exploring the impact of analysis software on task fMRI results. *Human Brain Mapping*, *40*(11), 3362–3384. https://doi.org/10.1002/hbm.24603

Bowring, A., Nichols, T. E., & Maumet, C. (2022). Isolating the sources of pipeline-variability in group-level task-fMRI results. *Human Brain Mapping*, *43*(3), 1112–1128. https://doi.org/10.1002/hbm.25713

Breuer, F. A., Blaimer, M., Heidemann, R. M., Mueller, M. F., Griswold, M. A., & Jakob, P. M. (2005). Controlled aliasing in parallel imaging results in higher acceleration (CAIPIRINHA) for multi-slice imaging. *Magnetic Resonance in Medicine*, *53*(3), 684–691. https://doi.org/10.1002/mrm.20401

Chou, I.-J., Tench, C. R., Gowland, P., Jaspan, T., Dineen, R. A., Evangelou, N., Abdel-Fahim, R., Whitehouse, W. P., & Constantinescu, C. S. (2014). Subjective discomfort in children receiving 3 T MRI and experienced adults' perspective on children's tolerability of 7 T: A cross-sectional questionnaire survey. *BMJ Open*, *4*(10), e006094. https://doi.org/10.1136/bmjopen-2014-006094

Clare, S., Francis, S., Morris, P. G., & Bowtell, R. (2001). Single-shot T measurement to establish optimum echo time for fMRI: Studies of the visual, motor, and auditory cortices at 3.0 T. *Magnetic Resonance in Medicine*, *45*(5), 930–933. https://doi.org/10.1002/mrm.1124

Constantinides, C. D., Atalar, E., & McVeigh, E. R. (1997). Signal-to-noise measurements in magnitude images from NMR phased arrays. *Magnetic Resonance in Medicine*, *38*(5), 852–857. https://doi.org/10.1002/mrm.1910380524

Cox, R. W. (1996). AFNI: Software for analysis and visualization of functional magnetic resonance neuroimages. *Computers and Biomedical Research, an International Journal*, *29*(3), 162–173. https://doi.org/10.

1006/cbmr.1996.0014

Crossland, M. D., Sims, M., Galbraith, R. F., & Rubin, G. S. (2004). Evaluation of a new quantitative technique to assess the number and extent of preferred retinal loci in macular disease. *Vision Research*, *44*(13), 1537–1546. https://doi.org/10.1016/j.visres.2004.01.006

Dadar, M., Fonov, V. S., & Collins, D. L. (2018). A comparison of publicly available linear MRI stereotaxic registration techniques. *NeuroImage*, *174*, 191–200. https://doi.org/10.1016/j.neuroimage.2018.03.025

De Martino, F., Moerel, M., Ugurbil, K., Formisano, E., & Yacoub, E. (2015). Less noise, more activation: Multiband acquisition schemes for auditory functional MRI. *Magnetic Resonance in Medicine*, *74*(2), 462–467. https://doi.org/10.1002/mrm.25408

Demetriou, L., Kowalczyk, O. S., Tyson, G., Bello, T., Newbould, R. D., & Wall, M. B. (2018). A comprehensive evaluation of increasing temporal resolution with multiband-accelerated protocols and effects on statistical outcome measures in fMRI. *NeuroImage*, *176*, 404–416. https://doi.org/10.1016/j.neuroimage.2018.05.011

Deshmane, A., Gulani, V., Griswold, M. A., & Seiberlich, N. (2012). Parallel MR imaging. *Journal of Magnetic Resonance Imaging*, *36*(1), 55–72. https://doi.org/10.1002/jmri.23639

Desikan, R. S., Ségonne, F., Fischl, B., Quinn, B. T., Dickerson, B. C., Blacker, D., Buckner, R. L., Dale, A. M., Maguire, R. P., Hyman, B. T., Albert, M. S., & Killiany, R. J. (2006). An automated labeling system for subdividing the human cerebral cortex on MRI scans into gyral based regions of interest. *NeuroImage*, *31*(3), 968–980. https://doi.org/10.1016/j.neuroimage.2006.01.021

de Zwart, J. A., van Gelderen, P., Kellman, P., & Duyn, J. H. (2002). Reduction of Gradient Acoustic Noise in MRI Using SENSE-EPI. *NeuroImage*, *16*(4), 1151–1155. https://doi.org/10.1006/nimg.2002.1119

Dietrich, O., Raya, J. G., Reeder, S. B., Reiser, M. F., & Schoenberg, S. O. (2007). Measurement of signal-to-noise ratios in MR images: In-

fluence of multichannel coils, parallel imaging, and reconstruction filters. *Journal of Magnetic Resonance Imaging*, *26*(2), 375–385. https://doi.org/10.1002/jmri.20969

Dilharreguy, B., Jones, R. A., & Moonen, C. T. W. (2003). Influence of fMRI data sampling on the temporal characterization of the hemodynamic response. *NeuroImage*, *19*(4), 1820–1828. https://doi.org/10.1016/S1053-8119(03)00289-1

Dowdle, L. T., Vizioli, L., Moeller, S., Akçakaya, M., Olman, C., Ghose, G., Yacoub, E., & Uğurbil, K. (2023). Evaluating increases in sensitivity from NORDIC for diverse fMRI acquisition strategies. *NeuroImage*, *270*, 119949. https://doi.org/10.1016/j.neuroimage.2023.119949

Dumoulin, S. O., & Knapen, T. (2018). How Visual Cortical Organization Is Altered by Ophthalmologic and Neurologic Disorders. *Annual Review of Vision Science*, *4*(1), 357–379. https://doi.org/10.1146/annurev-vision-091517-033948

Dumoulin, S. O., & Wandell, B. A. (2008). Population receptive field estimates in human visual cortex. *NeuroImage*, *39*(2), 647–660. https://doi.org/10.1016/j.neuroimage.2007.09.034

DuPre, E., Salo, T., Ahmed, Z., Bandettini, P. A., Bottenhorn, K. L., Caballero-Gaudes, C., Dowdle, L. T., Gonzalez-Castillo, J., Heunis, S., Kundu, P., Laird, A. R., Markello, R., Markiewicz, C. J., Moia, S., Staden, I., Teves, J. B., Uruñuela, E., Vaziri-Pashkam, M., Whitaker, K., & Handwerker, D. A. (2021). TE-dependent analysis of multi-echo fMRI with *tedana*. *Journal of Open Source Software*, *6*(66), 3669. https://doi.org/10.21105/joss.03669

Edelstein, W. A., Glover, G. H., Hardy, C. J., & Redington, R. W. (1986). The intrinsic signal-to-noise ratio in NMR imaging. *Magnetic Resonance in Medicine*, *3*(4), 604–618. https://doi.org/10.1002/mrm.1910030413

Engel, S. A., David, E. R., Wandell, B. A., Lee, A. T., Glover, G. H., Chichilnisky, E.-J., & Shadlen, M. N. (1994). fMRI of human visual cortex. *Nature*, *369*(6481), 525–525. https://doi.org/10.1038/369525a0

Engel, S. A., Glover, G. H., & Wandell, B. A. (1997). Retinotopic organization in human visual cortex and the spatial precision of functional MRI. *Cerebral Cortex*, *7*(2), 181–192. https://doi.org/10.1093/cercor/7.2.181

Esteban, O., Birman, D., Schaer, M., Koyejo, O. O., Poldrack, R. A., & Gorgolewski, K. J. (2017). MRIQC: Advancing the automatic prediction of image quality in MRI from unseen sites. *PLOS ONE*, *12*(9), e0184661. https://doi.org/10.1371/journal.pone.0184661

Esteban, O., Markiewicz, C. J., Blair, R. W., Moodie, C. A., Isik, A. I., Erramuzpe, A., Kent, J. D., Goncalves, M., Dupre, E., Snyder, M., Oya, H., Ghosh, S. S., Wright, J., Durnez, J., Poldrack, R. A., & Gorgolewski, K. J. (2019). fMRIPrep: A robust preprocessing pipeline for functional MRI. *Nature Methods*, *16*(1), 111–116. https://doi.org/10.1038/s41592-018-0235-4

Faraway, J. J. (2016). *Extending the Linear Model with R: Generalized Linear, Mixed Effects and Nonparametric Regression Models, Second Edition* (2nd ed.). Chapman and Hall/CRC. https://doi.org/10.1201/9781315382722

Fatima, A., Shahid, A. R., Raza, B., Madni, T. M., & Janjua, U. I. (2020). State-of-the-Art Traditional to the Machine- and Deep-Learning-Based Skull Stripping Techniques, Models, and Algorithms. *Journal of Digital Imaging*, *33*(6), 1443–1464. https://doi.org/10.1007/s10278-020-00367-5

Fischl, B. (2012). FreeSurfer. *NeuroImage*, *62*(2), 774. https://doi.org/10.1016/j.neuroimage.2012.01.021

Fischmeister, F. P. S., Höllinger, I., Klinger, N., Geissler, A., Wurnig, M. C., Matt, E., Rath, J., Robinson, S. D., Trattnig, S., & Beisteiner, R. (2013). The benefits of skull stripping in the normalization of clinical fMRI data. *NeuroImage: Clinical*, *3*, 369–380. https://doi.org/10.1016/j.nicl.2013.09.007

Foster, J. R., Hall, D. A., Summerfield, A. Q., Palmer, A. R., & Bowtell, R. W. (2000). Sound-Level Measurements and Calculations of Safe Noise Dosage During EPI at 3 T. *Journal of Magnetic Resonance*

Imaging, *12*(1), 157–163. https://doi.org/10.1002/1522-2586(200007)12:1%3C157::AID-JMRI17%3E3.0.CO;2-M

Gardner, J. L., Merriam, E. P., Schluppeck, D., Besle, J., & Heeger, D. J. (2018). *mrTools: Analysis and visualization package for functional magnetic resonance imaging data*. Zenodo. https://doi.org/10.5281/zenodo.1299483

Gattass, R., Sousa, A. P., & Gross, C. G. (1988). Visuotopic organization and extent of V3 and V4 of the macaque. *Journal of Neuroscience*, *8*(6), 1831–1845. https://doi.org/10.1523/JNEUROSCI.08-06-01831.1988

Geuter, S., Qi, G., Welsh, R. C., Wager, T. D., & Lindquist, M. A. (2018). *Effect Size and Power in fMRI Group Analysis* (p. 295048). bioRxiv. https://doi.org/10.1101/295048

Glover, G. H. (1991). Phase-offset multiplanar (POMP) volume imaging: A new technique. *Journal of Magnetic Resonance Imaging: JMRI*, *1*(4), 457–461. https://doi.org/10.1002/jmri.1880010410

Gomez, J., Natu, V., Jeska, B., Barnett, M., & Grill-Spector, K. (2018). Development differentially sculpts receptive fields across early and high-level human visual cortex. *Nature Communications*, *9*(1), 788. https://doi.org/10.1038/s41467-018-03166-3

Gorgolewski, K., Burns, C., Madison, C., Clark, D., Halchenko, Y., Waskom, M., & Ghosh, S. (2011). Nipype: A Flexible, Lightweight and Extensible Neuroimaging Data Processing Framework in Python. *Frontiers in Neuroinformatics*, *5*.

Gorgolewski, K. J., Storkey, A. J., Bastin, M. E., Whittle, I., & Pernet, C. (2013). Single subject fMRI test–retest reliability metrics and confounding factors. *NeuroImage*, *69*, 231–243. https://doi.org/10.1016/j.neuroimage.2012.10.085

Greene, C. A., Dumoulin, S. O., Harvey, B. M., & Ress, D. (2014). Measurement of population receptive fields in human early visual cortex using back-projection tomography. *Journal of Vision*, *14*(1), 17–17. https://doi.org/10.1167/14.1.17

Griswold, M. A., Jakob, P. M., Heidemann, R. M., Nittka, M., Jellus, V., Wang, J., Kiefer, B., & Haase, A. (2002). Generalized autocalibrating partially parallel acquisitions (GRAPPA). *Magnetic Resonance in Medicine*, *47*(6), 1202–1210. https://doi.org/10.1002/mrm.10171

Gudbjartsson, H., & Patz, S. (1995). The rician distribution of noisy mri data. *Magnetic Resonance in Medicine*, *34*(6), 910–914. https://doi.org/10.1002/mrm.1910340618

Halai, A. D., Welbourne, S. R., Embleton, K., & Parkes, L. M. (2014). A comparison of dual gradient-echo and spin-echo fMRI of the inferior temporal lobe. *Human Brain Mapping*, *35*(8), 4118–4128. https://doi.org/10.1002/hbm.22463

Heilmaier, C., Theysohn, J. M., Maderwald, S., Kraff, O., Ladd, M. E., & Ladd, S. C. (2011). A large-scale study on subjective perception of discomfort during 7 and 1.5 T MRI examinations. *Bioelectromagnetics*, *32*(8), 610–619. https://doi.org/10.1002/bem.20680

Himmelberg, M. M., Kurzawski, J. W., Benson, N. C., Pelli, D. G., Carrasco, M., & Winawer, J. (2021). Cross-dataset reproducibility of human retinotopic maps. *NeuroImage*, *244*, 118609. https://doi.org/10.1016/j.neuroimage.2021.118609

Horton, J. C., & Hoyt, W. F. (1991). The representation of the visual field in human striate cortex. A revision of the classic Holmes map. *Archives of Ophthalmology (Chicago, Ill.: 1960)*, *109*(6), 816–824.

Howley, E., Francis, S., & Schluppeck, D. (2023). fRAT: An interactive, Python-based tool for region-of-interest summaries of functional imaging data. *Journal of Open Source Software*, *8*(85), 5200. https://doi.org/10.21105/joss.05200

Huettel, S. A., Song, A. W., McCarthy, G., Huettel, S. A., Song, A. W., & McCarthy, G. (2014). *Functional Magnetic Resonance Imaging* (Third Edition, Third Edition). Oxford University Press.

Hutton, C., Josephs, O., Stadler, J., Featherstone, E., Reid, A., Speck, O., Bernarding, J., & Weiskopf, N. (2011). The impact of physiological noise

correction on fMRI at 7T. *NeuroImage*, *57*(1), 101–112. https://doi.org/10.1016/j.neuroimage.2011.04.018

Jaermann, T., Pruessmann, K., Valavanis, A., Kollias, S., & Boesiger, P. (2006). Influence of SENSE on image properties in high-resolution single-shot echo-planar DTI. *Magnetic Resonance in Medicine*, *55*(2), 335–342. https://doi.org/10.1002/mrm.20769

Jamil, R., Mauconduit, F., Ster, C. L., Ehses, P., Poser, B. A., Vignaud, A., & Boulant, N. (2021). Temporal SNR optimization through RF coil combination in fMRI: The more, the better? *PLOS ONE*, *16*(11), e0259592. https://doi.org/10.1371/journal.pone.0259592

Jaspan, O. N., Fleysher, R., & Lipton, M. L. (2015). Compressed sensing MRI: A review of the clinical literature. *The British Journal of Radiology*, *88*(1056), 20150487. https://doi.org/10.1259/bjr.20150487

Jenkinson, M., Bannister, P., Brady, M., & Smith, S. (2002). Improved Optimization for the Robust and Accurate Linear Registration and Motion Correction of Brain Images. *NeuroImage*, *17*(2), 825–841. https://doi.org/10.1006/nimg.2002.1132

Jenkinson, M., Beckmann, C. F., Behrens, T. E. J., Woolrich, M. W., & Smith, S. M. (2012). FSL. *NeuroImage*, *62*(2), 782–790. https://doi.org/10.1016/j.neuroimage.2011.09.015

Kenny, D. A., & Judd, C. M. (1986). Consequences of violating the independence assumption in analysis of variance. *Psychological Bulletin*, *99*(3), 422–431. https://doi.org/10.1037/0033-2909.99.3.422

Kriegeskorte, N., Lindquist, M. A., Nichols, T. E., Poldrack, R. A., & Vul, E. (2010). Everything you never wanted to know about circular analysis, but were afraid to ask. *Journal of Cerebral Blood Flow and Metabolism: Official Journal of the International Society of Cerebral Blood Flow and Metabolism*, *30*(9), 1551–1557. https://doi.org/10.1038/jcbfm.2010.86

LaHuis, D. M., Hartman, M. J., Hakoyama, S., & Clark, P. C. (2014). Explained Variance Measures for Multilevel Models. *Organizational Research Methods*, *17*(4), 433–451. https://doi.org/10.1177/

1094428114541701

Larkman, D. J., Hajnal, J. V., Herlihy, A. H., Coutts, G. A., Young, I. R., & Ehnholm, G. (2001). Use of multicoil arrays for separation of signal from multiple slices simultaneously excited. *Journal of Magnetic Resonance Imaging: JMRI*, *13*(2), 313–317. https://doi.org/10.1002/1522-2586(200102)13:2%3C313::aid-jmri1045%3E3.0.co;2-w

Lee, S., Papanikolaou, A., Logothetis, N. K., Smirnakis, S. M., & Keliris, G. A. (2013). A new method for estimating population receptive field topography in visual cortex. *NeuroImage*, *81*, 144–157. https://doi.org/10.1016/j.neuroimage.2013.05.026

Levenberg, K. (1944). A Method for the Solution of Certain Non-Linear Problems in Least Squares. *Quarterly of Applied Mathematics*, *2*(2), 164–168. http://www.jstor.org/stable/43633451

Liang, D., Liu, B., Wang, J., & Ying, L. (2009). Accelerating SENSE using compressed sensing. *Magnetic Resonance in Medicine*, *62*(6), 1574–1584. https://doi.org/10.1002/mrm.22161

Linhardt, D., Pawloff, M., Hummer, A., Woletz, M., Tik, M., Ritter, M., Schmidt-Erfurth, U., & Windischberger, C. (2021). Combining stimulus types for improved coverage in population receptive field mapping. *NeuroImage*, *238*, 118240. https://doi.org/10.1016/j.neuroimage.2021.118240

Liu, T. T. (2016). Noise contributions to the fMRI signal: An overview. *NeuroImage*, *143*, 141–151. https://doi.org/10.1016/j.neuroimage.2016.09.008

Lutkenhoff, E. S., Rosenberg, M., Chiang, J., Zhang, K., Pickard, J. D., Owen, A. M., & Monti, M. M. (2014). Optimized Brain Extraction for Pathological Brains (optiBET). *PLOS ONE*, *9*(12), e115551. https://doi.org/10.1371/journal.pone.0115551

Maclaren, J., Herbst, M., Speck, O., & Zaitsev, M. (2013). Prospective motion correction in brain imaging: A review. *Magnetic Resonance in Medicine*, *69*(3), 621–636. https://doi.org/10.1002/mrm.24314

Marčenko, V. A., & Pastur, L. A. (1967). DISTRIBUTION OF EIGENVALUES FOR SOME SETS OF RANDOM MATRICES. *Mathematics of the USSR-Sbornik*, *1*(4), 457. https://doi.org/10.1070/SM1967v001n04ABEH001994

Marquardt, D. W. (1963). An Algorithm for Least-Squares Estimation of Nonlinear Parameters. *Journal of the Society for Industrial and Applied Mathematics*, *11*(2), 431–441. http://www.jstor.org/stable/2098941

Maudsley, A. (1981). Multiple Line Scanning Spin Density Imaging. *Journal of Computer Assisted Tomography*, *5*(2), 289.

McGibney, G., Smith, M. R., Nichols, S. T., & Crawley, A. (1993). Quantitative evaluation of several partial fourier reconstruction algorithms used in mri. *Magnetic Resonance in Medicine*, *30*(1), 51–59. https://doi.org/10.1002/mrm.1910300109

McJury, M. J. (2022). Acoustic Noise and Magnetic Resonance Imaging: A Narrative/Descriptive Review. *Journal of Magnetic Resonance Imaging*, *55*(2), 337–346. https://doi.org/10.1002/jmri.27525

Merkel, C., Hopf, J.-M., & Schoenfeld, M. A. (2018). Spatial elongation of population receptive field profiles revealed by model-free fMRI back-projection. *Human Brain Mapping*, *39*(6), 2472–2481. https://doi.org/10.1002/hbm.24015

Mildner, T., Norris, D. G., Schwarzbauer, C., & Wiggins, C. J. (2001). A qualitative test of the balloon model for BOLD-based MR signal changes at 3T. *Magnetic Resonance in Medicine*, *46*(5), 891–899. https://doi.org/10.1002/mrm.1274

Misztal, I. (2008). Reliable computing in estimation of variance components. *Journal of Animal Breeding and Genetics*, *125*(6), 363–370. https://doi.org/10.1111/j.1439-0388.2008.00774.x

Moeller, S., Pisharady, P. K., Ramanna, S., Lenglet, C., Wu, X., Dowdle, L., Yacoub, E., Uğurbil, K., & Akçakaya, M. (2021). NOise reduction with DIstribution Corrected (NORDIC) PCA in dMRI with complex-valued parameter-free locally low-rank processing. *NeuroImage*, *226*, 117539.

https://doi.org/10.1016/j.neuroimage.2020.117539

Molloy, E. K., Meyerand, M. E., & Birn, R. M. (2014). The influence of spatial resolution and smoothing on the detectability of resting-state and task fMRI. *NeuroImage*, *86*, 221–230. https://doi.org/10.1016/j.neuroimage.2013.09.001

Mowinckel, A. M., & Vidal-Piñeiro, D. (2020). Visualization of Brain Statistics With R Packages ggseg and ggseg3d. *Advances in Methods and Practices in Psychological Science*, *3*(4), 466–483. https://doi.org/10.1177/2515245920928009

Murphy, K., Bodurka, J., & Bandettini, P. A. (2007). How long to scan? The relationship between fMRI temporal signal to noise ratio and necessary scan duration. *NeuroImage*, *34*(2), 565–574. https://doi.org/10.1016/j.neuroimage.2006.09.032

Murphy, K. J., & Brunberg, J. A. (1997). Adult claustrophobia, anxiety and sedation in MRI. *Magnetic Resonance Imaging*, *15*(1), 51–54. https://doi.org/10.1016/S0730-725X(96)00351-7

Nakagawa, S., & Schielzeth, H. (2013). A general and simple method for obtaining R2 from generalized linear mixed-effects models. *Methods in Ecology and Evolution*, *4*(2), 133–142. https://doi.org/10.1111/j.2041-210x.2012.00261.x

Nelder, J. A., & Mead, R. (1965). A Simplex Method for Function Minimization. *The Computer Journal*, *7*(4), 308–313. https://doi.org/10.1093/comjnl/7.4.308

NiPreps. (n.d.). https://www.nipreps.org/.

Oakes, T. R., Johnstone, T., Ores Walsh, K. S., Greischar, L. L., Alexander, A. L., Fox, A. S., & Davidson, R. J. (2005). Comparison of fMRI motion correction software tools. *NeuroImage*, *28*(3), 529–543. https://doi.org/10.1016/j.neuroimage.2005.05.058

Olman, C. A., Davachi, L., & Inati, S. (2009). Distortion and Signal Loss in Medial Temporal Lobe. *PLoS ONE*, *4*(12), e8160. https://doi.org/10.

1371/journal.pone.0008160

Papanikolaou, A., Keliris, G. A., Papageorgiou, T. D., Shao, Y., Krapp, E., Papageorgiou, E., Stingl, K., Bruckmann, A., Schiefer, U., Logothetis, N. K., & Smirnakis, S. M. (2014). Population receptive field analysis of the primary visual cortex complements perimetry in patients with homonymous visual field defects. *Proceedings of the National Academy of Sciences*, *111*(16), E1656–E1665. https://doi.org/10.1073/pnas.1317074111

Pardoe, H. R., Kucharsky Hiess, R., & Kuzniecky, R. (2016). Motion and morphometry in clinical and nonclinical populations. *NeuroImage*, *135*, 177–185. https://doi.org/10.1016/j.neuroimage.2016.05.005

Parker, D. L., & Gullberg, G. T. (1990). Signal-to-noise efficiency in magnetic resonance imaging. *Medical Physics*, *17*(2), 250–257. https://doi.org/10.1118/1.596503

Parrish, T. B., Gitelman, D. R., LaBar, K. S., & Mesulam, M.-M. (2000). Impact of signal-to-noise on functional MRI. *Magnetic Resonance in Medicine*, *44*(6), 925–932. https://doi.org/10.1002/1522-2594(200012)44:6%3C925::AID-MRM14%3E3.0.CO;2-M

Penny, W. D., Friston, K. J., Ashburner, J. T., Kiebel, S. J., & Nichols, T. E. (2011). *Statistical Parametric Mapping: The Analysis of Functional Brain Images*. Elsevier.

Petridou, N., Italiaander, M., van de Bank, B. L., Siero, J. C. W., Luijten, P. R., & Klomp, D. W. J. (2013). Pushing the limits of high-resolution functional MRI using a simple high-density multi-element coil design. *NMR in Biomedicine*, *26*(1), 65–73. https://doi.org/10.1002/nbm.2820

Pinheiro, J., & Bates, D. (2006). *Mixed-Effects Models in S and S-PLUS*. Springer Science & Business Media.

Poldrack, R. A. (2007). Region of interest analysis for fMRI. *Social Cognitive and Affective Neuroscience*, *2*(1), 67–70. https://doi.org/10.1093/scan/nsm006

Popescu, V., Battaglini, M., Hoogstrate, W. S., Verfaillie, S. C. J., Sluimer,

I. C., van Schijndel, R. A., van Dijk, B. W., Cover, K. S., Knol, D. L., Jenkinson, M., Barkhof, F., de Stefano, N., & Vrenken, H. (2012). Optimizing parameter choice for FSL-Brain Extraction Tool (BET) on 3D T1 images in multiple sclerosis. *NeuroImage*, *61*(4), 1484–1494. https://doi.org/10.1016/j.neuroimage.2012.03.074

Possanzini, C., Ham, K., Hoogeveen, R., & Stoesz, M. (2011). *dStream architecture The digital revolution in MRI*.

Possanzini, C., van Liere, P., Roeven, H., den Boef, J., Saylor, C., van Eggermond, J., Harvey, P., & Moore, E. (2011). Scalability & Channel Independency of the Digital Broadband DStream Architecture. *ISMRM*.

Posse, S., Shen, Z., Kiselev, V., & Kemna, L. J. (2003). Single-shot T2* mapping with 3D compensation of local susceptibility gradients in multiple regions. *NeuroImage*, *18*(2), 390–400. https://doi.org/10.1016/S1053-8119(02)00016-2

Posse, S., Wiese, S., Gembris, D., Mathiak, K., Kessler, C., Grosse-Ruyken, M.-L., Elghahwagi, B., Richards, T., Dager, S. R., & Kiselev, V. G. (1999). Enhancement of BOLD-contrast sensitivity by single-shot multi-echo functional MR imaging. *Magnetic Resonance in Medicine*, *42*(1), 87–97. https://doi.org/10.1002/(SICI)1522-2594(199907)42:1%3C87::AID-MRM13%3E3.0.CO;2-O

Preibisch, C., Castrillón G., J. G., Bührer, M., & Riedl, V. (2015). Evaluation of Multiband EPI Acquisitions for Resting State fMRI. *PLoS ONE*, *10*(9). https://doi.org/10.1371/journal.pone.0136961

Pruessmann, K. P., Weiger, M., Scheidegger, M. B., & Boesiger, P. (1999). SENSE: Sensitivity encoding for fast MRI. *Magnetic Resonance in Medicine*, *42*(5), 952–962. https://doi.org/10.1002/(SICI)1522-2594(199911)42:5%3C952::AID-MRM16%3E3.0.CO;2-S

Puckett, A. M., Bollmann, S., Poser, B. A., Palmer, J., Barth, M., & Cunnington, R. (2018). Using multi-echo simultaneous multi-slice (SMS) EPI to improve functional MRI of the subcortical nuclei of the basal ganglia at ultra-high field (7T). *NeuroImage*, *172*, 886–895. https://doi.org/10.

1016/j.neuroimage.2017.12.005

Reeder, S. B. (2007). Measurement of Signal-to-Noise Ratio and Parallel Imaging. In S. O. Schoenberg, O. Dietrich, & M. F. Reiser (Eds.), *Parallel Imaging in Clinical MR Applications* (pp. 49–61). Springer. https://doi.org/10.1007/978-3-540-68879-2_4

Risk, B. B., Murden, R. J., Wu, J., Nebel, M. B., Venkataraman, A., Zhang, Z., & Qiu, D. (2021). Which multiband factor should you choose for your resting-state fMRI study? *NeuroImage*, *234*, 117965. https://doi.org/10.1016/j.neuroimage.2021.117965

Saad, Z. S., Ropella, K. M., DeYoe, E. A., & Bandettini, P. A. (2003). The spatial extent of the BOLD response. *NeuroImage*, *19*(1), 132–144. https://doi.org/10.1016/S1053-8119(03)00016-8

Sartoretti, T., Reischauer, C., Sartoretti, E., Binkert, C., Najafi, A., & Sartoretti-Schefer, S. (2018). Common artefacts encountered on images acquired with combined compressed sensing and SENSE. *Insights into Imaging*, *9*(6), 1107–1115. https://doi.org/10.1007/s13244-018-0668-4

Schielzeth, H., Dingemanse, N. J., Nakagawa, S., Westneat, D. F., Allegue, H., Teplitsky, C., Réale, D., Dochtermann, N. A., Garamszegi, L. Z., & Araya-Ajoy, Y. G. (2020). Robustness of linear mixed-effects models to violations of distributional assumptions. *Methods in Ecology and Evolution*, *11*(9), 1141–1152. https://doi.org/10.1111/2041-210X.13434

Schmidt, C. F., Degonda, N., Luechinger, R., Henke, K., & Boesiger, P. (2005). Sensitivity-encoded (SENSE) echo planar fMRI at 3T in the medial temporal lobe. *NeuroImage*, *25*(2), 625–641. https://doi.org/10.1016/j.neuroimage.2004.12.002

Silva, A. C., Lee, S.-P., Iadecola, C., & Kim, S.-G. (2000). Early Temporal Characteristics of Cerebral Blood Flow and Deoxyhemoglobin Changes during Somatosensory Stimulation. *Journal of Cerebral Blood Flow & Metabolism*, *20*(1), 201–206. https://doi.org/10.1097/00004647-200001000-00025

Slipsager, J. M., Glimberg, S. L., Højgaard, L., Paulsen, R. R., Wighton,

P., Tisdall, M. D., Jaimes, C., Gagoski, B. A., Grant, P. E., van der Kouwe, A., Olesen, O. V., & Frost, R. (2022). Comparison of prospective and retrospective motion correction in 3D-encoded neuroanatomical MRI. *Magnetic Resonance in Medicine*, *87*(2), 629–645. https://doi.org/10.1002/mrm.28991

Smith, A. M., Lewis, B. K., Ruttimann, U. E., Ye, F. Q., Sinnwell, T. M., Yang, Y., Duyn, J. H., & Frank, J. A. (1999). Investigation of Low Frequency Drift in fMRI Signal. *NeuroImage*, *9*(5), 526–533. https://doi.org/10.1006/nimg.1999.0435

Smith, S. M. (2002). Fast robust automated brain extraction. *Human Brain Mapping*, *17*(3), 143–155. https://doi.org/10.1002/hbm.10062

Smith, S. M., & Brady, J. M. (1997). SUSAN—A New Approach to Low Level Image Processing. *International Journal of Computer Vision*, *23*(1), 45–78. https://doi.org/10.1023/A:1007963824710

Steinman, R. M. (1965). Effect of Target Size, Luminance, and Color on Monocular Fixation*. *JOSA*, *55*(9), 1158–1164. https://doi.org/10.1364/JOSA.55.001158

Stöcker, T., Kellermann, T., Schneider, F., Habel, U., Amunts, K., Pieperhoff, P., Zilles, K., & Shah, N. J. (2006). Dependence of amygdala activation on echo time: Results from olfactory fMRI experiments. *NeuroImage*, *30*(1), 151–159. https://doi.org/10.1016/j.neuroimage.2005.09.050

Takahashi, M., Uematsu, H., & Hatabu, H. (2003). MR imaging at high magnetic fields. *European Journal of Radiology*, *46*(1), 45–52. https://doi.org/10.1016/S0720-048X(02)00331-5

Tjandra, T., Brooks, J., Figueiredo, P., Wise, R., Matthews, P., & Tracey, I. (2005). Quantitative assessment of the reproducibility of functional activation measured with BOLD and MR perfusion imaging: Implications for clinical trial design. *NeuroImage*, *27*(2).

Todd, N., Josephs, O., Zeidman, P., Flandin, G., Moeller, S., & Weiskopf, N. (2017). Functional Sensitivity of 2D Simultaneous Multi-Slice Echo-Planar Imaging: Effects of Acceleration on g-factor and Physiological

Noise. *Frontiers in Neuroscience*, *11*, 158. https://doi.org/10.3389/fnins.2017.00158

Todd, N., Moeller, S., Auerbach, E. J., Yacoub, E., Flandin, G., & Weiskopf, N. (2016). Evaluation of 2D multiband EPI imaging for high-resolution, whole-brain, task-based fMRI studies at 3T: Sensitivity and slice leakage artifacts. *NeuroImage*, *124*, 32–42. https://doi.org/10.1016/j.neuroimage.2015.08.056

Tomasi, D., Caparelli, E. C., Chang, L., & Ernst, T. (2005). fMRI-acoustic noise alters brain activation during working memory tasks. *NeuroImage*, *27*(2), 377–386. https://doi.org/10.1016/j.neuroimage.2005.04.010

Triantafyllou, C., Hoge, R. D., & Wald, L. L. (2006). Effect of spatial smoothing on physiological noise in high-resolution fMRI. *NeuroImage*, *32*(2), 551–557. https://doi.org/10.1016/j.neuroimage.2006.04.182

van der Laan, M. J., Dudoit, S., & Pollard, K. S. (2004). Multiple testing. Part II. Step-down procedures for control of the family-wise error rate. *Statistical Applications in Genetics and Molecular Biology*, *3*, Article14. https://doi.org/10.2202/1544-6115.1041

van Dijk, J. A., de Haas, B., Moutsiana, C., & Schwarzkopf, D. S. (2016). Intersession reliability of population receptive field estimates. *NeuroImage*, *143*, 293–303. https://doi.org/10.1016/j.neuroimage.2016.09.013

Veraart, J., Fieremans, E., & Novikov, D. S. (2016). Diffusion MRI noise mapping using random matrix theory. *Magnetic Resonance in Medicine*, *76*(5), 1582–1593. https://doi.org/10.1002/mrm.26059

Veraart, J., Novikov, D. S., Christiaens, D., Ades-aron, B., Sijbers, J., & Fieremans, E. (2016). Denoising of diffusion MRI using random matrix theory. *NeuroImage*, *142*, 394–406. https://doi.org/10.1016/j.neuroimage.2016.08.016

Vranic, J. E., Cross, N. M., Wang, Y., Hippe, D. S., Weerdt, E. de, & Mossa-Basha, M. (2019). Compressed Sensing–Sensitivity Encoding (CS-SENSE) Accelerated Brain Imaging: Reduced Scan Time without Reduced Image Quality. *American Journal of Neuroradiology*, *40*(1), 92–98.

https://doi.org/10.3174/ajnr.A5905

Wald, L. L. (2012). The future of acquisition speed, coverage, sensitivity, and resolution. *NeuroImage*, *62*(2), 1221–1229. https://doi.org/10.1016/j.neuroimage.2012.02.077

Wald, L. L., & Polimeni, J. R. (2017). Impacting the effect of fMRI noise through hardware and acquisition choices – Implications for controlling false positive rates. *NeuroImage*, *154*, 15–22. https://doi.org/10.1016/j.neuroimage.2016.12.057

Wandell, B. A., Dumoulin, S. O., & Brewer, A. A. (2007). Visual Field Maps in Human Cortex. *Neuron*, *56*(2), 366–383. https://doi.org/10.1016/j.neuron.2007.10.012

Wang, L., Mruczek, R. E. B., Arcaro, M. J., & Kastner, S. (2015). Probabilistic Maps of Visual Topography in Human Cortex. *Cerebral Cortex (New York, NY)*, *25*(10), 3911–3931. https://doi.org/10.1093/cercor/bhu277

Webster, M. (2017). Bandpass temporal filtering [Online Mailing List]. In *JISCMail - FSL Archives*. https://www.jiscmail.ac.uk/cgi-bin/webadmin?A2=FSL;f6fd75a6.1709.

Weiger, M., Pruessmann, K. P., Österbauer, R., Börnert, P., Boesiger, P., & Jezzard, P. (2002). Sensitivity-encoded single-shot spiral imaging for reduced susceptibility artifacts in BOLD fMRI. *Magnetic Resonance in Medicine*, *48*(5), 860–866. https://doi.org/10.1002/mrm.10286

Welvaert, M., & Rosseel, Y. (2013). On the Definition of Signal-To-Noise Ratio and Contrast-To-Noise Ratio for fMRI Data. *PLOS ONE*, *8*(11), e77089. https://doi.org/10.1371/journal.pone.0077089

Westfall, P. H., & Young, S. S. (1993). *Resampling-based multiple testing: Examples and methods for p-value adjustment* (Vol. 279). John Wiley & Sons.

Worsley, K. J., Liao, C. H., Aston, J., Petre, V., Duncan, G. H., Morales, F., & Evans, A. C. (2002). A General Statistical Analysis for fMRI Data. *NeuroImage (Orlando, Fla.)*, *15*(1), 1–15. https://doi.org/10.1006/nimg.

2001.0933

Yakupov, R., Lei, J., Hoffmann, M. B., & Speck, O. (2017). False fMRI activation after motion correction. *Human Brain Mapping*, *38*(9), 4497–4510. https://doi.org/10.1002/hbm.23677

Yang, Q. X., Wang, J., Smith, M. B., Meadowcroft, M., Sun, X., Eslinger, P. J., & Golay, X. (2004). Reduction of magnetic field inhomogeneity artifacts in echo planar imaging with SENSE and GESEPI at high field. *Magnetic Resonance in Medicine*, *52*(6), 1418–1423. https://doi.org/10.1002/mrm.20303

Yoo, P. E., John, S. E., Farquharson, S., Cleary, J. O., Wong, Y. T., Ng, A., Mulcahy, C. B., Grayden, D. B., Ordidge, R. J., Opie, N. L., O'Brien, T. J., Oxley, T. J., & Moffat, B. A. (2018). 7T-fMRI: Faster temporal resolution yields optimal BOLD sensitivity for functional network imaging specifically at high spatial resolution. *NeuroImage*, *164*, 214–229. https://doi.org/10.1016/j.neuroimage.2017.03.002

Zaitsev, M., Akin, B., Levan, P., & Knowles, B. R. (2017). Prospective motion correction in functional MRI. *NeuroImage*, *154*, 33–42. https://doi.org/10.1016/j.neuroimage.2016.11.014

Zhang, N., Zhu, X.-H., & Chen, W. (2005). Influence of gradient acoustic noise on fMRI response in the human visual cortex. *Magnetic Resonance in Medicine*, *54*(2), 258–263. https://doi.org/10.1002/mrm.20512

Zhang, Y., Brady, M., & Smith, S. (2001). Segmentation of brain MR images through a hidden Markov random field model and the expectation-maximization algorithm. *IEEE Transactions on Medical Imaging*, *20*(1), 45–57. https://doi.org/10.1109/42.906424

Zong, X., Lee, J., John Poplawsky, A., Kim, S.-G., & Ye, J. C. (2014). Compressed sensing fMRI using gradient-recalled echo and EPI sequences. *NeuroImage*, *92*, 312–321. https://doi.org/10.1016/j.neuroimage.2014.01.045